Title
Majorana physics in entangled quantum matter: from Kitaev spin liquids to monitored quantum circuits

ISBN
9798189276903

Author
Klocke, Kai Christian

Publication Date
2026-05-01

Peer reviewed|Thesis/dissertation

Majorana Physics in Entangled Quantum Matter: from Kitaev Spin Liquids to Monitored Quantum Circuits

by

Kai Klocke

A dissertation submitted in partial satisfaction of the

requirements for the degree of

Doctor of Philosophy

in

Physics

in the

Graduate Division

of the

University of California, Berkeley

Committee in charge:

Professor Joel Moore, Chair
Associate Professor Michael Zaletel
Professor Katherine Birgitta Whaley

Spring 2026

Majorana Physics in Entangled Quantum Matter:
from Kitaev Spin Liquids to Monitored Quantum Circuits

Abstract

Majorana Physics in Entangled Quantum Matter:
from Kitaev Spin Liquids to Monitored Quantum Circuits

by

Kai Klocke

Doctor of Philosophy in Physics

University of California, Berkeley

Professor Joel Moore, Chair

Majorana fermions arise in a broad range of systems in condensed matter physics, not only as a useful abstraction but also as emergent quasiparticles, e.g., at the boundaries of topological insulators. In this dissertation, we consider two distinct settings wherein Majorana fermions play a central role: (i) non-abelian Kitaev spin liquids and (ii) entanglement dynamics in monitored quantum circuits

The Kitaev spin liquid is a paradigmatic model featuring non-abelian anyons and a chiral Majorana edge mode when time-reversal symmetry is broken. To this end, it presents an alluring platform for realizing topologically protected quantum information. However, experimental efforts to identify this putative phase have been hampered both by the difficulty of probing the charge neutral quasiparticles and by the presence of phonons and other deviations from the idealized toy model. Here we examine how judicious device design may suppress bulk phonon contributions to thermal transport, allowing for refined observation of transport mediated by the chiral Majorana edge mode. Moreover, we show that the bulk topological order can be revealed through universal features in the tunneling conductance across a point contact. Looking forward, we develop a roadmap for near-term experimental devices to demonstrate robust control of topologically protected qubits encoded in the bulk anyons.

Much as Majorana models form the building blocks for symmetry-protected topological order, Majorana circuits provide a powerful framework for studying the entanglement dynamics and phases of monitored quantum circuits. Here we show that the entanglement dynamics of Majorana circuits can be mapped exactly to the statistical mechanics of classical loop models. Harnessing this framework, we undertake a precise numerical characterization of the universality of entanglement transitions in symmetry classes BDI and D in both (1+1) and (2+1)-dimensional circuits. Furthermore, we employ duality relations for loop models to construct an analytically solvable interacting circuit which features not only the usual percolation criticality but also Berezinskii-Kosterlitz-Thouless critical lines and a tricritical point with Ising universality. Lastly, by generalizing to colored loop models for Majorana circuits with classical control, we provide a blueprint for engineering even more diverse entanglement dynamics which may include Hilbert-space fragmentation and subdiffusive transport.

Contents

List of Figures

List of Tables

Acknowledgments

Firstly, I would like to extend my deepest gratitude to my advisor Professor Joel Moore for his support, endless patience, and many stimulating conversations. No matter what new question or idea I brought to him, he was always prepared with insightful feedback to gently guide me.

I am also grateful to Professor Michael Zaletel for the advice and opportunities he afforded me throughout my time at Berkeley. Many thanks to Koh Yamakawa, Chunxiao Liu, Dan Borgnia, Yi Li and the other occupants of Birge for making these past few years so enjoyable.

I want to thank my longtime mentors, Michael Buchhold and Jason Alicea, for their support and continued collaboration. Their guidance over the years has fundamentally shaped the way that I approach physics. I am grateful to Michael for the copious amount of coffee, pizza, and laughter we have shared over many years of friendship, from Red Door cafe to Cologne. Thank you to Sebastian Diehl, Simon Trebst, Guo-Yi Zhu, and the many others who made my visits to Cologne so fruitful.

Reaching this point has only been possible with the unwavering support from my family and friends, to whom I extend my thanks. To my parents, for giving me so many opportunities growing up and for laughing with me along the way. To my aunt, uncle, and late grandfather, who have encouraged my curiosity and interest in the sciences since childhood. Lastly, I am forever grateful to Sarah, for keeping me grounded and reminding me that there is life to be enjoyed outside of my work.

Chapter 1

Introduction

In 1937, Italian physicist Etorre Majorana described real relativistic fermions which, by virtue of the wavefunction being real-valued, are their own antiparticles [229]. The eponymous Majorana fermion γ thus satisfies the identity $\gamma^2 = 1$ and commutation relations $\{\gamma_i, \gamma_j\} = 2\delta_{ij}$. Despite Majorana's original work receiving little attention at the time of its publication, Majorana fermions are a mainstay of contemporary physics, from condensed matter to quantum information.

In condensed matter systems, Majorana fermions offer a powerful framework for studying a diverse set of phenomena. From the Ising chain to Kitaev's honeycomb model [185], a number of paradigmatic Hamiltonian models may be viewed in terms of competing dimerizations of Majorana pairings. Moreover, Majorana representations provide a practical basis and graphical representation across a number of settings such as the classification of symmetry protected topological phases [336] or generalized Chalker-Coddington network models for disordered fractional quantum Hall states [247, 342, 219]. Beyond the blackboard, Majorana fermions may arise as emergent quasiparticles in topological phases of matter.This has spurred intense experimental effort to realize Majorana bound states in platforms ranging from quantum nanowires to $p + ip$ superconductors to fractional quantum Hall states [183, 118, 270, 35, 11, 227].

Such emergent Majorana modes are particularly alluring due to their potential applications in quantum computation and information [12, 176, 278, 279, 35, 11, 306, 339, 261, 184]. Given two Majorana modes $\gamma_{1/2}$, we may form a complex fermion $c = (\gamma_1 + i\gamma_2)/2$. The occupation of this fermionic mode yields a two-level system which might be used to encode information in the effective logical qubit $Z = i\gamma_1\gamma_2$. When γ_1 and γ_2 are well-separated relative to the bulk correlation length, the qubit state is encoded *non-locally*, and thus is protected against local error and decoherence channels. Furthermore, when such Majoranas appear as bulk anyons, non-trivial braiding statistics enables topologically-protected quantum gates in the non-locally encoded Hilbert space. To this end, Majorana fermions provide an elementary building block for constructing intrinsically fault-tolerant quantum memory and implementing topologically protected quantum computation.

1.1 Organization

The remainder of this dissertation is divided into two parts, which examine Majorana fermions in two distinct contexts.

Part I is concerned with Kitaev spin liquids (KSLs), where we are interested in detecting emergent Majorana quasiparticles and utilizing them to build topologically protected qubits. We begin in Ch. 2 with a review of the essential features of KSLs and candidate materials (e.g., α-$RuCl_3$). Then in Ch. 3 we examine thermal transport in phonon-coupled KSLs. While such coupling tends to destroy quantization of the transverse thermal conductivity in a Hall bar geometry, we demonstrate that judicious device design allows for careful control of phonon effects and thus more robust observation of quantization. We further show how thermal transport may be used to probe bulk anyons, revealing signatures of non-abelian topological order and yielding a novel scheme for thermal anyon interferometry. In Ch. 4 we build upon recent proposals for probing and controlling anyons in KSLs to develop minimal device designs for implementing quantum computing primitives via spin-liquid-based topological qubits.

In Part II, we turn our attention to monitored quantum circuits, where Majorana models provide a robust framework for studying entanglement phases and dynamics which arise in such systems. This section begins in Ch. 5 with a review of monitored quantum circuits and entanglement transitions. Next, in Ch. 6 we present an exact mapping between entanglement in Majorana circuits and the statistical mechanics of loop models. Building upon this mapping, Ch. 7 provides a detailed characterization of the symmetry classes and universality of entanglement transitions in monitored Majorana circuits in one and two spatial dimensions. The final two chapters concern generalizations beyond the strictly Gaussian limit of these circuits. In particular, Ch. 8 examines interacting Clifford circuits. We show that although local spin operators may be highly non-local fermionic operators, interactions are irrelevant in the renormalization-group sense, yielding an emergent long-wavelength loop picture. Moreover, we construct an exactly solvable interacting model exhibiting a diverse set of entanglement phases and critical points. Finally, Ch. 9 concerns hybrid circuits, wherein the Majorana circuit interacts with a classical agent such that operations are conditioned upon the local state of the system and agent. We show that such a setup allows for kinetic constraints to be imposed on the dynamics, enabling us to engineer dynamics exhibiting novel an robust entanglement structure.

Part I

Kitaev spin liquids

Chapter 2

Background

A quantum spin liquids (QSL) is an exotic phase of quantum matter which have garnered significant attention in condensed matter physics over the last several decades. Early work on QSLs arose from Philip Anderson's seminal paper proposing a resonating valence bond (RVB) ground-state for the antiferromagnetic Heisenberg model on a triangular lattice [14, 105, 368]. The RVB state, depicted schematically in Fig. 2.1(a), is a superposition over all dimer tilings of the lattice, where each dimer corresponds to a singlet state formed between the two spins. This state exemplifies two key characteristics of a quantum spin liquid (QSL): (i) long-range entanglement and (ii) the absence of magnetic order [307, 52]. Gapped QSL phases may support non-trivial topological order, featuring fractionalized quasiparticles which cannot be created in isolation. Despite decades of attention, definitive experimental evidence of a QSL phase has remained elusive.

2.1 Kitaev honeycomb model

While initial interest in QSLs was spurred by Philip Anderson, much of the work over the last two decades has been inspired by an exactly solvable model proposed by Alexei Kitaev [186]. Whereas other routes to spin liquid physics rely upon geometric frustration (e.g., triangle lattice anti-ferromagnets), the so-called Kitaev honeycomb model relies instead upon directional dependent spin interactions. For $\alpha \in \{x, y, z\}$ labeling the three types of bonds in the honeycomb lattice [see Fig. 2.2(a)], the Kitaev model is given by the spin-1/2 Hamiltonian,

$$H_0 = \sum_{\langle ij \rangle_\alpha} J_\alpha \sigma_i^\alpha \sigma_j^\alpha, \tag{2.1}$$

where $\langle ij \rangle_\alpha$ denotes the nearest-neighbor bond of type α connecting sites i and j. For every plaquette p there is a conserved $\mathbb{Z}_2$ flux W_p, defined as the product of the link terms $\sigma_i^\alpha \sigma_j^\alpha$ around the plaquette. The ground state of H_0 lies in the vacuum flux sector where $W_p = 1$ for all plaquettes [220, 185].

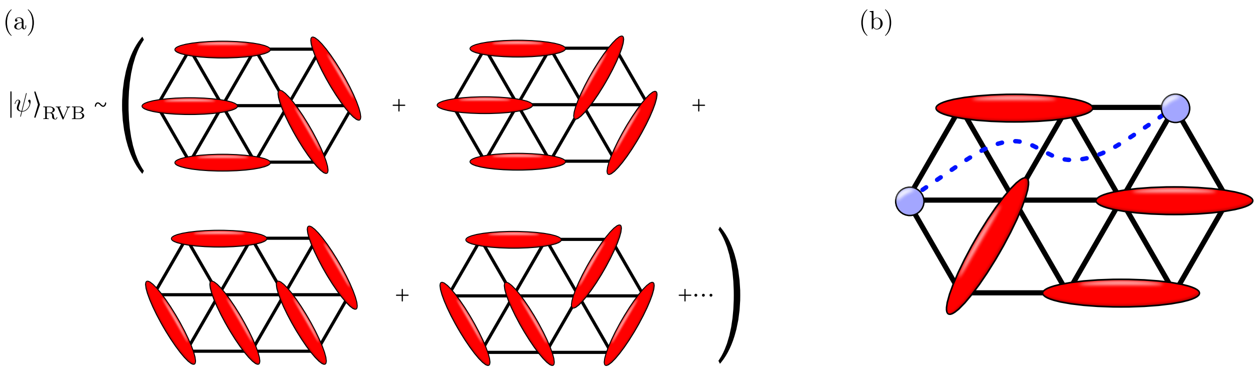

Figure 2.1: **Resonating valence bond state.** (a) Anderson's proposed resonating valence bond (RVB) ground-state for the triangular lattice antiferromagnetic Heisenberg model consists of a superposition of dimer coverings of the lattice. Each spin forms a singlet state (red oval) with one of its neighboring spins. (b) An excitation atop the RVB state can be created by splitting a singlet, leaving a pair of holes (blue circles) which may independently move through the RVB background.

This model may be transformed to a free-fermion problem by passing to a Majorana representation. For each spin we introduce four Majorana fermions such that the Pauli operators are $\sigma_i^\alpha = ib_i^\alpha c_i$, where b_i^α and c_i are denoted the gauge and matter Majoranas, respectively. The four Majoranas form a four dimensional Hilbert space within which the physical Hilbert space of the spin is that for which $b_i^x b_i^y b_i^z c_i = 1$. Denoting $u_{ij} = ib_i^\alpha b_j^\alpha$ on each bond, the Hamiltonian becomes $H_0 = -\sum_{\langle ij\rangle_\alpha} J_\alpha u_{ij} c_i c_j$. It is straightforward to show that the link terms u_{ij} are mutually commuting and conserved, forming a $\mathbb{Z}_2$ gauge field. In a fixed gauge sector (e.g., $u_{ij} = 1$ for the ground-state), the Hamiltonian is quadratic in the matter fermions,

$$H_0 = -i \sum_{\langle ij\rangle_\alpha} J_\alpha c_i c_j. \tag{2.2}$$

While the gauge fermions are always gapped, several distinct phases are realized by the matter fermions upon varying the bond strengths J_α [see Fig. 2.2(b)]. When one flavor of bond dominates, $|J_\alpha| > |J_\beta| + |J_\nu|$, the matter fermion spectrum is gapped. This yields three topologically distinct phases, denoted A_α, of gapped abelian $\mathbb{Z}_2$ spin liquid. When no flavor dominates, strong competition between the different bonds yields a gapless spectrum for matter fermions. This so-called B phase is a gapless abelian $\mathbb{Z}_2$ spin liquid protected by time-reversal symmetry. Upon breaking time-reversal symmetry, one may gap out the itinerant fermions in the B phase and realize non-abelian topological order.

In the fermion language, this can be achieved by a perturbation which introduces finite next-nearest-neighbor interactions between the matter fermions, $H_1 = -\kappa \sum_{\langle\langle ij\rangle\rangle} c_i c_j$. Each term may be viewed as product of two nearest-neighbor bonds, corresponding to a three-spin operator. Kitaev suggested that such a perturbation may be realized by applying

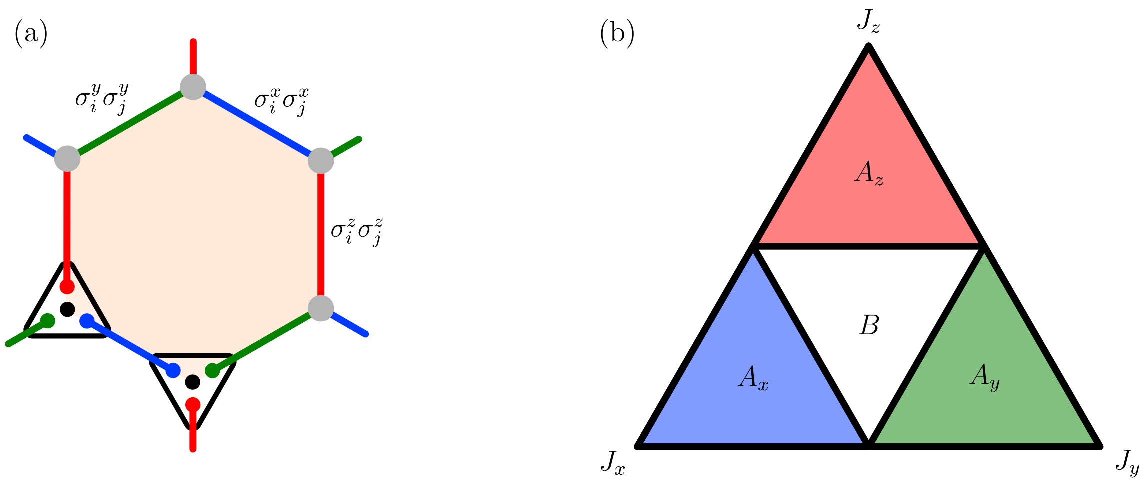

Figure 2.2: **Kitaev's honeycomb model.** (a) Direction-dependent interactions along the edges of a honeycomb lattice, which have been colored according to their direction. Each spin-1/2 (grey circle) may be decomposed into four Majorana fermions (triangular inset) such that interactions become quadratic in Majorana fermions. Hexagonal plaquettes (shaded orange) host conserved $\mathbb{Z}_2$ flux given by the product of bond interactions about the plaquette. (b) Phase diagram of the Hamiltonian in Eq. (2.1) in the plane $J_x + J_y + J_z = 1$. When one flavor of interaction dominates, we have a gapped abelian phase $A_{x/y/z}$. In the center of the phase diagram we have a gapless phase labeled B.

a weak Zeeman field $\Delta H = \sum_{i,\alpha} h_\alpha \sigma_i^\alpha$, with the effective interaction strength $\kappa \sim h^3/J^2$ arising at third-order in perturbation theory. Alternatively, time-reversal symmetry may be broken spontaneously by defining a Kitaev Hamiltonian on a non-bipartite lattice such as the decorated honeycomb lattice [359].

2.2 Non-abelian spin liquid phase

The resulting non-abelian spin liquid phase – the Kitaev spin liquid (KSL) – has Ising topological order with non-trivial excitations summarized in Fig. 2.3.

At the boundary, the KSL hosts a gapless chiral Majorana edge mode described by a chiral Ising conformal field theory (CFT) with central charge $c = 1/2$. Since this edge mode is charge-neutral, it does *not* mediate a quantized electrical conductance. It does, however, transport energy and so yields a half-integer quantized thermal Hall conductivity $\kappa_{xy} = \frac{1}{2}\kappa_0$, where $\kappa_0 = \pi k_B^2 T/6\hbar$ is the thermal conductivity quantum.

In the bulk, three types of gapped quasiparticles can appear: topologically trivial local bosons (I), emergent fermions (ψ), and non-Abelian Ising anyons (σ) that correspond to $\mathbb{Z}_2$ flux excitations [see Fig. 2.3(a)]. Non-Abelian properties of the Ising anyons descend from an

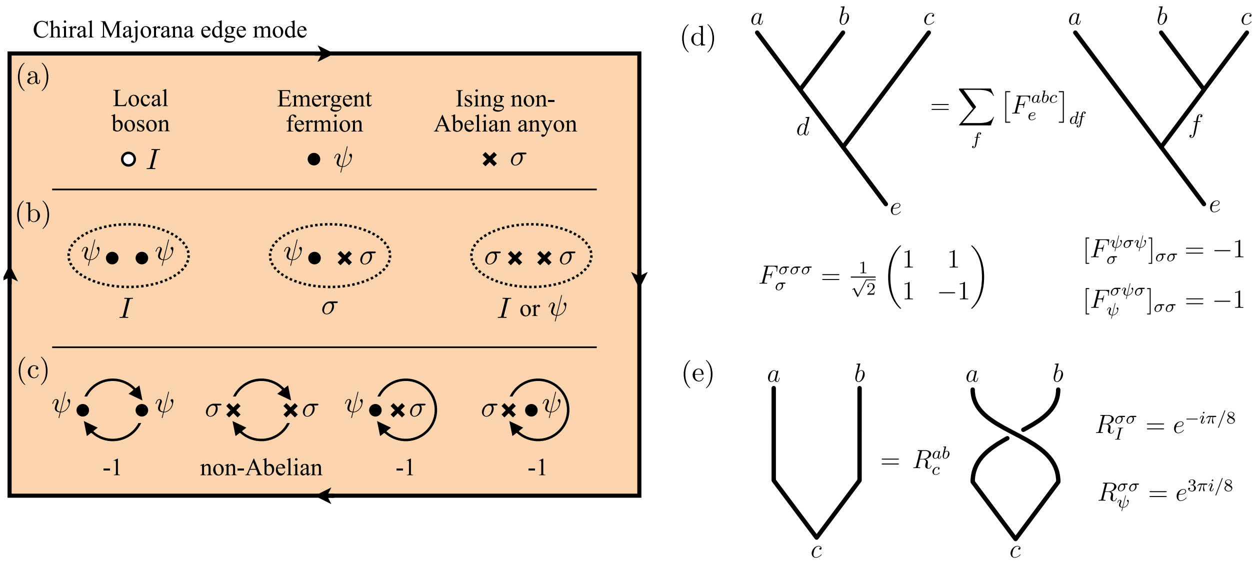

Figure 2.3: **Topological properties of the non-abelian Kitaev spin liquid phase** The boundary between the spin-liquid phase and a trivial phase hosts a chiral Majorana edge mode. The gapped bulk supports three types of quasiparticles enumerated in (a); their nontrivial fusion rules and braiding statistics are summarized in (b) and (c), respectively. (d) Formal expression of the F-matrix encoding relations between different orders for fusing three anyons. (e) Expression of the braiding phase R_c^{ab} accumulated when exchanging anyons a and b with fixed fusion channel c.

emergent Majorana zero mode that binds to a $\mathbb{Z}_2$ flux in this phase. A pair of well-separated Ising anyons (binding Majorana zero modes γ_1 and γ_2) thereby shares a single fermionic level [described by $f \equiv (\gamma_1 + i\gamma_2)/2$] that can be either empty or filled without changing the system's energy. In turn, these zero modes encode a locally indistinguishable ground-state degeneracy that grows exponentially as the number of bulk Ising anyons increases.

Fermions and Ising anyons obey fusion rules

$$\psi \times \psi = I, \quad \psi \times \sigma = \sigma, \quad \sigma \times \sigma = I + \psi \tag{2.3}$$

that specify how these quasiparticles behave when they coalesce [see Fig. 2.3(b)]. The first fusion rule dictates that two emergent fermions combine to form a local boson. The second indicates that an Ising anyon that absorbs an emergent fermion remains an Ising anyon; this property reflects the fact that the absorption merely changes the occupation of the fermionic two-level system shared jointly with some distant Ising anyon. The last fusion rule indicates that two Ising anyons can either annihilate or form an emergent fermion. These two 'fusion channels' correspond to the unoccupied and occupied states of their shared fermionic two-level system—which will no longer be degenerate when the associated Majorana zero modes are sufficiently close to hybridize appreciably.

Local bosons exhibit trivial braiding statistics with each other and with all other quasiparticle types. Emergent fermions of course exhibit fermionic statistics with each other, but also display nontrivial mutual statistics with Ising anyons: Dragging a fermion all the way around an Ising anyon or vice versa yields a statistical phase of -1. Finally, Ising anyons obey non-Abelian braiding statistics. That is, adiabatically swapping the location of Ising anyon pairs non-commutatively rotates the system's wavefunction within the ground-state manifold in a manner that depends only on topological properties of the anyon trajectories. Figure 2.3(c) summarizes the above quasiparticle braiding properties.

When fusing multiple anyons, the intermediate fusion channels depend on the order of fusion. Changing the fusion order may thus be viewed as a change of basis in fusion space, encoded in the F-matrix as depicted in Fig. 2.3(d). Notably, for fusion of three Ising anyons, the F-matrix coincides with the Hadamard matrix over a basis of allowed fusion outcomes (I and ψ). The fermions ψ and Ising anyons σ are mutual semions, accumulating a braiding phase -1 when wrapped around one another. By contrast, braiding of Ising anyons with one another is non-abelian. When the two Ising anyons have a fixed fusion outcome c, then exchange yields a statistical phase given by $R_c^{\sigma\sigma}$ [see Fig. 2.3(e)] which differs from conventional bosonic or fermionic statistics (± 1).

2.3 Fault-tolerant qubits

We stress that local indistinguishability of the ground-state subspace, nontrivial fusion rules, and non-Abelian braiding statistics are deeply related hallmarks of non-Abelian anyons [295]—which in the present context all elegantly descend from emergent Majorana zero modes bound to $\mathbb{Z}_2$ fluxes. These hallmarks further underlie utility for intrinsically fault-tolerant quantum computation. Here we review the essential details of how fault-tolerant qubits may be realized with the non-abelian Ising anyons which arise in a KSL.

As noted earlier, a pair of Ising anyons forms a complex fermion whose occupation corresponds to the fusion channel. This two-level system is degenerate but may be split by a Zeeman-like interaction term $i\gamma_0\gamma_1$, which will generally decay as $e^{-L/\xi}$ for separation L and bulk correlation length ξ. By taking the anyons to be well-separated relative to the correlation length, we then obtain a qubit with effectively degenerate levels. Moreover, since fusion is required to determine the occupation of fermionic mode, the two states are locally indistinguishable. Then for $2n$ well-separated Ising anyons, we have a fusion space of dimension 2^n in which we may encode a quantum state. Braiding of the bulk anyons will implement a unitary transformation on the degenerate fusion space. For a fixed encoding, appropriate braid operations will translate into topologically protected logical operations on the encoded state.

For Ising anyons there are two conventional choices of encoding, both of which fix the global topological charge to be in the vacuum sector. The sparse encoding uses $4n$ Ising anyons to encode n qubits, with each qubit encoded independently of the others in the fusion space of four Ising anyons. As depicted in Fig. 2.4(a), the logical qubit sate is given by the

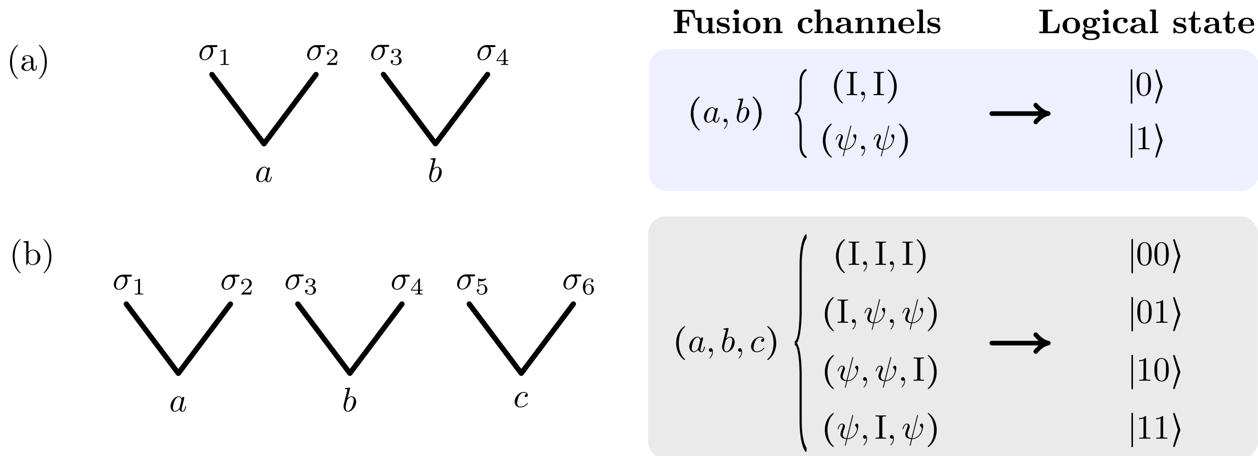

Figure 2.4: **Qubit encodings with Ising anyons.** Logical states are identified with elements of fusion space for multiple Ising anyons $\{\sigma_i\}$ where the total topological charge is trivial. (a) A single qubit is encoded with four Ising anyon via the pairwise fusion outcomes a and b. The trivial global charge restriction identifies $a = b$ as the codespace, with the logical state simply reflecting the value of $a = I, \psi$. (b) Dense encoding of two qubits in the fusion space of six Ising anyons. The state of the two qubits is identified with the fusion channels a and c of the first and last pair of Ising anyons, respectively. Requiring that the total fusion channel be trivial fixes the fusion channel b of the central two Ising anyons in this encoding.

fusion channel of the first two of the four anyons. By contrast, the dense encoding employs $2n + 2$ Ising anyons to encode n qubits, with the state of qubit j being the fusion outcome of anyons $2j - 1$ and $2j$. The final two anyons are kept to ensure that the global fusion channel is vacuum. As a result, they are generally highly entangled with the whole set of anyons, which may expose the system to greater risk of error. In Fig. 2.4(b) we depict the dense encoding of two qubits, but with the global parity given by the central anyon pair rather than the last pair. By applying the braiding and F-matrix rules depicted in Fig. 2.3, it is straightforward to show that simple braid sequences implement non-trivial logical operations on the encoded qubit. For explicit examples, see Fig. 4.12 and the corresponding discussion in Ch. 4.

2.4 Jackeli-Khaliullin Mechanism and Candidate Materials

At first glance, the bond-dependent Kitaev interaction appears unlikely to arise naturally in solid-state systems. However, a series of seminal works [159, 70, 71] identify a mechanism by which to approximately realize the Kitaev model in Mott insulating $4d$ and $5d$ honeycomb magnets. Here we briefly recall the key aspects of the Jackeli-Khaliullin mechanism. We consider valence electrons in a d^5 configuration, as arises for a heavy transition metal ion enclosed in an octahedral cage of oxygen atoms. The crystal field induces a splitting of the d orbitals such that the electrons lie in the t_{2g} orbitals. Strong spin-orbit coupling (SOC) further splits the t_{2g} orbitals, leaving a half-filled band with moment $j = 1/2$. Electronic interactions drive this $j = 1/2$ band to a Mott insulating phase. The remaining pseudospin degrees of freedom are subject to an effective Hamiltonian arising from superexchange. When the lattice consists of edge-sharing octahedra, destructive interference of two exchange paths suppresses the Heisenberg interaction, leaving behind a dominant bond-dependent Kitaev-type interaction. In real candidate materials, additional non-Kitaev terms arise which may spoil the spin-liquid phase and induce magnetic order, thereby complicating the search for Kitaev physics.

Following these proposals, numerous honeycomb materials have been put forward as candidate Kitaev spin liquids [287, 332, 151, 327]. Among these "Kitaev materials", α-$RuCl_3$ [280, 299, 310, 230, 168, 300, 22, 24, 93] displays particularly tantalizing behavior at low temperatures: in-plane magnetic fields suppress zigzag spin order [201, 207, 311, 352, 18, 23, 150, 165, 346, 21], possibly giving way to the *non-Abelian* QSL from the Kitaev honeycomb model [186]. Strikingly, recent experiments [177, 361, 54] have reported a half-integer-quantized thermal Hall conductivity at intermediate fields ~ 10 T, which is consistent with the emergence of a chiral Majorana edge mode [25] hosted by the non-Abelian Kitaev spin liquid (see also Refs. [357, 84] for related thermal transport experiments). Nonetheless, definitive verification of the underlying topological order and harnessing it for quantum information applications remain outstanding challenges.

2.5 Organization

Harnessing the potential of Kitaev spin liquids for quantum information purposes requires (at a minimum) the ability to create, detect, and manipulate fractionalized excitations on demand in the electrically insulating host platform. Herein we aim to address several of these requirements and provide more robust tools for identifying Majorana physics in Kitaev materials The subsequent chapters are organized as follows. In Chapter 3, we propose a novel scheme for interrogating topological order in candidate Kitaev materials through refined thermal-transport experiments. Then in Chapter 4 we utilize the results from Ch. 3 and other recent works to construct a roadmap for minimal implementations of quantum computing primitives in Kitaev candidate materials, highlighting the necessary conditions and likely roadblocks.

Chapter 3

Thermal transport in phonon-coupled Kitaev spin liquids

In general, thermal transport is one of the most promising experimental techniques for identifying topologically ordered chiral QSLs. Contrary to conventional probes of magnetic systems such as neutron scattering, quantized responses in thermal transport directly reflect the universal properties of a given topological order. For example, the quantized thermal Hall conductivity [1] is proportional to the edge theory's chiral central charge [172]—fractional values of which indicate non-Abelian topological orders. Quantized thermal transport correspondingly plays an analogous role to quantized electrical transport, which is a fundamental signature of electronic topological orders such as fractional quantum Hall states.

There is, however, a key conceptual difference between thermal and electronic transport: the chiral edge modes of QSLs are not the only heat carriers in the system. In fact, for most realistic materials, the quantized thermal Hall conductivity resulting from the chiral edge modes, κ_{xy}, is expected to be much smaller than the longitudinal thermal conductivity due to bulk acoustic phonons, κ_{xx}. For α-RuCl$_3$, the ratio of the two conductivities has been experimentally found [177, 361, 54] to be $\kappa_{xy}/\kappa_{xx} \sim 10^{-3}$ at the relevant temperatures between 3 K and 6 K. Given that bulk phonons not only produce large κ_{xx} but also couple to the chiral edge modes, one may naïvely expect that chiral edge transport is sufficiently disturbed that quantized κ_{xy} is no longer observable. Surprisingly, however, Refs. [360] and [340] showed that the experimentally measured thermal Hall conductivity remains (approximately) quantized in the conventional rectangular geometry [177, 361, 54], provided the sample is sufficiently large that the edge can effectively thermalize with the bulk. In fact, according to these works, the observation of quantized thermal transport *relies on* a sufficiently large edge-bulk coupling, as the thermal leads and sensors are expected to couple predominantly to lattice vibrations (i.e., bulk phonons) rather than the chiral edge modes.

Another, more recent, thread of research is concerned with employing anyonic edge in-

[1]We note that the thermal Hall conductivity is identical to the thermal Hall conductance in two dimensions.

terferometry to probe topological orders in chiral QSLs. By utilizing point contacts at which edge anyons may tunnel between counterpropagating edges, this approach allows for a direct observation of anyonic statistics as well as detection of individual bulk anyons. For fractional quantum Hall states, anyonic edge interferometry has an extensive theoretical literature [60, 87, 322, 40, 42, 182, 292, 143, 293] and has been demonstrated in recent electrical transport experiments [258, 349, 259]. Adapting electrical anyon interferometry techniques to chiral QSLs, however, is nontrivial because the edge and bulk anyons of such insulating systems do not carry electric charge. Over the last several years, a number of alternative schemes have been proposed to perform anyon interferometry in QSLs by exploiting conversion between charged and neutral edge modes at a superconducting interface [2], or by means of time-domain measurements using ancillary spins [191]. Further proposals have deviated from the typical anyon interferometry framework to highlight potential routes toward detecting individual bulk anyons or chiral edge modes in QSLs [106, 276, 335]. Though the possibility of heat-based anyon interferometry has also been noted [45], practical implementation of the idea raises an important conceptual challenge: one must reconcile anyon braiding by edge tunneling—a process relying on phase coherence—with conventional thermometry that requires large-scale thermalization and couples principally to bulk phonons.

In this chapter, we show that thermal transport is indeed a feasible route to realizing anyonic edge interferometry in a chiral QSL, as one can exploit edge-bulk thermalization while *also* harvesting phase-coherent edge transport in a single device. To this end, we consider the unconventional device geometry shown in Fig. 3.1 which consists of a mesoscopic central region flanked by two macroscopic lobes. Crucially, phase-coherent edge tunneling processes are confined to the mesoscopic region, where coupling to phonons has a negligible effect by construction, and thus may directly influence phonon thermodynamics in the macroscopic lobes. One can thereby accurately extract universal characteristics of the underlying QSL within the framework of currently available thermal transport experiments. In the simplest setup, wherein the upper and lower edges of the mesoscopic region decouple [Fig. 3.1(a)], our device enables refined measurement of the chiral central charge that is manifest in the dominant *longitudinal* thermal conductance rather than a subdominant thermal Hall conductivity. Adding a single constriction in the mesoscopic region [Fig. 3.1(b)] allows energy to backscatter between the upper and lower edges via anyon tunneling; remarkably, the temperature dependence of the resulting backscattered heat current reveals fingerprints of the anyonic quasiparticles hosted by the QSL. Finally, and most interestingly, adding a second constriction [Fig. 3.1(c)] defines an experimentally viable thermal anyon interferometer that solves the conceptual challenge noted above: individual anyons localized in the central region can be sensitively detected, together with their braiding statistics, by measuring the thermal conductance of the device, or the phonon temperature profile within either lobe. For concreteness, we focus on the non-Abelian Kitaev spin liquid [186]; the universal characteristics accessible by measuring the thermal conductance are then shown in Fig. 3.1. We also emphasize, however, that much of our results apply broadly to phonon-coupled chiral topological orders.

The rest of this chapter is organized as follows. In Sec. 3.1, we study large-scale thermal

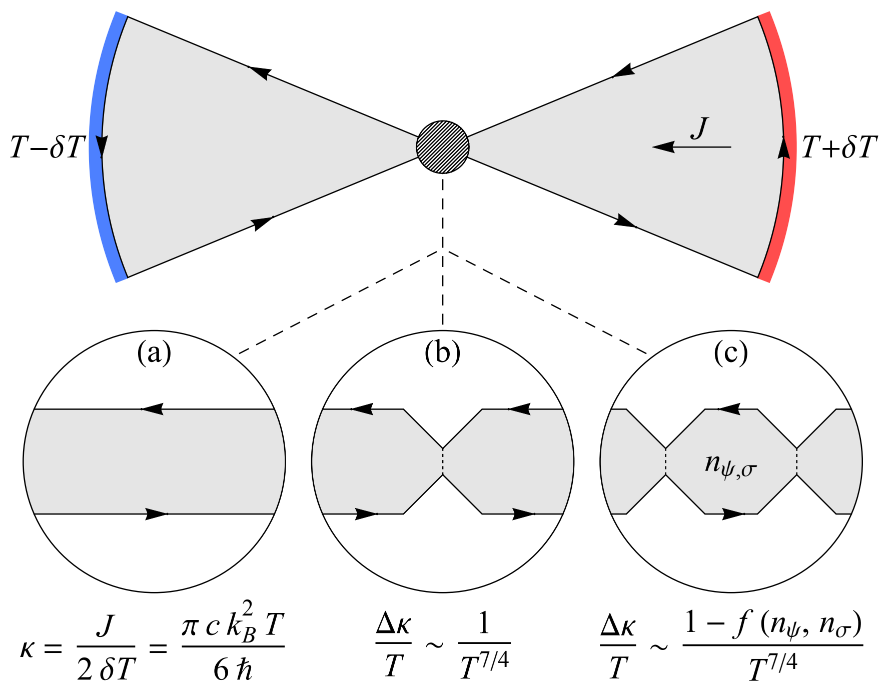

Figure 3.1: **Two-lobe device geometry for refined thermal transport**. Device geometry for extracting universal characteristics of the non-Abelian Kitaev spin liquid through conventional thermal transport in the presence of phonons. Two macroscopic lobes are bridged by a central mesoscopic region, across which heat current J flows upon applying a temperature differential $2\delta T$ across the device. The lobes facilitate edge-phonon thermalization, while the central region acts as a bottleneck for bulk phonon transport and thus emphasizes chiral edge transport. The central region may contain pinch points at which the edge separation becomes comparable to the bulk correlation length, allowing edge anyons to tunnel between the two chiral edge modes. If the phonon thermal conductance of the central region is sufficiently small, measurements of the heat current reveal the following universal spin liquid characteristics. (a) In the absence of any pinch points, the longitudinal thermal conductance of the device is proportional to the chiral central charge, $c = \frac{1}{2}$, which immediately confirms the presence of non-Abelian anyons. (b) For a single pinch point, the dominant low-temperature correction to the thermal conductance, $\Delta\kappa$, follows a nontrivial power law with universal exponent $7/4$ as a function of the temperature T, which reflects the tunneling of non-Abelian Ising anyons. (c) For two pinch points, the correction acquires an interference term, $f(n_\psi, n_\sigma)$, that is sensitive to the number of fermions (n_ψ) and Ising anyons (n_σ) between the two pinch points and thereby enables detection of individual bulk anyons.

transport in the device geometry of Fig. 3.1 and demonstrate how macroscopic temperatures and heat currents within the two lobes reflect mesoscopic edge processes in the central region. In the framework of this calculation, the edge processes are accounted for by a single dimensionless parameter β. In Sec. 3.2, we concentrate on the edge processes themselves in the presence of one [Fig. 3.1(b)] or two [Fig. 3.1(c)] point contacts. While the introduction of a single pinch point is sufficient to reveal Ising-anyon tunneling via a universal temperature dependence of β, the double-pinch geometry allows for interference effects to imprint signatures of anyon braiding on the large-scale thermal transport. In Sec. 3.3, we discuss the experimental conditions necessary to observe the signatures we identify and the challenges one might face in implementing the proposed thermal interferometry scheme. Finally, we close the chapter with a brief summary and outlook in Sec. 3.4.

3.1 Thermal transport

We consider the low-temperature thermal transport of a phonon-coupled chiral spin liquid in the device geometry of Fig. 3.1. In this geometry, two large lobes of radius R are connected by a narrow channel in a small central region of radius $r_0 \ll R$ (see Fig. 3.2). The narrow channel between the two lobes features a pinch region with one [Fig. 3.2(a)] or two [Fig. 3.2(b)] pinch points at which energy may tunnel between the counter-propagating top and bottom edges of the channel. We assume that each lobe is an annular section with opening angle $2\vartheta_0$, outer radius R, and inner radius r_0. While this assumption does not affect the main results of our work, it considerably simplifies the solution of our heat-transport equations.

Importantly, heat in our system is carried by two disparate degrees of freedom: the chiral edge mode and bulk acoustic phonons. Given that the thermal coupling between these two degrees of freedom is expected to be very small at low temperatures [360], we cannot assume that they are in thermal equilibrium at any given position along the edge of the system. Therefore, we consider two separate temperatures, corresponding to the edge mode ($T_{\rm e}$) and the bulk phonons ($T_{\rm b}$).

Thermal transport can be set up by attaching the outer edges of the right and left lobes to hot and cold leads, respectively, and probed by measuring (i) temperatures close to the central region (i.e., far from the leads) or (ii) the total heat current between the two leads [2]. Importantly, while the quantum effects of interest (see Fig. 3.1) rely on thermal tunneling between otherwise isolated chiral edge modes, the thermal leads and the temperature probes are expected to couple to the bulk phonons instead. Thus, an optimal detection of the quantum effects through thermal transport requires significant edge-bulk thermalization in the two lobes but negligible edge-bulk thermalization in the central region. Since the thermalization between the edge mode and the bulk phonons is known [360] to be significant

[2] In this work, we assume that the thermal leads have fixed temperatures and that the heat current between the two leads is measured. If instead the heat current is fixed and the lead temperatures are measured, the measurement of the heat current translates into the measurement of the longitudinal thermal conductance, defined as the ratio of the heat current and the temperature difference.

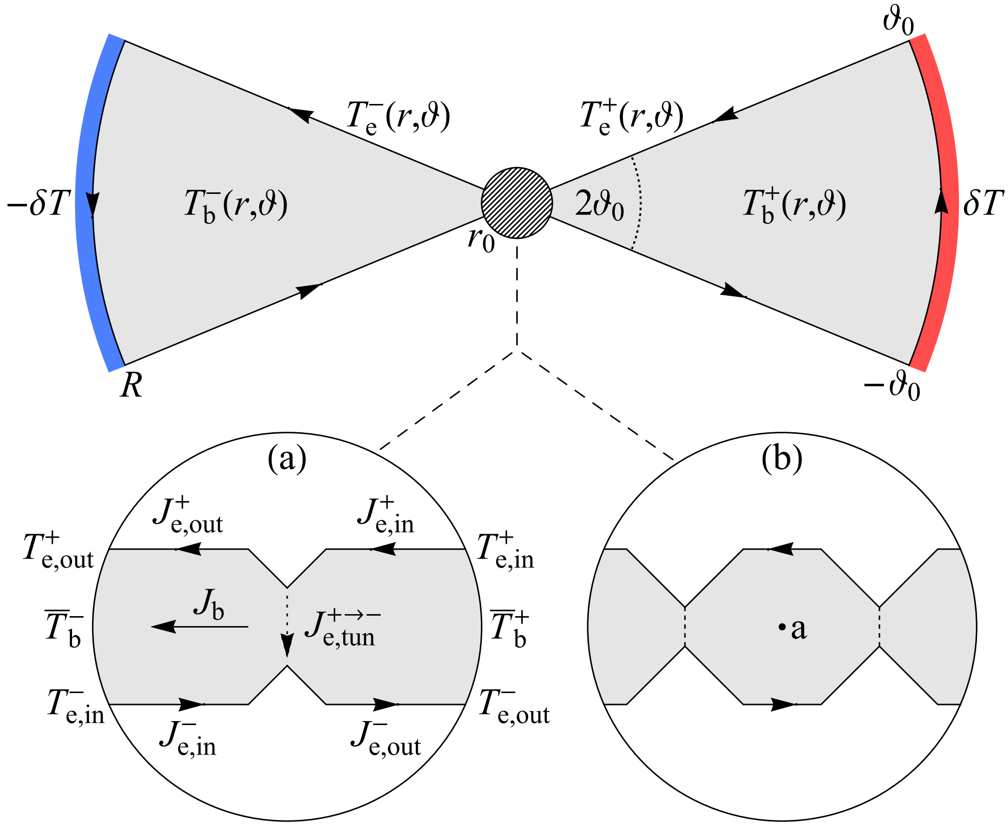

Figure 3.2: **Bulk and edge heat currents**. Thermal transport within a phonon-coupled chiral spin liquid in the device geometry of Fig. 3.1. All temperatures shown here, including those of the hot and cold leads ($\pm\delta T$), are small relative temperatures with respect to an average overall temperature T_0 that corresponds to T in Fig. 3.1. There are distinct relative temperatures for the edge mode (T_e) and the bulk phonons (T_b). Each lobe is an annular section with opening angle $2\vartheta_0$, outer radius R, and inner radius r_0. The central channel carries a bulk heat current J_b driven by the different mean bulk temperatures $\bar{T}_\mathrm{b}^\pm$ at its two ends, as well as chiral edge heat currents $J_\mathrm{e}^\pm$ determined by the local edge temperatures $T_\mathrm{e}^\pm$. For each edge, the tunneling heat current $J_{\mathrm{e,tun}}^{+\to-}$ associated with the pinch point(s) changes the edge heat current from $J_{\mathrm{e,in}}^\pm$ to $J_{\mathrm{e,out}}^\pm = J_{\mathrm{e,in}}^\pm \mp J_{\mathrm{e,tun}}^{+\to-}$. While these notations are shown for the single-pinch case (a), they readily generalize to the double-pinch case (b), where the tunneling heat current $J_{\mathrm{e,tun}}^{+\to-}$ has contributions from both pinch points and is sensitive to bulk anyons "a" in between them.

at length scales exceeding a characteristic edge-bulk thermalization length ℓ, this scenario is realized if the central region is mesoscopic, $r_0 \ll \ell$, while the two lobes are macroscopic, $R \gg \ell$.

Heat-Transport Equations

We now describe a general set of hydrodynamic equations governing the heat transport and the temperature distribution of our phonon-coupled chiral spin liquid. For a start, we assume that the system has an average overall temperature T_0 and that the temperatures $T^{\pm}$ shown in Fig. 3.2 are small variations with respect to this overall temperature. In this regime, we can readily linearize all of our equations in the temperature variations $T^{\pm}$. Also, we can use the inversion symmetry around the center of the system to establish the general relation $T^- = -T^+$, where $T^+_{\mathrm{b,e}}(r,\vartheta)$ $[T^-_{\mathrm{b,e}}(r,\vartheta)]$ correspond to the right (left) lobe, while $T^+_{\mathrm{e,in}}$ ($T^-_{\mathrm{e,in}}$) and $T^+_{\mathrm{e,out}}$ ($T^-_{\mathrm{e,out}}$) correspond to the top (bottom) edges in the central region.

We first describe the macroscopic thermal transport in the two lobes by employing the hydrodynamic equations introduced in Ref. [360]. Inversion symmetry permits us to focus on the right lobe alone. The bulk and edge temperatures $T_{\mathrm{b,e}}(r,\vartheta) \equiv T^+_{\mathrm{b,e}}(r,\vartheta)$ are specified in polar coordinates, (r,ϑ), with $r_0 < r < R$ and $|\vartheta| < \vartheta_0$. Importantly, the bulk temperature $T_{\mathrm{b}}(r,\vartheta)$ is defined within the entire lobe, while the edge temperature $T_{\mathrm{e}}(r,\vartheta)$ is only defined along the edge. We note that similar hydrodynamic equations were also considered in Ref. [340] but without making a distinction between bulk and edge temperatures.

The thermal transport within the lobe comprises three different kinds of thermal currents [360]. First, if we assume that the acoustic phonons are diffusive, there is a bulk heat-current density (heat current per unit length) proportional to the negative gradient of the bulk temperature, $\mathbf{j}_{\mathrm{b}} = -\kappa_{\mathrm{b}} \nabla T_{\mathrm{b}}$, where the coefficient $\kappa_{\mathrm{b}} \equiv \kappa_{xx}$ is the longitudinal thermal conductivity due to the phonons [3]. Second, the chiral edge mode carries a counterclockwise heat current $J_{\mathrm{e}} = (\pi c/12)(T_0 + T_{\mathrm{e}})^2$ [4] along the edge, where c is the chiral central charge of the edge conformal field theory (CFT). At linear order in the relative edge temperature T_{e}, this edge heat current is given by $J_{\mathrm{e}} = J_0 + \kappa_{\mathrm{e}} T_{\mathrm{e}}$, where $J_0 = \pi c T_0^2/12$ is a constant edge current, while $\kappa_{\mathrm{e}} = \pi c T_0/6$ is the quantized thermal Hall conductivity [177, 361, 54] associated with the chiral edge mode [5]. Third, there is a heat-current density (heat current per unit length) from the bulk phonons to the edge mode, which is driven by the temperature difference between these two degrees of freedom. At linear order, this exchange heat-current density must take the general form $j_{\mathrm{b}\to\mathrm{e}} = \lambda(T_{\mathrm{b}} - T_{\mathrm{e}})$, where λ is the linearized thermal coupling between the edge and the bulk. Importantly, λ is strongly suppressed at low temperatures and was argued in Ref. [360] to vanish as $\lambda \propto T^6$.

The equations governing the temperatures are then obtained by assuming a stationary state and imposing the conservation of energy. First of all, the divergence of the bulk heat-current density must vanish, $\nabla \cdot \mathbf{j}_{\mathrm{b}} = 0$, which translates into a Laplace's equation for the bulk temperature, $\nabla^2 T_{\mathrm{b}} = 0$. Using polar coordinates, this Laplace's equation then takes the

[3] We note that κ_{b} is the *two-dimensional* thermal conductivity which is the product of the usual three-dimensional thermal conductivity and the layer thickness.

[4] Here we have set $\hbar = k_B = 1$.

[5] We emphasize that this thermal Hall conductivity corresponds to a *thermally isolated* edge mode and could only be *directly* measured by using thermal leads and temperature sensors that couple to the edge mode rather than the bulk phonons.

separable form

$$\frac{\partial^2 T_{\mathrm{b}}(r,\vartheta)}{(\partial \ln r)^2} + \frac{\partial^2 T_{\mathrm{b}}(r,\vartheta)}{\partial \vartheta^2} = 0. \tag{3.1}$$

Next, along the upper and lower edges ($\vartheta = \pm\vartheta_0$), the normal component of the bulk heat-current density must match the exchange heat-current density, $\hat{\mathbf{n}}_\perp \cdot \mathbf{j}_{\mathrm{b}} = j_{\mathrm{b}\to\mathrm{e}}$, where $\hat{\mathbf{n}}_\perp$ is the unit vector pointing in the "outward" direction perpendicular to the edge. In polar coordinates, the resulting equations can be written as

$$-\frac{\kappa_{\mathrm{b}}}{r}\frac{\partial T_{\mathrm{b}}(r,\vartheta=\pm\vartheta_0)}{\partial\vartheta} = \pm\lambda\left[T_{\mathrm{b}}(r,\pm\vartheta_0) - T_{\mathrm{e}}(r,\pm\vartheta_0)\right]. \tag{3.2}$$

In contrast, along the outer edge ($r = R$), the presence of the lead invalidates the above constraint and imposes a fixed bulk temperature instead:

$$T_{\mathrm{b}}(R,\vartheta) = \delta T. \tag{3.3}$$

Finally, along all three edges, the spatial variation of the edge heat current must match the exchange heat-current density, $\nabla_\parallel J_{\mathrm{e}} = j_{\mathrm{b}\to\mathrm{e}}$, where $\nabla_\parallel$ is the derivative along the edge in the counterclockwise direction. In polar coordinates, the resulting equations read

$$\begin{aligned}\frac{\kappa_{\mathrm{e}}}{R}\frac{\partial T_{\mathrm{e}}(R,\vartheta)}{\partial\vartheta} &= \lambda\left[T_{\mathrm{b}}(R,\vartheta) - T_{\mathrm{e}}(R,\vartheta)\right],\\ \kappa_{\mathrm{e}}\frac{\partial T_{\mathrm{e}}(r,\pm\vartheta_0)}{\partial r} &= \mp\lambda\left[T_{\mathrm{b}}(r,\pm\vartheta_0) - T_{\mathrm{e}}(r,\pm\vartheta_0)\right].\end{aligned} \tag{3.4}$$

Thus, the characteristic edge-bulk thermalization length scale is found to be $\ell = \kappa_{\mathrm{e}}/\lambda$. We emphasize again that Eqs. (3.1)-(3.4) are directly taken from Ref. [360] and adapted to our unconventional device geometry.

We next describe the mesoscopic thermal transport between the two lobes through the central region. Since the edge-bulk thermalization is negligible in the narrow channel, it is not necessary to describe the full spatial dependence of the bulk temperature. Instead, we use a more coarse-grained picture (see Fig. 3.2), and assume a general phenomenological relation, $J_{\mathrm{b}} = \kappa_{\mathrm{c}}(\bar{T}_{\mathrm{b}}^+ - \bar{T}_{\mathrm{b}}^-)$, where J_{b} is the bulk heat current, carried by the phonons, through the narrow channel, $\bar{T}_{\mathrm{b}}^+$ ($\bar{T}_{\mathrm{b}}^-$) is the mean bulk temperature at the right (left) end of the channel, and κ_{c} is the thermal conductance [6] of the channel. Importantly, this relation does not assume that the phonons are diffusive in the central region. We note, however, that, in the specific case of diffusive phonons, the channel conductance is expected to be $\kappa_{\mathrm{c}} \sim \kappa_{\mathrm{b}} W/L$, where W and L are the width and the length of the channel, respectively. If the channel is narrow enough ($W \ll L$), the conductance κ_{c} is then much smaller than the conductivity κ_{b}.

Matching the bulk heat currents and the bulk temperatures between the two lobes and the narrow channel, we then immediately find $J_{\mathrm{b}} = \mp r_0 \int_{-\vartheta_0}^{+\vartheta_0} d\vartheta\, \hat{\mathbf{r}} \cdot \mathbf{j}_{\mathrm{b}}^{\pm}(r_0,\vartheta)$ and $\bar{T}_{\mathrm{b}}^{\pm} =$

[6] We use the symbol κ for both thermal conductivities and thermal conductances. In two dimensions, these quantities have the same dimensions and are directly comparable to each other.

$(2\vartheta_0)^{-1}\int_{-\vartheta_0}^{+\vartheta_0} \mathrm{d}\vartheta\, T_{\mathrm{b}}^{\pm}(r_0,\vartheta)$, where $\hat{\mathbf{r}}$ is the radial unit vector. Thus, the relation between the heat current and the mean temperature difference becomes

$$\kappa_{\mathrm{b}} r_0 \int_{-\vartheta_0}^{+\vartheta_0} \mathrm{d}\vartheta\, \frac{\partial T_{\mathrm{b}}^{\pm}(r=r_0,\vartheta)}{\partial r} \\ = \pm\frac{\kappa_{\mathrm{c}}}{2\vartheta_0}\int_{-\vartheta_0}^{+\vartheta_0} \mathrm{d}\vartheta\, \left[T_{\mathrm{b}}^{+}(r_0,\vartheta) - T_{\mathrm{b}}^{-}(r_0,\vartheta)\right].$$

However, this relation is too coarse grained and does not enable a unique solution for Eqs. (3.1)-(3.4). Therefore, we generalize this relation by imposing it on the integrands themselves rather than the integrals. Using the inversion symmetry of the system, and remembering the notation $T_{\mathrm{b}}(r,\vartheta) \equiv T_{\mathrm{b}}^{+}(r,\vartheta) = -T_{\mathrm{b}}^{-}(r,\vartheta)$, the equation governing the bulk temperature along the interface ($r = r_0$) of each lobe and the central region is then

$$\frac{\partial T_{\mathrm{b}}(r=r_0,\vartheta)}{\partial \ln r} = \alpha T_{\mathrm{b}}(r_0,\vartheta), \tag{3.5}$$

where $\alpha = \kappa_{\mathrm{c}}/(\kappa_{\mathrm{b}}\vartheta_0)$ is a dimensionless ratio of the channel conductance to the lobe conductance. We emphasize that this generalized relation is equivalent to the original coarse-grained one if the temperature variations are sufficiently small along the interface (which is expected for small-enough r_0 and/or ϑ_0).

Due to the negligible edge-bulk thermalization in the central region, the edge temperatures along the narrow channel can only change as a result of thermal tunneling between the counterpropagating top and bottom edges at the pinch points. Thus, if we consider the entire pinch region with one or two pinch points (see Fig. 3.2) as a single unit, the only relevant edge temperatures and heat currents are the incoming ($T_{\mathrm{e,in}}^{\pm}$ and $J_{\mathrm{e,in}}^{\pm}$) and the outgoing ($T_{\mathrm{e,out}}^{\pm}$ and $J_{\mathrm{e,out}}^{\pm}$) ones [7]. Given that there is no quantum coherence between the two incoming edges, we assume that, for each edge, the tunneling heat current to the other edge, $J_{\mathrm{e,tun}}(T)$, is fully determined by the absolute incoming temperature, $T = T_0 + T_{\mathrm{e,in}}$, of the given edge. At linear order in the relative temperatures $T_{\mathrm{e,in}}^{\pm}$, the net tunneling current from the top edge to the bottom edge (see Fig. 3.2) is then $J_{\mathrm{e,tun}}^{+\to-} = \kappa_{\mathrm{e,tun}}[T_{\mathrm{e,in}}^{+} - T_{\mathrm{e,in}}^{-}]$, where $\kappa_{\mathrm{e,tun}} = (dJ_{\mathrm{e,tun}}/dT)|_{T=T_0}$ is a tunneling thermal conductance. Since the incoming and outgoing heat currents are related to each other as $J_{\mathrm{e,out}}^{\pm} = J_{\mathrm{e,in}}^{\pm} \mp J_{\mathrm{e,tun}}^{+\to-}$ and to the incoming and outgoing temperatures according to $J_{\mathrm{e,in}}^{\pm} = J_0 + \kappa_{\mathrm{e}} T_{\mathrm{e,in}}^{\pm}$ and $J_{\mathrm{e,out}}^{\pm} = J_0 + \kappa_{\mathrm{e}} T_{\mathrm{e,out}}^{\pm}$, the incoming and outgoing temperatures are related by

$$T_{\mathrm{e,out}}^{\pm} = T_{\mathrm{e,in}}^{\pm} \mp \beta\left[T_{\mathrm{e,in}}^{+} - T_{\mathrm{e,in}}^{-}\right],$$

where $\beta = \kappa_{\mathrm{e,tun}}/\kappa_{\mathrm{e}}$ is a dimensionless parameter satisfying $0 < \beta < 1$. Physically, β is the fraction of excess energy in the hotter edge that tunnels to the colder edge in the entire pinch region. As we explore in Sec. 3.2, this quantity depends on the number of pinch

[7] We implicitly assume that the outgoing edge thermalizes with itself and reaches thermal equilibrium by the time it leaves the central region

points in the pinch region and, if there are two pinch points, on the total anyon content in between them (see Fig. 3.2). Finally, with the identifications $T^{\pm}_{\mathrm{e,in}} = T^{\pm}_{\mathrm{e}}(r_0, \vartheta_0) \equiv \pm T_{\mathrm{e}}(r_0, \vartheta_0)$ and $T^{\pm}_{\mathrm{e,out}} = T^{\mp}_{\mathrm{e}}(r_0, -\vartheta_0) \equiv \mp T_{\mathrm{e}}(r_0, -\vartheta_0)$, the equation governing the edge temperatures at the interface ($r = r_0$) of each lobe and the central region reads

$$T_{\mathrm{e}}(r_0, -\vartheta_0) = (2\beta - 1)\, T_{\mathrm{e}}(r_0, \vartheta_0). \tag{3.6}$$

Importantly, Eqs. (3.5) and (3.6) are exclusively for the bulk and edge temperatures of a single lobe, and they are only affected by the rest of the system through the parameters α and β. Together with Eqs. (3.1)-(3.4), they uniquely determine the temperature profile of the given lobe.

Perturbative Solution

Now we solve Eqs. (3.1)-(3.6) for the temperature profile of each lobe by employing the perturbative approach introduced in Ref. [360]. As we will later find, this perturbative approach is convergent in our device geometry whenever $\kappa_{\mathrm{e}} \ll \kappa_{\mathrm{b}} \vartheta_0$. To start with, we write the bulk and edge temperatures in series expansions as $T_{\mathrm{b,e}} = \sum_{n=0}^{\infty} T^{(n)}_{\mathrm{b,e}}$, where $T^{(0)}_{\mathrm{b,e}}$ are the unperturbed solutions in the absence of edge-bulk coupling ($\lambda = 0$), while $T^{(n)}_{\mathrm{b,e}}$ with $n > 0$ are perturbative corrections due to finite λ. The unperturbed solutions are given by

$$\begin{aligned} T^{(0)}_{\mathrm{b}}(r, \vartheta) &= \frac{\delta T [1 + \alpha \ln(r/r_0)]}{1 + \alpha \ln(R/r_0)}, \\ T^{(0)}_{\mathrm{e}}(r, \vartheta) &= 0, \end{aligned} \tag{3.7}$$

where the edge temperature vanishes because the hot and cold leads are assumed to couple exclusively to the bulk phonons. The perturbative corrections are then found by means of an iterative procedure. For each iteration step $n > 0$, we first obtain the edge temperature by solving the ordinary differential equations [see Eq. (3.4)]

$$\begin{aligned} \frac{\partial T^{(n)}_{\mathrm{e}}(R, \vartheta)}{\partial \vartheta} &= \frac{R}{\ell} \left[T^{(n-1)}_{\mathrm{b}}(R, \vartheta) - T^{(n)}_{\mathrm{e}}(R, \vartheta) \right], \\ \frac{\partial T^{(n)}_{\mathrm{e}}(r, \pm\vartheta_0)}{\partial r} &= \mp \frac{1}{\ell} \left[T^{(n-1)}_{\mathrm{b}}(r, \pm\vartheta_0) - T^{(n)}_{\mathrm{e}}(r, \pm\vartheta_0) \right], \end{aligned} \tag{3.8}$$

together with the boundary condition [see Eq. (3.6)]

$$T^{(n)}_{\mathrm{e}}(r_0, -\vartheta_0) = (2\beta - 1)\, T^{(n)}_{\mathrm{e}}(r_0, \vartheta_0). \tag{3.9}$$

Next, we find the bulk temperature by solving Laplace's equation within the lobe [see Eq. (3.1)],

$$\frac{\partial^2 T^{(n)}_{\mathrm{b}}(r, \vartheta)}{(\partial \ln r)^2} + \frac{\partial^2 T^{(n)}_{\mathrm{b}}(r, \vartheta)}{\partial \vartheta^2} = 0, \tag{3.10}$$

together with Neumann boundary conditions along the upper and lower edges at $\vartheta = \pm\vartheta_0$ [see Eq. (3.2)],

$$\frac{\partial T_{\mathrm{b}}^{(n)}(r, \vartheta = \pm\vartheta_0)}{\partial \vartheta} = \mp \frac{\lambda r}{\kappa_{\mathrm{b}}} \left[T_{\mathrm{b}}^{(n-1)}(r, \pm\vartheta_0) - T_{\mathrm{e}}^{(n)}(r, \pm\vartheta_0) \right], \tag{3.11}$$

Dirichlet boundary conditions along the outer edge at $r = R$ [see Eq. (3.3)],

$$T_{\mathrm{b}}^{(n)}(R, \vartheta) = 0, \tag{3.12}$$

and homogeneous boundary conditions along the interface with the central region at $r = r_0$ [see Eq. (3.5)],

$$\frac{\partial T_{\mathrm{b}}^{(n)}(r = r_0, \vartheta)}{\partial \ln r} = \alpha T_{\mathrm{b}}^{(n)}(r_0, \vartheta). \tag{3.13}$$

The iterative procedure is convergent if the perturbative corrections $T_{\mathrm{b,e}}^{(n)}$ are progressively smaller.

To understand how the thermal transport may be sensitive to edge tunneling processes in the central region, we seek the β-dependent components of the leading-order corrections $T_{\mathrm{b,e}}^{(1)}$ to the bulk and edge temperatures. For simplicity, we assume that the characteristic edge-bulk thermalization length, $\ell = \kappa_{\mathrm{e}}/\lambda$, is much larger than the central region, $\ell \gg r_0$, but much smaller than the lobe width, $\ell \ll R\vartheta_0 \lesssim R$. In this regime, the edge temperature fully thermalizes to δT along the outer edge of the lobe but retains a dependence on β close to the central region. By solving Eqs. (3.8) and (3.9) with $n = 1$ (see Appendix A.1), the edge temperatures along the upper and lower edges take the forms $T_{\mathrm{e}}^{(1)}(r, \vartheta_0) = \tilde{T}_{\mathrm{e}}^{(1)}(r, \vartheta_0)$ and $T_{\mathrm{e}}^{(1)}(r, -\vartheta_0) = \tilde{T}_{\mathrm{e}}^{(1)}(r, -\vartheta_0) + \beta \hat{T}_{\mathrm{e}}^{(1)}(r, -\vartheta_0)$, where $\tilde{T}_{\mathrm{e}}^{(1)}(r, \pm\vartheta_0)$ are independent of β, while

$$\hat{T}_{\mathrm{e}}^{(1)}(r, -\vartheta_0) = \frac{2\,\delta T \left\{1 + \alpha\left[\ln(\ell/r_0) - \gamma\right]\right\} e^{-r/\ell}}{1 + \alpha \ln(R/r_0)} \tag{3.14}$$

with $\gamma \approx 0.577$ the Euler-Mascheroni constant. The solution of Eqs. (3.10)-(3.13) for the bulk temperature can then be written as $T_{\mathrm{b}}^{(1)}(r, \vartheta) = \tilde{T}_{\mathrm{b}}^{(1)}(r, \vartheta) + \beta \hat{T}_{\mathrm{b}}^{(1)}(r, \vartheta)$, where $\tilde{T}_{\mathrm{b}}^{(1)}(r, \vartheta)$ and $\hat{T}_{\mathrm{b}}^{(1)}(r, \vartheta)$ are independent of β. Assuming that the temperature probe couples to the bulk phonons, the sensitivity of a local temperature measurement to tunneling processes in the central region is characterized by $\hat{T}_{\mathrm{b}}^{(1)}(r, \vartheta) = \partial T_{\mathrm{b}}^{(1)}(r, \vartheta)/\partial\beta$. For simplicity, we focus on the angular average of this temperature sensitivity, $\langle \hat{T}_{\mathrm{b}}^{(1)}(r) \rangle \equiv (2\vartheta_0)^{-1} \int_{-\vartheta_0}^{+\vartheta_0} \mathrm{d}\vartheta\, \hat{T}_{\mathrm{b}}^{(1)}(r, \vartheta)$, which provides a lower bound on the maximal temperature sensitivity at a given radius r within the lobe. In Appendix A.1, we solve Eqs. (3.10)-(3.13) with $n = 1$ to derive approximate expressions for this average temperature sensitivity in the limits of large and small $\alpha = \kappa_{\mathrm{c}}/(\kappa_{\mathrm{b}}\vartheta_0)$:

$$\langle \hat{T}_{\mathrm{b}}^{(1)}(r) \rangle = \frac{\partial \langle T_{\mathrm{b}}^{(1)}(r) \rangle}{\partial \beta} \approx \begin{cases} \frac{2}{\pi^2}\left[\ln(\ell/r_0) - \gamma\right] \frac{\kappa_{\mathrm{e}}\delta T}{\kappa_{\mathrm{b}}\vartheta_0} \sin\left[\frac{\pi \ln(R/\ell)}{\ln(R/r_0)}\right] \sin\left[\frac{\pi \ln(R/r)}{\ln(R/r_0)}\right] & (\alpha \gg 1), \\ \frac{8\ln(R/r_0)}{\pi^2} \frac{\kappa_{\mathrm{e}}\delta T}{\kappa_{\mathrm{b}}\vartheta_0} \sin\left[\frac{\pi \ln(R/\ell)}{2\ln(R/r_0)}\right] \sin\left[\frac{\pi \ln(R/r)}{2\ln(R/r_0)}\right] & (\alpha \ll 1). \end{cases} \tag{3.15}$$

From the dependence of $\langle \hat{T}_{\rm b}^{(1)}(r) \rangle$ on the radius r, we conclude that the temperature sensitivity is maximized at $r \sim \sqrt{R r_0}$ for $\alpha \gg 1$ and at $r \sim r_0$ for $\alpha \ll 1$. In both limits, the maximal temperature sensitivity is on the order of $\kappa_{\rm e} \delta T / (\kappa_{\rm b} \vartheta_0)$. This result shows that the iterative procedure is convergent for $\kappa_{\rm e} \ll \kappa_{\rm b} \vartheta_0$ and that, given fixed $\kappa_{\rm e}$ and $\kappa_{\rm b}$, the temperature sensitivity is significantly enhanced for $\vartheta_0 \ll 1$. In this limit, the angular average $\langle \hat{T}_{\rm b}^{(1)}(r) \rangle$ also provides an accurate lower bound on the maximal temperature sensitivity (corresponding to $\vartheta = -\vartheta_0$) at the given radius r. Thus, we find that, by appropriately tailoring the geometry of the sample, one may significantly enhance the visibility of corrections to the thermal transport which are, in turn, sensitive to edge tunneling processes in the central region.

In addition to local temperature measurements, these edge tunneling processes can also be detected by measuring the total heat current between the hot and the cold leads. Evaluating this heat current at the interface of the right lobe and the central region, it is given by $J = \kappa_{\rm e} [T_{\rm e,in}^{+} - T_{\rm e,out}^{-}] + J_{\rm b}$, where the two terms correspond to the edges and the bulk of the narrow channel (see Fig. 3.2), respectively. In terms of the bulk and edge temperatures $T_{\rm b,e}$ of the lobe at the interface, the total heat current then becomes

$$J = \kappa_{\rm e} \left[T_{\rm e}(r_0, \vartheta_0) - T_{\rm e}(r_0, -\vartheta_0) \right] + 2\kappa_{\rm c} \langle T_{\rm b}(r_0) \rangle. \tag{3.16}$$

Finally, up to the leading-order perturbative corrections, $T_{\rm b,e}^{(1)}$, the sensitivity of the heat current to tunneling processes in the central region is

$$\frac{\partial J}{\partial \beta} = -\kappa_{\rm e} \hat{T}_{\rm e}^{(1)}(r_0, -\vartheta_0) + 2\kappa_{\rm c} \langle \hat{T}_{\rm b}^{(1)}(r_0) \rangle. \tag{3.17}$$

For $\alpha \ll 1$, the first term, from Eq. (3.14), is approximately $-2\kappa_{\rm e} \delta T$, while the second term, according to Eq. (3.15), is positive and on the order of $\alpha \kappa_{\rm e} \delta T \ll \kappa_{\rm e} \delta T$. Therefore, we obtain that the heat-current sensitivity in this limit is $\partial J / \partial \beta \approx -2\kappa_{\rm e} \delta T$. Approaching $\alpha \sim 1$, the negative first term slightly decreases in magnitude, while the positive second term increases to the same order of magnitude, $\kappa_{\rm e} \delta T$, as the first term. Given that $\partial J / \partial \beta$ must be negative on physical grounds (since stronger tunneling means smaller energy transfer between the two lobes), we then deduce that the heat-current sensitivity must be suppressed for $\alpha \gg 1$, even though the approximate expression for $\langle \hat{T}_{\rm b}^{(1)}(r_0) \rangle$ in Eq. (3.15) is not accurate enough (simply zero) in this limit. We emphasize that this result is further confirmed by the simple heat-resistor picture introduced in the next subsection.

Heat-Resistor Picture

To understand the thermal transport in a less rigorous but more intuitive manner, we now consider the effective heat-resistor network shown in Fig. 3.3(a). Each heat resistor represents a heat-carrying component of our phonon-coupled chiral spin liquid and is analogous to an electrical resistor. In this analogy, temperature (heat current) then corresponds to voltage (electrical current). We note that the simple heat-resistor picture is complementary to the

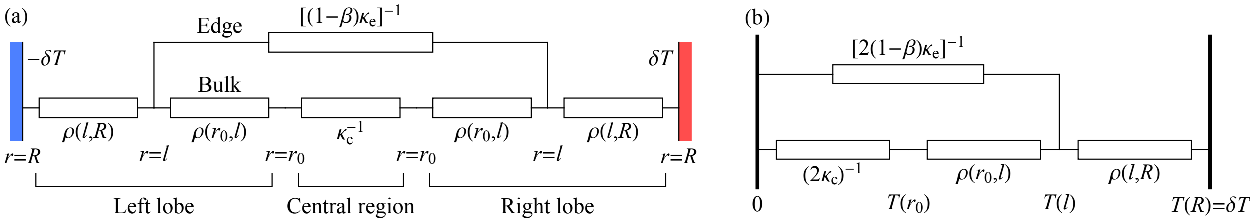

Figure 3.3: **Effective heat-resistor network**. (a) Effective heat-resistor network of the phonon-coupled chiral spin liquid. Each resistor represents a heat-carrying component of the system, with the resistors in the upper (lower) row accounting for the edge mode (bulk phonons). The right and left leads are fixed at temperatures δT and $-\delta T$, respectively. (b) Reduced heat-resistor network representing the right half of the system. The right lead is fixed at temperature δT, while the center of the system is fixed at temperature 0.

perturbative approach in the previous subsection and, as a result of its one-dimensional nature, is expected to be most reliable for $\vartheta_0 \ll 1$.

The heat-resistor network in Fig. 3.3(a) accounts for the entire system between the hot and cold leads. In terms of bulk phonon transport, the heat resistance of the central region is κ_c^{-1}, while each section of either lobe between radii r_1 and $r_2 > r_1$ corresponds to heat resistance

$$\rho(r_1, r_2) = \int_{r_1}^{r_2} \frac{\mathrm{d}r}{2\kappa_b r \vartheta_0} = \frac{\ln(r_2/r_1)}{2\kappa_b \vartheta_0}. \tag{3.18}$$

For radii $r > \ell$ in either lobe, the edge mode thermalizes well with the bulk phonons and, assuming $\kappa_e \lesssim \kappa_b \vartheta_0$, its effect on the thermal transport can be neglected. In contrast, within the central region and for radii $r < \ell$ in either lobe, the edge modes are thermally decoupled from the bulk phonons. Therefore, they facilitate direct thermal coupling between radius $r = \ell$ in the right lobe and radius $r = \ell$ in the left lobe. If the corresponding temperatures in the two respective lobes are $T^{\pm}(\ell)$, the top and bottom edges (see Fig. 3.2) then carry a net heat current $J_{\mathrm{e,in}}^{+} - J_{\mathrm{e,out}}^{-} = (1-\beta)\kappa_e[T^{+}(\ell) - T^{-}(\ell)]$ from the right lobe to the left lobe. Hence, the two edges can be represented with an effective heat resistance $[(1-\beta)\kappa_e]^{-1}$ between radii $r = \ell$ in the two lobes.

To analyze the heat-resistor network in Fig. 3.3(a), we first exploit the inversion symmetry around the center of the system to obtain the reduced heat-resistor network in Fig. 3.3(b). This network only contains the right half of the system between the right lead fixed at temperature δT and the center fixed at temperature 0. It is then clear that the temperature most sensitive to the tunneling parameter β is $T(\ell)$ at radius $r = \ell$ within the lobe. From Fig. 3.3(b), this temperature is given by

$$T(\ell) = \frac{\delta T\,[\rho(\ell,R)]^{-1}}{2(1-\beta)\kappa_e + [\rho(\ell)]^{-1} + [\rho(\ell,R)]^{-1}}, \tag{3.19}$$

while the corresponding temperature sensitivity becomes

$$\frac{\partial T(\ell)}{\partial \beta} = \frac{2\kappa_{\mathrm{e}}\delta T\,[\rho(\ell,R)]^{-1}}{\left\{2(1-\beta)\kappa_{\mathrm{e}} + [\rho(\ell)]^{-1} + [\rho(\ell,R)]^{-1}\right\}^2}, \tag{3.20}$$

where $\rho(\ell) = (2\kappa_{\mathrm{c}})^{-1} + \rho(r_0,\ell)$. Taking $\kappa_{\mathrm{e}} \ll \kappa_{\mathrm{b}}\vartheta_0$, which corresponds to the perturbative approach in the previous subsection, the temperature sensitivities for large and small $\alpha = \kappa_{\mathrm{c}}/(\kappa_{\mathrm{b}}\vartheta_0)$ are then found to be

$$\frac{\partial T(\ell)}{\partial \beta} \approx \begin{cases} \frac{\kappa_{\mathrm{e}}\delta T \ln(R/\ell)[\ln(\ell/r_0)]^2}{\kappa_{\mathrm{b}}\vartheta_0[\ln(R/r_0)]^2} & (\alpha \gg 1), \\ \frac{\kappa_{\mathrm{e}}\delta T \ln(R/\ell)}{\kappa_{\mathrm{b}}\vartheta_0} & (\alpha \ll 1). \end{cases} \tag{3.21}$$

Remarkably, Eqs. (3.15) and (3.21), obtained from the perturbative approach and the heat-resistor picture, respectively, give the same order of magnitude, $\kappa_{\mathrm{e}}\delta T/(\kappa_{\mathrm{b}}\vartheta_0)$, for the temperature sensitivity and the same qualitative dependence on the edge-bulk thermalization length ℓ. In particular, $\partial T(\ell)/\partial\beta$ vanishes for both $\ell \to R$ and $\ell \to r_0$ in the $\alpha \gg 1$ limit, whereas it vanishes for $\ell \to R$ but is maximal for $\ell \to r_0$ in the $\alpha \ll 1$ limit. By analyzing the general result in Eq. (3.20), we can further deduce that the temperature sensitivity is maximized if $[\rho(\ell)]^{-1}$ is very small while $[\rho(\ell,R)]^{-1}$ is similar to κ_{e}, which translates into $\kappa_{\mathrm{c}} \ll \kappa_{\mathrm{e}} \sim \kappa_{\mathrm{b}}\vartheta_0$. In this case, the temperature sensitivity reaches the largest order of magnitude that is theoretically possible: $\partial T(\ell)/\partial\beta \sim \delta T$.

The heat-resistor network in Fig. 3.3(b) can also be used to compute the total heat current leaving the right lead: $J = [\rho(\ell,R)]^{-1}[T(R) - T(\ell)]$. The sensitivity of the heat current to the tunneling parameter β is then

$$\frac{\partial J}{\partial \beta} = -[\rho(\ell,R)]^{-1}\frac{\partial T(\ell)}{\partial \beta}, \tag{3.22}$$

and, in the limit of $\kappa_{\mathrm{e}} \ll \kappa_{\mathrm{b}}\vartheta_0$, we readily obtain

$$\frac{\partial J}{\partial \beta} \approx \begin{cases} -\frac{2\kappa_{\mathrm{e}}\delta T[\ln(\ell/r_0)]^2}{[\ln(R/r_0)]^2} & (\alpha \gg 1), \\ -2\kappa_{\mathrm{e}}\delta T & (\alpha \ll 1). \end{cases} \tag{3.23}$$

Once again, these results are consistent with those of the perturbative approach. Also, from Eqs. (3.20) and (3.22), we find that the magnitude of the heat-current sensitivity is generally maximized when κ_{e} and $[\rho(\ell)]^{-1}$ are both much smaller than $[\rho(\ell,R)]^{-1}$, which precisely corresponds to the second case of Eq. (3.23). In this limit characterized by $\kappa_{\mathrm{e}} \ll \kappa_{\mathrm{b}}\vartheta_0$ and $\kappa_{\mathrm{c}} \ll \kappa_{\mathrm{b}}\vartheta_0$, the heat current itself takes a simple form: $J \approx 2\,\delta T[\kappa_{\mathrm{c}} + (1-\beta)\kappa_{\mathrm{e}}]$. Therefore, if the thermal conductance κ_{c} of the central region is known or negligibly small, measuring the thermal conductance of the entire device, $\kappa = J/(2\,\delta T)$, in the absence of any pinch points ($\beta = 0$) can be used to directly extract the edge thermal Hall conductivity κ_{e} and, hence, the chiral central charge of the corresponding edge CFT.

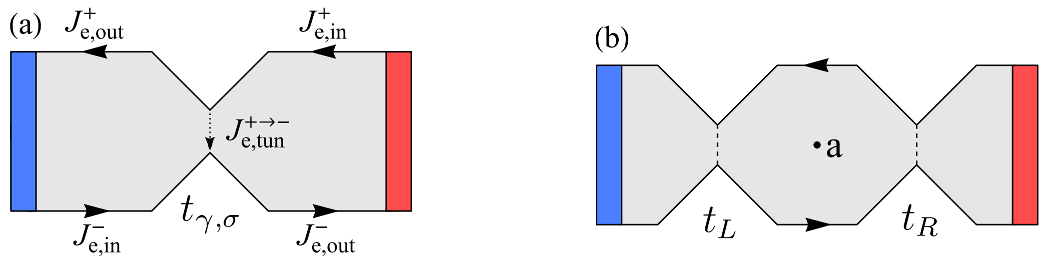

Figure 3.4: **Anyon tunneling at point contacts** (a) Single pinch and (b) double pinch geometries for a chiral spin liquid heated from the right and cooled from the left. In the double pinch geometry, we allow for a bulk quasiparticle of type "a" inside the region enclosed by the two pinch points. We imagine measuring the heat current immediately after the pinch point(s) such that energy exchange with phonons in the bulk may be neglected.

3.2 Tunneling conductance

The temperature profiles calculated in the previous section relied upon the parameter β describing the fraction of energy that jumps across the point contacts in the narrow central region. This quantity may be directly calculated by a perturbative treatment of the quasiparticle tunneling processes that shuttle between the upper and lower edges. Since the edges thermalize with the bulk in the macroscopic lobes, we may treat the edges as being initially decoupled. Let us denote $\gamma_i(x)$ the chiral Majorana mode on top ($i = 1$) and bottom ($i = 2$) edges, with the coordiante x taken to increase along the direction of propagation on each edge. We take a normalization of the edge field such that the commutation relation $\{\gamma_i(x), \gamma_j(y)\} = \delta(x-y)\delta_{i,j}$ is satisfied. Each edge then has a linear spectrum as given by the following Hamiltonian,

$$H_{\text{edge, i}} = \frac{-iv}{2}\int \mathrm{d}x {:}\gamma_i \partial_x \gamma_i{:} = v\int_0^\infty \frac{\mathrm{d}k}{2\pi}\gamma_i(-k)\gamma_i(k), \tag{3.24}$$

where $:\cdot:$ denotes normal ordering and momentum-mode occupation at finite temperature T is given by the Fermi-Dirac distribution $\langle\gamma(-k)\gamma(k)\rangle = n_F(k,T) = (e^{vk/k_BT}+1)^{-1}$. We now introduce pinch points which bring the upper and lower edges close to one another at coordinates x_i and $\tilde{x}_i$, respectively. Both fermions and Ising anyons may tunnel across such a point contact, as captured by the perturbing Hamiltonian

$$H_{\text{tun}} = \sum_i \left[-it_{\gamma,i}\gamma_1(x_i)\gamma_2(\tilde{x}_i) + e^{-i\pi/16}t_{\sigma,i}\sigma_1(x_i)\sigma_2(\tilde{x}_i)\right], \tag{3.25}$$

where $t_{\gamma,i}$ ($t_{\sigma,i}$) is the tunneling amplitude for fermions (Ising anyons) at the i-th point-contact. The phenomenology of such tunneling has been studied extensively [109, 108, 107], and one may straightforwardly evaluate the resulting corrections to thermal transport. In the interest of drawing a distinction between signatures inherent to quasiparticle tunneling versus those arising from quasiparticle braiding, we consider both single-pinch and double-pinch geometries (see Fig. 3.4).

Mirroring the analysis from Sec. 3.1, we couple the spin liquid to heating and cooling elements so as to establish a temperature differential between the opposing ends. We emphasize, however, that each heating or cooling element in Fig. 3.4 corresponds to an entire lobe connected to the central region (see Fig. 3.1) and accounts for the actual thermal lead coupling to the bulk as well as the edge-bulk thermalization. Thus, these effective heating and cooling elements directly set the temperatures of the incoming edges. In the low temperature limit, we may consider the scenario where the hot edge is held at temperature T while the cold end is held at zero temperature. We may then neglect heat current originating from the bottom edge where it couples to the cooling element, admitting a simplified analysis in terms of scattering rates at the pinch points.

Linear response via the Kubo formula

In the decoupled limit we recall that the thermal conductance of the edge is simply $\kappa = \kappa_e$. With finite tunneling, we seek the tunneling conductance $\kappa_{\text{tun}} = \beta\kappa_e$ such that $\kappa = \kappa_e - \kappa_{\text{tun}}$ as defined earlier. For weak tunneling, we may compute the tunneling conductance by perturbative treatment. To this end, let us define the tunneling current J_{tun} as the net heat current exchanged between the hot and cold edge via tunneling. This may be expressed in the Heisenberg picture as the energy flux from the upper edge,

$$J_{\text{tun}} \equiv \partial_t H_{\text{edge},1} = i\left[H_{\text{edge},1}, H_{\text{tun}}\right], \tag{3.26}$$

where $H_{\text{edge},1}$ is the unperturbed Hamiltonian for the upper edge as defined in Eq. (3.24). The leading order contribution to J_{tun} may be computed via the Kubo formula,

$$\langle J_{\text{tun}}(T_1, T_2)\rangle = -i\int_{-\infty}^{t} \mathrm{d}t'\ \langle[J_{\text{tun}}(t), H_{\text{tun}}(t')]\rangle_0\,, \tag{3.27}$$

where we send $t \to \infty$ and expectation values $\langle\cdot\rangle_0$ are evaluated with respect to the unperturbed edges at finite temperatures T_1 and T_2. The linearized thermal conductance through the point contacts is then given by taking an appropriate limit of the heat current,

$$\kappa_{\text{tun}} = \lim_{\delta T\to 0}\frac{\langle J_{\text{tun}}(T+\delta T, T-\delta T)\rangle}{2\delta T} \quad \text{or} \quad \lim_{T\to 0}\frac{\partial}{\partial T}\langle J_{\text{tun}}(T, 0)\rangle,$$

where the former corresponds to the scenario depicted in Fig. 3.2.

While we are interested in fermion and Ising anyon tunneling, let us consider a more generic scenario where a field ϕ with conformal dimension h_ϕ tunnels between the two edges at some arbitrary number of pinch points, given by the Hamiltonian

$$H_{\text{tun}} = e^{-i\pi h_\phi}\sum_i t_{\phi,i}\phi_1(x_i)\phi_2(\bar{x}_i). \tag{3.28}$$

Note that we assume the field ϕ to be normalized here such that the finite-temperature two-point correlation function takes the standard form,

$$G(z,T) \equiv \langle \phi(x_1,t_1)\phi(x_2,t_2)\rangle_0 = \left(\frac{i\pi T}{\sinh(\pi T z - i\epsilon)}\right)^{2h_\phi}, \quad z \equiv (t_1 - t_2) - (x_1 - x_2), \tag{3.29}$$

where we have adopted units with $v = 1$ for simplicity. The energy density along the upper edge commutes with the field ϕ on the bottom edge. We may therefore write the tunneling current in a simplified form,

$$J_{\text{tun}}(t) = -e^{-i\pi h_\phi}\sum_i t_{\phi,i}(\partial_t \phi_1(x_i,t))\phi_2(\bar{x}_i,t). \tag{3.30}$$

It is straightforward to observe that the commutator of J_{tun} and H_{tun} will consist of a product of bilinears on each edge, which become two-point functions upon taking the expectation value. Defining $z = (t-t') - (x_i - x_j)$ and $\bar{z} = (t-t') - (\bar{x}_i - \bar{x}_j)$, the Kubo formula in Eq. (3.27) may be rewritten as

$$\langle J_{\text{tun}}(T_1,T_2)\rangle = -i\sum_{ij} e^{-i2\pi h_\phi} t_{\phi,i}t_{\phi,j}\int_{-\infty}^{t} \mathrm{d}t' \left(G(\bar{z},T_2)\partial_t G(z,T_1) - G(-\bar{z},T_2)\partial_t G(-z,T_1)\right). \tag{3.31}$$

To evaluate the integral in Eq. (3.31), we may pass to momentum space. The Fourier transformed two-point function is given by,

$$G(k,T) \equiv (-1)^{h_\phi}\frac{(2\pi T)^{2h_\phi - 1}}{\Gamma(2h_\phi)} e^{k/2T}\left|\Gamma\left(h_\phi + \frac{ik}{2\pi T}\right)\right|^2. \tag{3.32}$$

This yields an intuitive expression,

$$\begin{aligned} \langle J_{\text{tun}}(T_1,T_2)\rangle &= e^{-i2\pi h_\phi}\sum_{ij} t_{\phi,i}t_{\phi,j}\int_{-\infty}^{\infty}\frac{\mathrm{d}k}{2\pi} G(k,T_1)G(-k,T_2)k\cos(k\Delta_{ij}) \\ \Delta_{ij} &\equiv z_{ij} - \bar{z}_{ij} = (x_i - x_j) - (\bar{x}_i - \bar{x}_j) \end{aligned} \tag{3.33}$$

where Δ_{ij} is the path length for the interference loop defined by tunneling through the i-th and j-th pinch points. In this form we see that momentum mode k contributes energy k with weight given by the product of Green's functions, modulated by the interference phase.

We may now compute the tunneling conductance for our proposed device by taking edge temperatures $T_{1/2} = T \pm \delta T$. In App. A.2, we show that the resulting tunneling conductance is

$$\begin{aligned} \kappa_{\text{tun}} &= -(2\pi T)^{4h_\phi - 1}\sum_{ij} t_{\phi,i}t_{\phi,j}F_\phi(2\pi T\Delta_{ij}), \\ F_\phi(x) &= \frac{-2\pi^2}{\Gamma(2h_\phi)^2} G^{2,4}_{4,4}\left(e^x \,\middle|\, \begin{matrix} 0,0,1-h_\phi,1-h_\phi \\ h_\phi,h_\phi,1,1 \end{matrix}\right), \end{aligned} \tag{3.34}$$

where $F_\phi(x)$ is expressed in terms of the Meijer G-function. It is now evident that κ_{tun} carries a power-law temperature dependence $T^{4h_\phi - 1}$, where the exponent reflects the conformal dimension h_ϕ of the tunneling field ϕ. Further temperature dependence is encoded in the scaling function F_ϕ, which depends on the ratio of the path length Δ_{ij} and the thermal coherence length $\xi \sim \hbar v/k_B T$ (recall that we have taken units $\hbar, v, k_B = 1$ here). Letting $x = 2\pi T\Delta_{ij}$, we have asymptotic scaling,

$$F_\phi(x) \approx F_\phi(0)\cdot\begin{cases}\dfrac{(1+4h_\phi)\Gamma(4h_\phi)}{\Gamma(2h_\phi)^2}e^{-h|x|}|x| & |x|\to\infty\\ 1-\dfrac{h_\phi(2+3h_\phi)}{2(3+4h_\phi)}x^2 & x\to 0\end{cases}, \qquad F_\phi(0)=\frac{2\pi^2 h_\phi^2\Gamma(2h_\phi)^2}{(1+4h_\phi)\Gamma(4h_\phi)}, \tag{3.35}$$

where we have normalized the expression with respect to the limiting behavior at $x = 0$. From the above we see that when the path length is small relative to the thermal coherence length ($|\Delta_{ij}| \ll \xi$), the tunneling conductance retains leading order $T^{4h_\phi-1}$ scaling, with subleading contributions at order $T^{4h_\phi+1}$. Tunneling at a single point contact fixes $\Delta_{ij} = 0$, for which F_ϕ is a constant and does not contain subleading temperature dependence. In the opposite limit, $|\Delta_{ij}| \gg \xi$, the interference contribution to the tunneling conductance is exponentially suppressed.

Fermion tunneling

In a KSL, tunneling of fermions at a point contact is a marginal perturbation, with $h_\gamma = 1/2$. From Eq. (3.34), we see that fermion tunneling induces a tunneling conductance which scales linearly in temperature. Fixing $h_\gamma = 1/2$, the scaling function $F_\gamma(x)$ becomes,

$$\begin{aligned} F_\gamma(x) &= -\frac{\pi^2}{8}\operatorname{csch}^3\left(\frac{x}{2}\right)\left[x(3+\cosh(x)) - 4\sinh(x)\right] \\ &= \int_0^\infty \mathrm{d}v\, v^2 n_F(v) n_F(-v)\cos\left(\frac{xv}{2\pi}\right). \end{aligned} \tag{3.36}$$

In the second line we have rewritten F_γ in a form akin to Fermi's golden rule, directly reflecting the Fermi-Dirac distribution $n_F(v) = (e^v+1)^{-1}$ for the edge fermions.

Before presenting the exact expresion for the tunneling conductance, let us address normalization conventions. In the standard form of the Hamiltonian given by Eq. (3.24) and (3.25), the edge fermions γ have momentum-mode occupation set by the Fermi-Dirac distribution, $\langle\gamma(k)\gamma(-k)\rangle = n_F(-k,T)$. However, in the CFT framework the normalized two-point function for $h_\gamma = 1/2$ is $G(k,T) = 2\pi i n_F(-k,T)$. The properly normalized field entering the Kubo formula calculations is thus $\sqrt{2\pi}\gamma$. We can reconcile this difference by absorbing the normalization constant into the tunneling amplitude, $t_\gamma \to t_\gamma/2\pi$. Having made consistent the normalization convention, we now evaluate Eq. (3.34) to determine the tunneling conductance.

With a single pinch point we have non-interference contributions with weight $F_\gamma(0) = \pi^2/6$ such that the tunneling conductance is

$$\kappa_{\text{tun}} = \frac{t_\gamma^2}{4\pi^2}(2\pi T)F_\gamma(0) = t_\gamma^2\frac{\pi T}{12} = t_\gamma^2\kappa_e. \tag{3.37}$$

We observe that the tunneling conductance carries the same temperature dependence as the unperturbed conductance κ_e. This may not be a readily distinguishable feature in noisy measurements when t_γ is perturbatively small, and so single-pinch fermion tunneling will not provide the robust and unambiguous signature of the underlying topoligical order we are interested in.

For a device geometry with two pinch points we gain an additional contribution from the interfering path involving tunneling at both point contacts. These processes are sensitive to the bulk anyon content in the region enclosed between the two pinch points. While the earlier calculations were carried out under the assumption of trivial topological charge in the bulk, fermion braiding in a KSL is strictly abelian. As a result, we may simply append the appropriate statistical phase in the expression for the conductance. Denoting $n_\sigma = 0, 1$ the parity of bulk Ising anyons in the interferometer region, the interference paths accumulate a statistical phase $(-1)^{n_\sigma}$. The total tunneling conductance is then,

$$\kappa_{\text{tun}} = \kappa_e \left[t_{\gamma,1}^2 + t_{\gamma,2}^2 + 2t_{\gamma,1}t_{\gamma,2}\frac{F_\gamma(2\pi T\Delta)}{F_\gamma(0)} \right], \tag{3.38}$$

Thus with two pinch points, the tunneling conductance will encode universal features of the underlying topological order (i.e., the anyon braid phases). The magnitude of the interference term depends on the temperature T and interferometer path length Δ through the scaling function $F_\gamma(2\pi T\Delta)$. As depicted in Fig. 3.5a, F_γ undergoes a sign change before decaying exponentially at large argument.

Scattering picture

We now consider an alternative scattering picture by which to derive the tunneling conductance. Noting that fermion tunneling is a quadratic perturbation, we may treat its effects exactly by considering the Heisenberg equations of motion for the fermion fields on both edges,

$$\begin{aligned} i\partial_t\gamma_1(x,t) &= -iv\partial_x\gamma_1(x,t) + i\sum_i t_{\gamma,i}\delta(x-x_i)\gamma_2(\bar{x}_i), \\ i\partial_t\gamma_2(x,t) &= -iv\partial - x\gamma_2(x,t) - i\sum_i t_{\gamma,i}\delta(x-\bar{x}_i)\gamma_1(x_i) \end{aligned} \tag{3.39}$$

Let us first consider the case of a single pinch point, fixing $x_i = \bar{x}_i = 0$. Then the equation of motion becomes $i\partial_t\vec{\gamma} = \left[-iv\partial_x\tau_0 + t_\gamma\delta(x)\tau_2\right]\vec{\gamma}$, where $\vec{\gamma} = (\gamma_1, \gamma_2)^T$ and τ_i are the Pauli matrices. Integrating about an infinitesimal window enclosing $x = 0$, one finds

$$\vec{\gamma}(0^+,t) = \begin{pmatrix} \mathcal{T} & \mathcal{R} \\ -\mathcal{R} & \mathcal{T} \end{pmatrix} \vec{\gamma}(0^-,t), \quad \mathcal{T} = \frac{4v^2 - t_\gamma^2}{4v^2 + t_\gamma^2}, \quad \mathcal{R} = \frac{-4t_\gamma v}{4v^2 + t_\gamma^2}, \tag{3.40}$$

where $\vec{\gamma}(0^\pm,t)$ is the field immediately before and after the pinch point. We have defined transmission and reflection coefficients $\mathcal{T}$ and $\mathcal{R}$, reflectively, where reflection corresponds to crossing the pinch point. Examining Eq. (3.40), it is clear that one can continuously

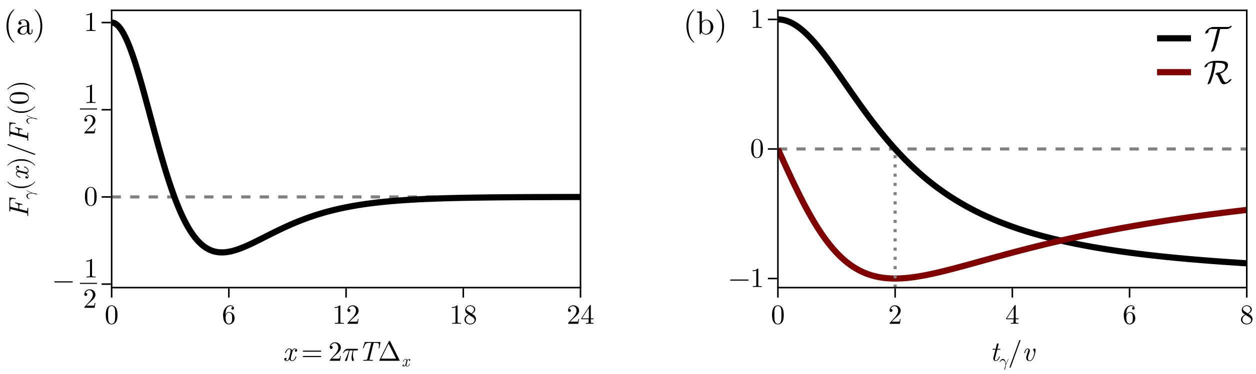

Figure 3.5: **Fermion tunneling** — (a) The magnitude of the tunneling conductance arising from fermion tunneling through two pinch points depends on the temperature T and interferometer path length Δ_x through the scaling function F_γ defined in Eq. (3.36). After passing through zero at $x \approx$, the magnitude is exponentially suppressed at large argument. (b) Scattering of an edge fermion at a pinch point yields transmission ($\mathcal{T}$) and reflection ($\mathcal{R}$) coefficients, defined in Eq. (3.40), which depend on the tunneling strength t_γ and edge velocity v. Perfect reflection occurs at $t_\gamma/v = 2$ (dotted vertical line), while reflection is suppressed in the weak and strong tunneling limits $t_\gamma \to 0, \infty$.

tune from perfect transmission ($\mathcal{R} = 0$) to perfect reflection ($\mathcal{T} = 0$) by modulating the tunneling strength (see Fig. 3.5b). Perfect reflection occurs when the tunneling strength becomes comparable to the edge velocity ($t_\gamma \to 2v$). Taking $t_\gamma \to \infty$, the point contact binds a pair of Majorana fermions, restoring perfect transmission with a statistical phase $\mathcal{T} = -1$ accumulated by edge fermions passing the pinch point.

For generic edge temperatures, the heat current passing through the pinch point is given by

$$\begin{aligned} J(T_1, T_2) &= \int_0^\infty \frac{\mathrm{d}k}{2\pi} k \left[(\mathcal{T}^2 - 1) n_F(k, T_1) + \mathcal{R}^2 n_F(k, T_2) \right] \\ &= \mathcal{R}^2 \int_0^\infty \frac{\mathrm{d}k}{2\pi} k \left[n_F(k, T_2) - n_F(k, T_1) \right] \end{aligned} \tag{3.41}$$

Taking $T_{1/2} = T \pm \delta T$, we find that the tunneling conductance is simply a product of the reflection probability $\mathcal{R}^2$ and the edge conductance κ_e,

$$\kappa_{\text{tun}} = \mathcal{R}^2 \int_0^\infty \frac{\mathrm{d}k}{2\pi} \left(\frac{k}{T} \right)^2 n_F(k, T) n_F(-k, T) = \mathcal{R}^2 \kappa_e. \tag{3.42}$$

In the limit of weak tunneling, the reflection probability becomes $\mathcal{R}^2 \approx (t_\gamma/v)^2$, such that the tunneling conductance computed here is consistent with the Kubo formula result in Eq. (3.37).

To extend this result to the two-pinch geometry, consider a wavepacket incident upon the pinch point region from the top edge. For simplicity, let us take the points along the upper and lower edges to be equally space, defining $\frac{1}{2}\Delta_x \equiv x_2 - x_1 = \bar{x}_1 - \bar{x}_2 = v\delta t$. We denote $\mathcal{T}_i = (4v^2 - t_{\gamma,i}^2)/(4v^2 - t_{\gamma,i}^2)$ the transmission coefficient for the i-th pinch point, and similarly for the reflection coefficient $\mathcal{R}_i$. Then the total transmitted component can be computed by a sum over all paths which exit along the upper edge,

$$\begin{aligned}\gamma_1(x_2^+, t) &= \sum_{n=0}^{\infty} \mathcal{T}_2 (\mathcal{R}_1\mathcal{R}_2)^n \mathcal{T}_1 \gamma_1(x_1^-, t - (2n+1)\delta t) \\ &= \int \frac{\mathrm{d}k}{2\pi} e^{ik(x_2 - vt)} \gamma_k \mathcal{T}_1\mathcal{T}_2 \sum_n \left(\mathcal{R}_1\mathcal{R}_2 e^{ikv2\delta t}\right)^n \\ &= \int \frac{\mathrm{d}k}{2\pi} e^{ik(x_2 - vt)} \gamma_k \mathcal{T}(k), \\ \mathcal{T}(k) &= \frac{\mathcal{T}_1\mathcal{T}_2}{1 - e^{ik\Delta_x}\mathcal{R}_1\mathcal{R}_2},\end{aligned} \tag{3.43}$$

where we have defined $\mathcal{T}(k)$ to be the total transmission coefficient at momentum k. Whereas the single pinch transmission coefficient $\mathcal{T}_i$ was momentum independent, the dynamical phase accumulated by tunneling paths which braid through both point contacts yields the momentum dependence of $\mathcal{T}(k)$. We may similarly define the total reflection probability

$$\begin{aligned}|\mathcal{R}(k)|^2 = 1 - |\mathcal{T}(k)|^2 &= \frac{\mathcal{R}_1^2 + \mathcal{R}_2^2 - 2\mathcal{R}_1\mathcal{R}_2\cos(k\Delta_x)}{1 + \mathcal{R}_1^2\mathcal{R}_2^2 - 2\mathcal{R}_1\mathcal{R}_2\cos(k\Delta_x)}, \\ &\approx \frac{1}{v^2}\left[t_1^2 + t_2^2 - 2t_1t_2\cos(k\Delta_x)\right]\end{aligned} \tag{3.44}$$

It is then straightforward to show that the thermal current and corresponding conductance induced by tunneling are given by

$$\begin{aligned}J(T_1, T_2) &= \int_0^\infty \frac{\mathrm{d}k}{2\pi} v^2 k\, |\mathcal{R}(k)|^2 \left[n_F(k, T_2) - n_F(k, T_1)\right] \\ \kappa_{\text{tun}} &= \partial_T \int_0^\infty \frac{\mathrm{d}k}{2\pi} v^2 k\, |\mathcal{R}(k)|^2 n_F(k, T) \\ &\approx \kappa_e \frac{1}{v^2}\left[t_{\gamma,1}^1 + t_{\gamma,2}^2 + (-1)^{n_\sigma} t_{\gamma,1} t_{\gamma,2} \frac{F_\gamma(2\pi\Delta_x k_B T/v)}{F_\gamma(0)}\right],\end{aligned} \tag{3.45}$$

where we have taken the perturbative expansion for weak tunneling amplitudes $t_{\gamma,i}$. We see that the this scattering calculation is not only consistent with the expression derived from applying the Kubo formula but also gives all higher order tunneling contributions.

Consider now the presence of non-trivial topological charge in the bulk region enclosed by the two pinch points. Tunneling paths which encircle the bulk anyon will acquire a statistical braid phase. Fermions have non-trivial braid phase with Ising anyons. Denoting n_σ the parity of Ising anyons in the interferometer region, braid statistics enter the path summation in Eq. (3.43) as $(-1)^{n_\sigma}$ for every loop. In practice this may simply be absorbed into one of the tunneling amplitudes, (e.g., $t_{\gamma,1} \to (-1)^{n_\sigma} t_{\gamma,1}$).

Ising anyon tunneling

We now consider the more relevant tunneling process that may take place at point contacts in this non-Abelian spin liquid phase—tunneling of Ising anyons with $h_\sigma = 1/16$. Appealing to the generic result in Eq. (3.34), we see that Ising anyon tunneling yields a tunneling conductance scaling with temperature like

$$\kappa_{\text{tun}} = \frac{t_\sigma^2 \pi^{7/4} \Gamma(1/8)}{256\Gamma(13/8)} T^{-3/4} = \kappa_e \tilde{t}_\sigma^2 T^{-7/4}, \tag{3.46}$$

where we have defined normalized tunneling amplitude $\tilde{t}_\sigma$ to bring the expression into a simpler form. The divergence in the low temperature limit comports with the observation that Ising anyon tunneling is a relevant perturbation, under which the system flows to a split bar wherein all energy is scattered to the bottom edge at the point contact. Such a 7/4 power law has been discussed by Nilsson and Akhmerov [265] in the context of electrical conductance measurements for a topological insulator in proximity with a superconductor. In both scenarios, this exponent comes from the scaling dimension of the tunneling operator that corrects the fermionic edge current. To the best of our knowledge, this power law is not reproduced by other less exotic phenomenology, and so provides a unique signature of fractional quasiparticles tunneling at the point contact in a single-pinch geometry.

To make connection with the scattering picture presented for fermion tunneling, consider a single point contact at $x_1 = \bar{x}_i = 0$. Then taking $\delta x > 0$ an arbitrary displacement from the pinch point, the Green's function $\langle \gamma_1(\delta x, t)\gamma_1(-\delta x, 0)\rangle$ probes the transmission along the upper edge. Expanding perturbatively in the tunneling strength t_σ, we seek the leading correction arising from Ising anyon tunneling.

As in the Kubo formula analysis, correlation functions are evaluated with the upper and lower edges treated as decoupled. Then at first order in t_σ one essentially has to consider a correlator like $\langle \sigma_1(0,t')\rangle_0 \langle \gamma_1(\delta x, t)\sigma(0,t')\gamma_1(-\delta x, 0)\rangle_0$. Both terms must vanish since the nontrivial primary fields exhibit vanishing ground-state expectation values (e.g., $\langle 0|\,\sigma\,|0\rangle = 0$). Put simply, tunneling a single Ising anyon cannot move a fermion from the top edge to the bottom edge, and so cannot affect the heat current along the edge.

The first non-trivial correction then comes at second order in Ising anyon tunneling,

$$\sim \int \mathrm{d}s_1\, \mathrm{d}s_2 \langle \gamma_1(\delta x, t)\left(H_{\text{tun}}(s_1)H_{\text{tun}}(s_2) - \langle H_{\text{tun}}(s_1)H_{\text{tun}}(s_2)\rangle_0\right)\gamma_1(-\delta x, 0)\rangle_0$$

where implicitly one employs a cluster decomposition to correlation functions on the two edges. Here we have adopted the shorthand $H_{\text{tun}}(t) = t_\sigma \sigma_1(0,t)\sigma_2(0,t)$ for the Ising anyon tunneling Hamiltonian in the interaction picture. As we show in Appendix A.2, this yields a reflection probability which diverges as $t_\sigma^2 k^{-7/4}$ as $k \to 0$. The corresponding correction to the heat current then vanishes as $T^{1/4}$, while the correction to the edge conductance diverges as $T^{-3/4}$ at low temperature.

Let us now consider the effect of braiding statistics in the two-pinch geometry. To get some effect beyond that found in the single pinch geometry, we should consider processes wherein an Ising anyon braids around the bulk, analogous to the braiding processes for fermions examined above. In this scenario, we may envision that a Majorana fermion incident on the constrictions splinters into two Ising anyons, one of which tunnels to the bottom edge. This tunneled Ising anyon later returns to the top edge by tunneling across at the other constriction. Such processes take a *single* Ising anyon around quasiparticles residing in the bulk. Recall that taking an Ising anyon around a Majorana fermion yields a statistical phase factor of -1. Then for n_ψ bulk Majorana fermions contained between the constrictions, this braiding process yields a phase $(-1)^{n_\psi}$. If the number of enclosed bulk Ising anyons n_σ is odd, then the braid non-trivially rotates the many-body wavefunction—killing the interference term. Putting these effects together, we must attach a factor of $(-1)^{n_\psi}\left[1+(-1)^{n_\sigma}\right]/2$ to corrections arising from $\mathcal{O}(t_{L,\sigma}t_{R,\sigma})$ Ising anyon braiding processes. Notice that when n_σ is odd the braiding phase becomes independent of n_ψ; this result is indeed required by the fusion rule $\sigma\times\psi=\sigma$. Taken all together, this yields the following Ising-anyon induced tunneling conductance in a two-pinch geometry,

$$\kappa_{\text{tun}} = T^{-3/4}\left\{\tilde{t}_{\sigma,1}^2+\tilde{t}_{\sigma,2}^2+\tilde{t}_{\sigma,1}\tilde{t}_{\sigma,2}(-1)^{n_\psi}\left[1+(-1)^{n_\sigma}\right]\frac{F_\sigma(2\pi T\Delta)}{F_\sigma(0)}\right\} \tag{3.47}$$

Unlike the fermion braiding correction, the interference term above is sensitive both to fermions *and* Ising anyons in the bulk, allowing for detection of individual bulk quasiparticles of either type.

General Result

Thus far we have calculated the tunneling conductance $\kappa_{\text{tun}}=\beta\kappa_e$, where β is the parameter describing the fraction of energy which tunnels across the constrictions. Collecting our two-pinch-geometry results, we obtain

$$\begin{aligned}\beta(\Delta_x,T) \;\approx\; & t_{\gamma,1}^2+t_{\gamma,2}^2+2(-1)^{n_\sigma}t_{\gamma,1}t_{\gamma,2}\frac{F_\gamma(2\pi\Delta_x T)}{F_\gamma(0)}\\ &+T^{-7/4}\left\{\tilde{t}_{\sigma,1}^2+\tilde{t}_{\sigma,2}^2+(-1)^{n_\psi}\left[1+(-1)^{n_\sigma}\right]\tilde{t}_{\sigma,1}\tilde{t}_{\sigma,2}\frac{F_\sigma(2\pi\Delta_x T)}{F_\sigma(0)}\right\}.\end{aligned} \tag{3.48}$$

In a single pinch geometry, this result simplifies further to $\beta(T)=t_\gamma^2+\tilde{t}_\sigma^2T^{-7/4}$. We see then that the tunneling conductance encodes distinct signatures of the underlying topological order both through the power-law temperature dependence and through interferometric terms sensitive to the bulk anyon content. To connect these results to our earlier analysis of heat exchange between the bulk phonons and the edge mode, β should be evaluated with respect to the overall system temperature T_0, assuming that the deviations δT are small.

While the particular expression for β derived here was for the case of Ising topological order ($c=\frac{1}{2}$) in a Kitaev spin liquid, a similar analysis could be carried out for other chiral topological orders. In general, the expression for β in a single pinch geometry will always feature a temperature dependence $\beta \propto T^{-\eta}$ where $\eta = 2 - 4h$ is determined by the conformal dimension h of the most relevant edge operator in the theory. Similarly, the details of the interference corrections arising in a multi-pinch geometry will then of course depend on the braiding statistics of the quasiparticles in the particular phase.

3.3 Discussion

In the previous two sections, we described how thermal transport in the unconventional device geometry of Fig. 3.1 can be used to probe the anyonic excitations of the non-Abelian Kitaev spin liquid. Our main focus was anyonic edge interferometry, using two point contacts, which can detect individual anyons and directly observe their nontrivial braiding statistics. In addition, we considered simpler measurements, requiring at most one point contact, for unambiguously identifying the underlying spin liquid via both the quantized thermal Hall conductivity [177, 361, 54] extracted in a more direct way and "smoking-gun" signatures of Ising-anyon tunneling. Indeed, it was described in Sec. 3.2 how the tunneling parameter β is determined by the edge tunneling processes in the central region, while it was explained in Sec. 3.1 how β (or a change in β) can be detected in the bulk thermal transport by measuring the temperature profile or the thermal conductance of the device. In this section, we discuss potential challenges in the experimental observation of these signatures and provide simple guidelines for implementing our proposal in realistic candidate materials, such as α-$RuCl_3$.

Thermalization Length

For effectively probing the quantum-coherent edge processes inside the central region via bulk thermal transport within the two lobes (see Fig. 3.2), the thermalization length ℓ between the edge mode and the bulk phonons must satisfy $r_0 \ll \ell \ll R$. On the one hand, if the central region is larger than the thermalization length, $r_0 \gg \ell$, thermalization with bulk phonons may disrupt the quantum coherence of the edge processes. On the other hand, if the lobes are smaller than the thermalization length, $R \ll \ell$, the edge mode is essentially decoupled from the bulk thermal leads and sensors.

The thermalization length is given by $\ell = \kappa_e/\lambda$, where $\kappa_e \propto T$ is the thermal Hall conductivity of the edge mode, and λ is the linearized thermal coupling between the edge mode and the bulk phonons. Since λ was argued [360] to be proportional to T^6, the thermalization length is then expected to diverge as $\ell \propto T^{-5}$ at low temperatures. Due to this strong temperature dependence of the thermalization length, our proposal is only applicable within a reasonable temperature range if the two characteristic sizes r_0 and R differ by orders of magnitude. Nevertheless, for $r_0 \sim 1$ μm and $R \sim 1$ cm [177], the range of applicability spans almost a decade in temperature, which is sufficient for observing all of our proposed signatures, including a reliable extraction of the universal power law $\beta \propto T^{-7/4}$ that corresponds to Ising-anyon tunneling.

Importantly, this range of applicability must also correspond to temperatures that are experimentally accessible but sufficiently small to be consistent with the other constraints described in the following subsections. However, we remark that, according to Ref. [360], the dominant low-temperature mechanism for the edge-bulk coupling $\lambda \propto T^6$ relies on the presence of disorder. Therefore, the range of applicability may be shifted to lower temperatures if an appropriate amount of disorder is artificially introduced in the material to reduce the thermalization length without destroying the underlying spin liquid.

Edge Coherence Length

For observing anyonic edge interferometry in the presence of thermal fluctuations at the edge, the separation between the two pinch points, Δ_x, must not exceed the thermal edge coherence length, $\xi \sim \hbar v/(k_B T)$, where v is the edge-mode velocity [60]. This constraint is directly manifest in our result for the fermion tunneling where the interference term in β [see Eq. (3.38)] is proportional to the function $F_\gamma[2\pi k_B T \Delta_x/(\hbar v)]$ [8] that is exponentially suppressed for large arguments. While our calculation of the Ising-anyon tunneling is based on zero-temperature correlators and only applies at low temperatures, $\Delta_x \ll \xi$ [9], we nevertheless expect a similar exponential suppression for the Ising-anyon tunneling in the high-temperature $\Delta_x \gg \xi$ limit [265].

Considering α-$RuCl_3$, if we assume that the edge velocity is controlled by the Kitaev interaction, $J \sim 100$ K, we can estimate the edge velocity as $v \sim Ja/\hbar$, where $a \sim 1$ nm is the lattice constant. The edge coherence length is then given by $\xi \sim Ja/(k_B T)$ and, for a pinch separation Δ_x, the temperature must satisfy $k_B T \lesssim Ja/\Delta_x$. Thus, taking $\Delta_x \sim 100$ nm, we find that anyon interferometry must be performed at temperatures below 1 K. We note that this constraint may be more stringent if the edge velocity is instead controlled by the bulk energy gap which is suggested by Ref. [177] to be $\Delta \approx 5$ K. Therefore, to minimize disruptions due to thermal fluctuations at the edge, it is ideal to keep the pinch separation Δ_x as small as possible. At the same time, however, the pinch separation must also be much larger than the bulk correlation length to avoid finite-size effects. Based on the exactly solvable Kitaev model, this correlation length is comparable to the lattice constant if the bulk gap is a sizeable fraction of the Kitaev interaction. Finally, we emphasize that the edge coherence length is only relevant for anyon interferometry and does not affect the simpler measurements using at most one pinch point.

Fluctuating Bulk Anyons

To detect individual bulk anyons through anyonic edge interferometry, we assume that the bulk anyons are localized at appropriate pinning sites in a stable way. For example, it is known that spin vacancies in the exactly solvable Kitaev model bind gauge fluxes [347,

[8] We have restored appropriate factors of $\hbar$, k_B, and v.

[9] At the same time, we also assume that the temperature is high enough that the tunneling is still perturbative.

348, 175], which correspond to Ising anyons in the non-Abelian spin liquid. Ideally, one would be able to control the total anyon content between the two pinch points *in situ* and observe the resulting changes in β by measuring appropriate phonon temperatures and/or the longitudinal thermal conductance. However, in the presence of thermally excited bulk anyons, uncontrolled anyon motion may lead to repeated switches in the total anyon content during the (presumably long) time scale of such a measurement, thereby washing out any interference effect resulting from the anyons localized at pinning sites.

We first present a sufficient (but not necessary) condition for observing anyon interferometry in the presence of thermally excited bulk anyons. In general, for a bulk energy gap Δ, the density of such thermal anyons is expected to be $\rho \sim \exp[-\Delta/(k_B T)]$. The average number of thermal anyons in the region between the two pinch points is then $\nu \sim N\rho$, where $N = A/a^2$ is the size of the region in terms of its area A and the lattice constant a. In turn, if $\nu \ll 1$, thermal anyons are sufficiently rare that they cannot be disruptive to anyon interferometry. Thus, our sufficient condition for observing anyon interferometry becomes $k_B T \ll \Delta/\ln N$, which is only slightly more stringent than the standard condition $k_B T \ll \Delta$ for probing universal low-energy properties. Indeed, if we assume $\Delta \approx 5$ K for α-$RuCl_3$ [177] and take $A \sim (100\text{ nm})^2$ as well as $a \sim 1$ nm, we find that the sufficient condition is satisfied for temperatures below ≈ 0.5 K.

However, even if this sufficient condition is not satisfied and there are many thermal anyons in the region between the two pinch points, anyon interferometry may still be observable if the total anyon content fluctuates sufficiently slowly with respect to the time scale of the measurement. While it is challenging to estimate the relevant time scales, the fluctuation rate is limited by the fact that the total anyon content can only change if an anyon is created or annihilated at the edge or if it goes through one of the pinch points. In turn, for a sufficiently small fluctuation rate, we anticipate that the measured quantity (e.g., thermal conductance) exhibits telegraph noise [2], repeatedly switching between a finite number of allowed values corresponding to different total anyon contents [see Eq. (3.48)] as a function of time.

Finally, we point out that distinct fingerprints of anyon interference may be statistically observable even if the measurement is obtained by accumulating signal over a time scale that is long compared to the time scales of fermion (n_ψ) and Ising-anyon (n_σ) fluctuations. To start with a simple problem, we assume that the only fluctations are in the fermion parity, $n_\psi = \{0, 1\}$, so that the measured quantity O (e.g., temperature or thermal conductance) can take only two different instantaneous values, $O_{n_\psi=0}$ and $O_{n_\psi=1}$. A standard stochastic process, the Goldstein-Kac process [130, 169], gives a solvable model for this problem if the time between two flips is assumed to be much longer than the time taken in the flipping process itself such that repeated *instantaneous* measurements result in telegraph noise. Taking a flip rate μ, we define the integrated measurement over a time interval τ to be $\int_0^\tau O(t)\,\mathrm{d}t = \tau\bar{O} + x$, where $\bar{O} \equiv (O_0 + O_1)/2$ is the mean value. Then, the probability for the integrated measurement to deviate from the mean value by x is

$$p(x,\tau) \quad = \quad e^{-\mu\tau}\left[\delta(x-\chi\tau) + \delta(x+\chi\tau)\right]$$

$$+\frac{e^{-\mu\tau}}{2\chi}\Big[\mu I_0(\mu\sqrt{\chi^2\tau^2-x^2}/\chi)$$
$$+\frac{\chi I_1(\mu\sqrt{\chi^2\tau^2-x^2}/\chi)}{\sqrt{\chi^2\tau^2-x^2}}\Big]\theta(\chi\tau-|x|), \tag{3.49}$$

where $\chi = |O_0 - O_1|/2$ is the standard deviation, θ is the Heaviside step function, and $I_{0,1}$ are modified Bessel functions of the first kind. This probability distribution is normalized for each integration time τ and consists of two parts: the δ-function pieces come from the probability that the system has not flipped from its initial state, and the remainder is a smooth function that dominates and approaches a Gaussian for $\mu\tau \gg 1$. Repeating the given measurement many times and for various integration times τ, the results can then be fit to Eq. (3.49) to determine the underlying value of χ which, in turn, can be compared to the predictions in Eq. (3.48).

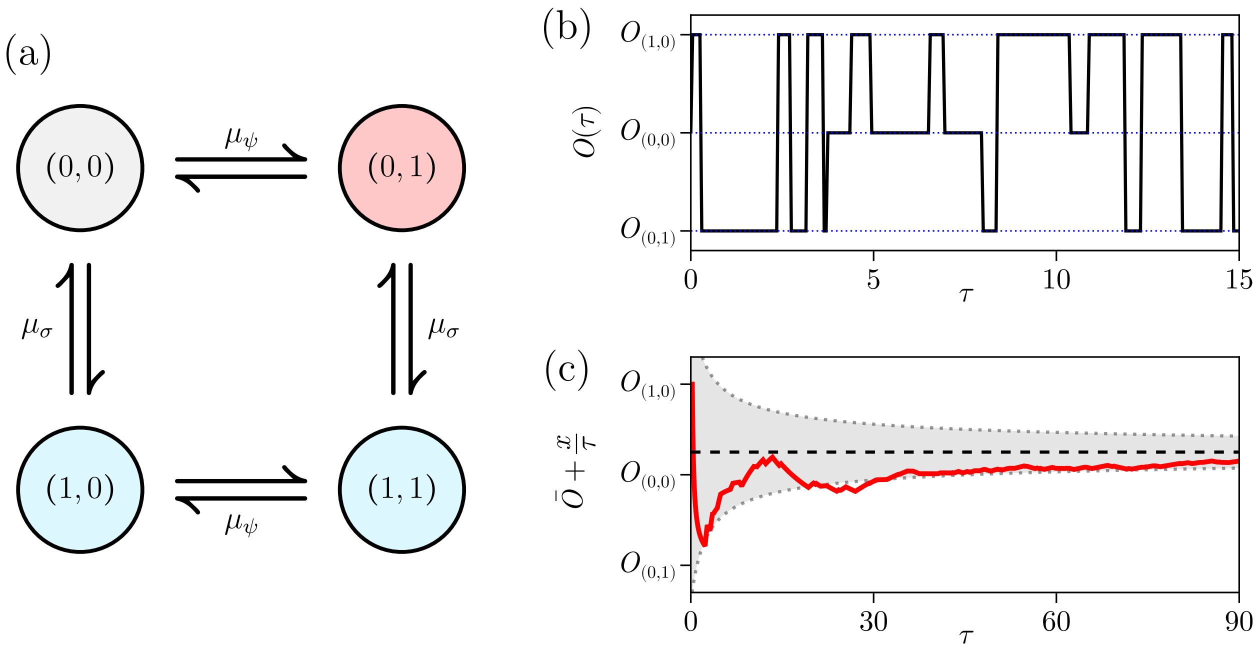

Figure 3.6: **Fluctuating anyon content** — (a) A Markov model with states labeled by the Ising anyon and fermion parities (n_σ, n_ψ), which flip at rates μ_σ and μ_ψ, respectively. States are colored by the total topological charge. (b) The instantaneous value (black) of an observable O exhibits telegraph noise, fluctuating between values $O_{(n_\sigma,n_\psi)}$ (blue) fixed by the topological charge. (c) The time averaged observable (red) $\bar{O}+x/\tau$ converges toward the steady-state average $\bar{O}$ (black dashed line), with fluctuations decaying in time according to Eq. (3.50). The shaded region corresponds to two standard deviations around $\bar{O}$.

If there are fluctuations in both n_σ and n_ψ, the model becomes a four-state Markov process with two distinct rates μ_σ and μ_ψ for the two kinds of flips between four different states labeled by (n_σ, n_ψ). Recognizing that the measured quantity O takes identical instantaneous values $O_{(n_\sigma,n_\psi)}$ for the topologically equivalent states $(1,0)$ and $(1,1)$, the variance of an integrated measurement is then

$$\begin{aligned} \langle x^2(\tau)\rangle \;\; = \;\; \tau^2 \Bigg\{ & \left[\frac{O_{(0,0)} - O_{(0,1)}}{4}\right]^2 \phi(\mu_\psi \tau) \\ & + \left[\frac{O_{(0,0)} - O_{(0,1)}}{4}\right]^2 \phi(\{\mu_\psi + \mu_\sigma\}\tau) \\ & + \left[\frac{O_{(0,0)} + O_{(0,1)} - 2O_{(1,0)}}{4}\right]^2 \phi(\mu_\sigma \tau) \Bigg\}, \end{aligned} \tag{3.50}$$

where we define the dimensionless function

$$\phi(x) = \frac{1}{x} - \frac{1 - e^{-2x}}{2x^2}. \tag{3.51}$$

As in the two-state model, repeated measurements for a range of integration times τ allow extraction of the instantaneous values $O_{(n_\sigma,n_\psi)}$ which are directly comparable with the predictions of Eq. (3.48). We further note that three distinct rates, μ_ψ, μ_σ, and $\mu_\psi + \mu_\sigma$, appear in Eq. (3.50). The need for three distinct rates to describe the τ-dependence of the variance $\langle x^2(\tau)\rangle$ can differentiate the noise of combined fermion and Ising-anyon flips from other possible sources of a single telegraph noise, for which the variance would simply be

$$\langle x^2(\tau)\rangle = \tau^2 \left(\frac{O_0 - O_1}{2}\right)^2 \phi(\mu\tau). \tag{3.52}$$

Note that Eq. (3.52) is also consistent with integration over the full probability distribution in Eq. (3.49).

Multi-Layer Samples

In this subsection, we briefly discuss how our results for a single two-dimensional layer generalize to more realistic multi-layer systems. For sufficiently weak inter-layer interactions, each layer remains an independent spin liquid with its own chiral edge mode and bulk anyons. Therefore, the edge tunneling processes in the central region are controlled by the individual layers, and we can define a distinct tunneling parameter β_i for each of the n layers labeled by $i = 1, \ldots, n$. In contrast, the phonons can move freely between the different layers and result in a bulk inter-layer thermalization within the two lobes. Thus, using the heat-resistor picture in Sec. 3.1, we anticipate that the temperatures and heat currents in an n-layer system are given by $T_n(\{\beta_i\}) = T_1(\bar\beta)$ and $J_n(\{\beta_i\}) = nJ_1(\bar\beta)$, respectively, where $\bar\beta = \frac{1}{n}\sum_{i=1}^n \beta_i$ is the mean tunneling coefficient, while $T_1(\beta)$ and $J_1(\beta)$ are the corresponding single-layer results for tunneling coefficient β.

For the simpler measurements using at most one point contact, the tunneling parameters are identical in all n layers. The measured temperatures are then not affected at all by the presence of $n > 1$ layers, while the measured thermal conductance is simply multiplied by n. Thus, for extracting the quantized thermal Hall conductivity κ_e or the universal power law $\beta \propto T^{-7/4}$ reflecting Ising-anyon tunneling, it is advantageous to detect the edge tunneling processes by measuring the thermal conductance of the device, as multi-layer systems can then actually result in a more accurate measurement. To strengthen this point, we also recall that, for $\kappa_e \ll \kappa_b \vartheta_0$ and $\kappa_c \ll \kappa_b \vartheta_0$, the thermal conductance of a single layer takes the simple form $\kappa = J/(2\,\delta T) = \kappa_c + (1-\beta)\kappa_e$ which, if κ_c is either known or negligibly small, enables direct extraction of κ_e in the absence of any point contacts and $\beta \propto T^{-7/4}$ in the presence of a single point contact.

For anyonic edge interferometry, however, the distinct layers are expected to have different tunneling parameters β_i, unless one can simultaneously stabilize the same kind of anyon in all layers. Thus, we expect that anyon interferometry is generally more observable in few-layer systems where different combinations of $\{\beta_i\}$ still result in only a small number of distinct $\bar{\beta}$. In particular, a few-layer system with a small number of discrete values could still be modeled with an expanded version of the Markov-chain model in the preceding subsection. However, such few-layer systems present a number of notable experimental challenges. First, the system must be thermally isolated, as significant thermal coupling to, for example, a substrate may weaken the sensitivity to $\bar{\beta}$. Second, it may not be straightforward to measure the temperature of such a few-layer system or to detect small (order κ_e) changes in the thermal conductance. Third, a few-layer system is expected to be more susceptible to crystallographic defects, such as stacking faults, that may have a detrimental effect on the underlying spin liquid.

Optimal Dimensions

Now we synthesize the constraints discussed in the preceding subsections to understand the optimal dimensions of the device geometry in Fig. 3.2. We start by considering the narrow channel in the central region that has length $L \sim r_0$ and width $W \ll L$. To allow for anyon tunneling between the two edges, the width of the channel must be reduced at each pinch point from W to $w \ll W$ that is on the order of the bulk correlation length. Thus, we expect that the ideal pinch width is larger than but comparable to the lattice constant: $w \sim 10$ nm. Conversely, to avoid anyon tunneling away from the pinch points, the channel width itself must be much larger than the bulk correlation length. At the same time, it is advantageous to keep the channel width as small as possible because the main purpose of the channel is to act as a bottleneck for bulk phonon transport. Also, for anyonic edge interferometry, where two pinch points are separated by Δ_x, the perimeter $P \sim \Delta_x + W$ must be minimized to avoid thermal edge decoherence (see Sec. 3.3), and the area $A \sim \Delta_x W$ must be minimized to avoid thermally excited bulk anyons (see Sec. 3.3). Therefore, we expect that the ideal channel width is $W \sim \Delta_x \sim 100$ nm. In terms of the channel length L, there is a trade off between increasing L to provide a better bottleneck for bulk phonon transport and making sure that L is much smaller than the edge-bulk thermalization length ℓ (see Sec. 3.3). We anticipate that $L \sim 1$ μm is generally a good compromise for the measurements proposed in this work.

Turning our attention to the two large lobes, we first recognize that the inner radius r_0 is set by the length of the channel: $r_0 \sim L \sim 1$ μm. The outer radius R should then be as large as possible to maximize the temperature range within which $r_0 \ll \ell \ll R$ (see Sec. 3.3). Based on the single crystals used in Ref. [177], we expect that $R \sim 1$ cm is a reasonable order of magnitude. Interestingly, the ideal opening angle $2\vartheta_0$ depends on the specific type of measurement. If the temperature profile is measured, the sensitivity to the tunneling parameter β is maximized for $\kappa_\mathrm{e} \sim \kappa_\mathrm{b}\vartheta_0$ [see Eq. (3.20)], which corresponds to a small opening angle $\vartheta_0 \ll 1$ in the experimental limit of $\kappa_\mathrm{e} \ll \kappa_\mathrm{b}$ [177, 361, 54]. In contrast, if the thermal conductance is measured, the analogous sensitivity is maximized for $\kappa_\mathrm{e} \ll \kappa_\mathrm{b}\vartheta_0$ [see Eq. (3.22)], which means that the opening angle should be as large as possible: $\vartheta_0 \lesssim 1$.

For the simpler measurements using at most one pinch point, it is optimal to measure the thermal conductance in a multi-layer system as different layers can add constructively (see Sec. 3.3). An accurate extraction of the quantized thermal Hall conductivity κ_e or the universal power law $\beta \propto T^{-7/4}$ also, however, requires the thermal conductance to have a simple dependence on the tunneling parameter β. Importantly, in the limit of $\kappa_\mathrm{e} \ll \kappa_\mathrm{b}\vartheta_0$ and $\kappa_\mathrm{c} \ll \kappa_\mathrm{b}\vartheta_0$, the heat transport is dominated by the central channel, and the thermal conductance of the device is simply $\kappa = \kappa_\mathrm{c} + (1-\beta)\kappa_\mathrm{e}$ per layer. If we further assume that the phonon mean-free path D is much larger than the channel length L, the channel width W, and the channel height $H = nd$ (where n is the number of layers, and $d \sim a$ is the interlayer separation), the phonons are ballistic inside the central channel, and the phonon thermal conductance of the channel is quantized at low temperature to $n\kappa_\mathrm{c} = \pi p k_B^2 T/(6\hbar)$, where p is a small integer corresponding to the number of gapless phonon modes [309]. The thermal conductance of the entire device (per layer) is then given by

$$\kappa = \frac{J}{2\,\delta T} = \frac{\pi k_B^2 T}{6\hbar}\left[\frac{p}{n} + c\,(1-\beta)\right]. \tag{3.53}$$

More specifically, the quantization of the phonon conductance $n\kappa_\mathrm{c}$ requires temperatures below $aT_D/\max(H,W)$, where T_D is the Debye temperature. Thus, to maximize the range of the quantization while keeping the number of layers as large as possible, the channel height should be similar to the channel width: $H \sim W \sim 100$ nm. For $a \sim 1$ nm and $T_D \sim 100$ K, we then expect that Eq. (3.53) holds at temperatures below 1 K.

For α-$RuCl_3$, the ratio of the thermal Hall conductivity κ_e and the longitudinal thermal conductivity κ_b has been experimentally found [177, 361, 54] to be $\kappa_\mathrm{e}/\kappa_\mathrm{b} \sim 10^{-3}$ at temperatures between 3 K and 6 K. Thus, for large opening angles, $\vartheta_0 \lesssim 1$, we expect $\kappa_\mathrm{e} \ll \kappa_\mathrm{b}\vartheta_0$ to be satisfied in the relevant temperature range. Moreover, since the phonon mean-free path has been estimated [54] to be $D \sim 10$ μm at the same temperatures, the optimal channel dimensions ($H \sim W \sim 100$ nm and $L \sim 1$ μm) correspond to ballistic phonons and a quantized phonon thermal conductance below 1 K. Finally, due to the small number of gapless phonon modes ($p = 4$ according to Ref. [309]) and the large number of chiral edge modes ($n = H/d \sim 100$), the thermal conductance of the device is dominated by the edge modes, and the thermal conductance per layer [see Eq. (3.53)] reduces to

$$\kappa = (1-\beta)\kappa_{\mathrm{e}} = \frac{\pi c k_B^2 T}{6\hbar}(1-\beta). \tag{3.54}$$

The thermal conductance κ in the absence of any pinch points ($\beta = 0$) is then directly proportional to the chiral central charge $c = \frac{1}{2}$, while the universal power law $\beta \propto T^{-7/4}$ can be extracted by measuring the thermal conductance at a range of temperatures in the presence of a single pinch point. We note that Eq. (3.54) is valid even if the channel height H is much larger than $W \sim 100$ nm (but much smaller than $D \sim 10\ \mu$m) because the number of chiral edge modes, $n = H/d$, still exceeds the number of thermally excited phonon modes, $p' \sim nT/T_D$.

We further emphasize that the half-integer chiral central charge $c = \frac{1}{2}$ and the universal power law $\beta \propto T^{-7/4}$ can also be extracted by measuring the thermal conductance in a single-layer ($n = 1$) system. From Eq. (3.53), the thermal conductance of the device is then proportional to $p + c(1-\beta)$. Crucially, even if the small integer p is not known, the measurement of the thermal conductance κ in the absence of any pinch points ($\beta = 0$) reveals the half-integer value of the chiral central charge if the ratio $6\hbar\kappa/(\pi k_B^2 T)$ is found to be half integer rather than integer. Moreover, since p is a constant at low temperature, it can be subtracted to confirm the universal power law $\beta \propto T^{-7/4}$ in the presence of a single pinch point.

3.4 Summary

In this chapter, we have proposed that anyonic edge interferometry can be realized in the non-Abelian Kitaev spin liquid by performing conventional thermal transport measurements in the unconventional device geometry depicted in Fig. 3.1. Individual anyons inside the mesoscopic central region can be detected by interference patterns of edge tunneling processes which, in turn, affect the bulk thermal transport within the two macroscopic lobes due to edge-phonon coupling.

To corroborate our proposal, we have synthesized two complementary calculations, each capturing some universal properties of the system under consideration. On the one hand, we have considered a set of linearized hydrodynamic equations [360, 340] to describe the large-scale thermal transport mediated by bulk acoustic phonons coupled to a chiral edge mode. By obtaining a perturbative solution to these equations and interpreting the results in terms of an effective heat-resistor network, we have understood how to optimize the geometry and the probe placement for maximizing the sensitivity of the thermal conductance or a locally measured temperature to coherent edge tunneling processes. On the other hand, we have utilized the CFT approach [2, 191] to investigate the edge tunneling processes themselves and understand how they can be used to detect individual anyons or extract universal properties of the underlying spin liquid. This treatment highlights unique signatures arising from bare tunneling at a single point contact and from braiding by tunneling in the presence of multiple point contacts.

While the main focus of this work has been the detection of individual anyons through edge interferometry, we emphasize that the device geometry in Fig. 3.1 can also be used to demonstrate the existence of anyons via simpler measurements that do not rely on anyon braiding. If the central region has sufficiently small phonon thermal conductance, the heat exchange between the two lobes is mediated almost exclusively by the chiral edge mode. In the absence of any point contacts, the thermal conductance κ of the device is then directly proportional to the chiral central charge of the edge theory. Hence, the chiral central charge, $c = \frac{1}{2}$, whose half-integer value immediately reveals the presence of non-Abelian anyons, can be extracted from the dominant *longitudinal* thermal conductance rather than a subdominant thermal Hall conductivity [177, 361, 54]. Moreover, in the presence of a single point contact, the leading-order correction to the thermal conductance follows a nontrivial power law, $\Delta\kappa/T \propto T^{-7/4}$, as a function of the temperature T. The universal exponent 7/4 is innately tied to the conformal dimension of the non-Abelian Ising anyons and would be difficult to reproduce from less exotic physics. Crucially, these non-interferometry measurements are within reach of the currently available thermal transport experiments [177, 361, 54] in existing candidate materials like α-$RuCl_3$. In this spirit, recent experimental efforts on a device with four macorscopic lobes [364], in tandem with numerical modeling of the geometry dependence, represent a first step along the path highlighted here.

Finally, we point out that our proposed measurements straightforwardly generalize to all kinds of chiral topological orders, including Abelian and non-Abelian chiral spin liquids, as well as their electronic counterparts such as fractional quantum Hall states. Even though thermal transport is experimentally more challenging than electrical transport, it provides complementary information on such electronic topological orders, for example, by giving direct access to the chiral central charge [25].

Chapter 4

Spin-liquid based topological qubits

Topological phases of matter hosting non-Abelian anyons (or closely related non-Abelian defects) can emerge in experimental platforms including topological superconductors [290, 183], fractional quantum Hall systems [239], and quantum spin liquids [185, 160, 19, 307, 365, 194, 52]. Interest in these settings is fueled in large part by their potential utility for intrinsically fault-tolerant topological quantum information processing [184, 261]. Three deeply related non-Abelian-anyon characteristics [295] underlie this technological promise: First, a collection of non-Abelian anyons nucleated in a host platform encodes a degeneracy consisting of locally indistinguishable states. Qubits encoded in that manifold correspondingly enjoy built-in resilience against dephasing errors from local environmental noise. Second, adiabatically braiding non-Abelian anyons nontrivially rotates the system's wavefunction within the degenerate subspace—enacting a set of 'rigid' quantum gates on the protected qubits. Third, non-Abelian anyons can 'fuse' into multiple quasiparticle types, with a history-dependent outcome. Measuring their fusion products thus provides a mechanism of quantum-state readout.

Building a functional prototype topological qubit requires definitive formation of a non-Abelian topological phase, on-demand creation and controlled manipulation of non-Abelian anyons, and detection of individual anyons and their possible fusion products. Topological qubit blueprints integrating these requirements were first proposed for quantum Hall systems [88, 47, 115] and later adapted to topological superconductors [118, 306, 10, 227, 270, 11, 35] (leading eventually to scalable designs [176]). Despite the rather different nature of the two platforms, both constitute electrically active systems amenable to gating and charge transport—key experimental tools for manipulation and detection. In the quantum Hall setting, for example, electrostatic gating can nucleate fractionally charged non-Abelian anyons that can be electrically detected via anyon interferometry [60, 88, 323, 41, 43, 182, 292, 143, 293]. Similarly, gating can manipulate non-Abelian domain-wall defects in topological superconductors [12], while electrical transport in conjunction with Coulomb charging effects enables interferometric readout [117, 278, 339, 279, 176].

How does one build and interrogate a topological qubit based on a non-Abelian quantum spin liquid? This question is nontrivial because spin liquids appear in electrically inactive spin systems. Consequently, one can not naively import the topological qubit designs and control techniques noted above to this setting. The question is also relevant given intense experimental investigations of a family of magnetic insulators dubbed Kitaev materials [160, 350, 332, 151, 166, 327, 243]—believed to exhibit Hamiltonians 'close' to the exactly solvable Kitaev honeycomb model [185]. The Kitaev model in particular harbors a magnetic-field-induced non-Abelian spin liquid phase, for which experimental evidence has been reported in α-$RuCl_3$ [23, 178, 20, 361, 53, 154] (see, however, Refs. [17, 357, 16, 78, 84, 209, 85]).

Numerous recent papers have devised schemes for creating and detecting non-Abelian anyons in spin liquids [2, 276, 198, 335, 192, 163, 344, 190, 222, 33, 345, 328, 145, 174, 173, 141] (see also the references in Sec. 4.1). We build on these results to propose spin-liquid-based topological qubit blueprints as well as protocols designed to validate the essential underpinnings of topological quantum computation in this setting. We develop two types of architectures that incorporate potentially scalable ingredients: (i) spin liquids integrated into magnetic tunnel junction arrays that allow local, real-time manipulation of the host platform, and (ii) semiconductor-spin liquid hybrids for which electrons bind non-Abelian anyons, enabling charged-based control of the latter. In both cases readout proceeds via anyon interferometry.

Following a philosophy similar to Ref. [3], we primarily focus on relatively simple geometries that allow for a series of proof-of-concept topological qubit experiments. We specifically present device designs and protocols for qubit initialization, verification of non-Abelian anyon fusion rules, demonstration of non-Abelian braiding, and extraction of topological qubit lifetimes. The required ingredients in turn allow one to realize both protected and unprotected quantum gates required for a universal gate set, which we also discuss in some detail drawing inspiration from earlier work in other settings [51, 184, 48, 88, 47, 125, 115, 126, 261, 7, 39, 44, 81, 12, 11, 124, 176]. Our designs moreover extend to scalable multi-qubit architectures. While many advances would be required to bring our proposals to life, we hope that the strategies developed here provide useful long-term guidance for quantum spin liquid experiments.

The remainder of this chapter is organized as follows. Section 4.1 sets the stage by surveying previously introduced anyon creation and detection strategies. In Sec. 4.2, we highlight two potential platforms — magnetic tunnel junction arrays or electrical setups — for realizing topologically protected qubits in a spin liquid. Next, Sec. 4.3 outlines anyon manipulation methods that use either proposed platform. Section 4.4 synthesizes these results to propose minimalist spin-liquid-based topological qubit designs and identify protocols for validating non-Abelian fusion rules, non-Abelian braiding, and qubit lifetime extraction. Section 4.5 adapts protocols for gates needed to achieve universal quantum computation in this setting. Finally, we conclude in Sec. 4.6 by highlighting various future challenges and opportunities.

4.1 Review of anyon generation and detection schemes

The remainder of this section reviews prior work on anyon generation and detection, some of which we will later leverage to propose potentially scalable anyon manipulation strategies and spin-liquid-based topological qubit designs.

In this section we review prior works on anyon generation and detection, some of which we will later leverage to propose potentially scalable anyon manipulation strategies and spin-liquid-based topological qubit designs. Broadly, the various schemes which have been proposed may be categorized as relying either on local probes or interferometric readout. We discuss both such scenarios here.

Detection via local probes

Detecting individual anyons in non-Abelian Kitaev spin liquids poses a daunting task because of the limited way in which the fractionalized degrees of freedom couple to local probes. For instance, electrons from a lead can not directly hybridize with emergent Majorana fermions born in the spin liquid (contrary to the situation for topological superconductors where Majorana fermions arise from physical electron and hole superpositions). A given anyonic excitation nevertheless corresponds to a localized packet of energy, which in turn generically couples to other local observables, e.g., through local magnetic correlations [163]. Given the absence of time-reversal symmetry, the anyons most naturally couple to the local magnetization density [238, 145]. Due to spin-orbit interaction combined with the finite charge gap of the quantum spin liquid, however, each anyon also locally induces electric polarization [276, 116] and orbital currents [26] (see also Refs. [57, 180] for the underlying mechanism), which may be experimentally observable by surface-probe techniques like scanning tunneling microscopy or atomic force microscopy. The key issue with this approach is that different anyons, or even trivial bosons, can exhibit similar signatures; any concrete route to detecting a specific anyon must therefore rely heavily on precise microscopic details and careful experimental calibration.

Alternative proposals aim to detect the Majorana zero modes attached to individual Ising anyons. In these proposals, an atomically thin spin-liquid layer is assumed to form a tunneling barrier between two electronic systems [66, 198], typically a scanning tunneling tip and a metallic substrate [335]. The inelastic part of the tunneling response is then sensitive to the local spin dynamics [106], and Majorana zero modes bound to Ising anyons are reflected in a sequence of distinctive features at the lowest voltages [334, 33, 328, 174, 173]. The feasibility of these inelastic tunneling setups is demonstrated by the recent observation of magnetic excitations in few-layer α-$RuCl_3$ using inelastic electron tunneling spectroscopy [358, 236]. Due to the inherently fractionalized nature of spin-liquid-based Majorana zero modes alluded to above, however, the low-energy spin dynamics never involves a single zero mode, but either a pair of hybridizing zero modes or a zero mode as well as a finite-energy mode [174, 173].

Therefore, any signature of an *individual* Ising anyon in this kind of detection scheme is necessarily indirect.

Interferometric readout

Whereas local probes may reveal some signatures of individual anyons in the bulk, anyon interferometry enables measurement of the total topological charge within an extended region that may contain many anyons. This type of more global detection is essential not only for reading out the logical qubit state encoded in bulk anyons, but also for implementing measurement-based quantum computation protocols. Universality of the anyon braiding statistics means that interferometric readout eschews many of the difficulties associated with local probes; charge neutrality of the anyons, however, remains a challenge, rendering conventional charge-based interferometry techniques from the quantum Hall setting [60, 88, 323, 41, 43, 182, 292, 143, 293] ineffective. Nonetheless, a number of schemes have been proposed to circumvent this issue by coupling the interfering anyons to more easily addressable degrees of freedom from which the statistical phase may be measured. These strategies range from time-domain measurements coupling local spin probes to the chiral Majorana edge mode [192] to electrical conductance measurements in heterostructures that mediate a coupling between anyons and electronic degrees of freedom [2, 141].

Here we focus on the approach detailed in the previous chapter—thermal anyon interferometry [190, 344, 345]—wherein the heat current carried by the edge mode is sensitive to the bulk topological charge. Consider a geometry as shown in Fig. 3.1(a) consisting of an interferometry region defined by two point contacts and flanked by two lobes. The point contacts may either be permanently fixed by etching the edge channels or dynamically induced by, e.g., tunable magnetic tunnel junctions which bend the outer edge of the spin liquid inward to form a pinch (see Sec. 4.2). Applying a temperature difference $T_{1/2} = T \pm \delta T$ across the device induces a heat current J, resulting in thermal conductance $\kappa = J/(2\delta T)$. Between the point contacts, bulk anyons encode some logical state to be read out via the total topological charge, specified by the number of Ising anyons (n_σ) and emergent fermions (n_ψ). Tunneling of Ising anyons at the point contacts, with strength $t_{\sigma,1/2}$, mediates an exchange of energy between the edges and permits the chiral edge mode to acquire a statistical phase when its path encloses the interferometry region. This braiding phase is directly reflected in thermal transport measurements as a distinct temperature-dependent correction that is sensitive to the bulk topological charge,

$$\frac{\Delta\kappa}{\kappa} \sim \frac{1}{T^{7/4}}\{t_{\sigma,1}^2 + t_{\sigma,2}^2 + (-1)^{n_\psi}[1 + (-1)^{n_\sigma}]t_{\sigma,1}t_{\sigma,2}\}, \tag{4.1}$$

in addition to less relevant corrections arising from fermion tunneling [190]. The piece $\propto t_{\sigma,1}t_{\sigma,2}$ represents a crucial interference term that can be understood from the braiding relations summarized in Fig. 2.3(c). For odd n_σ, the interference contribution vanishes, reflecting non-Abelian statistics of Ising anyons; that is, the paths whereby an edge Ising anyon does or does not encircle an odd number of bulk Ising anyons correspond to orthogonal states that cannot interfere. For even n_σ, this orthogonality property is removed—hence the revival of interference, which then depends on the number of enclosed fermions due to the statistical phase -1 arising when an edge Ising anyon encircles a bulk fermion.

For a Kitaev material with non-negligible coupling between the edge mode and bulk phonons (e.g., α-$RuCl_3$), edge-bulk thermalization in the macroscopic lobes allows for the edge-mediated conductance to be probed via much simpler measurements of the phonon temperature. Furthermore, the phonon contribution to the inter-lobe heat current can be suppressed by appropriate device geometry, making the interferometry signal $\Delta\kappa$ far more pronounced. In this manner, thermal transport measurements may reveal the topological charge between the pinch points, thereby enabling an interferometric readout of either individual anyons or a collection of anyons with a relatively simple device design. If the spin liquid sits upon a substrate and/or the pinch points are formed by, e.g., tunnel junctions, there are additional contributions to the thermal conductance that must be accounted for. Nonetheless, the interferometry signal retains a unique temperature dependence.

Lastly, we note that more scalable architectures would benefit from direct measurement of the local spin temperature at the edge rather than phonon temperature in macroscopic devices. Several schemes have been proposed for how to implement this, typically requiring more complicated heterostructures. One such scheme involves a quantum wire coupled to the chiral edge mode with a nearby trivial hole in the bulk making the coupling term more relevant [345].

4.2 Platforms

Probabilistic anyon generation via magnetic tunnel junctions

Ising anyons constitute gapped quasiparticles in the bulk of a 'pure' non-Abelian spin liquid. Starting from this clean setting, one can pursue creation of Ising anyons using two complementary strategies. The first applies judicious local perturbations that eliminate the energy gap for Ising anyons, such that they appear at prescribed locations in the system's minimum-energy configuration. Atomic-scale defects, e.g., vacancies or spin impurities, have been shown to stabilize Ising anyons via this mechanism, at least within particular microscopic models [347, 348, 92, 86, 341, 175, 163]. The second strategy seeks to trap Ising anyons as finite-energy, long-lived excitations above the ground state. Here, the chiral Majorana edge state residing at the boundary between the spin liquid and a trivial phase provides an appealing trapping center. The underlying CFT dictates that Ising anyons universally comprise the lowest-energy excitation for the edge state, with an energy $E_\sigma \sim \frac{1}{16}\frac{2\pi v}{L}$ that decreases as the edge circumference L increases (v denotes the edge velocity). Note that away from a boundary the hierarchy of excitations can easily flip such that Ising anyons cost much larger energy than emergent fermions. These observations suggest the potential for dynamically generating Ising anyons by non-adiabatically altering spin-liquid edge states [222]. One advantage of this approach is that it relies solely on universal edge physics rather than microscopic details of the host Kitaev material.

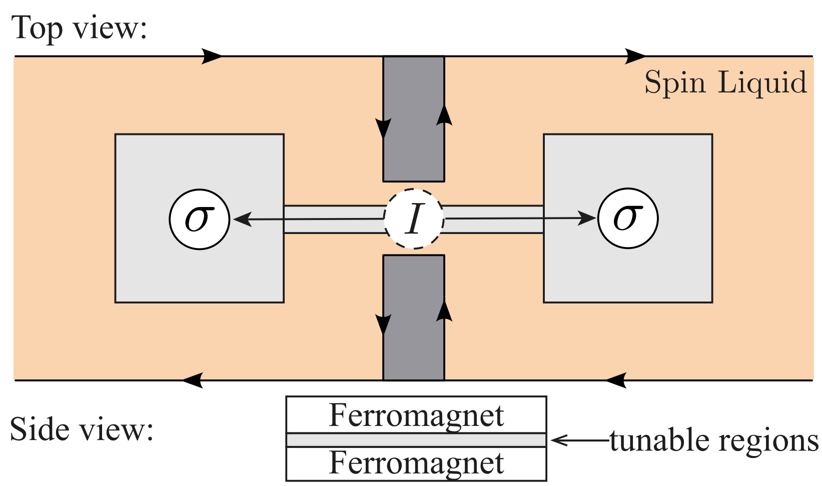

Figure 4.1: **Magnetic tunnel junction scheme for generation and readout of Ising anyons.** This setup consists of a non-Abelian Kitaev spin liquid (orange) punctuated by two "holes" of a topologically trivial phase (light gray). The holes are connected by a narrow "bridge" where the spin liquid is sandwiched between two ferromagnets, thus forming a tunnel junction. Dynamically switching the orientation of either ferromagnet yields control over the local Zeeman field, allowing one to tune the bridge between the topologically trivial phase and the spin-liquid phase. Diabatically tuning the bridge from the trivial phase to the spin-liquid phase, two Ising anyons σ are probabilistically nucleated on the two holes. Further tunable regions above and below the bridge (dark gray) enable interferometric detection of either Ising anyon by bending the chiral edge mode to form a pinch point.

Figure 4.1 sketches a spin-liquid-based setup for dynamical Ising-anyon generation. The non-Abelian spin liquid features two 'holes'—both realizing a topologically trivial phase—connected by a 'bridge'. Initially the bridge also resides in a trivial phase, thereby linking the two holes in a way that forms a common dumbbell-like edge state. We assume that the temperature is sufficiently low to prevent excitations along this dumbbell edge. Next, suppose that the bridge can be tuned from a trivial phase to the spin-liquid phase over a time scale τ, after which the two holes become decoupled and thus exhibit independent edge states. Purely adiabatic evolution would simply initialize the independent edge states into their ground state—hence no anyon generation. Conversely, too-rapid evolution would generate unwanted excitations in the bridge region. Reference [222] found that intermediate τ satisfying

$$\frac{L_b^2}{v^2}\Delta_{\text{bulk}} \lesssim \tau \lesssim \frac{L_b L_h}{v^2}\Delta_{\text{bulk}} \tag{4.2}$$

generates an Ising anyon in each hole with $\mathcal{O}(1)$ probability, without producing other spurious excitations. In Eq. (4.2), Δ_{bulk} is the bulk spin-liquid gap, while L_b and L_h are the length of the bridge and the perimeter of each hole, respectively. One can view the process as pulling a pair of Ising anyons out of the vacuum ($I \to \sigma\sigma$) and storing one in each hole. Since the generation is inherently probabilistic, measurement of σ through, e.g., thermal anyon interferometry is needed at the end of the protocol to collapse the wavefunction onto the desired sector. If readout does not detect an Ising anyon, the cycle repeats until successful. Once created, the Ising anyons are protected by the bulk gap and will not annihilate unless the bridge reverts to the trivial phase.

Equation (4.2) predicts a broad suitable τ window when $L_b \ll L_h$. The probability of successful creation, p_{suc}, also decreases with L_b/L_h (fixing all other parameters, shrinking L_h raises the energy cost for σ particles in the edge states and thus suppresses p_{suc}). Simulations nonetheless show that p_{suc} can remain $\mathcal{O}(1)$ even for $L_b \sim L_h$ [222]. The condition $L_b \ll L_h$ is therefore not strictly necessary. The width of the bridge, however, should not greatly exceed the bulk spin-liquid correlation length $\xi_{\text{bulk}} \sim v_{\text{bulk}}/\Delta_{\text{bulk}}$ (where v_{bulk} is the bulk emergent fermion velocity) in order to avoid a 2D phase transition during the dynamical bridge evolution. For a sense of scales, taking $v_{\text{bulk}} \sim 3 \times 10^3\,\text{m}\,\text{s}^{-1}$ and $\Delta_{\text{bulk}} \sim 5\,\text{K}$ yields $\xi_{\text{bulk}} \sim 5\,\text{nm}$; moreover, $L_{h,b} \sim 100\,\text{nm}$ yields typical bridge timescales of $\tau \sim 1 - 10\,\text{ns}$.

Experimentally, among the various Kitaev materials, α-$RuCl_3$ is of particular interest because of its reported (though actively debated) non-Abelian signatures when subjected to a magnetic field of $\gtrsim 7\,\text{T}$ [23, 178, 20, 361, 53, 154]. With that platform as inspiration, we postulate that the evolution from the topologically trivial to the spin-liquid phase can be realized by changing the Zeeman field from 'small' to 'large' values. Local Zeeman-field modifications can potentially be achieved on the required timescales by sandwiching the region of interest between two ferromagnets to form a magnetic tunnel junction. When the two ferromagnetic moments align, the Kitaev material experiences a net exchange field that we assume locally generates a spin-liquid phase. Conversely, in the anti-aligned configuration, we assume that cancellation of the exchange fields locally produces a trivial phase (e.g., magnetic order). Dynamical switching between the two configurations can be realized using the spin-transfer torque technique [286] on nanosecond timescales [91, 83, 133], thus meeting the requirements estimated above.

Electrical generation and readout

As an alternative route to on-demand anyon generation in a non-Abelian spin liquid, one may envision binding the anyons to electrons in a proximate metallic system, and then controlling the charged composite particles by electrical means. In particular, each electron in the proximate system can be viewed as a Kondo impurity from the perspective of the spin liquid, which—in the context of Kitaev spin liquids—is one of the localized defects proposed to stabilize non-Abelian Ising anyons [92, 86, 341]. Hence, a promising platform for the electrical generation of Ising anyons is the bilayer heterostructure containing a single layer of a non-Abelian Kitaev spin liquid and a monolayer metal with a sufficiently strong Kondo coupling between them [141].

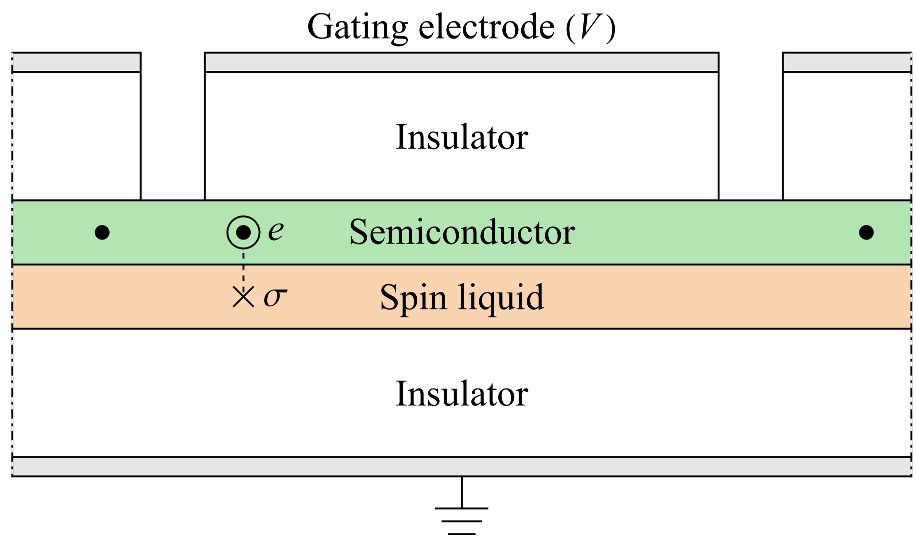

Figure 4.2: **Electrical generation of Ising anyons.** Numbers of electrons e and, thus, Ising anyons σ in distinct gate-defined regions are controlled by tunable gate voltages V.

There are two important caveats. First, the large density of anyonic composites in a metallic bilayer makes generating individual anyons difficult and introduces spurious braiding between distinct anyons. Hence, one should substitute the monolayer metal with a monolayer semiconductor. Second, the stabilization of Ising anyons through a Kondo coupling has been discussed in the context of static impurity spins rather than itinerant electrons. In contrast, if the electron hopping amplitude t exceeds the magnetic exchange J, which is the case in most real materials, the bound states of anyons and electrons are not expected to survive. To mitigate this problem, one may introduce electron dopants in the monolayer semiconductor that slow down the electron dynamics by acting like potential wells for the electrons [141]. Indeed, for a dopant potential depth $W > t$ and a distance n between neighboring dopants (in units of the lattice spacing), the effective hopping amplitude is reduced to $\tilde{t} \sim t^n/W^{n-1}$, which can be much smaller than J, thus realizing a quasistatic scenario in which the anyons remain bound to the electrons as they slowly move together [142]. We remark that arrays of electron dopants can be created with atomistic precision in monolayer semiconductors such as transition metal dichalcogenides using the focused electron beam of a scanning transmission electron microscope [97].

The above considerations lead to the electrical anyon generation scheme in Ref. [141] where the number of Ising anyons in each gate-defined region of the heterostructure can be controlled by tuning the appropriate gate voltage (see Fig. 4.2). If a given gate-defined region of the semiconducting layer—which can also be viewed as a quantum dot—is tuned into a Coulomb-blockade valley, its electron number cannot fluctuate and is fixed to a well-defined integer as long as the temperature and the effective electron hopping amplitude $\tilde{t}$ are much

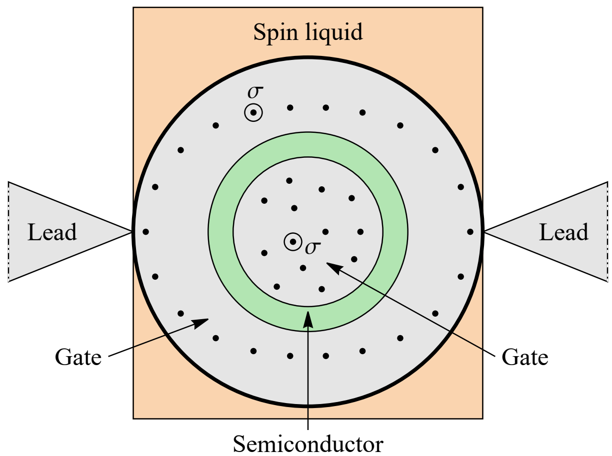

Figure 4.3: **Electrical readout of Ising anyons.** Top view of the heterostructure in Fig. 4.2 with two gate-defined regions; the edge of the semiconductor is marked by a thick line. Ising anyons σ generated in the central disk-shaped region can be interferometrically detected by measuring the electrical conductance of the surrounding ring-shaped region between two metallic leads. Note that electrons traveling between the two leads also have Ising anyons σ bound to them.

smaller than the charging energy. In turn, since each electron in the semiconducting layer binds an Ising anyon in the neighboring spin-liquid layer, this control over the local electron numbers enables the on-demand generation of an Ising anyon in each gate-defined region by simply tuning the appropriate electron number from zero to one.

One important advantage of the gate-controlled anyon generation approach in Ref. [141] is being naturally interfaced with an interferometric readout scheme for detecting the Ising anyons that are stabilized in various gate-defined regions. For example, in the minimal setup shown in Fig. 4.3, an Ising anyon generated at the central disk-shaped region readily shows up in the electrical conductance of the surrounding ring-shaped region between the two metallic leads. In contrast to the disk-shaped "generation" region, the ring-shaped "readout" region is tuned to a Coulomb-blockade peak so that its electron number can easily fluctuate between zero and one. This way, the ring-shaped region has a sizable electrical conductance carried by electrons traveling from one lead to the other one. Since each electron binds an Ising anyon inside the ring-shaped region and can travel either below or above the disk-shaped region, the electrical conductance contains an interference term between the two paths that is sensitive to Ising anyons stabilized at the disk-shaped region via braiding rules of the non-Abelian Kitaev spin liquid, i.e., an emergent Aharonov-Bohm effect.

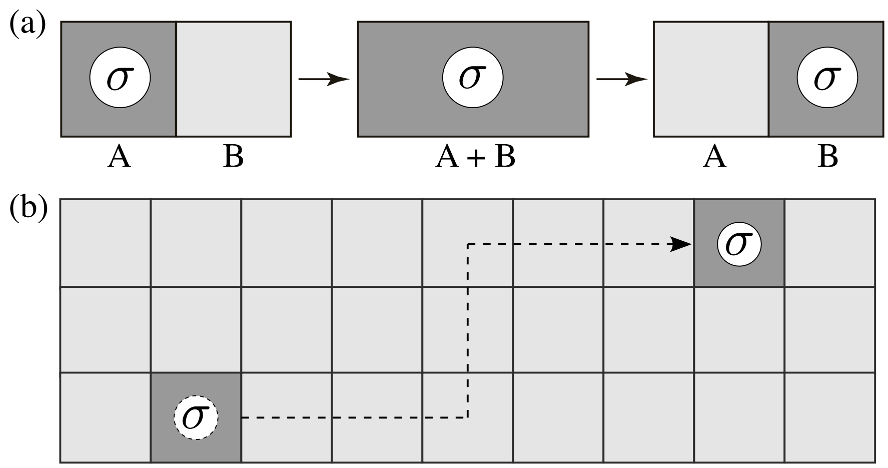

Figure 4.4: **Manipulation of Ising anyons in the magnetic tunnel junction scheme.** (a) Elementary 'inchworm move' for transporting an Ising anyon σ between two distinct magnetic tunnel junctions (gray squares). In each tunnel junction, the magnetic insulator is tuned to the trivial (dark gray) or the spin-liquid (light gray) phase. The individual images depict snapshots with adiabatic evolution in between. (b) In a scalable array of magnetic tunnel junctions, an Ising anyon can be transported arbitrarily far by combining elementary inchworm moves.

4.3 Manipulation of non-Abelian anyons

Having detailed two platforms in which Ising anyons may be controllably nucleated, we now examine how to move and manipulate these anyons within the spin-liquid.

Magnetic tunnel junction approach

Magnetic tunnel junctions provide a potentially scalable mechanism not only for dynamically generating Ising anyons as outlined in Sec. 4.2, but also for manipulating the anyons once formed. Manipulation requires an Ising anyon to reside within an array of independently tunable magnetic tunnel junctions that can toggle the adjacent magnetic insulator regions between trivial and spin liquid phases. Importantly, although the anyon generation protocol requires tuning between these phases on intermediate time scales—recall Sec. 4.2—subsequent manipulation steps proceed adiabatically to avoid generating unwanted additional excitations.

As a minimalist example, consider first two adjacent tunable regions A and B, initially with A in the trivial phase and B in the spin-liquid phase. Suppose further that an Ising anyon is trapped in the chiral Majorana edge state surrounding A. We can transport the anyon to region B using the 'inchworm move' sketched in Fig. 4.4(a): First, region B is adiabatically tuned from the spin-liquid to the trivial phase. At the end of this step the spin

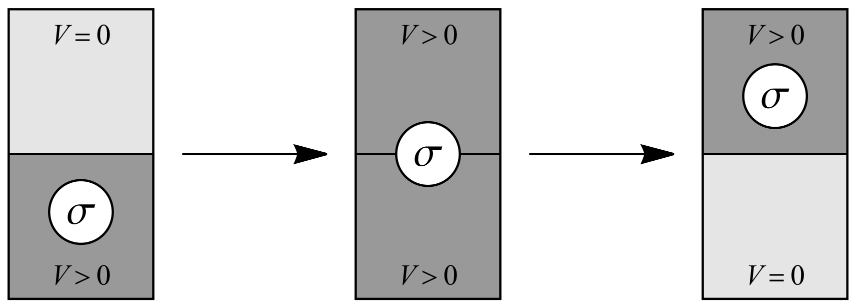

Figure 4.5: **Electrical manipulation of Ising anyons.** Elementary 'inchworm move' for transporting an Ising anyon σ between two distinct gated islands (gray squares). Each gated island is a gate-defined region of the heterostructure setup in Figs. 4.2 and 4.3 with a gate voltage V that is tunable to $V > 0$ (dark gray color) or $V = 0$ (light gray color). The individual images depict snapshots with adiabatic evolution in between.

liquid edge state encircles $A+B$, and hence the Ising anyon is delocalized across the perimeter of both regions. Second, adiabatically tuning A from trivial to spin liquid completes the migration of the Ising anyon to region B. Since the edge-state excitation energy scales like $\sim v/L$ where L is the characteristic size of each region, adiabaticity requires that each step occurs over a time scale that exceeds $\mathcal{O}\left(\frac{L^2}{v^2}\Delta_{\text{bulk}}\right)$, similar to the left-hand side of Eq. (4.2). This elementary move adapts straightforwardly to allow controlled manipulation of Ising anyons in more elaborate magnetic tunnel junction arrays; see, e.g., the manipulation sketched in Fig. 4.4(b).

Electrical approach

Just like its magnetic counterpart above, the electrical anyon generation scheme in Sec. 4.2 can be straightforwardly generalized to also allow for the manipulation of the anyons generated. Once again, we envision an array of independently tunable regions [cf. Fig. 4.4(b)] and an elementary 'inchworm move' to transport an Ising anyon between two neighboring regions A and B. In this case, however, the regions are defined by gating electrodes and controlled by tunable gate voltages V (see Fig. 4.2). Being attached to an electron, the Ising anyon can be localized at any given region A that has a positive voltage $V > 0$ with respect to the surrounding regions. Hence, in order to move the Ising anyon from region A to region B, we first adiabatically increase the voltage at region B from 0 to V (where 0 is a default reference value), then decrease the voltage at region A from V to 0. This inchworm move shown in Fig. 4.5 is entirely analogous to its counterpart in the magnetic approach [see Fig. 4.4(a)].

Importantly, it does not matter what the precise values of the voltages are during any step of the process. Indeed, while the equilibrium electron number is $N = CV/e$ for each

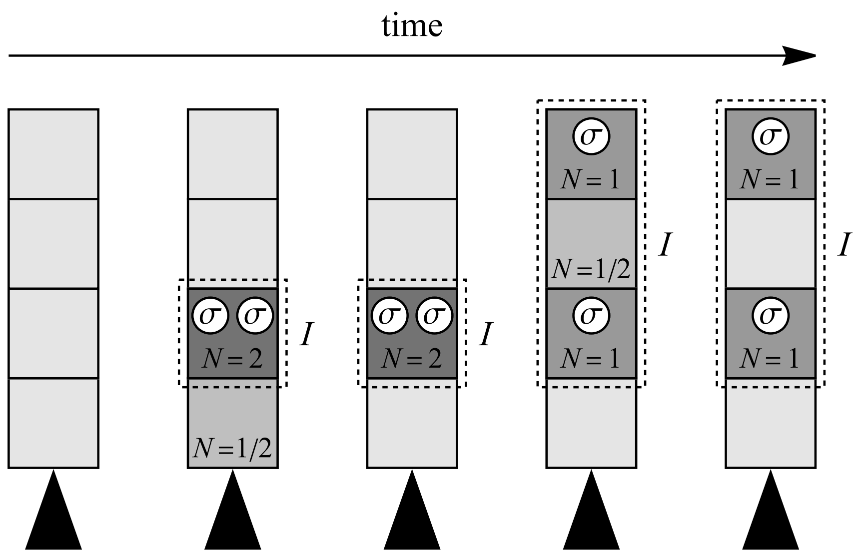

Figure 4.6: **Deterministic creation of an Ising-anyon pair in the electrical approach.** The individual images depict snapshots with adiabatic evolution in between. For each snapshot, the gray squares denote gated islands, while the black triangle marks a metallic lead; equilibrium electron numbers N are specified for gated islands with $N > 0$, and larger values of N are highlighted by darker shades of gray. The details of the process are explained in the text.

gated island (i.e., gate-defined region) of voltage V and capacitance C, the electron number cannot reach equilibrium as the surrounding islands of zero voltage—which have equilibrium electron numbers $N = 0$—act like an energy barrier for the electrons. More precisely, if the effective electron hopping amplitude $\tilde{t}$ is much smaller than both the voltage energy eV and the charging energy e^2/C, the tunneling of electrons in and out of the gated island is exponentially suppressed, and the lowest-energy state with exactly one electron—hence, one Ising anyon—can survive as a metastable state up to arbitrarily long time scales, regardless of the precise voltage V.

For the same reason, however, one must initially generate each pair of Ising anyons carefully to ensure that the system can actually reach its equilibrium state in which (i) two electrons are at distinct gated islands, (ii) each electron binds exactly one Ising anyon, and (iii) the two Ising anyons are in the trivial fusion channel I. Figure 4.6 illustrates a potential procedure for electrically pulling a pair of Ising anyons out of the vacuum, similar in spirit to the probabilistic dynamical anyon generation scheme reviewed in Sec. 4.2 (though here the process is deterministic!). In the first step, two Ising anyons are generated on the same gated island—the 'target island'—that is connected to a metallic lead by another gated island—the 'bridge island'. The target island is adjusted to equilibrium electron number $N = 2$, with each of the two electrons stabilizing one Ising anyon. At the same time, the bridge island is set to $N = 1/2$, so that it can facilitate the tunneling of electrons from the lead to the target island; afterwards, the bridge island is adiabatically tuned to $N = 0$, so that it can provide an obstacle to further electron tunneling. In the second step, the two Ising anyons are separated to two different target islands that are connected by another bridge island. The target islands are both adjusted to $N = 1$, each supporting one electron (i.e., one Ising anyon) in equilibrium, while the bridge island in between facilitates the equilibration; it is tuned to $N = 1/2$ and then to $N = 0$, precisely as in the first step above. We note that the metallic lead must be far away from the spin-liquid edge to ensure that the two Ising anyons σ are indeed pulled out of the vacuum and thus initialized in the trivial fusion channel I.

4.4 Spin-liquid qubit design and protocols

Minimal qubit architectures

In this section, we propose a series of spin-liquid qubit architectures—focusing on minimalist designs—that synthesize the creation, manipulation, and readout techniques discussed in previous sections. The simplest architectures for encoding a single topological qubit using the two respective approaches above are shown in Figs. 4.7(a) and 4.8(a), with the corresponding definitions of the degenerate qubit levels $|0\rangle$ and $|1\rangle$ specified in Figs. 4.7(b) and 4.8(b). In general, the encoding of a single topological qubit requires not two but four non-Abelian Ising anyons σ as accommodated in both designs. Indeed, if only two Ising anyons are nucleated from the vacuum, they necessarily fuse to the identity channel I, thus leaving no degeneracy to be exploited. In contrast, four Ising anyons support two degenerate ground states that can be distinguished by the fusion channel I or ψ of two arbitrarily chosen Ising anyons. This fusion channel of the first two anyons is identical to the fusion channel of the remaining two anyons [see Figs. 4.7(b) and 4.8(b)], so that the four anyons altogether still fuse to I.

For the magnetic tunnel junction approach, the minimal qubit design in Fig. 4.7(a) features a single tunable bridge connecting a set of three tunable holes on the left with another set of three on the right; constrictions on the top and bottom (also configurable via magnetic tunnel junctions) enable interferometric readout. Qubit initialization proceeds as sketched in Fig. 4.7(c): (i) first, one generates a single Ising anyon pair (shown in blue) following the probabilistic, repeat-until-success scheme summarized earlier, (ii) inchworm moves then shuttle the anyons to the outer holes, and (iii) a second anyon pair (shown in yellow) is then created opposite the bridge. Finally, interferometric readout—which is needed to confirm successful anyon creation in step (iii)—initializes the qubit into a well-defined state $|0\rangle$ or $|1\rangle$. More precisely, given the encoding specified in Fig. 4.7(b), detecting the topological charge on, say, the right three holes will return a measurement of either I or ψ when the creation protocol is successful—in turn collapsing the wavefunction onto either $|0\rangle$ or $|1\rangle$ depending on the outcome.

For the electrical approach, the minimal qubit architecture in Fig. 4.8(a) contains a set of gated islands, each with its own capacitance and tunable voltage, as well as three metallic

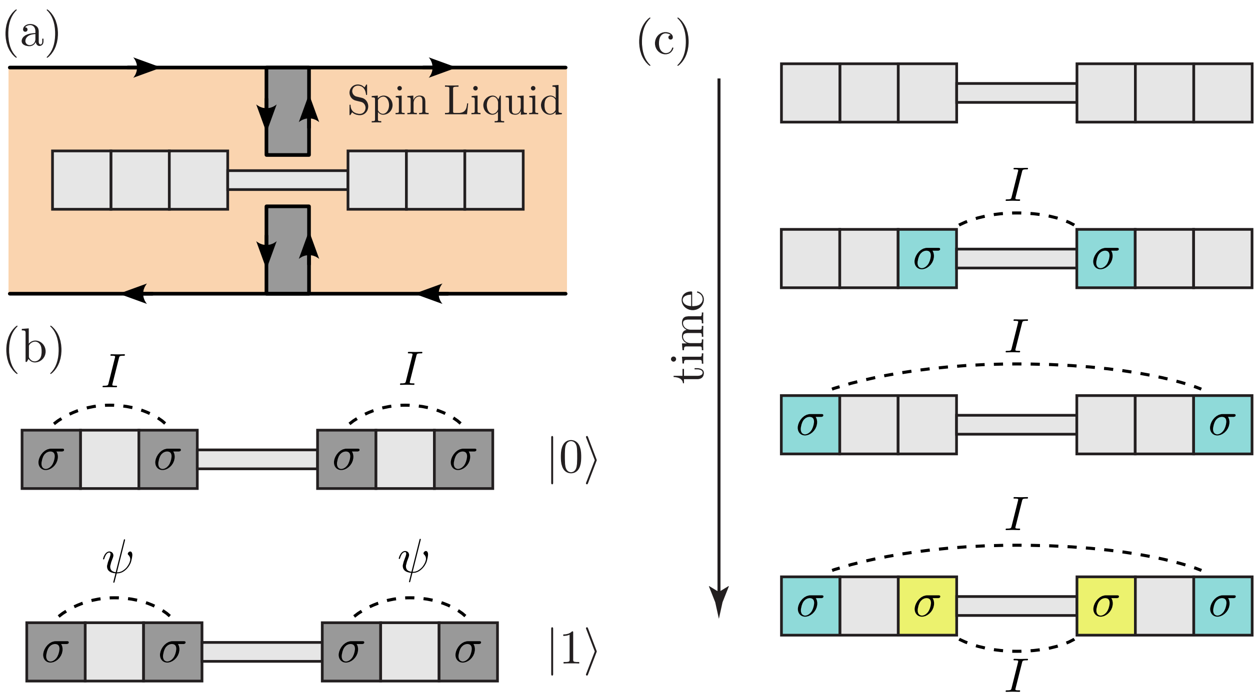

Figure 4.7: **Minimal qubit design and fusion experiment in the magnetic tunnel junction setup.** (a) Minimal set of tunable regions defining a single topological qubit. (b) Encoding the qubit into four Ising anyons σ localized at regions tuned to the trivial phase (dark gray color). The two degenerate states $|0\rangle$ and $|1\rangle$ differ in fusion channels, I or ψ, between pairs of Ising anyons σ connected by dashed lines. (c) Qubit initialization protocol for setting up the qubit in the superposition state $(|0\rangle + |1\rangle)/\sqrt{2}$. Repeatedly implementing this initialization protocol, one can statistically demonstrate the nontrivial fusion rule $\sigma \times \sigma = I + \psi$, as described in the text.

leads. As shown in Fig. 4.8(b), two pairs of Ising anyons can be localized at the top and bottom rows of square-shaped islands, with the two qubit states $|0\rangle$ and $|1\rangle$ distinguished by the identical fusion channels, I or ψ, of the individual pairs. The interferometric readout of this fusion channel is depicted in Fig. 4.8(c); by tuning the four islands that form a ring around the bottom row to the same voltage, $\bar{V} = e/[2(C_\uparrow + C_\downarrow + C_\rightarrow + C_\leftarrow)]$, corresponding to equilibrium electron number $N = 1/2$ (i.e., a Coulomb-blockade peak), there is a measurable electrical conductance between the left and right leads, which depends on the fusion channel of the two Ising anyons inside (see Sec. 4.2). We note that, in contrast to the bottom lead, which is used for creating pairs of Ising anyons (see Fig. 4.6), the left and right leads that enable the interferometric readout must be directly above the edge of the spin liquid. Also, the four localized Ising anyons must be well separated from the ring islands to avoid qubit decoherence from spurious interactions with the Ising anyon traveling between the leads.

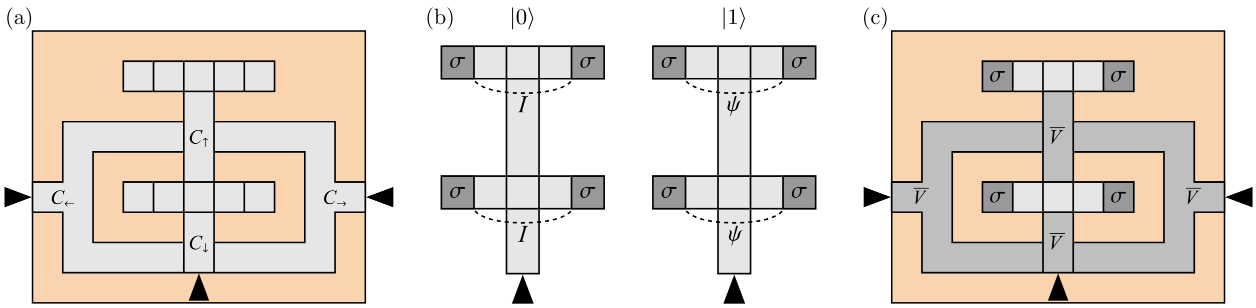

Figure 4.8: **Minimal qubit design in the electrical approach.** (a) Minimal set of gated islands (gray regions) and metallic leads (black triangles) required for a single topological qubit. Each gated island is a gate-defined region of the heterostructure setup in Figs. 4.2 and 4.3 with its own gate voltage V and capacitance C. Some gated islands have their capacitances specified. (b) Encoding of a single topological qubit into four Ising anyons σ localized at gated islands with positive gate voltages (dark gray regions). The two degenerate states $|0\rangle$ and $|1\rangle$ differ in fusion channels, I or ψ, between pairs of Ising anyons σ connected by dashed lines. (c) Interferometric readout. Tuning the four islands around the bottom two Ising anyons to the same voltage, $\bar{V} \equiv e/[2(C_\uparrow + C_\downarrow + C_\rightarrow + C_\leftarrow)]$, corresponding to a Coulomb-blockade peak, and measuring the electrical conductance between the left and right leads, the fusion channel of the bottom two Ising anyons is interferometrically detected.

To initialize the qubit in Fig. 4.8, one starts by creating a single pair of Ising anyons (see Fig. 4.6). Once the first pair of Ising anyons is created, qubit initialization can proceed in two different ways [see Figs. 4.9(a) and 4.9(b)], each creating another pair of Ising anyons with appropriate inchworm moves beforehand and afterwards. At the end of the first protocol shown in Fig. 4.9(a), each pair of Ising anyons is shared between the top and bottom rows, and initializing the qubit into a well-defined state $|0\rangle$ or $|1\rangle$ thus requires readout, as in the magnetic tunnel junction approach above. In contrast, for the second protocol depicted in Fig. 4.9(b), the two pairs of Ising anyons end up in the two respective rows, and the qubit is deterministically initialized in the state $|0\rangle$ without any readout.

Fusion protocols

As noted earlier, nontrivial fusion rules and non-Abelian statistics comprise intimately linked properties of non-Abelian anyons [295]. Probing fusion rules nonetheless entails a significant practical advantage—in particular requiring simpler geometries and manipulations compared to braiding. In fact, repeatedly implementing the initialization protocols described above for the minimal qubit architectures from Figs. 4.7(a) and 4.8(a) essentially realizes an experimental demonstration of the nontrivial Ising-anyon fusion rule $\sigma \times \sigma = I + \psi$!

For concreteness, let us first focus on the magnetic tunnel junction design from Fig. 4.7(a).

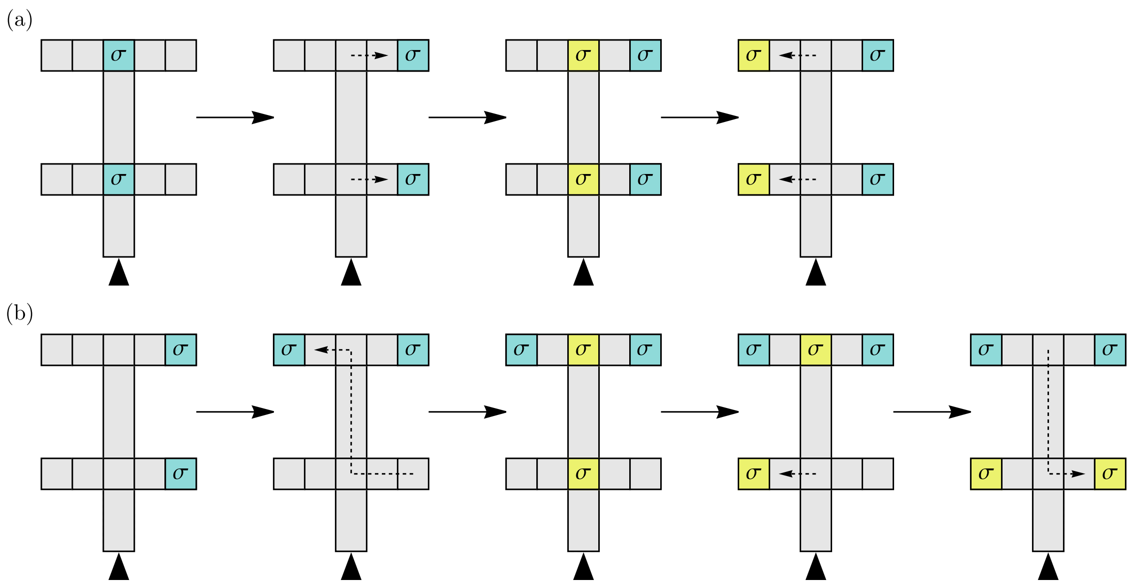

Figure 4.9: **Qubit initialization and fusion experiment in the electrical approach.** Two different protocols for initializing the qubit by creating two pairs of Ising anyons σ—with each of the blue and yellow pairs fusing to the identity channel I—and positioning them via appropriate inchworm moves (dashed arrows). Depending on the protocol, the qubit is initialized in either a superposition state $(|0\rangle + |1\rangle)/\sqrt{2}$ (a) or the basis state $|0\rangle$ (b). Repeatedly implementing these initialization protocols, one can statistically demonstrate the nontrivial fusion rule $\sigma \times \sigma = I + \psi$, as described in the text.

Suppose that the first two steps of the initialization protocol in Fig. 4.7(c) have been successfully carried out, leading to the configuration in the third row of Fig. 4.7(c) featuring an Ising anyon at each of the outermost holes. Those anyons were effectively pulled out of the vacuum and hence reside in the identity fusion channel I. Next suppose that one attempts to create a second pair of Ising anyons to arrive at the configuration in the fourth row of Fig. 4.7(c), and let p_{suc} denote the success probability. When successful, the second pair generated also resides in the identity fusion channel. Notice that the resulting initialized qubit state $|\Psi_{\text{init}}\rangle$ differs from either the $|0\rangle$ or $|1\rangle$ qubit levels sketched in Fig. 4.7(b). A basis change (related to so-called F-symbols in the underlying topological quantum field theory) allows one to recast $|\Psi_{\text{init}}\rangle$ in terms of the latter, yielding the equal superposition

$$|\Psi_{\text{init}}\rangle = \frac{1}{\sqrt{2}}(|0\rangle + |1\rangle). \tag{4.3}$$

(See, e.g., Ref. [3] for details and conventions leading to the above relation.) That is, the qubit has been initialized into a state for which the left pair and the right pair of Ising anyons each fuse into the I and ψ channels with equal probability. After the attempted creation of the second Ising-anyon pair, interferometric readout of the anyon charge on, say, the right set of holes returns the following possible outcomes, along with their probabilities:

- a single σ particle with probability $1 - p_{\text{suc}}$ (i.e., the attempt failed),
- an I particle with probability $p_{\text{suc}}/2$,
- a ψ particle with probability $p_{\text{suc}}/2$.

Resolving equal probabilities for the latter two outcomes via successive initialization protocols would yield compelling evidence for the fusion rule $\sigma \times \sigma = I + \psi$ as claimed.

A skeptic may reasonably counter, however, that equal probabilities for I and ψ could alternatively arise for more trivial reasons, e.g., from processes that randomly split a pair of ψ fermions into the left and right halves of the qubit. The single-σ outcome that occurs with probability $1-p_{\text{suc}}$ would be unaffected by such events, since $\psi \times \sigma = \sigma$. Moreover, the I and ψ outcomes could still occur with equal probability. A relatively simple control experiment can plausibly rule out this undesirable scenario: Run the above fusion experiment for the case where the first attempted Ising anyon pair creation failed, such that the left and right halves begin in the I sector rather than the σ sector. When the second Ising anyon pair creation *also* fails, interferometric detection should preferentially return I. By contrast, random ψ generation would be expected to return I and ψ again with equal likelihood, even though this control experiment has nothing to do with nontrivial fusion rules.

For the electrical approach, the nontrivial fusion rule $\sigma \times \sigma = I + \psi$ can be similarly demonstrated by initializing the qubit via the steps shown in Figs. 4.9(a), and then interferometrically reading out the resulting state [see Fig. 4.8(c)]. Given that the probability of success for anyon-pair creation is $p_{\text{suc}} = 1$ in the electrical approach, this readout measurement should return outcomes I and ψ with equal 50% probabilities, thus reflecting the nontrivial fusion rule above. For a control experiment ruling out more trivial explanations, one can initialize the qubit by following the steps in Fig. 4.9(b) instead of Fig. 4.9(a), in which case the final readout measurement should return the same outcome I every single time.

Lifetime demonstration

Various factors influence the coherence times of a topological qubit [3, 149, 152, 308, 285, 129]. Finite-temperature and/or non-equilibrium effects can generate bulk anyons that surreptitiously braid around a subset of anyons encoding the qubit—producing dephasing errors. Alternatively, such effects can generate bulk emergent fermions that decay in a way that flips the qubit or even exits the computational subspace entirely. (One can view the latter mechanism as analogous to quasiparticle poisoning events in topological-superconductor-based qubit designs [3, 147].) We will assume in what follows that bulk quasiparticles are *not* generated on experimentally relevant time scales, and that the system instead remains confined

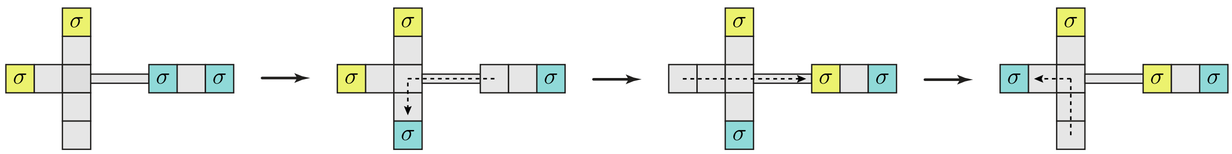

Figure 4.10: **Braiding experiment in the magnetic tunnel junction setup.** The qubit is initialized in the logical state $|0\rangle$ such that Ising-anyon pairs of the same color fuse to the identity channel I. Braiding is facilitated by four additional tunnel junctions which allow the anyons to be moved past one another by the sequence of inchworm moves depicted. Here, exchange of the first and third anyons enacts a unitary rotation gate $R_Y(-\pi/2)$ on the qubit. Interferometric readout of the resulting qubit state allows for verification of the non-Abelian braiding statistics underpinning the logical gate.

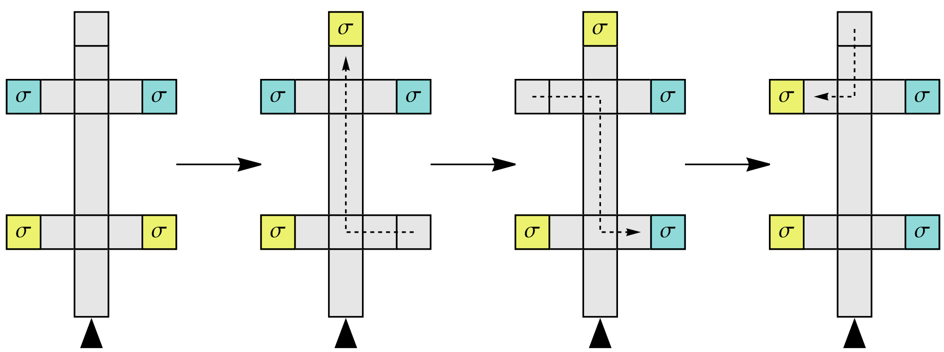

Figure 4.11: **Braiding experiment in the electrical approach.** Following qubit initialization in state $|0\rangle$ [see Fig. 4.9(b)], two Ising anyons σ are exchanged with each other via appropriate inchworm moves. (Note that each of the blue and yellow pairs fuse to the identity channel I.) Repeatedly implementing this exchange protocol both once and twice after qubit initialization, one can statistically demonstrate non-Abelian braiding of Ising anyons, as described in the text.

to the low-energy qubit subspace with high probability. This situation can arise provided that the temperature and the frequency associated with environmental noise both fall well below the spin liquid's bulk excitation gap.

Even in this scenario, a topological qubit will still generically be subject to decoherence. To see why, it is useful to invoke a further idealization by assuming that the topological qubit is encoded in exactly degenerate states that can not be distinguished via any local measurements and hence is perfectly immune to arbitrary local noise sources. Exact degeneracy means that the qubit's oscillation frequency ω_0, given by the *time-averaged* splitting between the qubit $|0\rangle$ and $|1\rangle$ states, vanishes. Perfect noise immunity further implies that the qubit's *instantaneous* splitting $\omega(t)$ is pinned to its time-averaged splitting, i.e., noise can not stochastically modulate the $|0\rangle$ and $|1\rangle$ energy difference; the dephasing time T_2 correspondingly diverges in this ideal limit.

In practice, the degeneracy will not vanish exactly, yet can generically be exponentially small in the spatial separation between Ising anyons encoding the qubit. Here the qubit states exhibit neither perfect local indistinguishability nor perfect immunity against local noise. One could, for instance, locally measure the difference in energy density between $|0\rangle$ and $|1\rangle$, with the measurement becoming increasingly difficult as system parameters are tuned to decrease the exponentially small splitting towards the perfect-qubit limit. As a corollary, imperfect noise immunity implies that local noise can also (weakly) modulate the $|0\rangle$ and $|1\rangle$ energy difference, yielding a finite T_2 time that tends to increase and eventually diverge on approaching the perfect-qubit limit.

The link between qubit energy splitting, local indistinguishability, and dephasing implies scaling relations between ω_0 and T_2 that are unique to topological qubits [3]. For a particular noise model, Ref. [3] in particular derived the relation

$$\omega_0 \sim \frac{1}{T_2} \sim e^{-L/\xi}, \tag{4.4}$$

where L is the separation between Ising anyons that dominate the residual energy splitting and ξ is the spin liquid correlation length. (Relations linking the qubit relaxation time T_1 with T_2 also arise [3].) Verifying Eq. (4.4)—which crucially links time-averaged behavior (ω_0) to fluctuations (T_2)—would validate the qubit's predicted ability to encode quantum information in an intrinsically fault-tolerant manner.

Fortunately, the same architectures used for fusion enable testing this prediction using a standard Ramsey protocol: (i) Initialize the qubit into $|0\rangle$, (ii) apply a $\pi/2$ pulse to rotate the qubit to an equal superposition of $|0\rangle$ and $|1\rangle$, (iii) wait for a time t_{wait}, (iv) apply a second $\pi/2$ pulse, and then (v) read out the qubit state in the computational basis. The t_{wait} dependence of the readout probabilities reveals both ω_0 and T_2. Requisite $\pi/2$ pulses can be implemented using unprotected gates, e.g., by pulsing the central bridge in Fig. 4.7 to couple the inner Ising anyons for a prescribed duration; see Sec. 4.5 for further discussion. (One can alternatively generate protected $\pi/2$ pulses in more elaborate geometries—considered later—that enable braiding the inner Ising anyons.) Moreover, altering the ratio L/ξ on the right side of Eq. (4.4) may be achieved in a fixed device geometry by changing parameters such as the magnetic field to vary ξ at fixed L.

Non-Abelian braiding protocols

Although the minimal architectures in Figs. 4.7(a) and 4.8(a) are sufficient for encoding, initializing, and reading out a single topological qubit, they do not permit the non-Abelian braiding processes that would perform topological quantum gates on the qubit. We can remedy this deficit at the expense of adding more tunable regions, as shown in Figs. 4.10 and 4.11 for the two approaches.

With these expanded architectures, non-Abelian braiding can be demonstrated in each approach by initializing the qubit in the state $|0\rangle$ and then exchanging two anyons that do not fuse to the identity channel I through appropriate inchworm moves (see Figs. 4.10 and 4.11). Since the qubit ends up in an equal superposition of $|0\rangle$ and $|1\rangle$, interferometric readout is expected to return outcomes I and ψ with equal 50% probabilities, demonstrating that an exchange of two anyons corresponds to a nontrivial quantum gate. A simple control experiment can rule out more mundane explanations for this maximally random distribution—e.g., random ψ generation addressed also for the fusion protocols above. Specifically, one may repeat the steps in Figs. 4.10 and 4.11 *twice* after each successful initialization of the qubit. This double exchange rotates the state from $|0\rangle$ to $|1\rangle$, and interferometric readout should then deterministically return outcome ψ.

4.5 Demonstration of elementary quantum gates

Having described how to nucleate, braid, and fuse anyons, we now consider how to implement the elementary quantum gates which are necessary for universal quantum computation. A standard choice of a universal gate set is the set of Clifford unitaries supplemented by a non-Clifford "magic" gate. Recall that the Clifford group is generated by (i) the single-qubit phase gate $P = e^{i\pi Z/4}$, (ii) the basis-changing Hadamard gate $H = (X + Z)/\sqrt{2}$, and (iii) the two-qubit controlled-NOT gate $\text{CNOT} = e^{i\frac{\pi}{4}(1-Z)\otimes(1-X)}$. In the following, we adopt the notation $R_O(\theta) \equiv e^{i\theta O/2}$ as the unitary rotation gate through angle θ with respect to Pauli operator O acting on the logical qubits.

We focus on minimal demonstrations of one- and two-qubit gates. For the multi-qubit scenario, the implementation of logical operations depends sensitively on the choice of encoding. A set of $2n$ Ising anyons forms a 2^{n-1} dimensional "fusion space" in which one can encode quantum information ($n = 2$ corresponds to the single-qubit case discussed in the previous section). A logical encoding corresponds to an embedding that maps the logical qubit codespace to a subspace of the fusion space. In the following, we consider two encodings of n_q logical qubits: (i) the *sparse* encoding, using $4n_q$ anyons, and (ii) the *dense* encoding, using $2n_q + 2$ anyons. Encoding (i) straightforwardly extends the single topological qubit by using an Ising anyon quartet for each additional qubit, only partially taking advantage of the degenerate subspace generated by the anyons. Encoding (ii) fully exploits the accessible states by using only *two* Ising anyons for each additional qubit. Despite the latter's more economical use of Hilbert space, however, encoding (i) is more commonly pursued because encoding (ii) is more susceptible to corruption by errors [305].

Topologically protected braid gates

Since the logical state is encoded in the fusion channels of bulk anyons, braiding the anyons applies a topologically protected operation on the encoded state. Let us denote by $\mathcal{R}_i$ the braid group generator corresponding to a clockwise exchange of anyons σ_i and σ_{i+1}. For $2n$

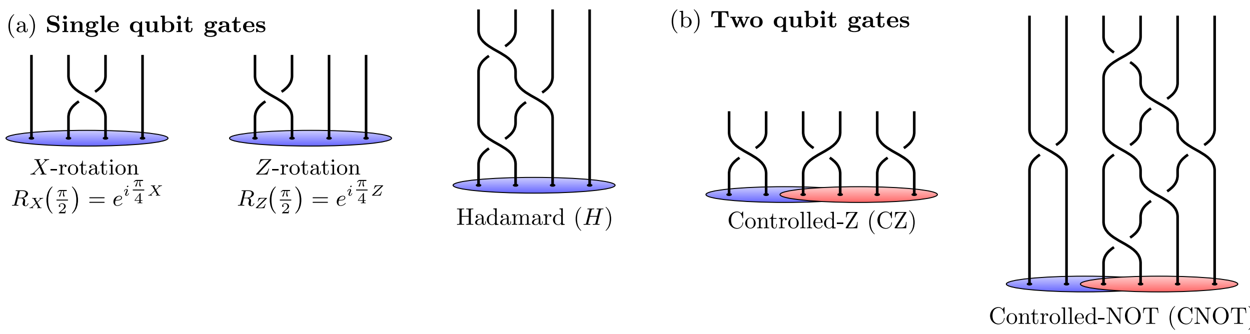

Figure 4.12: **Elementary quantum gates via braiding.** (a) Single-qubit braid gates for a logical qubit encoded in 4 Ising anyons. All such single-qubit braid gates may be implemented in the minimal architectures of Figs. 4.10 and 4.11. (b) Two-qubit braid gates for logical qubits encoded in 6 Ising anyons. The two qubits correspond to the two groups of four anyons inside the blue and red ellipses.

anyons, these generators are faithfully represented by the Clifford algebra representation of the group $SO(2n)$ [123, 260]. We may thus identify the anyon fusion space with the parity-even sector of the Hilbert space for n qubits. Let γ_j be the emergent Majorana zero mode operator bound to σ_j, and let $f_j = (\gamma_{2j-1} + i\gamma_{2j})/2$ span a corresponding set of n complex fermions that one can use to conveniently enumerate the degenerate manifold. Then the braid operators may be written, up to a phase, as Clifford unitaries acting on the qubits,

$$\mathcal{R}_j = e^{\frac{\pi}{4}\gamma_j\gamma_{j+1}}.$$

For a single logical qubit, there is no difference between the sparse and dense encodings, both of which use 4 anyons. Here, braiding generates the full set of Clifford operations [125, 7, 126]. Nearest-neighbor braids yield the $\pi/2$ rotation gates $\mathcal{R}_1 \sim R_Z(\pi/2)$ and $\mathcal{R}_2 \sim R_X(\pi/2)$ acting on the logical qubit. Composition of such braids give a simple implementation of the Hadamard gate, as depicted in Fig. 4.12(a). In Figs. 4.10 and 4.11, we show minimal architectures for demonstrating single-qubit braid gates for the tunnel-junction and charge-based schemes, respectively.

With two logical qubits, the sparse and dense encodings yield distinct sets of logical gates generated via braiding. The sparse encoding gives a straightforward generalization of the single-qubit case, using four anyons per qubit. As such, single-qubit gates remain the same as before, involving only the group of four anyons corresponding to the qubit being acted upon. Since the total topological charge of each qubit is trivial, the two-qubit SWAP gate $\frac{1}{2}(1 + X_1X_2 + Y_1Y_2 + Z_1Z_2)$ may be implemented by a sequence of braids which exchange the four anyons encoding each of the qubits. More generally, however, braiding in the sparse encoding may only produce unentangled (separable) two-qubit states [48]. This limitation can be seen from the fact that non-trivial entangling gates [e.g., controlled-NOT (CNOT) or controlled-Z (CZ)] require access to the joint parity $Z_1 Z_2$ of the logical qubit, which corresponds to a 4-fermion unitary not possible via braiding alone.

By contrast, the dense encoding of two logical qubits employs only 6 anyons. This is achieved by allowing the two qubits to "share" two anyons such that the following correspondence between logical operators and fusion channels holds: $Z_1 \sim (2f_1^\dagger f_1 - 1)$, $Z_2 \sim (2f_3^\dagger f_3 - 1)$, and $Z_1 Z_2 \sim (2f_2^\dagger f_2 - 1)$. To this end, single-qubit gates remain largely the same from the single-qubit case, with $R_{Z_1}(\pi/2) \sim \mathcal{R}_1 = e^{\frac{\pi}{4}\gamma_1\gamma_2}$ and $R_{Z_2}(\pi/2) \sim \mathcal{R}_5$. As the joint parity $Z_1 Z_2$ now corresponds to a fermion bilinear, two-qubit entangling gates may be implemented via anyon braiding [125]. Figure 4.12(b) depicts the braid sequence that implements CZ and CNOT gates on two densely encoded qubits. Thus, we may implement the full two-qubit Clifford group for 6 anyons exclusively by braiding. Crucially, this statement does *not* generalize to the case of more than two densely encoded qubits. There we no longer have access simultaneously to individual qubit Clifford gates and pairwise two-qubit joint parities $Z_j Z_{j+1}$. Moreover, it becomes nontrivial to implement the SWAP gate since naive exchange of the pairs of anyons corresponding to two qubits implements the fermionic fSWAP gate. Nonetheless, six anyons suffice to demonstrate topologically protected two-qubit Clifford gates and explore coherence times therein.

Measurement-assisted gates

In both qubit architectures we consider here, anyon interferometry allows for measurement of the total topological charge within an enclosed region of the spin liquid. Such measurements not only enable quantum-state readout, but also enrich the realizable set of logical operations. Namely, supplementing anyon braiding with topological charge measurements allows for the full Clifford group to be implemented for an arbitrary number of logical qubits.

As a demonstration of this measurement-assisted gate set, consider the sparse encoding of two qubits in the fusion space of 8 anyons. Preparing a maximally entangled Bell state $\frac{1}{\sqrt{2}}(|00\rangle + |11\rangle)$ requires a four-fermion unitary operation which cannot be realized by braiding. However, measuring the total charge of anyons $\sigma_{3,4,5,6}$ projects the state into an eigenspace of the joint parity operator $Z_1 Z_2$. Thus, an EPR pair may be produced by a sequence of braids and measurements,

$$\frac{1}{\sqrt{2}}(|00\rangle + |11\rangle) = U_\pm P_{ZZ}^\pm H_1 H_2 |00\rangle\,,$$
$$U_+ = \mathbb{1}, \quad U_- = X_2,$$

where $P_{ZZ}^\pm = \frac{1}{2}(1 \pm Z_1 Z_2)$ are projectors onto the parity sectors and $U_\pm$ is a unitary correction conditioned on the measurement outcome. If the anyon pairs may be nucleated deterministically (as in the charge-based scheme), we may slightly simplify this protocol by nucleating four nested pairs of Ising anyons rather than using Hadamard gates [see Fig. 4.13(b)]. More generally, the entangling CZ gate may be applied to an arbitrary two-qubit input state by a combination of measurements and conditional braid gates, with the assistance of an ancillary pair of anyons.

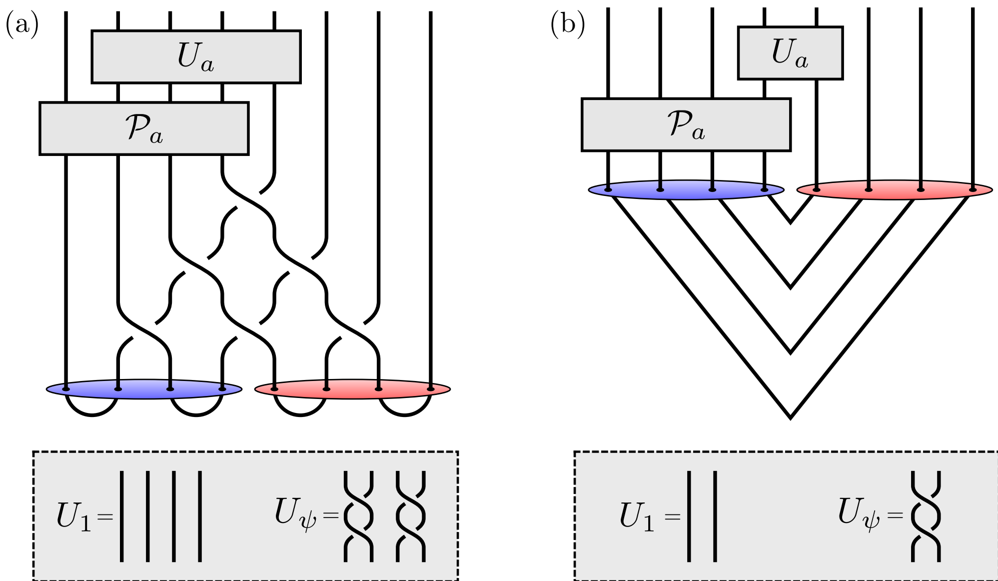

Figure 4.13: **Measurement-assisted Bell pair generation**. Two different schemes for preparing Bell pairs from two logical qubits (blue and red ellipses) encoded in 4 Ising anyons each. Both schemes employ projective readout $\mathcal{P}_a$ of the topological charge a for a group of 4 anyons followed by a unitary correction U_a conditioned on the measurement outcome. When the measurement reveals the topological charge to be in the vacuum sector ($a = 1$), we have successfully prepared the logical Bell pair $\frac{1}{\sqrt{2}}(|00\rangle + |11\rangle)$. If instead we measure a fermionic topological charge ($a = \psi$), the state lies outside the logical codespace and must be corrected by additional braiding. (a) If the two logical qubits are initially prepared in the logical $|0\rangle$ state, we follow the approach of Ref. [47], applying a sequence of braids prior to measuring the topological charge. (b) If pairs of anyons are nucleated from vacuum and dragged apart so as to give a nested structure, no additional braids are necessary prior to measurement. Moreover, the correction after observing $a = \psi$ needs fewer braids than in (a). The need for braiding can be fully eliminated by instead resetting the state via measuring the total charge of the central 4 anyons, then repeating until we get the desired measurement outcome.

Non-topological phase gates

Realizing a *universal* gate set in this setting necessarily requires that we supplement topological braid operations with a non-topological operation for non-Clifford gates or magic state injection. To this end, we consider here how to demonstrate generic single-qubit rotation gates. Broadly, there are two approaches to implementing generic phase gates: (i) temporarily inducing a level splitting so as to acquire a dynamical phase, or (ii) using anyon interferometry to effectively achieve a superposition of braid operations [44, 81]. Here we describe minimal setups required for demonstrating non-topological phase gates by both of these approaches.

Interaction-based phase gate

As discussed in Sec. 4.4, the two logical qubit states are degenerate when the anyons are sufficiently well separated so as to suppress interactions. However, interactions may in principle be harnessed for non-topological operations [48]. Suppose that we allow two anyons σ_i and σ_j to hybridize for a prescribed time Δt. The interactions induce a finite energy splitting ω in the basis where σ_i and σ_j have definite fusion channel. The net effect is then to apply a unitary gate $R_{\hat{O}}(\theta = \omega\Delta t)$, where the operator $\hat{O} = Z, X$ depends on which anyon pair one couples. A minimal demonstration of this unprotected phase gate can be achieved in the single-qubit architectures depicted in Figs. 4.7 and 4.8 by first initializing the qubit in a computational basis state, then inducing interactions for a prescribed time, and finally verifying the final qubit state via interferometric readout. In the tunnel junction setup, we can allow adjacent anyons to hybridize by temporarily tuning the intervening junction(s) to a trivial state. (Since the non-Abelian anyons in this approach are only metastable, the hybridization must occur on a time scale shorter than that at which the anyons relax.) Interactions may be similarly generated in the electrical scheme by bringing the anyons close together via a sequence of "inchworm" moves as described previously. This method requires no additional machinery beyond what was already required for qubit initialization and readout, offering a simple proof of principle that can be used for qubit lifetime demonstrations as discussed in Sec. 4.4. Nonetheless, we note that if the level splitting ω varies or oscillates rapidly with respect to the tuning parameter (e.g., anyon separation [77]), it may be challenging to accurately apply a desired phase gate.

Interferometry-based phase gates

Whereas the interaction-based phase gate distinguishes between the two qubit states by an induced energy splitting, the interferometry-based scheme relies instead upon anyon braiding statistics. Consider a single logical qubit encoded in anyons σ_i for $i = 1, 2, 3, 4$ (enumerated from left to right as in Figs. 4.14 and 4.15). We allow an Ising anyon σ_{probe} to travel along two interfering paths which enclose qubit anyons σ_i and σ_j, resulting in a braid phase of $+1$ or -1 for fusion channels I and ψ, respectively. This process enacts a logical phase gate whose angle θ depends on microscopic parameters setting (i) the relative dynamical (non-braid) phase for the two paths, (ii) the relative amplitudes for the two paths, and (iii) the number of anyons we send through the interferometer. We distinguish two types of interferometry-based phase gates: continuous-time and discrete-time gates.

For both the magnetic tunnel junction and electrically gated setups, we have already demonstrated how to perform anyon interferometry for qubit readout. The same architecture can be used to implement arbitrary phase gates. With tunnel junctions, consider the process depicted in Fig. 4.14. We allow for Ising anyon tunneling at a pinch point for finite time Δt. Since anyons σ_3 and σ_4 are enclosed by the interfering paths, the tunneling enacts a

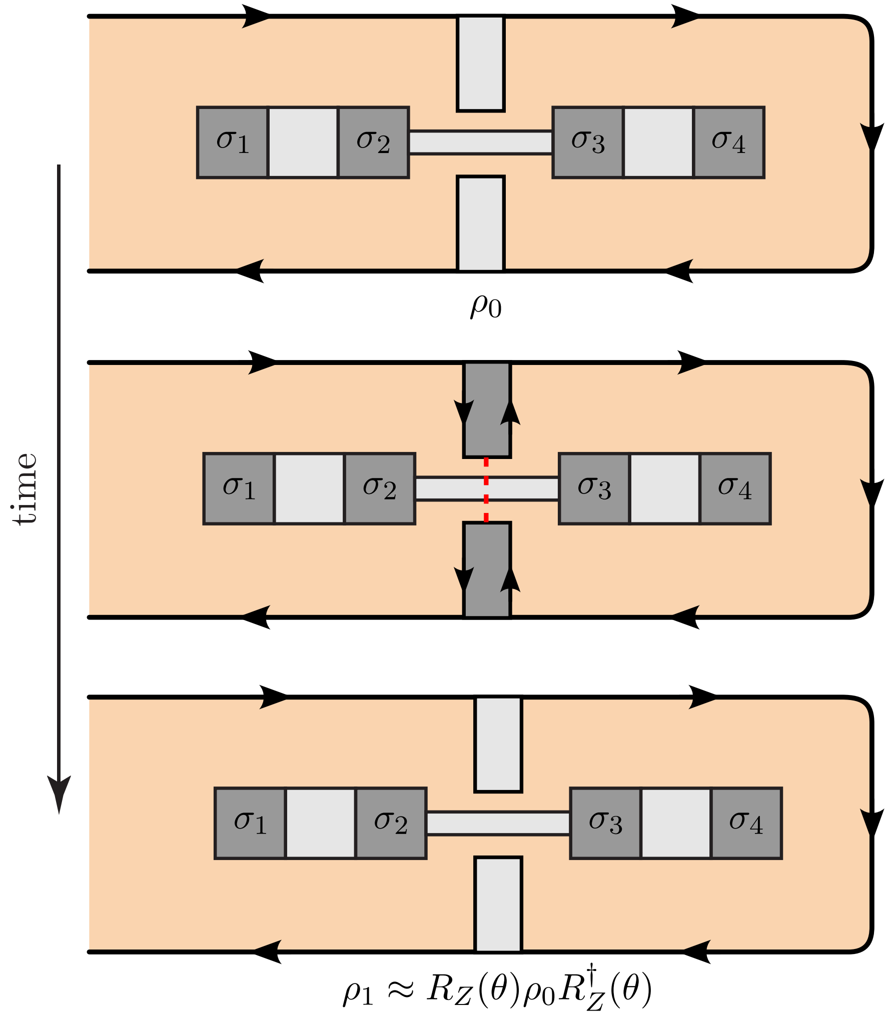

Figure 4.14: **Tunneling-based phase gate scheme in the magnetic tunnel junction setup.** Starting from an initial logical-state density matrix ρ_0 encoded in the Ising anyons $\sigma_{1,2,3,4}$, the edge is deformed to produce a point contact with Ising-anyon tunneling (dashed red line) for a finite time Δt. The resulting density matrix ρ_1 approximately corresponds to ρ_0 acted upon by a phase gate $R_Z(\theta)$, where the angle θ depends on the tunneling strength, the time Δt, and the edge temperature T through Eq. (A.38).

phase gate $R_Z(\theta)$. For fixed geometry and temperature, the gate angle θ is tunable via the time Δt and tunneling strength t_σ, which depends exponentially on the distance across the point contact [110, 72, 77]. At finite temperature, this tunneling process also induces finite decoherence of the logical qubit state. See Appendix A.3 for further details on how the gate angle θ and the decoherence rate depend on the relevant tuning parameters. In the electrical setup, a similar phase gate may be implemented. Passing a current from left to right through

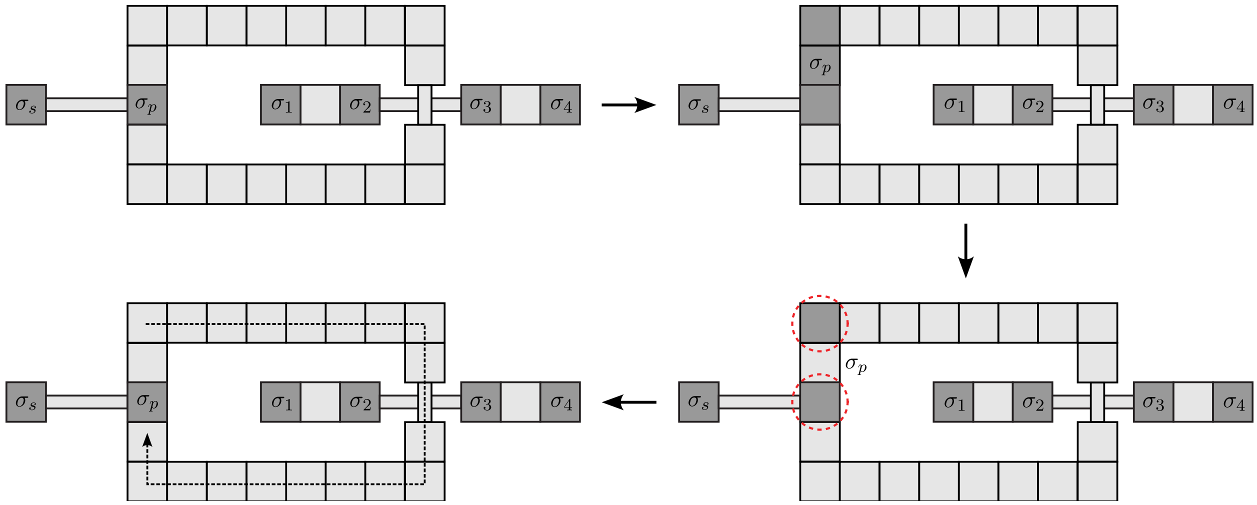

Figure 4.15: **Discrete-time phase gate scheme in the magnetic tunnel junction setup.** The procedure starts with a logical qubit encoded in the Ising anyons $\sigma_{1,2,3,4}$, as well as two auxiliary Ising anyons σ_s (spectator) and σ_p (probe). The hole on which σ_p resides is initially enlarged and then smoothly pinched in half, resulting in a superposition of two possible anyon locations (dashed red circles). To produce the necessary interference, one of the two holes on which σ_p may be residing is dragged around qubit anyons σ_1 and σ_2, resulting in a braid phase that depends on the fusion channel of σ_1 and σ_2. Finally, the two holes for σ_p are merged.

the interferometry loop depicted in Fig. 4.8(c) drags electron-anyon pairs along one of two paths enclosing the qubit anyons. In this case, there are fewer tuning parameters since the interferometry no longer relies on edge tunneling of Ising anyons. Furthermore, since the anyons are bound to electrons in the semiconductor, interference is now sensitive not only to the anyonic braiding statistics but also to the Aharonov-Bohm phase [141]. As such, the phase-gate angle θ may controlled by tuning the relative amplitudes for the two paths and the Aharonov-Bohm phase (through, e.g., an out-of-plane magnetic field).

Rather than relying upon a continuous stream of interfering anyons, we may instead use discrete-time operations to perform a tunable phase gate with individual probe anyons. In the tunnel junction architecture, interferometric readout and the corresponding phase gate rely upon deforming the spin liquid edge to form a pinch point where Ising anyon tunneling takes place. To interfere with individual anyons, we must instead move the whole process into the bulk of the spin liquid. As depicted in Fig 4.15, we may nucleate a pair of Ising anyons consisting of a spectator σ_s and a probe σ_p. In order to get two interfering paths for σ_p, we first grow the hole on which it resides and then pinch it off, resulting in a superposition between σ_p residing on one of two holes. One of these two holes may then be dragged around two qubit anyons to acquire the braid phase before merging back to the other hole. The

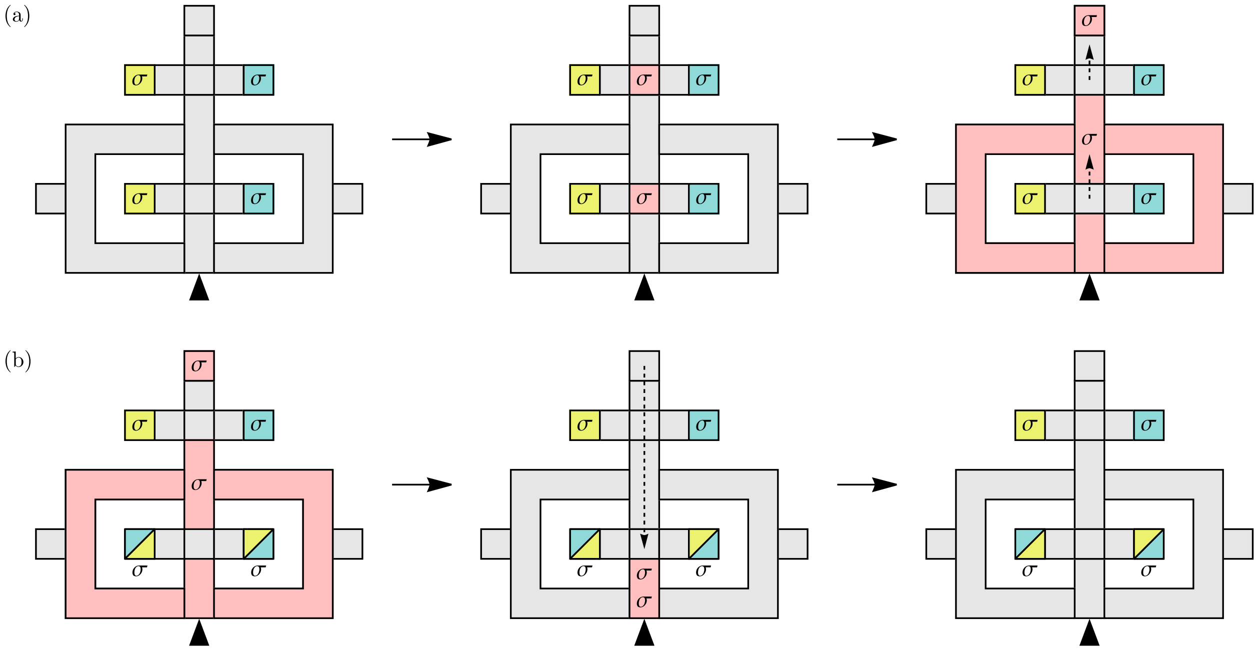

Figure 4.16: **Discrete-time phase gate scheme in the electrical approach.** (a) First step at zero time ($t = 0$). The qubit is initialized in the superposition state $(|0\rangle + |1\rangle)/\sqrt{2}$ [see Fig. 4.9(a)]; an auxiliary pair of Ising anyons σ is created (see Fig. 4.6); one auxiliary anyon is delocalized among the four islands that form a ring around the bottom pair of qubit anyons. (b) Second step at finite time ($t > 0$). The auxiliary Ising anyons are brought together and annihilated. Due to the time evolution beforehand, the qubit ends up in the new state $(|0\rangle + e^{i\theta}|1\rangle)/\sqrt{2}$, where the phase-gate angle θ is proportional to the evolution time t.

relative amplitude of the two interfering paths can be tuned by varying the speed and position at which the hole is pinched off. Moreover, by modulating the circumference L of one of the two holes after pinching, we may induce an energy difference (recall $E \sim 2\pi/L$) and thus a dynamical phase between the interfering paths. In comparison to the tunneling-based phase gate, this refined scheme requires a more complicated architecture and more movement of anyons in the bulk. However, this additional effort is rewarded with decoherence effects being better controlled here. In Appendix A.3, we provide further details on the effective logical operation applied to the qubit by this process.

An analogous discrete-time phase gate may also be implemented in the electrically gated setup with minimal modification to the single-qubit architecture already introduced above. Specifically, as depicted in Fig. 4.16, one nucleates a pair of auxiliary anyons from the vacuum, delocalizes one of these auxiliary anyons along the interferometry loop surrounding a pair of qubit anyons, and then annihilates the two auxiliary anyons back into the vacuum after a finite time t. Since the kinetic energy of the auxiliary anyon along the interferometry loop depends on the fusion channel of the two qubit anyons inside [141], this operation implements an appropriate phase gate of angle θ. Importantly, the energy difference between the two fusion channels can be as little as $0.1\,\mu\mathrm{eV}$ for the realistic parameters described in Ref. [141], which means that the phase-gate angle can be controlled with an accuracy $\theta \sim 0.1$ on nanosecond timescales t. In addition to varying the operation time t, the phase-gate angle θ may also be tuned by an out-of-plane magnetic field via the Aharonov-Bohm effect.

Magic-state distillation for imperfect phase gates

Thus far, we have outlined several distinct approaches for implementing non-Clifford phase gates. All of these methods are susceptible to noise or imperfect calibration, which will tend to spoil the encoded quantum state and its evolution. Nonetheless, noisy phase gates in tandem with ideal (topologically protected) Clifford operations allow one to realize clean phase gates via magic-state distillation [48]. In particular, given several noisy copies of a magic state, an appropriate sequence of measurements and unitary gates may be used to produce a single higher fidelity magic state. While 'magic state distillation' will require many more qubits and gates or tunnel junctions, it is a key operation to demonstrate when scaling beyond one or two qubits. In the meantime, however, noisy phase gates empower a more robust characterization of the minimal qubit designs presented here.

4.6 Summary

Quantum spin liquids have persisted as a topic of great theoretical and experimental interest for decades, yet the question 'What does a topological qubit based on non-Abelian spin liquids look like?' has remained largely unanswered. Building on recent theory insights, we have proposed two classes of potentially scalable topological qubit designs for non-Abelian spin liquids realized in Kitaev materials—and potentially other families of magnetic insulators. The first class uses Kitaev materials integrated into magnetic tunnel junction arrays that enable dynamically tuning select patches of the system between spin-liquid and trivial phases. The second class couples Kitaev materials to semiconductors—binding the non-Abelian anyons to electric charges and enabling all-electrical control of the charge-anyon composites.

Both designs offer pathways to anyon creation, manipulation, and interferometric readout desired for fault-tolerant quantum information applications. We have specifically identified architectures and protocols that one can exploit to experimentally demonstrate non-Abelian fusion rules and braiding properties; extract topological qubit lifetimes and oscillation frequencies to verify topological protection of quantum information; and establish a gate set needed for universal quantum computation in this setting. Our emphasis was on minimal devices needed for establishing each of these fundamental elements of topological quantum computation with spin liquids. Nevertheless, the basic design principles naturally extend to

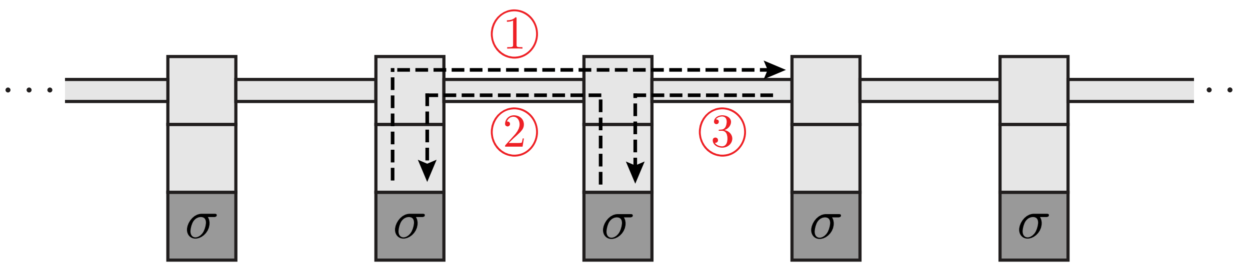

Figure 4.17: **Scalable qubit architecture in the magnetic tunnel junction setup.** Generalizing the single-qubit braiding scheme from Fig. 4.10, this architecture consists of a series of storage points where Ising anyons are held between braiding operations. These storage points are connected by horizontal bridges that are used not only for nucleating Ising-anyon pairs but also for lateral movement of anyons past one another. The elementary braiding operation is implemented by a sequence of moves (dashed lines) making use of this auxiliary space.

more complex architectures. For instance, Fig. 4.17 presents a multi-qubit array that allows for braiding any pair of non-Abelian anyons.

Even the simplest single-qubit devices require nontrivial experimental advances to realize in practice. Our work does, however, spotlight nearer-term challenges and opportunities: Can one optimize the probabilistic anyon-generation protocol in the magnetic tunnel junction design to increase the success probability towards unity? Are there variations on the magnetic tunnel junction approach that provide local control of the Kitaev material with less experimental overhead? For example, one might attempt to reposition the pair of ferromagnetic metals in Fig. 4.1, instead placing both side-by-side *above* the Kitaev material [1]. In the parallel configuration, the adjacent part of the Kitaev material clearly feels a net exchange field; in the antiparallel configuration, the net exchange field effectively *spatially* averages to zero provided the spin-liquid correlation length is long compared to the size of the ferromagnets. Such a modification could simplify fabrication while also being applicable to bulk Kitaev materials. In the electrical design, can first-principles calculations provide useful guidance for designing appropriate Kitaev material-semiconductor interfaces? More broadly, the electrical approach naturally applies also to *Abelian* spin liquids, where charge-Abelian anyon bound states can form via a similar mechanism. Can one utilize that technique to control topological qubits based on Abelian spin liquids hosting extrinsic non-Abelian defects [38]?

[1]We thank Charlie Marcus for suggesting this possibility.

Part II

Monitored quantum circuits

Chapter 5

Background

Analog quantum circuits, incorporating unitary gates, mid-circuit measurements, and quantum feedback, extend beyond traditional Hamiltonian or dissipative quantum systems. By utilizing measurement as a resource for irreversible quantum dynamics, quantum circuits offer a unique platform for shaping and manipulating entanglement. They enable applications such as quantum error correction [324, 296, 100, 200, 223, 37, 267, 228, 317], expedited state preparation, and the exploration of novel phenomena like measurement-induced entanglement transitions [213, 318, 80, 29, 56, 217, 216, 156, 302, 303, 248, 266, 112, 79]. In particular, the efficient preparation of entanglement patterns associated to circuit analogues of topologically nontrivial or gapless ground states has recently attracted attention due to the challenge of preparing such states by exclusively using unitary operations [277, 49, 331, 337, 225, 114, 158, 330, 329, 226, 157]. In recent years, *random* quantum circuits have garnered attention as simplified model systems for entanglement and dynamics in (open) quantum systems.

5.1 Entanglement Phases

Many-body entanglement has emerged as a fundamental concept in understanding and classifying quantum phases of matter [363]. In an equilibrium setting, it can serve as a tool to discern ground states of gapped from gapless Hamiltonians, to identify topological order, and to distinguish between generic and non-generic excited states [187, 211, 76]. Recently, this notion of many-body entanglement has been extended beyond static Hamiltonian states to characterize dynamically generated quantum states, in particular those arising in monitored quantum circuits. Analogous to Hamiltonian systems, robust *entanglement structures*, such as area-law or volume-law scaling, arise in quantum circuits and can be used to characterize the generated quantum states [113, 282].

The robustness of these entanglement structures against small variations in microscopic circuit parameters defines *entanglement phases of matter*, akin to phases of matter in thermal equilibrium, which depend only on global properties, such as underlying symmetries, the range of quantum gates and measurements, and the spatial geometry. This perspective of defining entanglement phases in quantum circuits is intricately connected to the concept of universality in statistical mechanics – stating that macroscopic features of a many-body system are governed by a few global properties, such as symmetries, interaction range, and dimensionality – and it anticipates a *symmetry classification of entanglement phases* in monitored quantum circuits.

Along these lines it has been recognized that in generic quantum circuits with measurements, the presence or absence of a U(1)-symmetry, associated with the conservation of the total particle number or magnetization, dramatically alters the potential phases [167, 103, 281, 6, 68]. However, a comprehensive classification of circuit phases in terms of their symmetries is presently absent.

5.2 Measurement-induced phase transitions

A novel phenomenon observed in the context of monitored quantum circuits is a measurement-induced phase transition in entanglement, which we review briefly here. Consider a generic random quantum circuit which may consist of local random unitary gates and projective measurements, applied at random locations in space and time. If one averages over the ensemble of unitaries, measurement outcomes, and positions, the ensemble averaged state is a featureless, infinite-temperature state $\rho \propto \mathbb{1}$. However, each individual circuit trajectory produces a non-trivial state which may have finite entanglement. Thus trajectory-averaged entanglement quantities may attain finite expectation value and represent the typical entanglement structure in a state produced by random circuit evolution. Upon varying the parameters characterizing the random circuit, such average entanglement quantities may undergo a transition akin to equilibrium phase transitions.

A paradigmatic model for such an entanglement transition is the measurement-induced phase transition in a monitored random unitary circuit [318, 213, 214]. Consider a circuit where two-qubit unitary gates are applied with probability $1 - p$ and local projective measurements (e.g., of Z_l) occur with probability p. Two-qubit unitary gates tend to generate entanglement, driving the evolution toward a volume-law entangled state. By contrast, local measurements localize correlations and destroy long-range entanglement, driving the system toward an area-law entangled state. In this system, one observes a second-order transition in the trajectory-averaged entanglement entropy at a critical measurement strength p_c, separating an area-law phase at $p > p_c$ and a volume-law phase at $p < p_c$. For random Clifford unitaries, numerical simulation shows that this measurement-induced phase transition lies in the percolation universality class. More generally, such entanglement transitions may arise even in the absence of unitary gates, for example by the competition between incompatible measurements which try to stabilize topologically distinct area-law phases.

5.3 Numerically Tractable Circuits

Generic random quantum circuits are complex, making analytic treatment and numerical simulation challenging. To this end, much work on random circuits has focused on restricted but tractable subclasses, such as stabilizer circuits and Gaussian circuits, which we review here.

Stabilizer Circuits

Recall that an L-qubit stabilizer state with density matrix ρ is defined by a group $\mathcal{S} = \{S_i\}$ of (signed) Pauli operators such that $S_i \rho S_i = \rho$. These $|\mathcal{S}| = 2^n$ operators are the stabilizers of the state ρ, with $n \leq L$ saturated for pure states. Given a generating set of stabilizers $\mathcal{G} = \{G_1, \ldots, G_n\}$, the state may be written as a product of projectors $\rho = 2^{-n} \prod_{i=1}^{n}(1 + G_i)$. Each Pauli string G_i can be represented by a phase ± 1 and a bitstring of length $2L$ encoding the operator content [131]. As a result, a stabilizer state admits a compact representation in a *tableau* of $\mathcal{O}(L^2)$ bits, in contrast to the $\mathcal{O}(2^L)$ complex coefficients requires to specify a generic wavefunction.

A stabilizer circuit is one in which the evolution preserves the stabilizer nature of the state. We are thus restricted to Clifford operations, which map the generators $\mathcal{G}$ to a new set of Pauli strings. In addition to Clifford unitary gates (e.g., Hadamard, CNOT, and phase gates), this constraint permits projective measurements of Pauli operators. From the Gottesman-Knill theorem, it is known that stabilizer circuits may be efficiently simulated by tracking the evolution of a generating set of stabilizers [131]. Indeed, the new set of generators after applying an operation can be computed in $\mathcal{O}(L^2)$ time, while entanglement entropy across a cut can be computed in $\mathcal{O}(L^3)$ time [1]. The tableau representation of stabilizer circuits has been a key tool, empowering detailed numerical studies and providing a basis for phenomenological models of entanglement dynamics in random quantum circuits [213, 156, 315, 257].

Gaussian Circuits

Now consider taking a Jordan-Wigner transformation such that the state and circuit operations may be represented in terms of Majorana fermions γ_i for $i = 1, \ldots, 2L$. A Gaussian state $\rho \propto e^{-\vec{\gamma}^\dagger H \vec{\gamma}}$ is fully described by the two-point correlation function $\langle \gamma_i \gamma_j \rangle = \left(\frac{1}{1+e^{2H}}\right)_{ij}$. Thus it may be compactly represented by the $\mathcal{O}(L^2)$ elements of the correlation matrix. A Gaussian circuit consists of operations (e.g., unitary rotation gates $e^{\theta \gamma_i \gamma_j}$) which map one Gaussian state to another. Evolution of the state under such dynamics is efficiently computable through transformations applied to the correlation matrix. While still computationally tractable, Gaussian circuits have offered a distinct avenue from Clifford stabilizer circuit by which to study entanglement phases and dynamics which arise in (monitored) quantum systems [8, 56, 74, 28].

5.4 Organization

While stabilizer and Gaussian circuits are efficiently simulable, an exact analytic treatment of entanglement dynamics remains challenging except for a select few exactly solvable models or in the limit of large onsite dimension. Over the course of the next several chapters, we seek to close this gap by developing a statistical mechanics framework for characterization and symmetry classification of entanglement phases in monitored quantum circuits. To this end, we begin by turning our attention to the intersection of Gaussian and stabilizer circuits. This restricted class of *Majorana stabilizer circuits* provides an analytically tractable starting point for more in-depth study of entanglement in monitored circuits. In Ch. 6, we detail an exact mapping between such Majorana circuits and classical loop models. Then in Ch. 7 we carry out a symmetry classification and detailed numerical characterization of entanglement phases and critical points which arise in these Majorana stabilizer circuits. Building upon these results, we provide insight into more generic stabilizer circuits in Ch. 8 by introducing non-Gaussian interaction terms. Finally, in Ch. 9 we engineer novel and robust entanglement structures in carefully constructed hybrid quantum-classical circuits, highlighting the power of this framework.

Chapter 6

Loop models for Majorana circuits

In a Gaussian Majorana model all information about the state is encoded in the two-point Majorana correlation functions $\langle i\gamma_l\gamma_m\rangle$. If one asks, in addition, that the Majorana state is also a stabilizer state, then all Majoranas have definite pairings $\langle i\gamma_l\gamma_m\rangle = 0, \pm 1$. Such a stabilizer state can be graphically represented by a pairing diagram wherein nodes l and m are connected by an open arc if and only if $|i\langle\gamma_l\gamma_m\rangle| = 1$. Any generic Gaussian state can then be written as a linear combination of Majorana stabilizer states or, alternatively, of pairing diagrams. Evolving the state over time leads to rearrangement of the Majorana pairings, with fermion world lines tracing out loops in space-time.

When restricting to Majorana stabilizer states, there are three permissible discrete operations on a pair of Majoranas γ_l and γ_m, depicted in Fig. 6.1(a). The identity $\mathbb{1}_{lm}$ leaves the pairings unmodified, amounting to uninterrupted propagation forward in time. By contrast, the so-called Temperley-Lieb (TL) generators e_{lm} result in spatial propagation of loops. On the Majoranas, this generator acts as a projector onto the local fermion parity,

$$e_{lm} \propto \mathcal{P}_{lm} = \tfrac{1}{2}(1 + i\gamma_l\gamma_m)\,.$$

In particular, for initial pairings (k,l) and (m,n), e_{lm} implements a *loop surgery* to yield new pairings (l,m) and (k,n), as depicted in Fig. 6.1(b). Finally, the braid operator b_{lm} acts as the Majorana swap operator

$$\mathcal{R}_{lm} = \tfrac{1}{\sqrt{2}}\left(1 + \gamma_l\gamma_m\right)\,,$$

exchanging the two Majoranas and causing the world lines to cross over one another.

A brickwall circuit in d-spatial dimensions built from these elementary operations then exactly specifies a loop configuration on a $(d+1)$-dimensional spacetime lattice. When the number of Majoranas is conserved at all times (e.g., as for a spin-chain after a Jordan-Wigner transformation), the space-time is *fully packed* with loops. Properties of the Majorana state and dynamics are then encoded in the corresponding loop configuration. For instance, the entanglement and mutual information between two distinct subregions in space A, B are

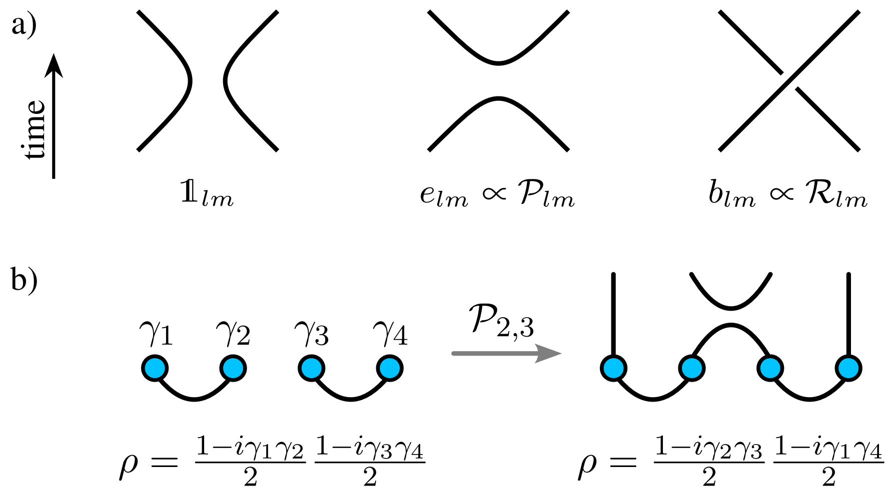

Figure 6.1: **Graphical representation of Majorana pairings.** (a) Local generators of the loop algebra and the correspond Majorana operation relevant for Majorana circuits. The non-trivial generators e_{lm} generate a Temperley-Lieb subalgebra and are proportional to the fermion parity projector $\mathcal{P}_{lm}$. The b_{lm} generate a braid group and are proportional to the Majorana swap operators $\mathcal{R}_{lm}$. (b) Rewiring of Majorana worldlines under the action of projective measurement $\mathcal{P}_{2,3}$ on a state represented by the density matrix ρ.

given by the number of arcs connecting A and B [188], independent of the sign of the Majorana parities [1].

6.1 Algebraic description of loops

Given this close connection between Majorana stabilizer states and loop configurations, we now introduce some generic properties of loop models. A graphical calculus of loops is broadly described by a braid-monoid or Birman-Wenzl-Murakami (BMW) algebra.Arbitrary loop configurations may be constructed by appropriate products of the algebra generators depicted in Fig. 6.1(a): identity $\mathbb{1}$, the monoid e_{lm}, and the braid b_{lm}. This algebra and the resulting loops are characterized by a few key relations. Ambient isotopy [Fig. 6.2(a)] means that loops may be continuously deformed while holding endpoints fixed and not breaking any loops. Closed loops may be removed and replaced by a scalar factor n, the loop fugacity, as depicted in Fig. 6.2(b). Finally, braiding or twisting a loop is associated with a twist factor ω [see Fig. 6.2(c)]. When viewing the loops as worldlines, the fugacity n and twist factor ω may be related to the local dimension and spin-statistics, respectively.

[1]Diagrammatic representations including the parity sign are possible but follow a more complicated loop algebra than required here [188].

The Temperley-Lieb (TL) algebra is an important subalgebra generated by the identity and monoid (e_{lm}) operators. In the absence of any twists or crossings, the TL algebra generates planar loop configurations and is characterized solely by the fugacity n. Such an algebra is closely related to the 2D classical Potts model as well as a family of 1D spin chains including the XXZ chain.

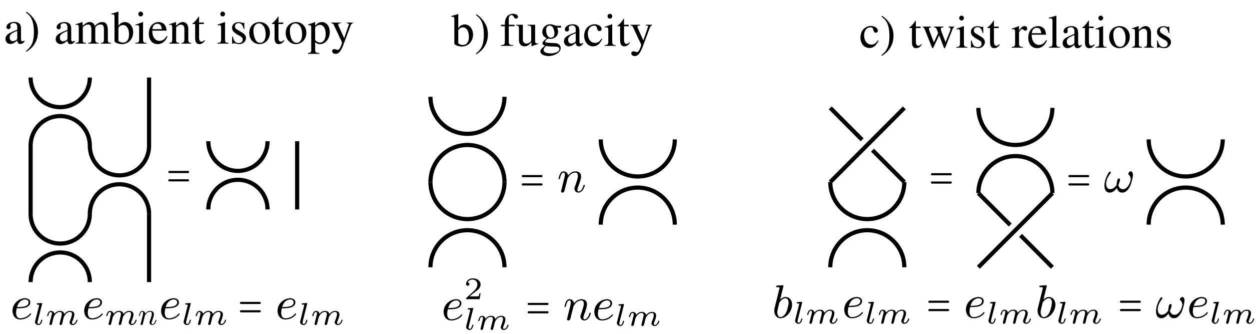

Figure 6.2: **Loop algebra relations.** The loop algebra generators depicted in Fig. 6.1(a) satisfy three elementary relations. (a) Ambient isotopy of loops allows smooth deformation. (b) Closed loops can be replaced by a scalar factor n, the loop fugacity. (c) Untwisting loops after a braid operation introduces a scalar factor ω.

6.2 Loop algebra for Majorana circuits

For a brick-wall Majorana stabilizer circuit consisting of projective parity measurements $\mathcal{P}_{lm}$ and swaps $\mathcal{R}_{lm}$, we would like to specify the appropriate loop model and the corresponding non-linear sigma model (NLσM) dictating long-wavelength behavior. Here, braiding phases and the sign of the measurement outcome poses a challenge to specifying a loop representation. In particular, the two possible measurement outcomes correspond to $\mathcal{P}_{lm}$ and $\mathcal{P}_{ml}$. Distinguishing such phase information in the graphical language of loops would require non-trivial twisting relations ($\omega \neq 1$), thereby complicating the relative weights in the trajectory-averaged loop ensemble.

Throughout this work, we are interested exclusively in the dynamics of entanglement and mutual information in Majorana models, such that only the connectivity $|\langle i\gamma_l\gamma_m\rangle|$ matters. Braiding phases can thus be neglected and we fix $\omega = 1$. This yields the equivalence relation $b_{lm} \sim b_{lm}^{-1}$ on the space of loop configurations, reducing the braid-monoid algebra to the Brauer algebra $\mathcal{B}(n)$ [63]. Under this equivalence relation, a given loop configuration now represents an equivalence class of circuits.

To determine the loop fugacity, note that the projector $\mathcal{P}_{lm}$ is always accompanied by a normalization of the state (i.e. $|\psi\rangle \to \frac{\mathcal{P}_{lm}}{\sqrt{\langle\mathcal{P}_{lm}\rangle}}|\psi\rangle$). Due to the normalization, projective measurements automatically satisfy the loop isotopy condition. We may thus identify the generator e_{lm} as the operator which acts on any state $|\psi\rangle$ as the normalized projective measurement $\mathcal{P}_{lm}$. In addition, the idempotence of projectors $\mathcal{P}_{lm}^2 = \mathcal{P}_{lm}$ fixes the loop fugacity $n = 1$. By contrast, in a Trotterized treatment of Hamiltonian evolution, the loop fugacity is fixed by the projector algebra without normalization, yielding $n = \sqrt{2}$. This difference in fugacity and twist factor yields striking differences in the physics arising from Hamiltonian evolution and stabilizer circuit dynamics for Gaussian Majorana models.

6.3 Loop-circuit dictionary

Loop-Circuit Dictionary

Here, we connect the key observables of the loop model framework to the Majorana circuits, providing a mapping between the two pictures. In passing from loops in $(d+1)$-dimensional space-time to the dynamics of Majorana fermions in d-dimensions, one dimension in the loop picture is designated as time. The state of the Majorana circuit at a given time corresponds to the surface of the loop model along one direction. There are two such temporal surfaces: (i) that at $t = 0$ where boundary conditions on the loops correspond to a choice of initial state for the Majoranas, and (ii) that at time $t = T$ corresponding to the final state produced by the circuit. Correlations in this output state amount to *boundary* correlations in the loop model. By contrast, loop correlations in the space-time bulk require the ability to peek at the state midway through the circuit evolution.

To track information regarding both the surface and the bulk of the loop model, we keep track of not only the loop connectivity, but also their integrated path lengths. Any open arc is labeled by a tuple (l, m, ℓ), where l and m represent the endpoints and ℓ is the path length. In a numerical simulation this information is readily incorporated into the update scheme: Consider a state with initial pairings (k, l, ℓ_1) and (m, n, ℓ_2) where l and m are nearest neighbors. Measuring the parity $i\gamma_l\gamma_m$ yields a state with new pairings and loop lengths $(k, n, \ell_1 + \ell_2 + 1)$ and $(l, m, 1)$. When $k = m$, such a measurement closes the loop with total length $\ell_1 + 1$ which is then recorded in a histogram for the trajectory.

Loop length distributions

The central observable for the loop models we consider here is the probability distribution for the length of loops, both along the (temporal) surface and through the space-time bulk. The surface loop length between two points l, m at fixed time T describes the distances between two entangled Majorana fermions γ_l, γ_m in the circuit. The distribution of surface loops thus yields complete information on the quantum state at time T with regard to its entanglement and mutual information. The bulk loop length yields information on out-of-time ordered correlators (OTOCs), explored below.

For an open arc connecting Majoranas γ_l and γ_m on the $t = T$ boundary, we define the surface length $\ell_{\text{surf}}^{\alpha}$ along the α-direction. For example, consider $d = 2$ with $\ell_x\hat{x} + \ell_y\hat{y}$ the vector connecting sites l and m. Using periodic boundary conditions (PBC), the surface

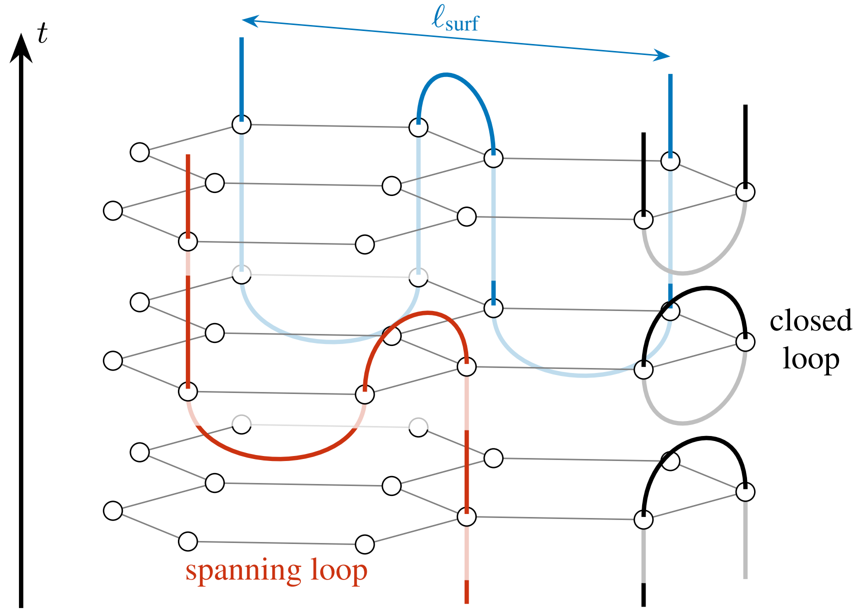

Figure 6.3: **Majorana loop models in 3D space-time.** The loop model description emerges from the dynamics of the Majorana fermions in space-time. The final state produced by the corresponding circuit is insensitive to closed loops contained in the space-time bulk (such as the black loop). Dynamical purification is sensitive to the presence of spanning loops (red) which connect the two temporal boundaries. Open arcs with both ends on a single temporal boundary (blue) have both a bulk path length ℓ_{bulk} and a projected surface length ℓ_{surf}.

lengths of the loop are defined as $\ell^{\alpha}_{\text{surf}} \equiv \min\left(|\ell_\alpha|, L_\alpha - |\ell_\alpha|\right)$. We define the corresponding length distributions $P^{\alpha}_{\text{surf}}(\ell)$ as that obtained in the stationary state of the circuit when taking a pure initial state with only local pairings.

Characteristics of the entanglement dynamics during the evolution are encoded in the bulk loop length distribution $P_{\text{bulk}}(\ell)$. It is the probability distribution for the total path length of a randomly selected loop. Here we need to make a distinction between open arcs and closed loops, as these will generically exhibit distinct length distributions. During the circuit evolution, many closed loops are formed, but the number of open arcs is fixed by boundary conditions and remains constant. If we impose PBC in time, all loops are closed and there is no need to make this distinction. In practice, temporal PBC can be implemented with the assistance of ancilla measurements, which is discussed in Sec. 7.4 together with the subtle but important role of boundary conditions for the bulk loop statistics.

Surface observables: Entanglement entropy and mutual information

Observables described by the loop distribution of a temporal surface at time $t = T$ correspond to the entanglement content of the Majorana fermion state $\rho(T)$ produced by the circuit. We consider the von Neumann entanglement entropy $S_A \equiv -\operatorname{Tr}[\rho_A \log_2 \rho_A]$ for a subsystem A, where the reduced density matrix $\rho_A \equiv \operatorname{Tr}_{\bar{A}}[\rho]$ is obtained by tracing out the complementary system $\bar{A}$, and the mutual information $I_2(A,B) \equiv S_A + S_B - S_{AB}$ between subsystems A and B. For Majorana stabilizer states, these measures of entanglement are determined wholly by the non-vanishing two-point Majorana correlations $|\langle i\gamma_l\gamma_m\rangle| = 1$. Thus the connectivity encoded by the loop representation contains all necessary information to specify S_A and $I_2(A,B)$. The mutual information $I_2(A,B)$ therefore corresponds precisely to the number of loops connecting subsystems A and B, while the von Neumann entanglement entropy for a pure state is $S_A = \frac{1}{2} I_2(A,\bar{A})$, reflecting that each Majorana arc carries a half qubit of entanglement. Multipartite entanglement measures such as the tripartite mutual information $I_3(A,B,C)$ vanish due to the additivity of mutual information in the loop framework.

When considering $d = 2$, we will frequently consider the entanglement entropy of a cylindrical subsystem of length ℓ, with boundaries encircling the system in the $\hat{x}$ or $\hat{y}$ directions. For such a partition, the entanglement entropy can be computed from the surface loop length distribution [188]. In particular, the average entanglement entropy for subsystem A in a cylindrical region of length ℓ along the $\hat{x}$ direction is given by

$$\langle\!\langle S_\ell^x \rangle\!\rangle = L_y \sum_{\ell'} \min(\ell,\ell') P^x_{\text{surf}}(\ell') \,. \tag{6.1}$$

The mutual information between such cylindrical subsystems can be computed in a similar manner. The case of $d = 1$ follows naturally by taking $L_y = 1$ in the above.

Spanning loops and purification

A single loop connecting the two temporal surfaces at $t = 0$ and $t = T$ correspond to Majorana fermions, which remain unpaired during the entire circuit evolution. Such loops are called *spanning* and reflect the dynamical purification under measurement: Consider a maximally mixed initial state $\rho(t = 0) \propto \mathbb{1}$, corresponding to each Majorana being unpaired at $t = 0$. The purity of the Majorana state ρ at time $t = T$ is given by the total entropy $S_L(T) = -\operatorname{Tr}[\rho(T)\log_2 \rho(T)]$. Each unpurified qubit at time T corresponds to two unpaired Majorana fermions and thus to half the number of spanning loops $n_s(T)$, i.e., $S_L(T) = \frac{1}{2} n_s(T)$.

In the loop model framework, the spanning number, i.e., the dynamical purification, serves as an accurate quantifier for the different loop model phases and the critical point separating them [271, 252, 256, 255]. To do so, we assume fixed aspect ratios T/L_y and L_x/L_y. Then for small distance δ from the critical point, we employ a scaling ansatz,

$$\begin{aligned} n_s(\delta, L) &= f(x)\left[1 + \beta L^{y_{\text{irr}}}\right] , \\ x &= L^{1/\nu}\delta\left[1 + \alpha\delta\right] , \end{aligned} \tag{6.2}$$

where y_{irr} is the dimension of the leading irrelevant operator and $\alpha \neq 0$ gives a polynomial correction.

Bulk loops, watermelons, and OTOCs

Beyond the distribution of bulk loop lengths $P_{\text{link}}(\ell)$, bulk properties of the loop model are captured by the watermelon correlators $G_k(r)$, the probability that two patches in space-time separated by distance r are connected by exactly k distinct arcs. For example, $G_2(r)$ gives the probability that two points with separation r lie along the same loop. When the points do not lie along the same fixed-time slice, then $G_k(r)$ takes the form of an out-of-time order correlator (OTOC) for the Majoranas. Watermelon correlators can be accessed in the circuit by an ancilla-based measurement scheme.

For example, the two-leg watermelon correlator $G_2(r)$ can be measured by considering space-time points (t_1, l) and (t_2, m) separated by distance r. Consider ancilla A and B, each consisting of a pair of definite parity, e.g. $|\langle i\gamma_{A,1}\gamma_{A,2}\rangle| = 1$. After evolving the circuit to time t_1 (t_2), a "marked" loop can be effectively inserted into the circuit by coupling the ancilla and bulk via measurement of $i\gamma_{A,2}\gamma_l$ $(i\gamma_{B,2}\gamma_m)$. The history of the world lines which had been passing through these points in space-time is then effectively stored in the remaining ancilla $\gamma_{A,1}$ and $\gamma_{B,1}$. We then evolve the circuit to late time $t_f \gg t_2$ and impose boundary conditions on the bulk qubits (e.g., by measurement) such that the only remaining open arcs are those through the ancilla. Had we taken only individual Majoranas for each ancilla, then the watermelon correlator $G_2(r)$ would explicitly take the form of an OTOC, $\langle\gamma_A(t_f)\gamma_A(0)\gamma_B(t_f)\gamma_B(0)\rangle - \langle\gamma_A(t_f)\gamma_A(0)\rangle\langle\gamma_B(t_f)\gamma_B(0)\rangle$, which for stabilizer states coincides with the mutual information between the ancilla $I_2(A, B)$. By construction, the mutual information $I_2(A, B)$ counts the number of loops connecting points (t_1, l) and (t_2, m) in space-time such that $G_2(r) = \frac{1}{2}I_2(A, B)$. For higher order correlators $G_k(r)$, additional ancilla are required, but the general procedure remains the same.

6.4 Numerical Technique

Let us close this chapter by highlighting the benefits of the loop model representation in numerical simulations of quantum circuits. In short, the loop model representation allows for a substantially more efficient numerical simulation of Majorana circuits [188, 255] reaching system sizes of up to 10^8 qubits far exceeding those accessible via standard Clifford circuit methods. To understand this efficiency gain of about two orders of magnitude in number of simulated qubits remember that, in the tableau representation of conventional Clifford simulations, an N qubit stabilizer state requires $\mathcal{O}(N^2)$ memory, and each Clifford operation (e.g., a measurement) requires $\mathcal{O}(N^2)$ time. By contrast, in the loop model representation, the loop connectivity compactly encodes the state in only $\mathcal{O}(N)$ space and can be updated after a measurement in $\mathcal{O}(1)$ time. This substantial computational advantage of the loop model representation is further enhanced by noting that a circuit of depth t acts as a transfer matrix on the loop connectivity. Two such depth t circuits can be efficiently composed in time $\mathcal{O}(N)$, yielding a new circuit of depth $2t$.

The loop model simulations are then carried out as follows: We begin by preparing a "pool" of N_p shallow circuits (loop configurations) of depth $t = 1$. In particular, we perform N measurements $\mathcal{P}_{lm}$ chosen at random with the prescribed relative probabilities for the circuit. Then all trajectories are evolved to depth T by $\log_2(T)$ rounds of concatenation. When concatenating, the circuits are randomly translated with respect to one another in order to enlarge the accessible configuration space as well as to reduce spurious correlations arising from finite N_p. From this pool, N_s independent sample trajectories are drawn by choosing two random elements, translating them with respect to one another, and concatenating. Due to self-averaging in large systems, random translations before concatenating allow one to take $N_s \gg N_p$.

For each such sample, quantities such as the entanglement entropy and the spanning number may be directly computed from the loop connectivity after imposing appropriate boundary conditions at the temporal boundaries. Moreover, for periodic boundary conditions (PBC), the entanglement entropy averaged over all cuts can be efficiently computed in one $\mathcal{O}(N)$ shot. By contrast, computing entanglement entropy in the tableau (Clifford) representation requires $\mathcal{O}(N^3)$ time for *each* subsystem, making it far more costly. To probe bulk loop statistics, we track not only the loop connectivity, but also the total length of each loop, storing the lengths of closed loops in a histogram during the evolution.

While Majorana stabilizer circuits are a restricted class of stabilizer circuits, this highly efficient numerical simulation scheme empowers unparalleled precision in studying paradigmatic models for entanglement dynamics and measurement-induced transitions in random quantum circuits. For example, in the subsequent study of 2D Majorana circuits in Ch. 7.4 we are able to simulate system sizes up to $N \sim 10^8$ qubits in the loop representation. By contrast, the conventional Clifford tableau representation is limited to $N \sim 10^4$ qubits using comparable computational resources. Moreover, the loop model simulation algorithm is highly parallelizable and limited in performance primarily by memory bandwidth, inviting GPU acceleration in future works.

Chapter 7

Universality and symmetry classes of entanglement phases

Having introduced a broad family of loop models, and identified the relevant case for Majorana models, we now explore the statistical mechanics of such models. The behavior of correlation functions and observables at large distances in loop models is determined by two ingredients: the loop fugacity n and the underlying symmetry of the loop model. Despite realizing a different loop fugacity, the transfer matrix of both the Hamiltonian and measurement-only circuit are generated by the operators $\mathcal{P}_{lm}$, which are quadratic in Majorana fermions. Thus each Hamiltonian symmetry class has a corresponding symmetry class counterpart in the measurement-only circuit. The loop fugacity then yields a fine structure of universality classes for each symmetry class.

The remainder of this Chapter is organized as follows. We begin in Sec. 7.1 by distinguishing the two symmetry classes which arise in Majorana circuits, defining the notion of *orientability*. In Sec. 7.2 we review the statistical mechanics description of loop models and identify the relevant non-linear sigma models (NLσM) for the symmetry classes. Subsequently in Sec. 7.3 and 7.4 we carry out a detailed characterization of the entanglement phases and critical points which arise in Majorana stabilizer circuits in both symmetry classes.

7.1 Orientability Symmetry

For quadratic Majorana theories, particle-hole (PH) symmetry is always present and we thus distinguish two different symmetry classes based on whether time-reversal symmetry is present or not. In class BDI time-reversal is present, which enables a bipartition of the Majorana lattice into sublattices A and B, such that each operator $\mathcal{P}_{lm}$ acts exactly on one Majorana fermion on sublattice A and on one Majorana fermion on sublattice B. The paradigmatic example of such a model is Kitaev's honeycomb model in two spatial dimensions [186]. In the loop model framework, this symmetry is known as "orientability".

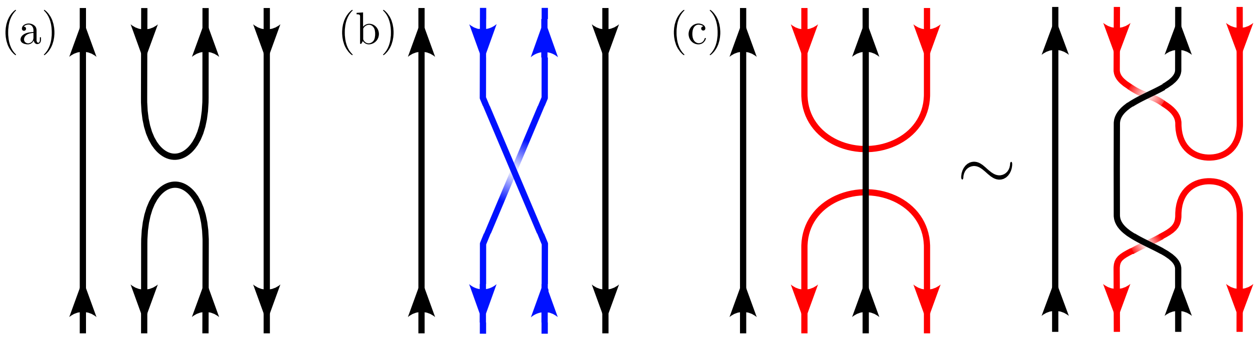

Figure 7.1: **Orientability of worldlines.** Worldlines get assigned a fixed orientation for the even or the odd sublattice. (a) Nearest neighbor measurements preserve this orientation. By contrast, (b) nearest-neighbor crossings and (c) next-nearest neighbor measurements mix the orientations and break the associated symmetry.

It allows to assign a unique orientation to each lattice site, either forward or backward in time, such that each loop carries this orientation through space-time.

In the absence of time-reversal, no bipartition of the lattice can be found, translating to the absence of orientable loop configurations. In the loop framework, the latter is known as non-orientable loops models or completely packed loop models with crossings (CPLC). This is symmetry class D and paradigmatic Hamiltonian models include the Yao-Kivelson model [359], the Kitaev honeycomb model with next-nearest neighbor interactions as well as in the presence of a magnetic field. In the following, we will synonymously apply the language of Hamiltonian symmetry classes and loop model symmetry classes, i.e., we will refer to symmetry class BDI for orientable loop models and symmetry class D for non-orientable ones.

To better illustrate the notion of orientability symmetry, consider the TL algebra resulting from nearest neighbor measurements $\mathcal{P}_{l,l+1}$. Let all odd Majorana worldlines γ_{2l-1} furnish a representation of $U(1)$ while all odd worldlines γ_{2l} furnish the adjoint representation, corresponding to forward and backward evolution in time [63]. Then the generators $\mathcal{P}_{l,l+1}$ are invariant under action of a $U(1)$ symmetry [1]. As shown in Fig. 7.1a, the application of $\mathcal{P}_{l,l+1}$, preserves the local orientations. Extending to the Brauer algebra by including swaps $\mathcal{R}_{l,l+1}$ changes the situation: nearest neighbor swaps exchange even and odd worldlines and thus locally violate orientability, see Fig. 7.1b. By contrast, a next-nearest neighbor swap $\mathcal{R}_{l,l+2}$ respects the alternating orientations and leaves the $U(1)$ symmetry intact [63]. Since next-nearest neighbor measurements $\mathcal{P}_{l,l+2}$ can be expressed as a measurement $\mathcal{P}_{l+1,l+2}$ conjugated by a swap $\mathcal{R}_{l,l+1}$, they also violate orientability, as shown in Fig. 7.1c. More generally, any

[1] A way to define a symmetry operator for orientability is provided in Ref. [58]. Consider the TL algebra with a bipartition between odd and even Majoranas. Define $Q \equiv \sum_i (\mathcal{P}_{2i-1,2L} + \mathcal{P}_{2i,2L-1} - \mathcal{R}_{2i-1,2L-1} - \mathcal{R}_{2i,2L})$. This commutes with all $\mathcal{P}_{2i-1,2j}$ but does not commute with $\mathcal{P}_{2i,2j}$ or $\mathcal{P}_{2i-1,2j-1}$.

measurement $\mathcal{P}_{l,l+m}$ with m odd (even) preserves (violates) the orientation, whereas any swap $\mathcal{R}_{l,l+m}$ with m even (odd) preserves (violates) the orientation.

This framework can be further generalized: a given circuit has a time-reversal invariant representation and it preserves orientability whenever we can find a bipartition into two sublattices A, B such that (i) all measurements are of the form $\mathcal{P} \sim \mathbb{1} + i\gamma_{A_l}\gamma_{B_m}$ with A_l (B_m) being on sublattice A (B), i.e., measure *inter-sublattice parities* and (ii) all swaps are of the form $\mathcal{R} \sim \mathbb{1} - \gamma_{A_l}\gamma_{A_m}$ or $\mathcal{R} \sim \mathbb{1} - \gamma_{B_l}\gamma_{B_m}$, i.e., exchange Majoranas only within a given sublattice.

7.2 Statistical mechanics of loops

A d-dimensional Majorana circuit corresponds to a $d+1$-dimensional loop model in space-time. Each lattice site l with Majorana fermion γ_l at a given time t when measurements or swaps are performed represents a vertex in a regular space-time lattice. When all Majorana fermions are included in at least one measurement $\mathcal{P}_{lm}$ during the circuit evolution, the loop model is fully packed, meaning that every vertex in the lattice has coordination number $z = 4$. Then the space of possible loop configurations is generated by routing loops through each vertex in one of the three ways depicted in Fig. 6.1(a). Such a model is described by a partition function of the form

$$Z = \sum_{\mathcal{C}} W(\mathcal{C}) n^{N(\mathcal{C})} ,$$

where the sum is over all possible loop configurations $\mathcal{C}$. Each term in the sum involves two components: (i) a "local" part $W(\mathcal{C})$ and (ii) a "non-local" part $n^{N(\mathcal{C})}$. The local term $W(\mathcal{C})$ is a product of Boltzmann weights associated to the choice of loop connections at each vertex, giving the probability of performing the unique series of measurements and swaps (or Hamiltonian evolution steps) that yields the loop configuration $\mathcal{C}$. This is the product of local measurement and swap probabilities (or Hamiltonian matrix elements A_{lm}). The non-local term $n^{N(\mathcal{C})}$ accounts for the loop fugacity n associated to each of the $N(\mathcal{C})$ closed loops in configuration $\mathcal{C}$.

As a side remark, we note that the weight $n^{N(\mathcal{C})}$ poses a challenge to Monte Carlo simulations of loop models for any fugacity $n \neq 1$ since it cannot be represented by a local update rule for evolving a single time slice. This singles out stabilizer circuits with $n = 1$ as a particularly attractive example for simulating novel entanglement phases. For larger integer fugacity $n \in \mathbb{Z}_+$, simulation is possible by more complicated Monte-Carlo methods involving the whole space-time lattice [252, 256, 254, 253, 313] or additional ancilla degrees of freedom (see Ch. 9).

Non-linear sigma models

A field theory formulation of the loop model partition function Z is provided by $Z = \int D[Q]\exp(-S[Q])$ with the non-linear sigma model (NLσM) action

$$S[Q] = \frac{1}{2g}\int \mathrm{d}^d x\ \mathrm{Tr}\left[(\nabla Q)^2\right] + (\text{topological terms}) \tag{7.1}$$

Here Q takes values in $\mathbb{CP}^{n-1}$ for symmetry class BDI and $\mathbb{RP}^{n-1}$ for symmetry class D. The field Q is parametrized by a vector z, which is complex for class BDI and real for class D, such that $Q^{\alpha\beta} = z^\alpha \bar{z}^\beta - \delta_{\alpha\beta}$ is a traceless $n \times n$ Hermitian (orthogonal) matrix with normalization condition $z^\dagger z = n$. At short distances, the coupling constant g scales with the microscopic diffusion constant $\mathcal{D}_{\mathrm{mic}} \sim g^{-2}$, which is derived in Sec. 7.4. The relevant case $n = 1$ is obtained by taking $n \to 1^+$ as a replica limit or alternatively by considering a supersymmetric formulation [161, 63, 232]. From the NLσM identified for each symmetry class, we may predict the phases and entanglement transitions which arise in the corresponding Majorana circuits.

7.3 (1+1)-dimensional circuits

We now turn our attention to a family of 1D Majorana circuits based

In (1+1)-dimensions, the NLσM supports the following phases. For orientable class BDI, the system is always localized, except for at the critical points separating different topological phases. By contrast, non-orientable class D may support a metallic state akin to weak anti-localization, known as Goldstone phase. The transition from the localized (short-loop) phase to the Goldstone phase is an order-disorder transition driven by $\mathbb{Z}_2$ vortex proliferation in the $\mathbb{RP}^{n-1}$ theory [161, 255, 104]. Despite taking place in two-dimensions, this transition and the Goldstone phase are not prohibited by the Mermin-Wagner theorem since a non-hermitian representation is required for treating the $n = 1$ loop model [161, 255].

This section is organized as follows. We begin by reviewing paradigmatic loop models (and corresponding Majorana circuits) for the two symmetry classes, highlighting the phases expected from the NLσM and the universality of transitions. Then we introduce a more general family of Majorana circuits which arise from projective measurement of local Pauli operators. Through numerical simulation we demonstrate the the long wavelength behavior of such circuits is wholly captured by the corresponding Majorana loop model and respective NLσM.

Paradigmatic loop model

A representative model encompassing both symmetry classes can be found by considering the loop model introduced in Ref. [255], consisting of nearest-neighbor generators $\mathbb{1}_{l,l+1}$, $e_{l,l+1}$ and $b_{l,l+1}$ of the loop algebra. In terms of a Majorana circuit, this amounts to allowing

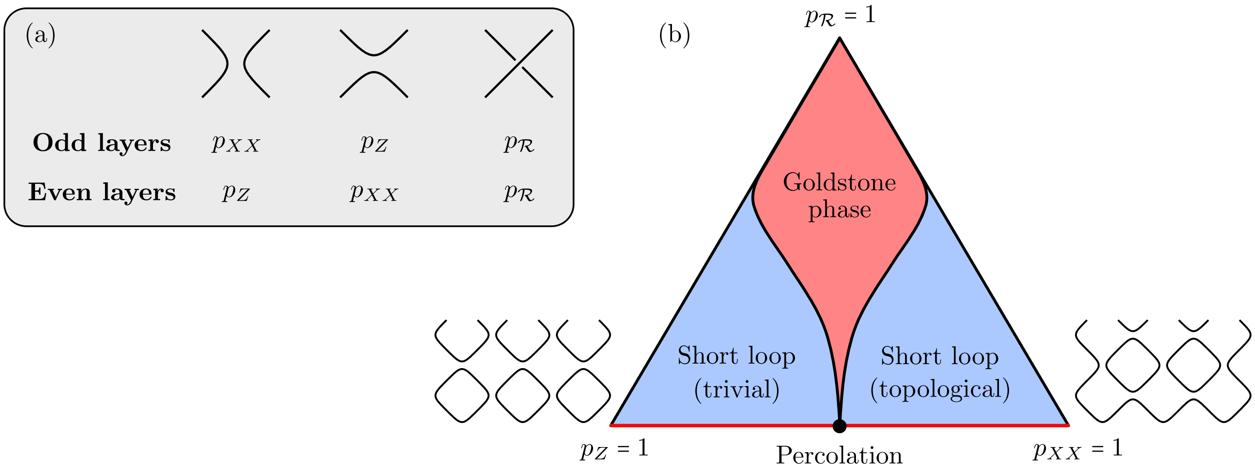

Figure 7.2: **Completely-packed loop model with crossings.** (a) Loops live on a tilted square lattice with the configuration at each vertex occurring with probabilities which alternate between the two sublattices. (b) Phase diagram for the resulting loop model, adapted from Ref. [255]. Along the bottom axis (red line), where $p_\mathcal{R} = 0$, loops are non-crossing and thus orientable. At the self-dual point $p_Z = p_{XX} = 1/2$, there is a percolation critical point (black dot) separating two topologically distinct short-loop phases (shaded blue). Loop configurations at the fixed points $p_Z = 1$ and $p_{XX} = 1$ are depicted to highlight the presence or absence of a single long loop in these phases. Finite crossing probability $p_\mathcal{R}$ opens an extended Goldstone phase (shaded red) between the two short loop phases.

measurements of fermion parity $\mathcal{P}_{l,l+1}$ and Majorana swap gates $\mathcal{R}_{l,l+1}$. Taking the Jordan-Wigner (JW) transformation, these operations correspond to measurements or rotation gates of Pauli operators Z_l ($i\gamma_{2l-1}\gamma_{2l}$) and $X_l X_{l+1}$ ($i\gamma_{2l}\gamma_{2l+1}$) on odd and even layers of the circuit, respectively. The loop model can be viewed as a stochastic sampling from evolution under the transfer matrix,

$$\begin{aligned} T &= T_1 T_3 \dots T_{L-1} T_2 T_4 \dots T_L, \\ T_{2l-1} &= (1 - p_Z - p_\mathcal{R})\mathbb{1}_{2l-1,2l} + p_Z e_{2l-1,2l} + p_\mathcal{R} b_{2l-1,2l} \\ T_{2l} &= (1 - p_{XX} - p_\mathcal{R})\mathbb{1}_{2l,2l+1} + p_{XX} e_{2l,2l+1} + p_\mathcal{R} b_{2l,2l+1} \end{aligned}, \tag{7.2}$$

where $p_\mathcal{R}$, p_Z, and p_{XX} are the probabilities of swaps, Z_l measurements, and $X_l X_{l+1}$ measurements, respectively. Fixing $p_{XX} = 1 - p_\mathcal{R} - p_Z$ enforces a symmetry under $\pi/2$ rotation, which exchanges the two sublattices. These operator probabilities and the resulting phase diagram are depicted in Fig. 7.2.

In the absence of swaps ($p_\mathcal{R} = 0$), we have an exactly solvable orientable loop model which maps to the 1-state Potts model [231, 354]. The loop model arising here has been studied in the quantum circuit context previously as a *projective Ising model* [294, 202, 304] or a measurement-only version of the *repetition code* [215, 251]. Varying the probability of applying the generators on odd or even sublattices drives a transition between two topologically inequivalent short-loop phases, with the transition mapping exactly to critical 2D bond percolation. The short-loop phases correspond to dimerized ground states in the Potts model given by a configuration of short loops over even or odd bonds (see Fig. 7.2b). The latter is equivalent to a stationary state in the circuit with dimerized Majorana parities that features area law entanglement and zero (one) pairs of Majorana edge states for $p_Z > p_{XX}$ ($p_Z < p_{XX}$). At the transition, the loop length distribution exhibits algebraic scaling $\ell^2 P(\ell) = \sqrt{3}/\pi$ [64, 162] and entanglement entropy in the circuit grows logarithmically $S_L \sim \frac{\tilde{c}}{3}\log(L)$ with $\tilde{c} = \frac{3\sqrt{3}\log(2)}{2\pi}$.

Restoring swaps ($p_{\mathcal{R}} \neq 0$), loops are free to cross over one another, yielding the so-called completely-packed loop model with crossings (CPLC). In this model, the the percolation critical point broadens into an extensive Goldstone phase separating the two short loop phases (see Fig. 7.2b). Both the critical point at the boundary of the Goldstone phase as well as the phase itself display universal scaling behavior distinct from percolation [255]. The correlation length exponent here is found to be much larger $\nu \approx 2.75$ in comparison to the percolation exponent $\nu = 4/3$. Within the Goldstone phase, loop correlation functions attain logarithmic corrections. For example, the boundary loop length distribution takes on a scaling form $P(\ell) = \ell^{-2}\log(\ell)/(2\pi^2)$, in contrast to the $P(\ell) \propto \ell^{-2}$ scaling at a critical point. Circuits realizing this Goldstone phase therefore display a peculiar and universal logarithmic correction to entanglement, purification and bulk correlation functions [255, 224, 104].

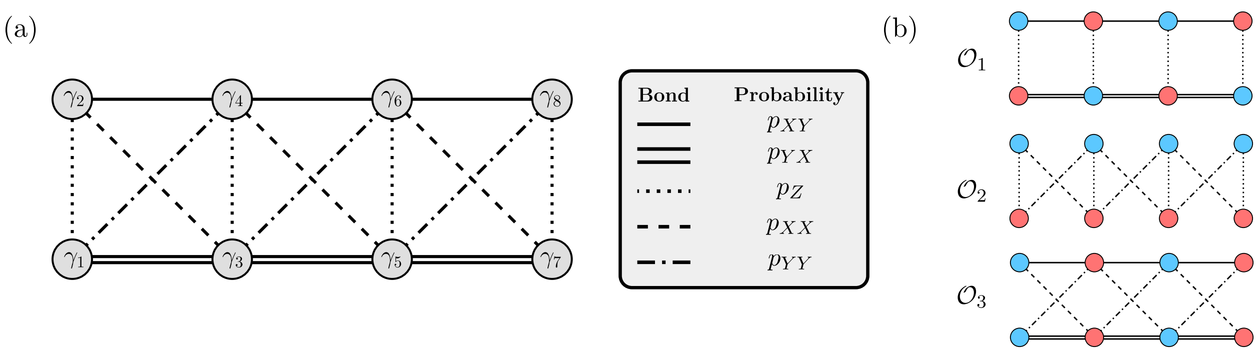

Figure 7.3: **Lattice representation of a Majorana circuit.** (a) Each allowed two-fermion parity check is represented by a bond on the lattice. The measurement probability for the Pauli operator corresponding to a bond are shown in the accompanying table. (b) Orientable subsets $\mathcal{O}_{1,2,3}$ correspond to different bipartitions of the lattice.

Local Pauli Circuits

Let us now consider a broader family of monitored quantum circuits, where we will demonstrate that the orientability symmetry and paradigmatic models just introduced capture the entanglement phases and transitions. We will restrict our attention to circuits constructed from measurements of operators which act on single or nearest-neighbor pairs of qubits. There are exactly five such types of Pauli operators that are Majorana bilinears: $\mathcal{O} = \{Z_l, X_lX_{l+1}, Y_lY_{l+1}, X_lY_{l+1}, Y_lX_{l+1}\}$. It is convenient to represent the corresponding Majorana circuit as a weighted graph, see Fig. 7.3a. Each vertex γ_l of the graph corresponds to a Majorana fermion, and each bond $\hat{O} = i\gamma_l\gamma_m$ specifies a parity-check, measured with probability p_O. Edges which share a vertex correspond to anti-commuting measurements, and thus the typical degree of each vertex is a measure of frustration amongst the allowed measurements. For the set of Paulis $\mathcal{O}$ given above, this graph has the structure of a cross-linked two-leg ladder, shown in Fig. 7.3a. We consider a translationally invariant circuit such that any two identical bonds are measured with the same probability.

In each temporal "layer" of the circuit we employ a *diluted* brickwall structure. For each brick we either perform a measurement with probability p or apply the identity with probability $1-p$. If a measurement is performed, the corresponding Pauli operator $\hat{O}$ is chosen with probability p_O. Throughout this paper we take $p = L^{-1}$ such that a unit timestep $\Delta t = 1$ in the circuit corresponds to L randomly selected measurements at randomly selected positions. When discussing the transfer matrix for a circuit, we implicitly refer to the corresponding brickwall circuit with $p = 1$, which should not affect the universal properties of the circuit [2]. Throughout this section we will use the mutual information $I_2(A, B)$ between subsystems of size $|A| = |B| = L/8$ separated by distance $L/8$.

Orientable Gaussian Circuits

From the set of allowed Pauli operators, one can form three translationally invariant and orientable subsets:

$$\begin{aligned}
\mathcal{O}_1 &= \{Z_l, X_lY_{l+1}, Y_lX_{l+1}\},\\
\mathcal{O}_2 &= \{Z_l, X_lX_{l+1}, Y_lY_{l+1}\},\\
\mathcal{O}_3 &= \{X_lY_{l+1}, Y_lX_{l+1}, X_lX_{l+1}, Y_lY_{l+1}\}.
\end{aligned}$$

The corresponding bipartite Majorana graphs are shown in Fig. 7.3b. It is convenient to define two global unitary transformations $U_Z \equiv \exp\left(i\frac{\pi}{4}\sum_l Z_l\right)$, $U_{Z,\text{odd}} \equiv \exp\left(i\frac{\pi}{4}\sum_l Z_{2l-1}\right)$, consisting of a $\frac{\pi}{2}$-rotation of each or each odd Pauli-Z (i.e. a product of the $\mathcal{R}_{2l-1,2l}$ operators). Application of $U_{Z,\text{odd}}$ maps $\mathcal{O}_1 \leftrightarrow \mathcal{O}_2$, making the two circuits identical upon parity sign flips, and it leaves $\mathcal{O}_3$ invariant. Application of U_Z leaves all three subsets invariant.

Each orientable subset $\mathcal{O}_{1,2,3}$ contains at least one further subset of operators whose projectors form a TL algebra. The set of measurements $\{Z_l, X_lX_{l+1}\} = \{i\gamma_{2l-1}\gamma_{2l}, i\gamma_{2l}\gamma_{2l+1}\}$, for instance, corresponds precisely to the paradigmatic orientable loop model discussed previously.

[2] In the non-orientable circuit, i.e., the CPLC, the identity operation is required in order to realize a robust Goldstone phase. In the orientable case, where we apply transfer matrix methods, no such requirement is present.

Applying $U_{Z,\mathrm{odd}}$, U_Z or their product to $\{Z_l, X_l X_{l+1}\}$ yields three further sets of measurements that realize the same TL algebra and thus the same universal behavior. Since both U_Z and $U_{Z,\mathrm{odd}}$ correspond to constant-depth local unitary circuits, the topology of the two area-law states is preserved — local swaps transform the dimerization pattern but do not add or remove edge modes.

Two further *independent* TL algebras $\{d_l = \mathcal{P}_{2l-1,2l+1}\}, \{f_l = \mathcal{P}_{2l,2l+2}\}$ are realized by the sets $\{Y_l X_{l+1}\} = \{i\gamma_{2l-1}\gamma_{2l+1}\}$ and $\{X_l Y_{l+1}\} = \{i\gamma_{2l}\gamma_{2l+2}\}$. Application of U_Z exchanges $\{d_l\} \leftrightarrow \{f_l\}$, while under $U_{Z,\mathrm{odd}}$, $\{Y_l X_{l+1}\} \leftrightarrow \{X_{2l-1}X_{2l}, Y_{2l}Y_{2l+1}\}$ and $\{X_l Y_{l+1}\} \leftrightarrow \{Y_{2l-1}Y_{2l}, X_{2l}X_{2l+1}\}$. Together, the two sets realize two *independent* 1-state Potts models. While in principle the parameters for these Potts models can be tuned independently, translational invariance of the measurement probabilities yields an additional constraint. For the set $\{Y_l X_{l+1}, X_l Y_{l+1}\}$, translational invariance places both Potts models exactly at the critical point [3] but with distinct timescales fixed by p_{XY} and p_{YX}. In contrast, for the set $\{X_l X_{l+1}, Y_l Y_{l+1}\}$ both Potts models are identical but can be tuned through different phases.

Apparent measurement-altered criticality

Once we extend the measurements to include any full subset $\mathcal{O}_{1,2,3}$, the circuit remains orientable but is no longer described by uncoupled TL algebras. Instead, the Potts models are coupled by a relevant, Gaussian operator. To see this, consider the circuit consisting of measurements of the operators in the orientable set $\mathcal{O}_1$. Measuring operators $\{x_l, Y_{l+1}, Y_l X_{l+1}\}$ yields two independent critical 1-state Potts models, which are then coupled by measurements of $\{Z_l\}$. This Gaussian term is relevant and introduces a time- and length scale, pushing the circuit into an area law phase, as seen in Fig. 7.4a.

Despite interchain coupling p_Z driving the system into an area-law phase, the correlation length may remain exponentially large when there is strong anisotropy between the measurement probabilities p_{XY} and p_{YX}. In other words, when there is a significant difference in the characteristic timescales of the two critical Potts models which are to be coupled. This yields an intriguing dynamical regime: A circuit of finite size or depth displays long-range correlations and apparent critical behavior, up to exponentially large distances, which is tunable by $\{Z_l\}$-measurements – a general feature when Potts models are weakly coupled by a relevant operator.

Let us define $q = \min\{p_{YX}, p_{YX}\}/(p_{XY} + p_{YX})$, which measures the anisotropy between the two Potts models. At strong anisotropy and weak coupling, i.e., $q, p_Z \ll 1$, the typical timescale on which each of the two Potts models evolves is $\approx q^{-1}, (1-q)^{-1}$. Weak coupling between the two models then provides an additional channel for the *slow* Potts model to spread correlations via the *fast* one. Consider for instance the case $p_{YX} \ll p_{XY}$ such that odd Majoranas $\{\gamma_{2l-1}\}$ evolve much faster than even ones $\{\gamma_{2l}\}$. In order for a pair $\gamma_{2l}\gamma_{2l+2m}$ on the slow chain to become entangled, a loop endpoint must travel m sites. This can be accomplished either by waiting $\geq q^{-m}$ layers for rare, even-mode measurements or by taking

[3] This can be made more apparent by a unitary transformation $\prod_l e^{-i\pi X_{2l-1}X_{2l}/4}$: it maps the circuit to a variant of the cluster-model [204], whereas here XZX and Z are measured with equal probabilities.

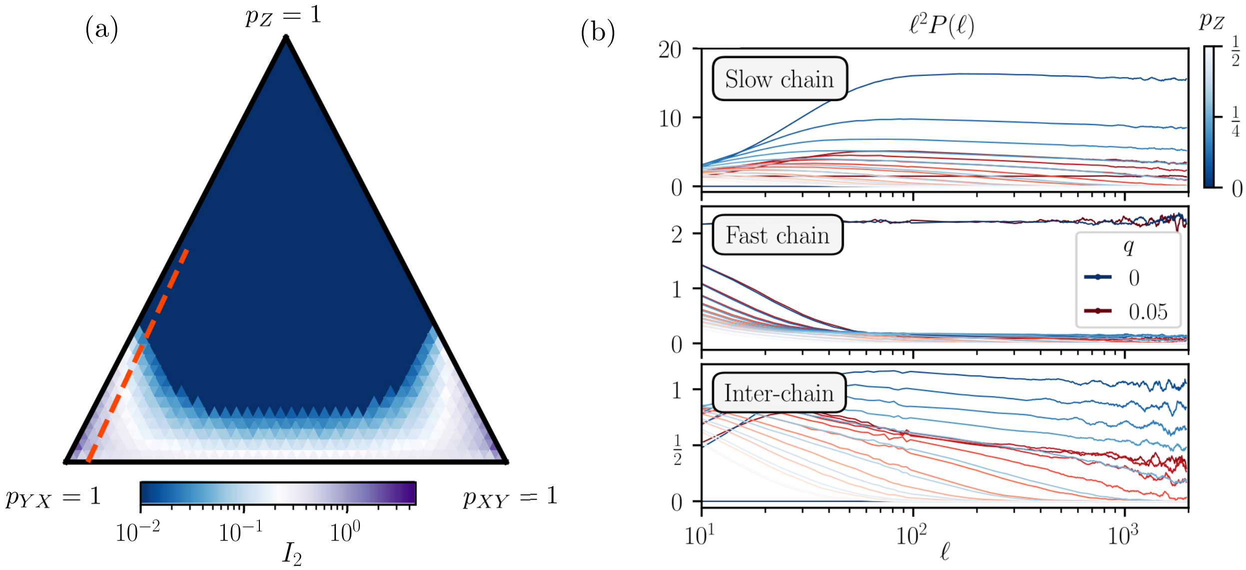

Figure 7.4: **Orientable Gaussian Majorana circuit.** Results for numerical simulation of the orientable circuit with measurements of operators $\mathcal{O}_1$ with $p_X + p_{XY} + p_{YX} = 1$. (a) Phase diagram showing the steady-state mutual information I_2 computed at system size $L = 1024$. For $p_Z > 0$ the circuit is in an area law state, which is highlighted by the rapid vanishing of entanglement on a logarithmic scale. At large anisotropy ($|p_{XY} - p_{YZ}| \approx 1$), rare Z-measurements induce a peculiar state with exponentially large correlation length, i.e., a strongly enhanced mutual information, and tunable correlations between the two legs of the ladder. The red dashed line marks anisotropy parameter $q = 0.05$. (b) Length distributions for fermionic loops restricted to either chain or spanning between the two chains. The slow and fast chains see a strong enhancement and suppression, respectively, of long loop probability at finite coupling p_Z. At large ℓ, $\ell^2 P(\ell)$ approaches a constant when $q = 0$ (blue) and decays very slowly at $q = 0.05$ (red) in the slow chain, corresponding to approximately critical entanglement induced via the coupling. For weak coupling, the fast chain also exhibits almost constant $\ell^2 P(\ell)$, indicating that criticality was modified but not destroyed. The inter-chain loop length distribution shows that finite entanglement is shared between the chains at long distances.

the fast-lane, harnessing frequent odd-mode measurements to travel the same distance in $\geq (1-q))^{-m} p_Z^{-2}$ layers. At long distances $m \gtrsim 2\log(p_Z)\log(q/(1-q))$, the latter process dominates. Correlations in the slow chain are then significantly enhanced by the weak coupling. Hence, the fast (slow) Potts model acts as bath for the slow (fast) one, enhancing (reducing) its tendency to form long loops $\ell \gg 1$. A similar scenario has been observed in other monitored quantum systems, in particular when coupling two critical Ising chains by measurements [249].

The modification of the length distribution $P(\ell)$ for loops within and between the two Majorana chains is seen in Fig. 7.4b. Both intra-chain distributions converge to an approximate power-law $\ell^2 P(\ell) \to \alpha_\ell$, whereas α_ℓ decays very slowly with ℓ on a logarithmic scale. This reflects the exponentially large correlation length ξ, such that for loop lengths $\xi > \ell \gg 1$ a power-law behavior, reminiscent of a critical state, is observed. As a consequence, each individual chain displays a logarithmic growth of the entanglement entropy at finite system size. For the slow (fast) chain, the magnitude of the probability density is enhanced (reduced) by roughly one order of magnitude. Long loops are almost exclusively accumulated in the slow chain and, to a lesser extent, between the chains. From the asymptotic value $\lim_{\xi > \ell \gg 1} \ell^2 P(\ell) = \frac{\tilde{c}}{3}$, we can extract the coefficient $\tilde{c}$ for the logarithmic growth of the intra-chain entanglement entropy $S_{L/2} = \frac{\tilde{c}}{3} \log(L)$. This value is no longer universal. Instead it can be tuned by adjusting the anisotropy and coupling strength via the measurement probabilities. Since the correlation length ξ diverges for $p_Z \to 0$, this provides a knob to control both the amount of long-range correlated loops in each individual chain as well as the length scale up to which the apparent critical behavior can be observed.

We note that similar scenarios have emerged in related, orientable loop models; earlier works on coupled network models for the spin quantum Hall effect have shown that coupling two critical 1-state Potts models via a Gaussian operator immediately opens a gap, leading to a finite but large correlation length [34, 69]. Such a model is akin to the circuit which arises if instead we take orientable set $\mathcal{O}_2$. Here, the individual chains can be tuned away from criticality. The phase diagram would then consist of two lines of critical percolation, meeting at the decoupled point $p_{XX} = p_{YY} = 1/2$. Another related scenario arises at the orientable boundary of the CPLC phase diagram studied in Ref. [255], which gives rise to a coupled Potts model interpretation and a the correlation length that grows exponentially large with the tuning parameter.

Non-Orientable Gaussian Circuits

Once the set of measured Gaussian operators no longer admits a bipartition of the Majorana graph, e.g., the union of $\mathcal{O}_{1,2,3}$, the circuit and corresponding loop model are no longer orientable. The paradigmatic non-orientable loop model is the completely-packed loop model with crossings (CPLC) discussed previously. Here we confirm that non-orientable Gaussian circuits indeed display the universal behavior of CPLC by examining bulk and boundary correlation functions for the following setup.

Consider a circuit wherein one measures the operators $\{XY, YX\}$ with equal probability $p_{XY} = p_{YX} = \frac{1}{4}$ and add measurements of $\{Z, XX, YY\}$ such that $p_Z + p_{XX} + p_{YY} = \frac{1}{2}$. The circuit is symmetric for $p_{XX} \leftrightarrow p_{YY}$, i.e., under the global unitary U_Z. The two limits $p_Z = 0, \frac{1}{2}$ are both orientable and correspond to two topologically distinct area law phases. As shown in Fig. 7.5, the area law phases are separated by an extended phase with increased mutual information and entanglement. By examining a cut along the symmetric point $p_{XX} = p_{YY} = \frac{1}{4}(1 - 2p_Z) \equiv p$ (white dashed line in Fig. 7.5), we show that the entangled phase exhibits all key characteristics of the CPLC Goldstone phase.

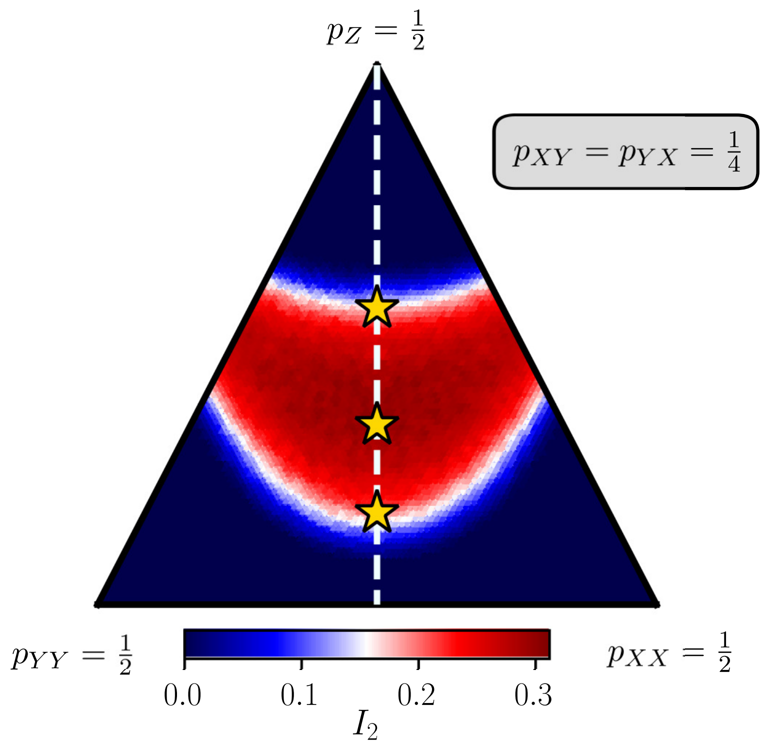

Figure 7.5: **Non-orientable Gaussian circuit phase diagram.** Phase diagram of a non-orientable circuit in the $p_{XX} + p_{YY} + p_Z = \frac{1}{2}$ plane at fixed $p_{XY} = p_{YX} = \frac{1}{4}$, given by the two-interval mutual information I_2 for system size $L = 4096$. The extended phase with finite I_2 is the Goldstone phase. The white dashed line gives the $p_{XX} = p_{YY}$ cut used in Fig. 7.6. The marked points give exemplary points which are either on the critical line or deep within the Goldstone phase.

Correlation length critical exponent: Two critical points, $p_{c,1} = 0.12$ and $p_{c,2} = 0.21$, separate the Goldstone phase from the area law phases. At both points, a finite-size scaling collapse of the mutual information I_2 (Fig. 7.6a) confirms the CPLC exponent $\nu = 2.75$ [255].

Loop length distribution: Both critical points feature a power law scaling of the loop length distribution $P(\ell)$. It approaches a constant $\ell^2 P(\ell) \to \alpha$ with $\alpha \approx 0.64$ in Fig. 7.6b, which is consistent with the value from CPLC: $\alpha = \frac{2.035}{\pi} \approx 0.648$ arising from the renormalized spin stiffness [255, 304]. In the Goldstone phase, the distribution acquires the characteristic logarithmic correction $\ell^2 P(\ell) \sim \beta \log(\ell)$, with $\beta \approx 0.0565$ being consistent with the CPLC value $\frac{1}{2\pi^2} \approx 0.0507$ [255, 304].

Entanglement entropy: We compute the steady-state entanglement entropy $S_A(L)$ of a contiguous subsystem of $|A|$ qubits in a system of size L. For both the critical points and the

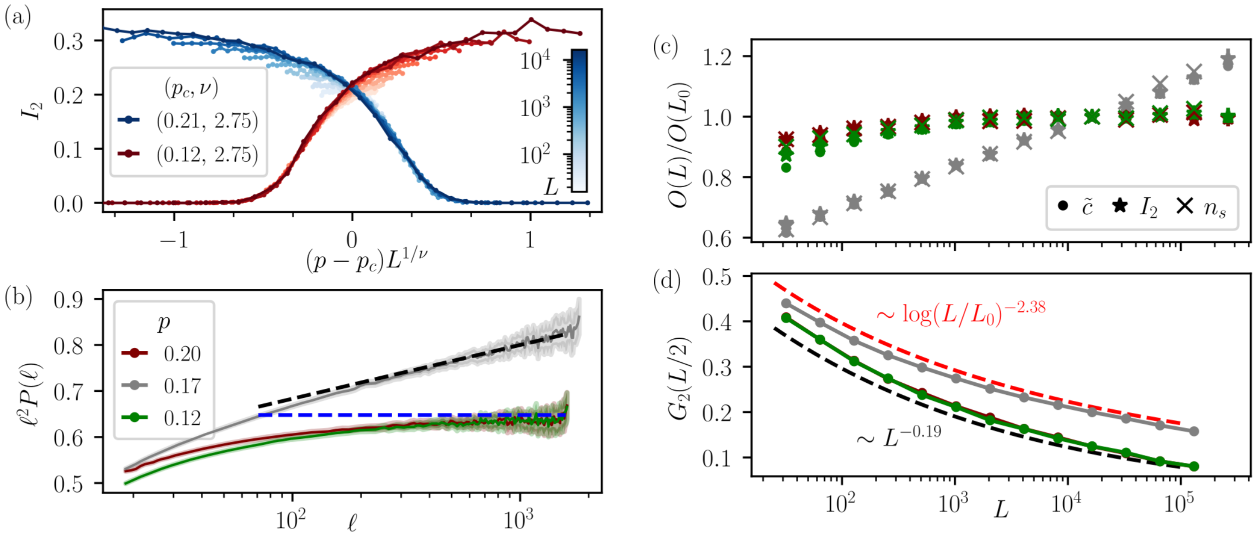

Figure 7.6: **Universality in a non-orientable Gaussian circuit.** Data are taken along the line-cut in Fig. 7.5 with $p_{XY} = p_{YX} = \frac{1}{4}$ and $p \equiv p_{XX} = p_{YY} = \frac{1}{4}(1 - 2p_Z)$ in the steady state $T = 8L$ for system sizes up to $L = 2^{17}$. (a) Scaling collapse of the mutual information I_2 identifies the critical points $p_{c,1} = 0.12$, $p_{c,2} = 0.21$ and a joint critical exponent $\nu \approx 2.75$. (b) Loop length distribution $P(\ell)$ normalized by ℓ^2 to highlight the asymptotic behavior. In the Goldstone phase (grey), CPLC predicts a logarithmic correction $\ell^2 P(\ell) = \frac{1}{2\pi^2}\log(\ell)$ (dashed black line). By contrast, at the critical points $p = p_{c,1/2}$, (maroon and green), CPLC predicts a conventional critical scaling $\ell^2 P(\ell) \approx 2.035/\pi$ [255] (dashed blue line). (c) System-size dependence of the log-law coefficient $\tilde{c}$ (circles), mutual information I_2 (stars), and spanning number n_s at circuit depth $T = L$ (crosses), normalized against the value at $L_0 = 2^{14}$. In the Goldstone phase (gray) we observe logarithmic corrections, $O(L) \propto \log(L)$, whereas at the transition $p = p_{c,1/2}$ all three quantities approach a system-size independent value. (d) The scaling of the two-leg watermelon correlator $G_2(L/2)$ is consistent with CPLC [255]. At the transition, there is power-law decay $G_2(L/2) \sim L^{-2x_2}$ with $x_2 \approx 0.096$ (dashed black line), whereas in the Goldstone phase correlations decay slower than algebraic, $G_2(L/2) \sim \log(L/L_0)^{-\alpha_2}$ with $\alpha_2 \approx 2.38 \pm 0.2$.

entangled phase, we make the ansatz $S_A(L) = \frac{\tilde{c}(L)}{3}\log_2\left[\frac{L}{\pi}\sin\left(\frac{\pi|A|}{L}\right)\right] + \beta$. The critical points $p_{c,1/2}$ display an expected logarithmic scaling, $\tilde{c}(L), I_2(L) \sim$ const, shown in Fig. 7.6c. In the Goldstone phase, the logarithmic correction to the loop distribution leads to an enhanced entanglement with $\tilde{c}, I_2 \propto \log(L)$.

The precise form of the entanglement and mutual information follow from the loop length distribution $P(\ell)$. At the critical points, $P(\ell) = \alpha\ell^{-2}$ yields $I_2 = \alpha\log(4/3)$ and $S_A = \alpha\log(|A|) + \text{const}$. In contrast, the distribution $P(\ell) = \beta\log(\ell/\ell_0)\ell^{-2}$ for cut-off length-scale ℓ_0 yields $I_2 = \beta\log(4/3)\log(|A|/\ell_0) + \text{const}$ (we took $|A| = L/8$) and $S_A = \frac{1}{2}\beta\left[\log(|A|\right]^2 +$

$\beta\log(|A|)(1-\log(\ell_0))+\text{const}$. For universal prefactor $\beta=\frac{1}{2\pi^2}$ from CPLC, we expect $I_2\sim\frac{\log(4/3)}{2\pi^2}\log(L)\approx 0.0146\log(L)$ and $\tilde{c}\sim\frac{3\log(2)}{2\pi^2}\log(L)\approx 0.105\log(L)$. Indeed the data at $p=\frac{1}{6}$ exhibits a logarithmic growth of I_2 ($\tilde{c}$) with prefactor 0.0194 (0.0974), both comparable to the universal CPLC values.

Dynamical purification: A further signature of the Goldstone phase is logarithmic corrections in the mutual information between the two temporal boundaries, i.e., in the spanning number n_s [255]. At a conventional critical point with dynamical critical exponent $z=1$ and for fixed circuit aspect ratio $T=L$, n_s is independent of L. This is confirmed at the critical points $p_{c,1/2}$ and shown in Fig. 7.6c. In the Goldstone phase, however, a logarithmic correction $n_s\propto\log(L)$ appears. This yields logarithmic corrections to the dynamical purification in the circuit when starting from a mixed initial state [224, 104]. As a result, there is an anomalous slowing of the purification. We find a prefactor of the logarithmic correction of 0.19, whereas $\frac{1}{2\pi}\approx 0.159$ is expected from the renormalized spin-stiffness in CPLC [255].

Bulk correlations: Finally, we examine correlations in the spacetime bulk of the circuit, which are expressed via the two-leg watermelon correlator $G_2(L/2)$. At the critical points $p_{c,1/2}$ in the circuit, $G_2(L/2)$ shows slow power-law decay as L^{-2x_2} with exponent $x_2=0.095$ consistent with the behavior in loop models with crossings [255], see Fig. 7.6d. In the Goldstone phase, these correlations fall off even slower, decaying as $G_2(L/2)\propto\log(L/L_0)^{-\alpha_2}$ with a fitted exponent $\alpha_2=2.38\pm0.2$. Previous work found $\alpha_2\approx1.9$ [255] and the slow decay limits the accuracy of the estimate.

Summary

By studying a family of (1+1)-dimensional measurement-only Majorana circuits consisting of local Pauli measurements, we have identified entanglement phases and the universality of entanglement transitions supported by the circuits. We showed that these are accurately captured by the predictions from the NLσM and the paradigmatic loop models for the two symmetry classes. In the orientable case, we observe topologically distinct area-law phases separated by an entanglement transition in the percolation universality class. By careful construction we further highlight a setup where relevant coupling between Majorana chains leads to a scenario akin to weak-localization, with large but finite correlation length. For non-orientable circuits, we demonstrated the emergence of an extended Goldstone phase and distinct universality of entanglement transitions consistent with CPLC, even for circuits which do not explicitly contain swap operations.

7.4 (2+1)-dimensional circuits

We now turn our attention to Majorana circuits in $(2+1)$-dimensions. Whereas in $(1+1)$-dimensions, the two symmetry classes exhibited starkly different phase diagrams, in $(2+1)$-

dimensions the NLσM for both symmetry classes supports the following phases: (i) a long-loop phase with $\mathcal{D} \neq 0$ at the largest distances, yielding long-range entangled Majorana pairs akin to a disordered metal for which the topological terms are irrelevant, (ii) a short-loop phase with a diffusion constant $\mathcal{D}$ flowing to zero under renormalization group transformations, yielding area-law entanglement akin to localized fermions states but with distinct topological properties. At the transition from the metallic to the localized regime, a phase transition occurs with universal scaling behavior depending on the symmetry class and the fugacity n [256, 313].

While for $n = 2$ the metallic phases of the action $S[Q]$ in $(2+1)$ dimensions are known from the Hamiltonian case, the $n = 1$ limit describes loops undergoing Brownian motion with diffusion constant $\mathcal{D} \sim g^{-2}$. For $n = 1$, the intermediate distance behavior, i.e., on distances $\ell \leq L_x L_y$ of the *spatial* volume, of Brownian random walkers is the same for both symmetry classes. This, however, manifestly changes on larger distances $\ell \geq L_x L_y$: here, the Brownian random walkers have non-zero probability of forming space-time volume filling loops which occupy a non-zero fraction of the *space-time* lattice. These macroscopic loops are sensitive to the symmetry class and yield a means to distinguish symmetry classes BDI and D in a measurement-only quantum circuit.

Taking advantage of the Majorana representation of Kitaev's honeycomb model (see Ch. 2), we consider a family of "Kitaev circuits", illustrated in Fig. 7.7. For orientable class BDI, we focus on the measurement-only Kitaev circuit in Fig. 7.7a which consists of direction-dependent parity checks measuring XX, YY, or ZZ along bonds of the corresponding flavor, with probabilities $K_{x,y,z}$. For non-orientable class D, we introduce finite probability J to perform next-nearest neighbor measurements (see Fig.7.7c), corresponding to a three qubit Pauli operator formed by the product of bonds. We begin first with a careful characterization of the long loop phase which arises in both symmetry classes, followed by precise numerical determination of universality at the entanglement transition.

Long loops and the Majorana liquid phase

When the non-commuting measurements introduce a sufficient degree of frustration, the endpoints of the Majorana world lines no longer remain confined to a finite area but start to undergo a random Brownian motion. This generates long loops in the circuit and stabilizes a Majorana liquid or metallic phase with characteristic $L \log L$ entanglement. The entanglement structure in the stationary state is determined by the surface loop distribution in the loop model. In the liquid phase, this distribution does not distinguish between the two symmetry classes BDI and D, which we discuss below. A universal distinction between BDI and D, however, is observable in the bulk loop distribution.

Surface loops and entanglement

The entanglement structure of a Majorana state $\rho(T)$ at time $t = T$ is captured by the probability distribution $P^{x,y}_{\mathrm{surf}}(\ell)$ of open loop arcs along the temporal boundary of the loop

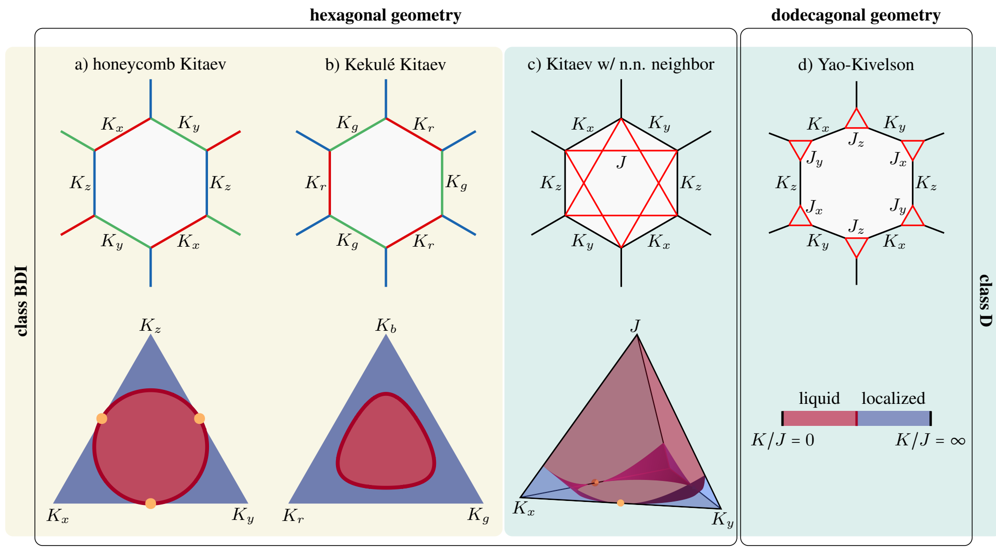

Figure 7.7: **Kitaev circuits and entanglement phase diagrams** The top row shows the family of "Kitaev circuits" considered in this section. They are all made up of bond-directional two-qubit parity checks XX, YY, and ZZ sampled with probabilities K_x, K_y, and K_z in varying circuit geometries. From left to right, this is (a) the conventional honeycomb model, (b) a Kekulé Kitaev model where the parity check assignment of the bonds of the honeycomb lattice forms a Kekulé pattern, (c) the honeycomb model augmented by next-nearest neighbor parity checks (rendering the lattice geometry non-bipartite), and (d) the Yao-Kivelson circuit on the decorated honeycomb model where every vertex is replaced by a triangle (red) with three different types of bond-directional parity checks. The bottom row shows the entanglement phase diagrams as a function of the sampling probabilities of the various XX, YY, and ZZ parity checks. Localized phases with area-law entanglement are shown in blue, while delocalized phases with liquid-like $L\log(L)$-entanglement scaling are marked in red. The dark red contour marks the phase boundary, i.e. the quantum Lifshitz-type localization transition between the two principal phases, whose critical behavior we discuss in the manuscript. The orange circles mark special points at which the theory is captured by percolation (in a dimensional reduction).

model. In the liquid phase, the loop length distribution exhibits power-law scaling

$$P^{\alpha}_{\text{surf}}(\ell) \sim \ell^{-2}\,.$$

For a cylindrical subsystem of length L and circumference L_y, Eq. (6.1) yields an entanglement entropy $S(L, L_y) \sim L_y \log(L)$. Such a logarithmic violation of the area-law of fermions in 2D is often associated with the presence of a Fermi surface [351, 128, 212, 326], but it is also expected for metallic states with non-vanishing conductivity in the presence of weak disorder [59].

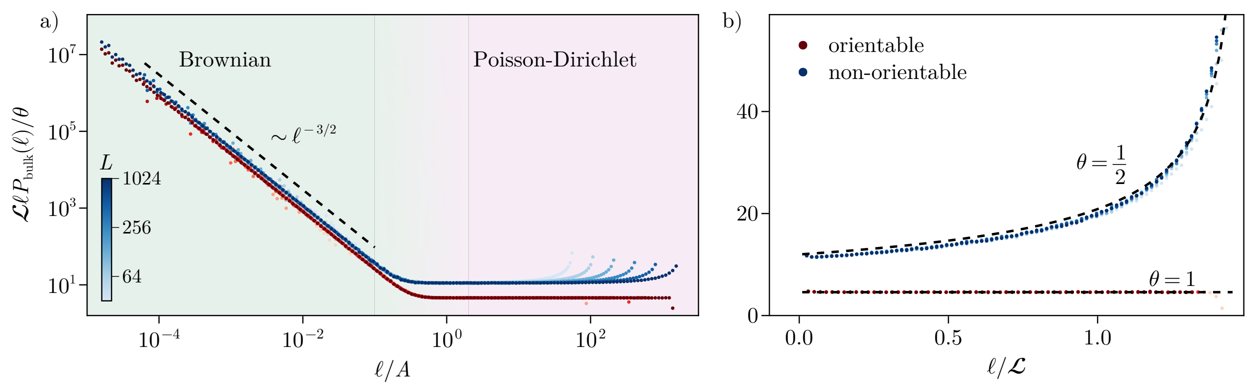

Figure 7.8: **Bulk loop statistics.** Distribution of bulk loop lengths $P_{\mathrm{bulk}}(\ell)$ in the measurement-only Kitaev circuit with PBC in both time and space. The isotropic point of the non-orientable circuit $K_x = K_y = K_z = J = 1/4$ (blue) is contrasted with the orientable circuit $K_x = K_y = K_z = 1/3$ (red). (a) Both the orientable and non-orientable cases exhibit the expected Brownian scaling regime $\ell P_{\mathrm{bulk}}(\ell) \propto \ell^{-3/2}$ for loop lengths $\ell \lesssim L_x L_y$. (b) Breaking orientability leads to a distinct scaling behavior for macroscopic loops $\ell \gg L_x L_y$, following a Poisson-Dirichlet (PD) distribution with universal parameter θ as in Eq. (7.3). We find $\theta = 1$ and $\theta = 1/2$ in the orientable and non-orientable circuits, respectively, with the corresponding fit shown as a black dashed line.

The scaling of $P^{\alpha}_{\mathrm{surf}}(\ell)$ and of the entanglement entropy is a general feature of the liquid phase for both class BDI and D. Let us denote $\tilde{c}_\alpha$ for $\alpha = x, y$ as the coefficient for the entanglement $S = \tilde{c}_\alpha L_\alpha \log(L)$ for a cut along the α-direction. Away from the critical point, this coefficient is generally not universal but rather varies continuously with microscopic details of the model (i.e. the lattice geometry and the bond weights). This may be seen analogously to a smooth deformation of the Fermi surface yielding a continuous modification of the logarithmic entanglement scaling in the Hamiltonian setting, an analogy, which we develop further below.

The effect of orientability here is a rather trivial one. Suppose that we fix the length ℓ_x. In the orientable case, there are fewer allowed Majorana pairings for any ℓ_x, as correlations between sites on the same sublattice must necessarily vanish. As a result, the typical total loop length $\ell = \sqrt{\ell_x^2 + \ell_y^2}$ is longer, and the probability density $P_{\mathrm{surf}}(\ell_x)$ is reduced by a constant factor.

Bulk loops and universal circuit correlations

The two symmetry classes BDI and D are distinguishable by their bulk loop statistics. On short distances $\ell \leq L_x L_y$ and away from the critical point, Brownian motion in three space-time dimensions yields a mean-field decay

$$P_{\text{bulk}}(\ell) \propto \ell^{-\tau}$$

with $\tau = 5/2$ and a fractal dimension $d_f = 3/(\tau - 1) = 2$ for both symmetry classes, depicted in Fig. 7.8(b). However, Brownian walkers in 3D have a non-zero probability of never returning to their starting point, and to form "macroscopic" loops which occupy a non-zero fraction of the space-time volume. The statistics of such extensive loops provide an unambiguous means for distinguishing between the two symmetry classes.

For finite system sizes, macroscopic loops are sensitive to the spatiotemporal boundary conditions. Here, one distinguishes *absorbing* boundary conditions, yielding open Majorana world lines, such as, e.g. a mixed initial state, from *reflecting* boundary conditions in space-time [4]. For the latter, all world lines are closed including at the final and initial time. This is realized by starting with a pure initial state at $t = 0$ and by terminating the circuit at $t = T$ with a fixed set of measurements that closes all world lines. With reflecting boundaries all loops are closed, and macroscopic loops manifest in the distribution $P_{\text{bulk}}(\ell)$ giving rise to a distinct scaling regime at distances $\ell \geq L_x L_y$, shown in Fig. 7.8(b). Here, macroscopic loops follow a Poisson-Dirichlet (PD) distribution [137, 254, 32]

$$\ell \cdot P_{\text{bulk}}(\ell) = \frac{\theta}{\mathcal{L}} \left(1 - \frac{\ell}{f\mathcal{L}}\right)^{\theta - 1}, \quad (\ell \gg L_x L_y) \tag{7.3}$$

where $\mathcal{L}$ is the total number of links in space-time (i.e. the volume). Whereas f is a non-universal quantity, the parameter θ is a *universal* parameter which depends only on the loop fugacity n and the symmetry class. In the most general case, one finds $\theta = n$ for symmetry class BDI, while for symmetry class D, $\theta = n/2$. For the Majorana circuits at hand with fugacity $n = 1$, this leads the normalized bulk loop length distribution to approach a constant

$$\ell \cdot P_{\text{bulk}}(\ell) \sim \mathcal{L}^{-1} \qquad \text{(orientable)} \tag{7.4}$$

for $\ell \to \mathcal{L}$ in class BDI, while class D displays a square-root divergence

$$\ell \cdot P_{\text{bulk}}(\ell) \sim \mathcal{L}^{-1/2}(\mathcal{L} - \ell/f)^{-1/2} \qquad \text{(non-orientable)}\,. \tag{7.5}$$

Such a divergence reflects the tendency for a concentration of probability density in larger macroscopic clusters, due to the greater mobility of loops without the BDI constraint of time-reversal. The results of numerical simulations, shown in Fig. 7.8(b), confirm the PD scaling regime for macroscopic loops, with the parameter θ consistent with loop fugacity $n = 1$.

In order to access the universal part of the PD distribution, i.e., the parameter θ, one faces two challenges: (i) implementing measurements of loop quantities in space-time and on

[4] Strictly speaking, macroscopic loops would emerge also for periodic boundary conditions in time, which are, however, challenging to implement in a circuit.

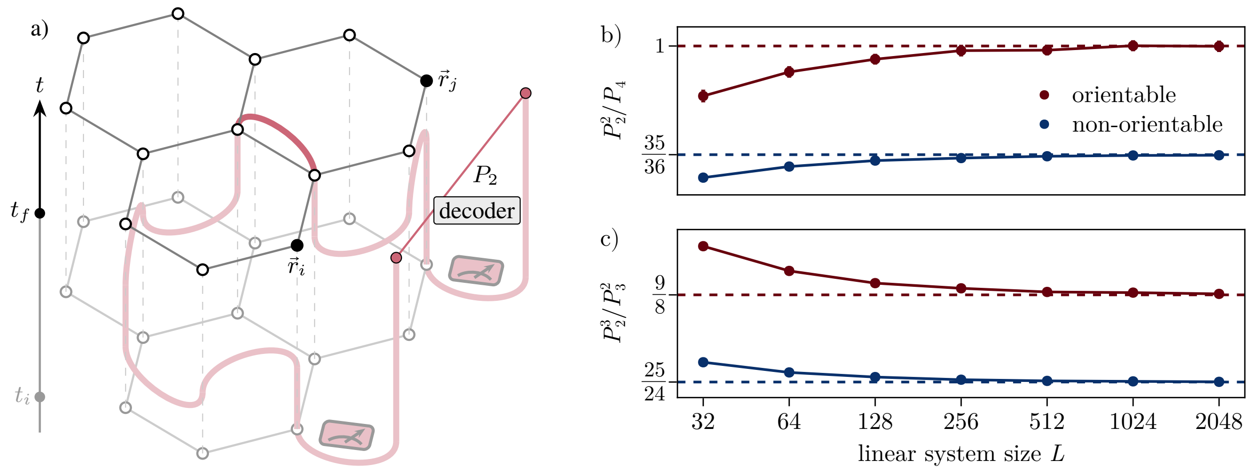

Figure 7.9: **Loop statistics reveal universal ratios of long-distance loop connectivities.** (a) Illustration of an ancilla scheme for probing the statistics of macroscopic loops, shown here for the correlator P_2 that requires two ancilla probes. The two ancillae have a well-defined parity iff they are connected by a long string through the bulk. The definite parity can be probed by a *decoder* taking the Majorana parity measurement outcomes in the bulk as input. This scheme can be generalized to probe P_n as defined in Eq. (7.6), i.e., the probability that n points $\vec{r}_1, \ldots, \vec{r}_n$ in space-time lie along the same loop. The distance $r_{ij} \equiv |\vec{r}_i - \vec{r}_j|$ is taken to be macroscopically large such that non-zero P_n necessarily implies that the points lie along an infinite loop. At initial time t_i, a marked loop is injected into the circuit at each $\vec{r}_i$ by preparing a pair of ancilla Majoranas and then measuring the parity between one ancilla and the corresponding bulk Majorana. In the qubit language, this amounts to measuring the parity between a system qubit and an ancilla qubit. After running the circuit to late times (t_f), all system Majoranas are projected out. Information about P_n is then encoded in the mutual information between different ancillae. The ratios (b) P_2^2/P_4 and (c) P_2^3/P_3^2 in the entangled phase approach universal values (dashed lines) which differ for the two symmetry classes. Data shown here are taken at the isotropic point, but the ratios are universal throughout the entire phase. Data averaged over 100 disorder realizations with 10,000 samples each.

distances $\ell \gg L_x L_y$ much larger than the spatial extent and (ii) eliminating the dependence on the non-universal parameter f in Eq. (7.3). Let us start by solving the latter. Consider m points $\vec{r}_i$ with $i = 1, \ldots, m$ in space-time which are separated by macroscopic distances $|\vec{r}_i - \vec{r}_j| \gtrsim L_x, L_y$. In the thermodynamic limit, if any two points $\vec{r}_i$ and $\vec{r}_j$ are on the same loop, then that loop is macroscopic. The probability that all m points lie along the same loop is [61]

$$P_m \equiv P(\vec{r}_1, \ldots, \vec{r}_m) = f^m \frac{\Gamma(1+\theta)\Gamma(m)}{\Gamma(m+\theta)}. \tag{7.6}$$

Here, Γ is the Γ-function and the non-universal quantity f appears as a prefactor. Thus, f can be eliminated by taking appropriate ratios $P_{m_1}^{k_1}/P_{m_2}^{k_2}$ for $m_1 k_1 = m_2 k_2$, leading to universal quantities which distinguish the two symmetry classes [254].

We propose a way to measure the probabilities P_m directly by generalizing existing ancilla schemes [138, 188]. Since P_2 is simply the large-separation limit $r \to \infty$ of the two-point watermelon correlator $G_2(r)$, it may be measured via the protocol described earlier in Sec. 6.3. For higher-order quantities P_m, we use m ancillae to insert marked loops at all m points in space-time, as depicted in Fig. 7.9. Once again we evolve the circuit to late times and then measure all bulk Majoranas, leaving open loops only terminating on the ancillae. The mutual information between groups of ancillae counts precisely the probability that the space-time points where we measured the bulk and ancilla had been along the same loop, so a quantity like P_3 amounts to requiring $I_2(A,B) = I_2(B,C) = I_2(C,A) = 1$. In practice this can be obtained by comparing the magnitude of $I_2(A,B)$ before and after tracing out ancilla C, where the latter case simply reduces to P_2. Here we consider such a scheme with four points $\vec{r}_i$ at separations on the order of L_y and measure P_2, P_3, and P_4 to obtain the following ratios,

$$\frac{P_2^2}{P_4} = \frac{\Gamma(1+\theta)\Gamma(4+\theta)}{6\Gamma(2+\theta)^2} = \begin{cases} 1, & \theta = 1 \\ \frac{35}{36}, & \theta = \frac{1}{2} \end{cases},$$

$$\frac{P_2^3}{P_3^2} = \frac{\Gamma(1+\theta)\Gamma(3+\theta)^2}{4\Gamma(2+\theta)^3} = \begin{cases} \frac{9}{8}, & \theta = 1 \\ \frac{25}{24}, & \theta = \frac{1}{2} \end{cases}.$$

Importantly, both give values which differ between the two symmetry classes. In Fig. 7.9, we show that the ratios indeed converge toward the universal value as system size is increased. This then offers a practical scheme for distinguishing between the long-loop phases which would otherwise not be possible from the steady-state entanglement.

We stress that this scheme relies on taking appropriate boundary conditions. If we instead implement (open) absorbing boundaries in space-time, any macroscopic loop will be cut into an extensive number of individual *open loops*. Then the loop length distribution matches the first passage time distribution for a random walk in one spatial dimension with absorbing boundaries

$$P_{\text{bulk}}(\ell) \sim P_{\text{FP}}(\ell) \sim \ell^{-5/2} e^{-\alpha\ell}$$

with $\alpha^{-1} \sim L_x L_y$. In this case, the expression in Eq. (7.6) no longer holds and one cannot straightforwardly obtain universal ratios which distinguish the symmetry classes.

Analytical entanglement scaling and phase boundaries from the diffusion picture

Viewing the dynamics in the metallic phase as Majorana world lines undergoing Brownian motion in space-time allows us to establish a direct link between (i) the NLσM in Eq. (7.1), (ii) the entanglement entropy and, (iii) for class BDI, the microscopic measurement probabilities. Note that the latter enables *accurate analytical predictions*, for symmetry class BDI, for the entanglement scaling and the location of the transition line between the metallic and the localized phases for arbitrary geometries.

We start by considering loop endpoints undergoing Brownian motion in space-time with an effective diffusion constant $\mathcal{D}$ at large wavelengths. The entanglement entropy at a fixed time $t = T$ is then determined from open arcs terminating at the temporal boundary. Designating one of the arc endpoints as the "start", we may view the arc as the path of a random walker which starts near and eventually terminates upon an absorbing boundary at $t = T$. Then the total bulk length of the arc is equivalent to the first passage time τ of the random walker [5]. The distribution of first passage times for one absorbing boundary in three dimensions is known to be $P_{\mathrm{FP}}(\tau) \approx \sqrt{\frac{2}{\pi}}\tau^{-3/2}$. During this time, both endpoints undergo Brownian motion in the two-dimensional spatial plane, yielding a distribution for the distances between endpoints $P_{\mathrm{2D}}(r,\tau) \approx \frac{2r}{\mathcal{D}\tau}e^{-r^2/\mathcal{D}\tau}$. Averaging with respect to the time τ, yields the expected distribution of spatial displacements

$$P_{\mathrm{surf}}(r) = \int \mathrm{d}\tau \, P_{\mathrm{FP}}(\tau) P_{\mathrm{2D}}(r,\tau) = \sqrt{2\mathcal{D}}/r^2$$

with $r^2 = \ell_x^2 + \ell_y^2$. The entanglement entropy along a cut depends on the distribution of loop lengths projected along a fixed axis. For isotropic Brownian motion in space, this gives

$$P^x_{\mathrm{surf}}(\ell_x) = 4\int_0^\infty \mathrm{d}\ell_y \, \frac{P_{\mathrm{surf}}(r)}{2\pi r} = \frac{2\sqrt{2\mathcal{D}}}{\pi \ell_x^2}.$$

From this distribution we infer that the logarithmic entanglement scaling has coefficient $\tilde{c}_x = 6\sqrt{2\mathcal{D}}\pi$. Varying the relative measurement probabilities of different bonds will generally introduce some anisotropy to the Brownian motion such that $\mathcal{D}^x \neq \mathcal{D}^y$ and $\tilde{c}_\alpha \propto \sqrt{D^\alpha}$. This scaling of the logarithmic entanglement proportional to the square root of the diffusion constant appears also in monitored fermion systems with unitary dynamics [67, 281], and is seemingly generic for measurement-induced fermion liquid-type phases.

The effective diffusion constant $\mathcal{D}$ emerges at long wavelengths from the renormalization group (RG) flow of the NLσM in Eq. (7.1). The NLσM is a single-parameter theory, initialized with the microscopic short-distance diffusion constant $\mathcal{D}_{\mathrm{mic}}$, which depends on the lattice geometry. The RG flow only depends on the fugacity n, the symmetry class and the dimensionality d. For $n = 1$ and $d = 3$, each symmetry class thus has a one-to-one correspondence $\mathcal{D}_{\mathrm{mic}} \leftrightarrow \mathcal{D}$. For bipartite lattices, i.e., for class BDI, the random walker is always on the same sublattice after two steps and the microscopic diffusion constant is readily inferred from the measurement probabilities. Consider the measurement-only Kitaev circuit, where bonds are measured with probabilities $K_x + K_y + K_z = 1$. The diffusion constants may be estimated by considering the mean-squared displacement of a random walker with jump rates

[5] More precisely, the movement of the loop endpoint along the temporal direction should be viewed as a persistent random walk, where the direction of propagation is reflected whenever the Majorana is involved in a measurement. This yields a mild correction to the timescales, but does not alter the universality.

set by K_α and bonds of unit length. Setting $\mathcal{D}^z_{\text{mic}}$ as the diffusion constant for the direction parallel to the ZZ-bonds and $\mathcal{D}^\perp_{\text{mic}}$ as the diffusion constant perpendicular to it yields

$$\mathcal{D}^z_{\text{mic}} = \frac{9}{8}K_z(K_x + K_y)\,,\ \mathcal{D}^\perp_{\text{mic}} = \frac{1}{6}(2\mathcal{D}^z_{\text{mic}} + 9K_xK_y)\,,$$
$$\mathcal{D}_{\text{mic}} = \frac{1}{2}(\mathcal{D}^z_{\text{mic}} + \mathcal{D}^\perp_{\text{mic}}) = \frac{3}{4}(K_xK_y + K_xK_z + K_yK_z)\,.$$

The total diffusion constant $\mathcal{D}_{\text{mic}}$ is *invariant under continuous rotation* of $K_{x/y/z}$ with respect to the isotropic point – this explains the circular symmetry of both the metallic phase and its phase boundary, as numerically found in Refs. [206, 319, 366].

We emphasize two particular regimes: (i) In the vicinity of the isotropic point $K_\alpha = 1/3$, i.e., deep in the metallic phase, we expect the RG flow corrections to $\mathcal{D}$ to be weak. Thus setting $\mathcal{D} = \mathcal{D}_{\text{mic}}$ proves to be a good approximation in the vicinity of the isotropic point, see Fig. 7.10(a). Since under RG, the diffusion constant will generally flow towards a smaller value, $\mathcal{D}_{\text{mic}}$ at the isotropic point serves as an upper bound for the average entanglement growth in each direction $\mathcal{D} \le 1/4$. (ii) In the vicinity of the critical line marking the transition between the metallic and the localized phase, the renormalization of $\mathcal{D}_{\text{mic}}$ is strong and $\mathcal{D}_{\text{mic}} \gg \mathcal{D}$. Nevertheless, the one-to-one correspondence $\mathcal{D}_{\text{mic}} \leftrightarrow \mathcal{D}$ [6] allows us to extract the position of the critical line for any bipartite geometry. At $K_x = K_y = \frac{1}{2}$ and $K_z = 0$, the location of the critical point is exactly known: the system decouples into disconnected one-dimensional strings each of which displays percolation critical behavior [188]. Using this point as an estimate for the critical value $\mathcal{D}_{\text{mic,c}}$ provides

$$\text{critical diffusion constant: } \mathcal{D}_{\text{mic},c} = \frac{3}{16}. \tag{7.7}$$

For the Kitaev honeycomb lattice, this yields a circular contour in parameter space [see Fig. 7.10(b)] which coincides exceptionally well with numerical estimates for the entanglement transition. To further underpin the strength of the diffusion picture, we provide the numerically obtained phase diagram for the measurement-only Kekulé-Kitaev geometry illustrated in Fig. 7.7(b). This system also belongs to symmetry class BDI but its phase diagram exhibits a different shape of the critical line as displayed in Fig. 7.10(c). Using Eq. (7.7) again provides a rather accurate estimate for its phase boundary based on a calculation of the diffusion constant as

$$\mathcal{D}_{\text{mic}} = \frac{3}{8}\big[K_gK_r(2 - 3K_gK_r) + K_b(K_g + K_r)(2 + K_gK_r) - 3K_b^2(K_g^2 - K_gK_r + K_r^2)\big],$$

where again we have considered the mean-squared displacement of a random walker after two steps along lattice edges, averaging over starting points in the unit cell.

Lastly, let us consider a more rigorous approximation scheme for the entanglement entropy. We note that even deep in the metallic phase, the microscopic diffusion constant $\mathcal{D}_{\text{mic}}$

[6] Neglecting the effect of anisotropy in the microscopic values.

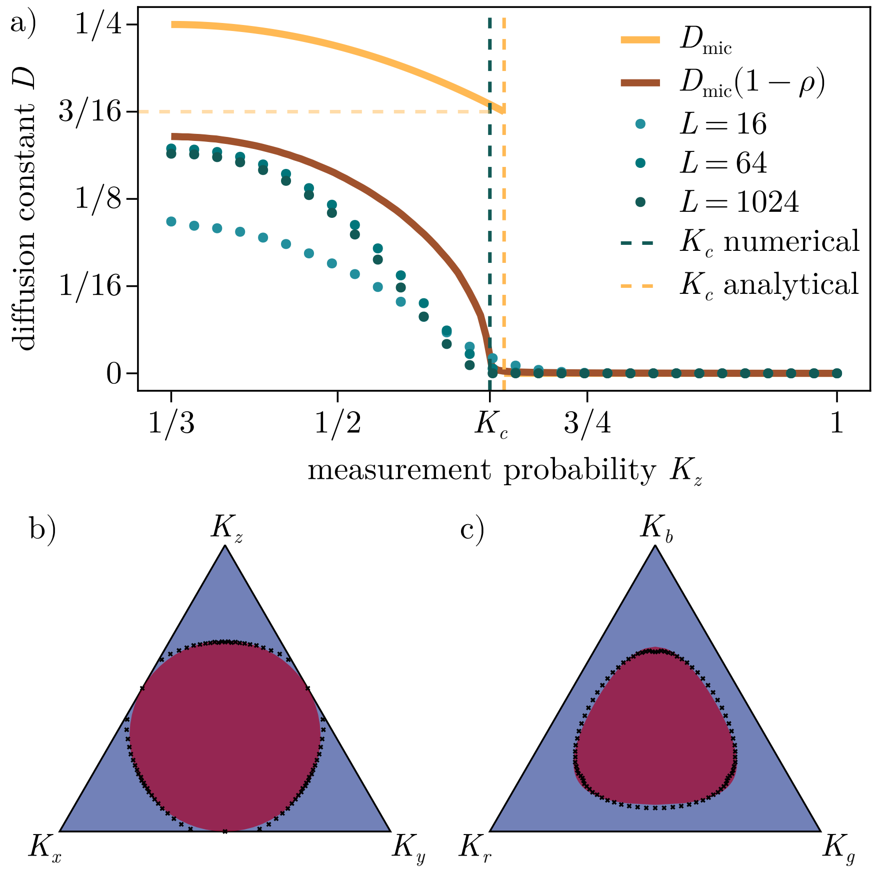

Figure 7.10: **Effective diffusion constant** for the critical phase of the measurement-only Kitaev model. (a) A comparison of the effective diffusion constant $\mathcal{D}$ extracted from the distribution $P_{\rm surf}(\ell)$ (blue) and the microscopic diffusion constant $\mathcal{D}_{\rm mic}$ (orange), computed along the line $K_x = K_y = \frac{1}{2}(1 - K_z)$. At the transition, $\mathcal{D}$ vanishes, while the microscopic $\mathcal{D}_{\rm mic}$ crosses the threshold value $\mathcal{D}_{\rm mic,c} = \frac{3}{16}$. The vertical dashed lines mark the critical measurement probability K_c found by finite-size scaling in Fig. 7.12 (blue) and by $D_{\rm mic}$ (orange). Rescaling by the numerically obtained fraction $1 - \rho$ of volume available to the Brownian walkers brings $\mathcal{D}_{\rm mic}(1 - \rho)$ (brown) and $\mathcal{D}$ closely in line with one another. Phase diagrams for the measurement-only (b) Kitaev and (c) Kekulé-Kitaev models. We show a direct comparison of the phase boundary determined via the microscopic diffusion constant $\mathcal{D}_{\rm mic} = \mathcal{D}_{\rm mic,c}$ (solid colors) and via scaling collapse of the spanning number (black crosses).

is larger than $\mathcal{D}$ determined from the entanglement scaling by a factor of approximately 3/2. This difference reflects the fact that the microscopic calculation treated the loop endpoints as *non-interacting* Brownian walkers. In actuality, due to the Pauli principle, the loops are constrained to not overlap with themselves or one another, corresponding to an effective excluded volume. To account for this, consider the role of a nonzero density ρ of closed loops in the bulk of space-time. These act as obstructions to the Brownian motion of open arc endpoints, suppressing diffusion. At leading order, this may be treated as a uniform probability ρ that at any step the random walker remains in place, sending $\mathcal{D} \to \mathcal{D}(1-\rho)$. The density ρ is hard to extract analytically but easily accessible numerically. We find that the fraction ρ varies continuously from $\rho \approx 1/3$ at the isotropic point to $\rho = 1$ in the area-law phase. In Fig. 7.10(a), we show that the rescaled microscopic diffusion coefficient $\mathcal{D}_{\text{mic}}(1-\rho)$ better matches the fitted $\mathcal{D}$, reproducing the magnitude deep in the metallic phase and going to zero continuously at the transition. Thus, accounting for the excluded volume effect accurately captures the interactions neglected in $\mathcal{D}_{\text{mic}}$. Alternatively we might arrive at the same correction by considering a self-avoiding walk on a lattice with coordination number z and connectivity constant μ. Here the quantity $1-\rho$ corresponds to the ratio μ/z, which falls in the range $\mu/z \in [1.2, 1.5]$ for various 3D lattices [153].

The direct relation between the entanglement scaling, i.e., the prefactor $\tilde{c}$ of the metallic $L\log(L)$ term, and the effective diffusion constant $\mathcal{D}$ at distance L allows us to numerically track the RG flow of $\mathcal{D}$ from its microscopic starting point $\mathcal{D}_{\text{mic}}$ towards its asymptotic value as illustrated in Fig. 7.10(a) for linear system sizes $L = 16, 64, 1024$. This is remarkable, since in $d = 3$ dimensions, the NLσM is no longer perturbatively controlled and the RG flow of $\mathcal{D}$ is not accessible analytically. We emphasize the connection between $\tilde{c}$, the diffusion constant for Brownian motion of loops, and their relation to the logarithmic entanglement scaling found in weakly disordered Fermi liquids. In the ground state of a disordered metal with disorder strength γ, the diffusion constant is related to the Fermi velocity v_F and the disorder by $\mathcal{D} \sim v_F^2/\gamma$, implying $\tilde{c} \sim v_F/\sqrt{\gamma}$. Indeed, such proportionality is expected from calculations of the entanglement entropy from a Fermi surface [351, 128, 212, 326].

Quantum Lifshitz criticality and universal scaling behavior at the entanglement transition

In both symmetry classes, the Majorana liquid and localized (area-law) phases are separated by a critical line exhibiting quantum Lifshitz scaling of the entanglement entropy. At this critical line, the effective diffusion constant vanishes, resulting in an area law for the entanglement entropy. The distribution of Majorana loop lengths, however, is not yet localized but displays universal algebraic scaling behavior that clearly differentiates the two symmetry classes. This unique combination of universal algebraic scaling and the area law leads to the distinctive subleading entanglement scaling characteristic for quantum Lifshitz criticality.

In the Kitaev honeycomb model for symmetry class BDI, the critical line is reached by tuning the probabilities K_α. Quantum Lifshitz scaling is observed, except at the three points where one of the $K_\alpha = 0$, reducing the model to an array of one-dimensional chains. For class D, we set the next-nearest neighbor bond measurement probabilities to $J_x = J_y = J_z = J$ and tune J, K_α through the critical regions [see Fig. 7.7(c)]. For $J > 0$, quantum Lifshitz scaling is generally present.

Quantum Lifshitz entanglement and surface loops

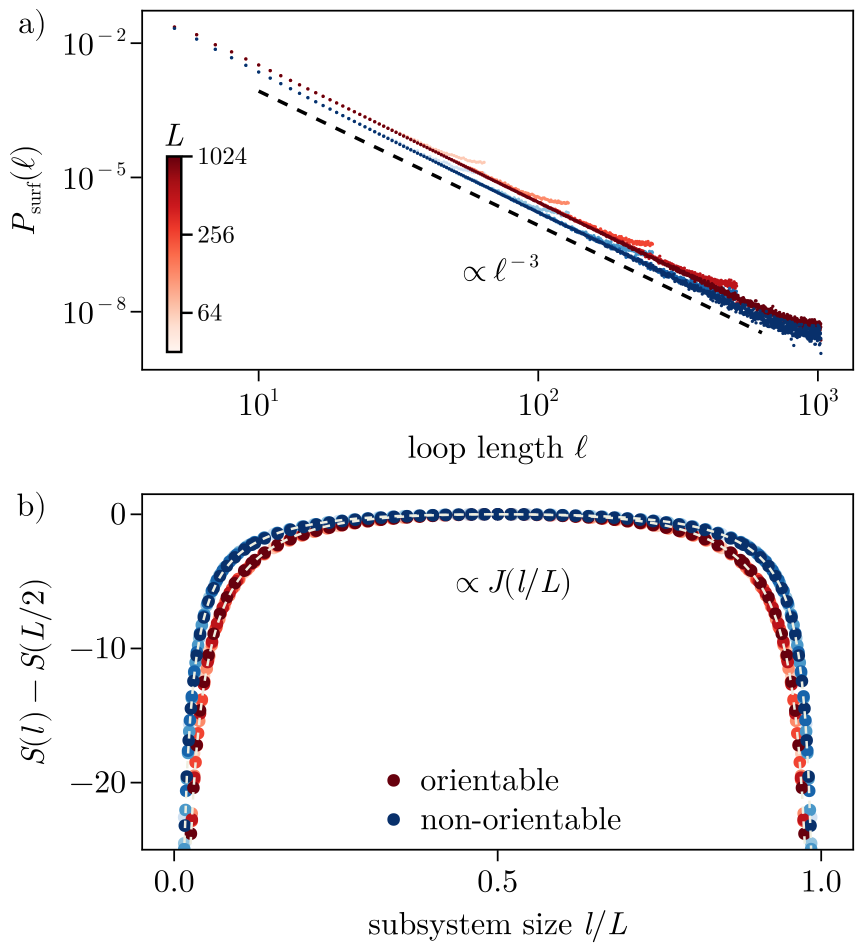

Figure 7.11: **Quantum Lifshitz criticality from surface loops.** (a) Surface loop length distribution at the critical point along the line $K_x = K_y = (1 - K_z)/2$ for the orientable (red) and $K_x = K_y = J = (1-K_z)/3$ for the non-orientable (blue) loop models. The dashed black line reflects an asymptotic scaling $P_{\mathrm{surf}}(\ell) \sim \ell^{-3}$. (b) Data collapse of the subsystem entanglement entropy $S(\ell)$ onto a single curve described by the Lifshitz scaling function $J(l/L)$ of Eq. (7.8). In both panels we show data for linear system sizes $L = 64, 128, 256, 512, 1024$.

The entanglement entropy in the loop framework is computed from Eq. (6.1). At a genuine two-dimensional transition we observe an algebraic decay of surface loop lengths, $P_{\mathrm{surf}}(\ell) \propto \ell^{-\gamma_{\mathrm{surf}}}$. Away from the percolation points with one $K_\alpha = 0$, we find that $\gamma_{\mathrm{surf}} \approx 3$, shown in Fig. 7.11(a). This is faster than in the Majorana liquid phase, where $\gamma_{\mathrm{surf}} = 2$ leads to an $L\log(L)$–growth. As a result, the transition exhibits a subsystem dependence of the entanglement entropy $S(\ell, L) = aL + bJ(\ell/L)$. Here $J(u)$ is the "Lifshitz" scaling function [7]

$$J(u) = \log\left(\frac{\theta_3(i\lambda u)\theta_3(i\lambda(1-u))}{\eta(2iu)\eta(2i(1-u))}\right), \tag{7.8}$$

where θ_3 is the Jacobi theta function, η is the Dedekind eta function, and λ is a fitting parameter [15, 321]. In Fig. 7.11(b) we show the collapse of the entanglement data onto a curve accurately described by this Lifshitz scaling function. For both symmetry classes, we find $\lambda = 3.4 \pm 0.1$ for cuts along either direction of the system.

Although derived initially for a quantum Lifshitz model [15], this torus entanglement scaling has been observed in a variety of $(2+1)$-dimensional CFTs [155, 75]. Notably, the Rényi entropy takes precisely the form of Eq. (7.8) also for quantum dimer models and resonating valence bond (RVB) states [320, 321]. Given the close link between models of dimers, loops, and height fields [325, 197, 291, 5, 15, 107], one may expect that this entanglement scaling ought to extend also to the case of loops with fugacity $n = 1$ (relevant to the quantum circuits at hand). Indeed, higher fugacity loop models have been employed in numerical studies to verify the Lifshitz scaling of entanglement in quantum magnets [155, 170]. Similarly, the bond-length distribution in the antiferromagnetic Heisenberg model on the square lattice exhibits the same scaling exponent as $P_{\mathrm{surf}}(\ell)$ in our circuit model [301]. We note here that quantum Lifshitz scaling is compatible with the simultaneous presence of conformal symmetry and an area law of the entanglement in $(2+1)$ dimensions. It is remarkable that this entanglement scaling, though apparently quite universal, has been reported previously only in the context of *interacting* circuits [366, 205]. For fermion-parity symmetric circuits, the mapping to an interacting dimer model suggests that Lifshitz entanglement scaling is quite generic. More broadly, requiring conformal invariance at the entanglement transition imposes strict constraints such that one might generically expect scaling of the form Eq. (7.8) except at fine-tuned points.

Correlation length exponent ν

To accurately determine the critical point K_c and the correlation length exponent ν, we consider the spanning number n_s for fixed aspect ratios $L_x = 2L_y$ (i.e. $L_x \times L_x$ plaquettes) and circuit depth $t = L_y$. We then perform a finite-size scaling (FSS) analysis using an ansatz generically of the form in Eq. (6.2) and a cubic B-spline to fit the scaling function. Moreover, by taking sufficiently large system sizes and a narrow window around the critical point, we find that any irrelevant scaling variables may be dropped from the ansatz. In Fig. 7.12 we show the resulting data collapse for the transition in (i) the (orientable) honeycomb Kitaev circuit along the line $K_x = K_y = (1 - K_z)/2$ and (ii) the (non-orientable) honeycomb Kitaev circuit with next-nearest neighbor parity checks along $K_x = K_y = J = (1 - K_z)/3$.

The results are summarized in Tab. 7.1. We find consistent values of ν in both symmetry classes for several other lattice geometries.These results thereby highlight that the entanglement transitions in (2+1)-dimensional measurement-only Majorana circuits have *distinct*

[7] For unit aspect ratio of the spatio-temporal volume.

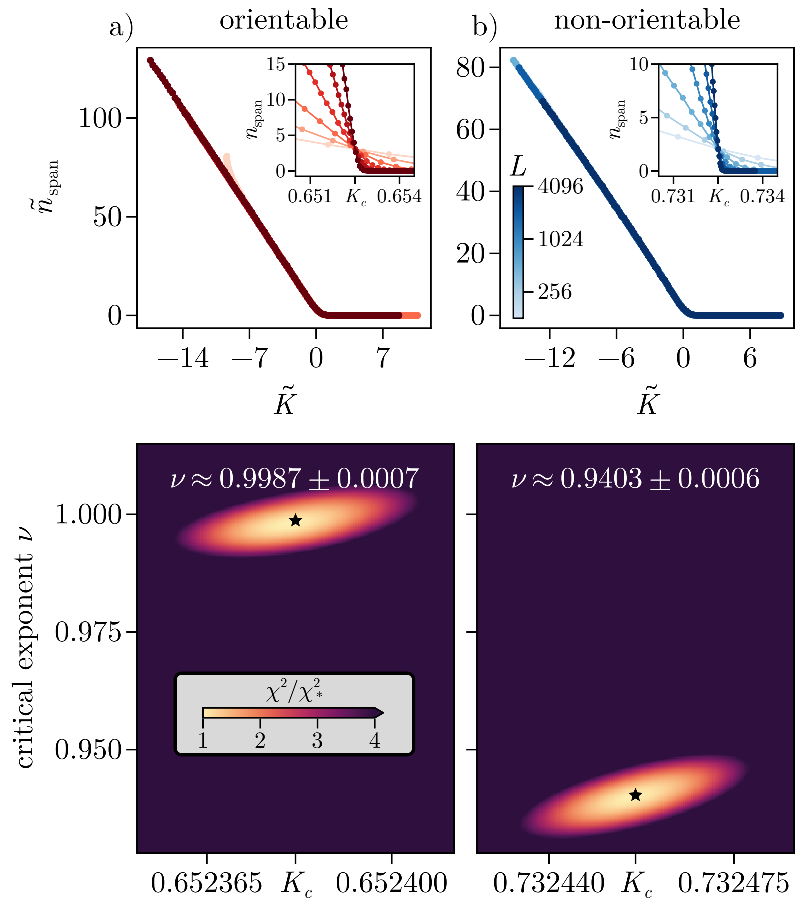

Figure 7.12: **Correlation length exponent from spanning number.** Taking $K = K_x$, we have (a) $K_y = K_z = (1 - K)/2$ for symmetry class BDI and (b) $K_y = K_z = J = (1 - K)/3$ for class D. Top panels: Scaling collapse and raw data (inset) of the spanning number in the vicinity of the transition, with scaling variable $\tilde{K}$ as defined in Eq. (6.2). Data shown is for system sizes $L = 2^7, 2^8, 2^9, 2^{10}, 2^{11}, 2^{12}$ Bottom panels: Error estimation of critical exponent ν. Fixing all other scaling coefficients, we vary the estimated K_c and ν and evaluate the cost function. The heatmap then shows the normalized cost function χ^2/χ^2_* for the FSS analysis of the spanning number shown in the top panels, stars mark the minima (K_c^*, ν^*). The colormap has been truncated at four times the minimum cost to give a visual estimate for the uncertainty in K_c^* and ν^*. The error value has been estimated from the $\chi^2_* + 4$ contour. The optimization was performed on system sizes $L \geq 256$ for $\tilde{K} \in (-6, 6)$, $\tilde{K} \in (-7, 7)$ for the orientable and non-orientable case, respectively. In both cases, the final cost function divided by the number of degrees of freedom is sufficiently close to one $|\chi^2_r - 1| < 0.025$, indicating a good fit.

universality depending on the presence or absence of orientability, i.e., depending on the symmetry class. We fix the critical points K_c at the values reported here and use them in all further analysis.

symmetry	BDI (orientable)	D (non-orientable)
K_c	0.6523817 ± 0.0000021	0.7324564 ± 0.0000015
ν	0.9987 ± 0.0007	0.9403 ± 0.0006

Table 7.1: **Critical point and correlation length exponent** from the spanning number in Fig. 7.12.

Fisher exponent τ

At the transition and throughout the extended critical phase, the bulk loop length distribution is expected to follow a power-law $P_{\text{bulk}}(\ell) \propto \ell^{-\tau}$, where the Fisher exponent τ is related to the fractal dimension d_f via the hyperscaling relation $\tau = (d/d_f) + 1$. In the extended critical phase, the Brownian nature of the loops yields $d_f = 2$ and thus $\tau = 5/2$. By contrast, a mean-field analysis [13, 233, 250, 256] predicts anomalous dimension $\eta = 0$, corresponding to $d_f = 5/2$ and $\tau = 11/5$ at the transition. Tuning to the critical point determined from FSS of the spanning number, we obtain the exponent τ by fitting a power-law to the bulk loop length distribution $P_{\text{bulk}}(\ell)$. The result is provided in Tab. 7.2.

These results deviate very slightly from previous numerical studies on 3D classical loop models, where hyperscaling gave $\tau = 2.184 \pm 0.003$ for the orientable case [271] and $\tau = 2.178 \pm 0.002$ for the non-orientable case. In both symmetry classes, the decay of $P_{\text{bulk}}(\ell)$ is *slower* than expected for $\tau = 11/5$, indicative of small but finite renormalization due to fluctuations beyond the mean-field prediction. However, the difference in τ between the two symmetry classes is rather subtle, making it challenging to distinguish them even at the large system sizes accessible in the loop framework.

Finally, we note that a direct observation of the Fisher exponent τ might be practically infeasible as it would require access to the bulk lengths of loops in space-time. As an alternative, it might be far more practical to employ ancilla probes [138, 188] to instead extract the anomalous dimension η, from which we may determine τ via hyperscaling relations, see below.

symmetry	BDI (orientable)	D (non-orientable)
τ	2.1819 ± 0.0005	2.1875 ± 0.0005
d_f	2.5383 ± 0.0011	2.5263 ± 0.0011

Table 7.2: **Fisher exponent and fractal dimension** from Fig. 7.13.

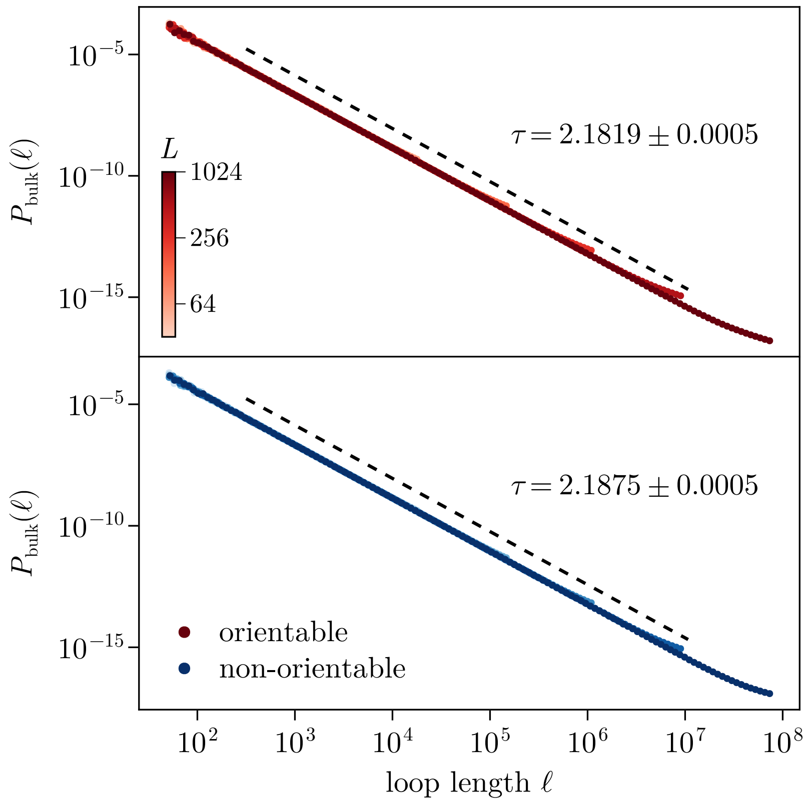

Figure 7.13: **Fisher exponent at the critical point.** Shown is the power-law scaling of the bulk length distribution for closed loops $P_{\mathrm{bulk}}(\ell)$ at the transition with circuit depth $t = 4L_y$. Data are shown for linear dimension $L_y = 32, 64, 128, 256, 512, 1024$. We fix $K = K_c$ known from the spanning number collapse in Fig. 7.12. The black dashed line marks the power-law found by fitting $P_{\mathrm{bulk}}(\ell) \sim \ell^{-\tau}$ to all data in the scaling regime $10^{5/2} \leq \ell \leq 10^{-2} L^3$. In both symmetry classes, the resulting Fisher exponent τ deviates clearly from the mean-field value $\tau = 11/5$.

Anomalous dimension η

The anomalous dimension η can be determined by examining the finite-size scaling behavior of the total *length* of spanning loops $\mathcal{M}$,

$$\mathcal{M} L^{-(5-\eta)/2} = f(L^{1/\nu}(K - K_c)).$$

Moreover, this provides a second, independent estimate of the correlation length exponent ν. In Fig. 7.14, we show the scaling collapse of $\mathcal{M}$ in both symmetry classes. The results are displayed in Tab. 7.3. We note that the estimates for ν obtained in this finite-size scaling analysis are independent of the values extracted from the spanning number collapse, Tab. 7.1.

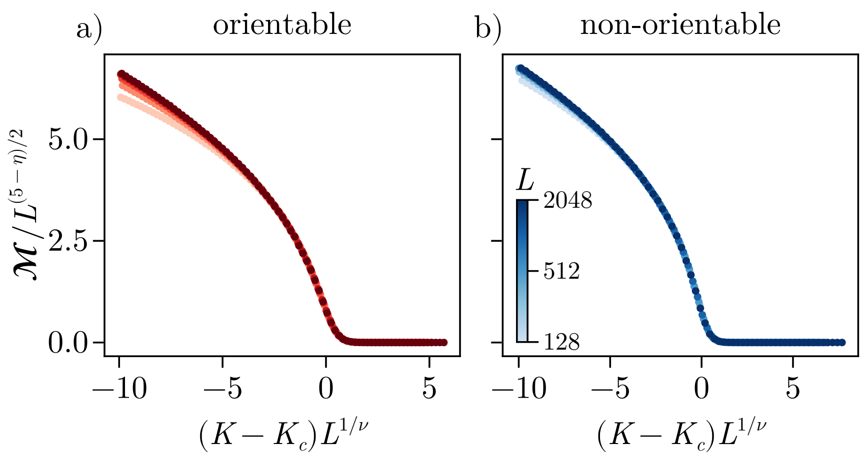

Figure 7.14: **Anomalous dimension.** Scaling collapse of the quantitiy $\mathcal{M}/L^{(5-\eta)/2}$ as a function of $x = (K - K_c)L^{1/\nu}$ for the orientable (a) and non-orientable (b) circuit. Data shown is for linear system sizes $L = 128, 256, 512, 1024, 2048$. To avoid the need for higher order terms in the finite-size scaling ansatz, optimization was restricted to $x \in (-1, 2)$ and $x \in (-2, 2)$ for the orientable and non-orientable case respectively, $L \geq 256$. Also here the cost function per degree of freedom is close to one, $|\chi_r^2 - 1| < 0.05$.

Both approaches yield almost perfect agreement, which is a strong internal consistency check of our numerical approach.

symmetry	BDI (orientable)	D (non-orientable)
ν	1.002 ± 0.002	0.942 ± 0.004
η	-0.084 ± 0.004	-0.066 ± 0.007
η (alt)	-0.073 ± 0.007	-0.066 ± 0.009

Table 7.3: **Anomalous dimension**. Top rows: anomalous dimension η and correlation length exponent ν from the spanning lengths in Fig. 7.14. Bottom row: Anomalous dimension η, obtained in an alternative way from the watermelon correlators in Fig. 7.15.

An alternative way to obtain an estimate for the anomalous dimension η is to probe the two-leg watermelon correlator $G_2(r)$. At the transition, this correlator decays algebraically with the distance r, $G_2(r) \propto r^{-(1+\eta)}$. Analogously to the correlators P_n discussed in Fig. 7.9 which we considered earlier, $G_2(r)$ can be measured in an experiment by using an ancilla scheme: $G_2(r)$ is the average mutual information between two ancillae that were entangled with the circuit at space-time points separated by a distance r.

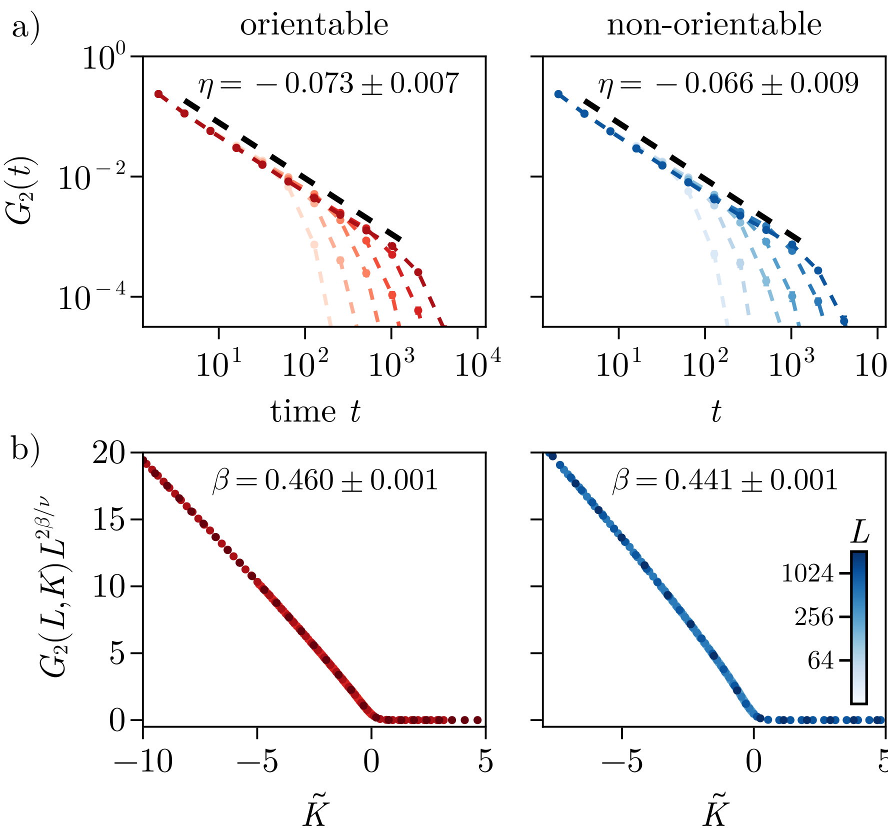

Figure 7.15: **Watermelon correlator.** (a) Scaling of the two-leg watermelon correlator $G_2(r)$ at the critical point for the orientable (red) and non-orientable (blue) circuit. The separation r is varied by increasing the circuit depth t between the two points where ancillae couple to the bulk. Data here and in (b) are shown for system sizes $L = 32, 64, 128, 256, 512, 1024$. The black dashed lines show a regime of power-law scaling $t^{-(1+\eta)}$, from which we find $\eta = -0.073 \pm 0.007$ for the orientable class and $\eta = -0.066 \pm 0.009$ for the non-orientable class. (b) Scaling collapse of the two-leg watermelon correlator $G_2(K, r)$ at macroscopic distances $r \sim L$. The rescaled correlator $G_2(K, L)L^{2\beta/\nu}$ is a smooth function of the scaling variable $\tilde{K}$ defined in Eq. (7.9). The critical point K_c and critical exponent ν are fixed using the results from FSS of the spanning number in Fig. 7.12. We find order parameter exponent $\beta = 0.460 \pm 0.001$ in the orientable circuit and $\beta = 0.441 \pm 0.001$ in the non-orientable circuit.

Here, one would entangle ancillae at identical spatial positions but at times t_1, t_2 such that $r = |t_1 - t_2|$. Then, for a fixed system size, the scaling of $G_2(r)$ can be studied by simply varying the temporal separation (i.e. the circuit depth). As shown in Fig. 7.15(a), we observe a power-law decay of the watermelon correlator with respect to the space-time separation that allows one to extract the anomalous dimension for both symmetry classes, displayed

symmetry	BDI (orientable)	D (non-orientable)
β	0.460 ± 0.001	0.441 ± 0.001

Table 7.4: **Order parameter exponent** from the watermelon correlator of Fig. 7.15.

in Tab. 7.3. We note that this approach is highly sensitive to subleading corrections and small deviations from the exact local of the critical point. We consider it thus generally less accurate to extract η in this manner.

Order parameter exponent β

In the loop framework, the Majorana liquid phase acquires a non-zero ferromagnetic-type order parameter, represented by the probability that two infinitely far separated space-time coordinates are connected by a single closed loop, i.e., $P_2 \sim |K - K_c|^{2\beta}$. The critical exponent β associated to this order parameter can be detected in an ancilla scheme similar to Fig. 7.9. In practice, for systems of linear dimension L, one measures $G_2(r)$ for large space-time separations $r \sim L$. This introduces a subleading correction $G_2(r) = Ar^{-x_2} + P_2$, where $x_2 = 2$ for Brownian loops [256, 250]. For even moderate system sizes L, this subleading correction becomes negligible. We may then treat finite-size effects for G_2 similarly to those for the order parameter in percolation,

$$\begin{aligned} G_2(r \sim L, K) &= L^{-2\beta/\nu} f(\tilde{K}), \\ \tilde{K} &= (K - K_c) L^{1/\nu} \left[1 + A(K - K_c)\right]. \end{aligned} \tag{7.9}$$

In the liquid phase, this scaling function reduces to the simpler form $G_2(r \sim L, K) \propto |K_c - K|^{2\beta}$ on distances L much larger than the correlation length ξ.

We determine β by fitting the ansatz in Eq. (7.9) to the data in a narrow window enclosing the critical point. In order to avoid systematic drift in the fitted exponents, we fix ν and K_c at the values found previously from examining the spanning number. The resulting scaling collapse is shown in Fig. 7.15(b). This yields accurate estimates of the critical exponent β from the ancilla scheme which clearly distinguish both symmetry classes and which are summarized in Tab. 7.4.

Hyperscaling and Discussion

Having obtained several independent estimates of various critical exponents, we now examine their consistency with one another via hyperscaling relations. We further comment on the reliability of the different approaches for determining critical exponents and justify the choice of values reported in Table 7.6.

Given the Fisher exponent τ, the anomalous dimension is given by the scaling relation $\eta = 5 - \frac{6}{\tau - 1}$. The resulting values are given in Tab. 7.5. For class BDI, scaling gives a value

hyperscaling relation	BDI (orientable)	D (non-orientable)
$\eta = 5 - \frac{6}{\tau - 1}$	-0.0766 ± 0.0021	-0.0526 ± 0.0021
$\beta = \nu(\eta + 1)/2$	0.4590 ± 0.0020	0.4400 ± 0.0040
$\beta = 3\nu(\tau - 2)/(\tau - 1)$	0.4611 ± 0.0013	0.4454 ± 0.0012

Table 7.5: **Hyperscaling relations** and corresponding alternative estimates of critical exponents.

of η which lies between the two estimates determined earlier in Tab. 7.3. In symmetry class D, scaling suggests a slightly smaller but not inconsistent magnitude of η than previously found. The anomalous dimension η is notoriously difficult to determine directly, even for the large system sizes accessible with our loop model simulations. Computing η via the hyperscaling relation is highly susceptible to small deviations in the Fisher exponent τ and thus even smallest uncertainties in the critical point K_c. By contrast, determining η directly via FSS of $\mathcal{M}$ leaves K_c as a fitting parameter and is generally found to be more robust. This is supported not only by the near perfect scaling collapse shown in Fig. 7.14, but also by the close agreement with the value of ν found by FSS of the spanning number. As such we opted to report the corresponding value of η in Tab. 7.6.

Hyperscaling allows for two alternative ways of estimating the order parameter exponent β: (i) given exponents η and ν from the FSS of $\mathcal{M}$, one finds $\beta = \nu(\eta + 1)/2$, and (ii) using the correlation length exponent ν and Fisher exponent τ from the FSS of $\mathcal{M}$ and $P_{\text{bulk}}(\ell)$, one finds $\beta = 3\nu(\tau - 2)/(\tau - 1)$. We find that both approaches give values consistent with one another and clearly distinct in the two symmetry classes. Moreover, hyperscaling gives values of β which are in very good agreement with those found from the FSS analysis of the watermelon correlator $G_2(r, K)$ (see Tab. 7.4). For consistency we also report β as determined by the hyperscaling relation $\beta = \nu(\eta + 1)/2$ in Tab. 7.6.

Lastly, let us comment on how the exponents we determine here compare with previous numerical studies. The orientable loop model was studied previously in Ref. [271]. Our results for the measurement-only Kitaev model yields critical exponents perfectly consistent with these earlier results (see Tab. 7.6), confirming the universality of the entanglement transition. With our loop model simulations allowing us to reach appreciably larger system sizes (by two orders of magnitude), we are able to refine the estimated critical exponents to greater precision.

By contrast, the non-orientable loop model was studied only relatively recently in Ref. [313]. Unlike the orientable case, the critical exponents we report for this symmetry class seem to differ appreciably from these previous estimates. In particular, whereas we find $\nu = 0.9403 \pm 0.0006$, Ref. [313] suggested a smaller value $\nu = 0.918 \pm 0.005$. This in turn leads to a systematic difference in all other critical exponents found by hyperscaling relations or FSS

critical exponent	ν	η	d_f	β
this work (10^8 qubits)				
BDI / orientable	0.9987 ± 0.0007	-0.084 ± 0.004	2.5383 ± 0.0011	0.4590 ± 0.0020
D / non-orientable	0.9403 ± 0.0006	-0.066 ± 0.007	2.5263 ± 0.0011	0.4400 ± 0.0040
literature (10^6 qubits)				
BDI / orientable [271]	0.999 ± 0.002	$-0.068 \pm 0.018^*$	2.534 ± 0.009	$0.4650 \pm 0.0033^\dagger$
D / non-orientable [313]	0.918 ± 0.005	-0.091 ± 0.009	$2.546 \pm 0.005^*$	$0.4168 \pm 0.0051^\dagger$

Table 7.6: **Summary of critical exponents in (2+1)-dimensions.** Here we summarize the critical exponents of the localization transition in symmetry class BDI and D, comparing results from loop model simulations (with up to 10^8 qubits) to previous results in the literature (with up to 10^6 qubits). Where multiple approaches to determine an exponent were given, we report the most reliable quantity. Refs. [271, 313] have determined *either* the anomalous or fractal dimension and calculated the other via the scaling relation $\eta = 5 - 2d_f$, indicated by the asterisk (*). The critical exponent β in both works was obtained via the hyperscaling relation $\beta = \nu(3 - d_f)$, indicated by the asterisk (†). We note that the literature values for class D deviate from the ones obtained in this work.

which involves ν [8]. To reconcile this apparent discrepancy, we have simulated two alternative circuit/lattice geometries, including the L-lattice studied in Ref. [313], which has allowed us to track down its source: In our approach we have expanded the FSS ansatz by *non-linear* terms, which we find to give superior data collapses over wider parameter ranges and system sizes. This also allows us to smoothly interpolate between our estimates and the ones found in Ref. [313] as a function of (i) the range of included system sizes (ii) the choice of scaling variable, and (iii) the density of spline points. Such an analysis leads one to conclude that an improved FSS ansatz for the numerical finite-size data of Ref. [313] would give a somewhat higher estimate of the critical exponent ν, perfectly consistent with what we report here.

Despite the discrepancy with earlier works, there is strong reason to believe that the critical exponent values we report here represent the most accurate and precise determination for this symmetry class to date. Our numerical simulations reach system sizes which are much larger than previously studied, enabling greater control over subleading corrections in the FSS analysis. This is further bolstered by the internal consistency between the two

[8]For instance, consider the anomalous dimension η as found by FSS of $\mathcal{M}$. From the RG flow [13], one expects that $\nu^{-1} - 2 + \eta$ is a constant. Thus, a small error in the fitted value of ν is compensated by a corresponding shift in η. For $\Delta(\nu^{-1}) = (0.9403^{-1} - 0.918^{-1})$, one finds $\Delta\eta = 0.026$, almost precisely matching the difference in reported values of η. Since the fractal dimension was determined in Ref. [313] via the scaling relation $d_f = (5-\eta)/2$, we find that the discrepancy in d_f can also be accounted for using a similar reasoning. Finally, the assumption that $\nu^{-1} + \eta$ is constant in tandem with the scaling relation $\beta = \nu(1+\eta)$ allows one to show that $\Delta\beta = \Delta\nu = 0.0223$, consistent with the values reported in Tab. 7.6.

independent approaches for estimating ν. Moreover, the universal value $\nu \approx 0.94$ in symmetry class D is supported by numerical studies of two additional lattice geometries, namely the measurement-only Yao-Kivelson model and Cardy's 3D L-lattice [189].

Summary

As we have seen throughout this section, (2+1)-dimensional Majorana circuits and their corresponding 3D loop models exhibit a rich set of phenomena not present in lower dimensions. Here the measurement-only circuit analog of Kitaev's honeycomb model provided a paradigmatic model for detailed study of the physics which arises from the $\mathbb{CP}^{n-1}$ and $\mathbb{RP}^{n-1}$ NLσM for loop fugacity $n = 1$. Harnessing the efficient simulability of Majorana loop models, we presented the most precise characterization to date of criticality and universal scaling behavior at the transition, summarized in Tab. 7.6. At the phase transition, we make the unexpected observation of quantum Lifshitz scaling of the entanglement entropy—a feature previously associated only with *interacting* circuits. This finding suggests a new and unexplored connection between loop models in $(2+1)$ dimensions, monitored free fermions, and $(2+1)$-dimensional conformal field theories, warranting further investigation. In contrast to the circuits in (1+1)-dimensions, the phase diagram of (2+1)-dimensional circuits in both symmetry classes are markedly similar, featuring an extended long loop phase with $L\log(L)$ entanglement scaling. Despite these similarities, we identified accessible ancilla qubit probes by which universal indicators of the two symmetry classes may be observed from the circuit entanglement dynamics. In short, the mapping of entanglement dynamics in these circuits to simple loop models enabled analytic insights and numerical precision which is wholly infeasible even in more generic (2+1)-dimensional Clifford circuits.

7.5 Outlook

To briefly summarize the main results presented in this chapter, we have investigated entanglement in measurement-only Majorana circuits to elucidate that (i) monitored quantum circuits give rise to robust entanglement phases, i.e. dynamic phases of matter that are stable to local variations of the circuit parameters (measurement probabilities in our case), (ii) the notions of symmetry and dimensionality can be used, akin to their Hamiltonian counterparts, to define universal behavior of the entanglement phases and the quantum criticality of phase transitions between them, and (iii) that the particle-hole symmetric Majorana circuits, relevant to these monitored circuits, can be recast in terms of Majorana loop models. These Majorana loop models are a powerful resource as they not only allow to recast the entanglement phases in terms of localization physics of loops and map their phase transitions to non-linear sigma models, but they also provide a numerical framework allowing to simulate up to 10^8 qubits. This has allowed us to clearly discriminate the universality classes of orientable versus non-orientable loop models, relevant to Majorana circuits in symmetry classes BDI and D, respectively and determine their critical exponents to unprecedented precision.

Furthermore, this work suggests a broader perspective on the tenfold way classification of free fermionic wave functions. The connection between orientable and non-orientable loop models offers a unified framework for embedding both free Majorana circuits (fugacity $n = 1$) and ground states of free Majorana Hamiltonians (fugacity $n = \sqrt{2}$) within symmetry classes BDI and D. This raises intriguing possibilities for future research, such as exploring whether other symmetry classes allow similar embeddings or investigating higher loop fugacities (see Ch. 9). This approach could refine the tenfold way classification by distinguishing universality not only by symmetry classes but also by Hamiltonian dynamics versus monitored circuits. Moreover, this offers a tractable handle on broader emerging questions regarding symmetry as an organizing principle in *open* quantum systems [218, 208, 297, 210].

Chapter 8

Interacting circuits

8.1 Introduction

In the previous chapter we undertook a thorough characterization of the entanglement phases and transitions which arise in Gaussian Majorana stabilizer circuits. However, this is a highly restricted class of circuits. Building upon the loop model framework for Majorana circuits, we now examine the effect of non-Gaussian operations in stabilizer circuits.

Whereas individual operations in a Gaussian Majorana circuit correspond to a unique loop configuration, we show here that measuring non-Gaussian operators creates superpositions of loop configurations. This is analogous to Hamiltonian systems, where interactions create superpositions of Gaussian states. In many situations, however, a unique loop model may emerge on a coarse grained scale. Here we adopt a perspective inspired by the renormalization group (RG) framework and consider measurements of non-Gaussian operators $\{\hat{O}_l\}$ as perturbations on top of an otherwise Gaussian stabilizer circuit. We note that this situation is quite general: the frustration graph of an arbitrary set of measured operators always contains a subgraph that can be represented by measurements of Gaussian fermion operators [99]. The remaining operators then act as non-Gaussian perturbation.

To accommodate interactions, numerical simulations of the circuit models studied in this chapter are carried out in the Clifford tableau representation. In contrast to the Gaussian Majorana circuits studied previously, generic Clifford circuits produce states which support non-zero multipartite entanglement. To this end, we use the tripartite mutual information $I_3(A,B,C) = I_2(A,B) + I_2(A,C) - I_2(A,BC)$ with A,B,C consecutive regions of size $L/4$ as an order parameter for distinguishing phases and performing scaling analysis about the transition.

This chapter is structured as follows. First in Sec. 8.2 we consider the RG relevance of Jordan-Wigner (JW) strings which arise from interaction terms or local Clifford terms which are nonlocal in the Majorana language. Then in Sec. 8.3 we study an orientable Gaussian circuit perturbed by symmetry breaking interactions, demonstrating the emergence of non-orientable universality and the CPLC Goldstone phase. Finally, Sec. 8.4 examines

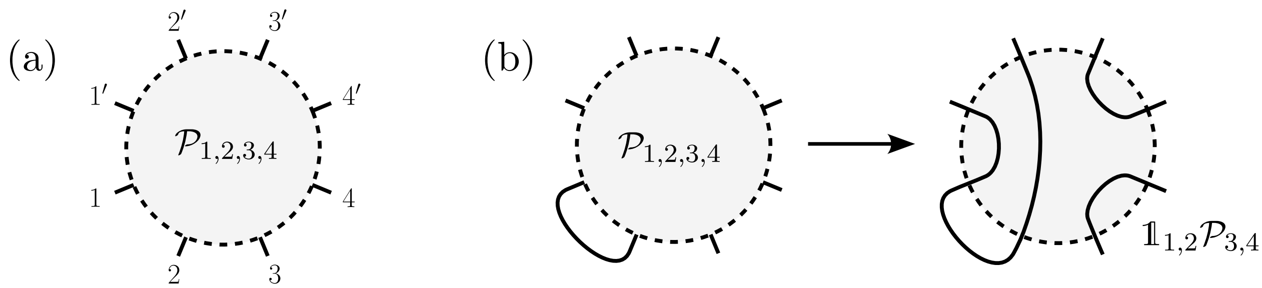

Figure 8.1: **Four-fermion measurements.** (a) Measuring the total parity on four Majoranas γ_l for $l = 1, 2, 3, 4$ can be represented by an 8-leg vertex, where the unprimed and primed indices denote incoming and outgoing worldlines, respectively. (b) When one of the local fermion parities is known due to a closed loop entering the vertex, the measurement reduces to a parity-check on two fermions, restoring a vertex-free loop diagram.

an interacting Majorana stabilizer circuit which maps to *coupled* loop models, yielding novel entanglement phases and critical behavior.

8.2 Jordan-Wigner Strings and RG Relevance

Starting from a (1+1)-dimensional Gaussian circuit, i.e., a well-defined 2D loop model, the notion of relevance and irrelevance in the RG sense for non-Gaussian perturbations in 2D statistical mechanics is applicable. Thus, measuring a set of non-Gaussian operators $\{\hat{O}_l\}$, which preserve the symmetries of the Gaussian circuit, is an irrelevant perturbation when added to an extended thermodynamic phase of either short or long loops. It may, however, become relevant near a Gaussian critical point and modify the critical behavior of the circuit analogously to a Wilson-Fisher fixed point. Further, when the circuit becomes dominated by non-Gaussian measurements it may approach a strong coupling fixed point. In this section we distinguish between interaction terms which preserve or violate orientability symmetry.

Symmetry Preserving Non-Gaussian Perturbations

The effect of symmetry-preserving non-Gaussian measurements in a loop model can be illustrated by starting with a Gaussian stabilizer circuit and introducing a perturbatively small probability of measuring non-Gaussian operators which are symmetry-preserving, e.g., preserve parity and orientability and are thus even under time-reversal.

Let us take for example four-fermion parity checks, such as $Z_l Z_{l+1} = \gamma_{2l-1}\gamma_{2l}\gamma_{2l+1}\gamma_{2l+2}$ or $X_l X_{l+2} = \gamma_{2l}\gamma_{2l+1}\gamma_{2l+2}\gamma_{2l+3}$. The projective measurement $\mathcal{P}_{1,2,3,4} = \frac{1}{2}(\mathbb{1} - \hat{O}_{1,2,3,4})$ of a general four-fermion operator $\hat{O}_{1,2,3,4} = \gamma_1\gamma_2\gamma_3\gamma_4$ corresponds to an "8-leg vertex" in the loop model. It has four incoming and four outgoing worldlines (see Fig. 8.1a), which, in contrast to two-fermion measurements, have *no* unambiguous connection between individual pairs of fermions. Instead, $\mathcal{P}_{1,2,3,4}$ yields a superposition of all possible ways of connecting the legs incident on the vertex with a fixed total parity. This gives rise to several, equivalent representations of $\mathcal{P}_{1,2,3,4}$ in the loop framework. For instance, the projector can be written as

$$\mathcal{P}_{1,2,3,4} = \mathbb{1} - i\sqrt{2}\left(e^{-\frac{i\pi}{4}}\mathbb{1} - \sqrt{2}\mathcal{P}_{2,3}\right)\mathcal{P}_{1,3}\mathcal{P}_{2,4} + i\sqrt{2}\left(e^{+\frac{i\pi}{4}}\mathbb{1} - \sqrt{2}\mathcal{P}_{2,3}\right)\mathcal{P}_{1,2}\mathcal{P}_{3,4}. \tag{8.1}$$

So far, the sum is *not* restricted to terms which respect the symmetry, e.g., orientability, of the Gaussian circuit and so may include both symmetry preserving and symmetry breaking terms.

In the context of an otherwise Gaussian circuit, however, this interaction vertex may simplify. Whenever the parity of two of the four fermions is already known *or* measured in the future, the four-fermion measurement reduces to a two-fermion parity check, as revealed from $\mathcal{P}_{1,2}\mathcal{P}_{1,2,3,4} = \mathcal{P}_{1,2,3,4}\mathcal{P}_{1,2} = \mathcal{P}_{1,2}\mathcal{P}_{3,4}$ and depicted in Fig. 8.1b. This provides access to two important limits: (i) When the circuit is dominated by local Gaussian measurements, an extensive number of local parities is known immediately before or after application of $\mathcal{P}_{1,2,3,4}$. Then $\mathcal{P}_{1,2,3,4}$ can almost always be replaced by two-fermion measurements. (ii) In turn, when non-Gaussian measurements are dominant, few Gaussian parity checks will induce a cascade of fixed local parities, which collapses the circuit onto a short loop state. Both cases give rise to a loop model interpretation, in which the topology of the short loop (area law) phase depends on (i) the Gaussian or (ii) the non-Gaussian measurements.

This observation is readily generalized to measurements of arbitrary symmetry-preserving Majorana operators $\hat{O} \sim \gamma_1, ...\gamma_{2n}$ with $n > 2$. When the parity of m bilinears in $\hat{O}$ is known, then it reduces to the measurement of an $2(n-m)$ Majorana operator. The size of the reduced operator corresponds precisely to the mutual information between the support of $\hat{O}$ and its complement in the circuit. Mutual information is thus a reliable indicator of the relevance of a $2n$-fermion operator in a Gaussian circuit. In an area law phase with short loops, and for contiguous support of $\hat{O}$, it will not grow with n. At a critical point with long loops (logarithmic entanglement growth), it will grow $\sim \log(n)$, such that higher-order operators become increasingly relevant. In this case, the $2n$-fermion measurements will not collapse onto a single loop configuration but instead will yield a superposition of all symmetry-allowed configurations.

A further important consequence of the above discussion is that symmetry-preserving non-Gaussian measurements indeed inherit the symmetry of the Gaussian circuit. Consider for instance orientability: when the worldlines entering the $2n$-fermion vertex form an orientable, bipartite lattice, the corresponding vertex is collapsed onto its bipartite part and cannot break orientability. In turn, when the worldlines instead form a non-bipartite lattice, the $2n$-fermion vertex will collapse onto its non-orientable part. Thus $2n$-fermion parity checks, which are compatible with orientability, i.e., even under time-reversal, will inherit the (non-) orientable structure of the underlying Gaussian circuit.

Parity Violating Measurements

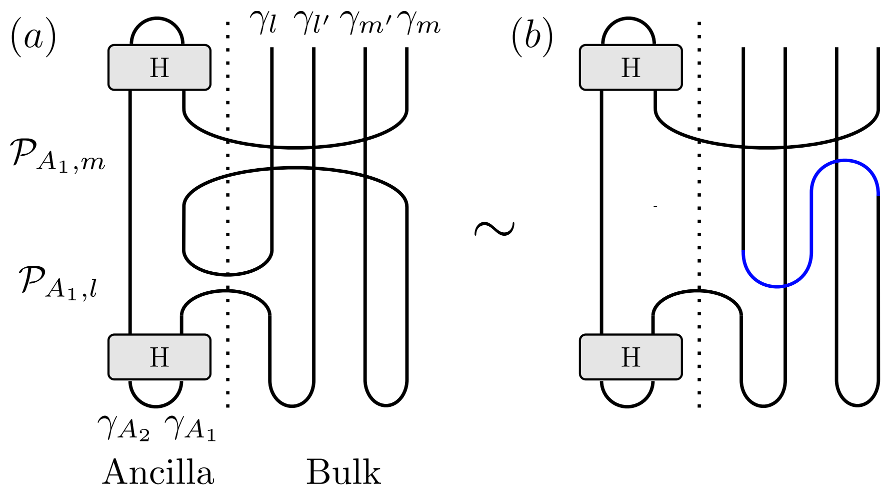

Figure 8.2: **Ancilla-mediated parity non-conserving measurements:** (a) Two sequential single Majorana measurements mediated via an ancilla qubit, $\mathcal{P}_{A_1,l}$ at time t_1 and $\mathcal{P}_{A_1,m}$ at time t_2. At the end of the evolution, the ancilla is decoupled from the bulk by a measurement in the X basis. (b) An equivalent circuit generating the same final state involves a connection (blue) of bulk loops that is non-local in both space and time. This can be viewed as an effective swap $\mathcal{R}_{l,m}$ after the first measurement $\mathcal{P}_{A_1,l}$. If γ_l and γ_m are in separate bipartitions of the Majoranas, this effective swap facilitates a breaking of the worldline orientability.

A second important class of non-Gaussian operations appearing in generic Clifford circuits are those which violate the total parity $\bar{Z} = \prod_{l=1}^{L} Z_l$. In general, a parity breaking Pauli operator, e.g., a single X or Y, maps to an odd-length JW string of Majorana fermions attached to one (w.l.o.g., the left) spatial boundary of the circuit. For Clifford circuits, two consecutive parity violating measurements, i.e., X_l, X_m can be expressed as a parity conserving, $X_l X_m$, and a parity violating, X_m, measurement. We show that in the Majorana framework, this process is equivalent to an effective long-range swap $\mathcal{R}_{2l,2m-1}$. Depending on the measured operators, their spatial position, and the time between measurements, such swaps are non-local in space-time and may bridge large distances. Moreover, these swaps yield a potential mechanism for violating orientability, allowing a CPLC Goldstone phase to emerge.

To include parity breaking measurements in the Majorana framework, we recast them as parity-preserving ones by introducing two ancilla fermions [51]. We place an ancilla qubit A consisting of two Majorana modes $\gamma_{A_1}, \gamma_{A_2}$ at the left boundary of the system, as in Fig. 8.2. Performing a Z_A-measurement followed by a Hadamard gate, the ancilla is prepared in an eigenstate $\langle X_A \rangle = 1$ without well-defined parity. For a parity non-conserving operator $\hat{O}$

acting in the bulk, prepending X_A yields a new operator $\hat{O} \rightarrow X_A\hat{O} = \gamma_{A_1}\hat{O}$ that is even in Majorana modes. This now conserves the parity of the joint system, $Z_A\bar{Z}$ and leaves the bulk unmodified compared to measuring only $\hat{O}$.

To illustrate the effect of the ancilla, we consider the following simple example. Consecutively measure two single Majorana fermions: $\hat{O} = \gamma_l$ at time t and $\hat{O}' = \gamma_{l'}$ at time t'. In the ancilla framework, this yields the Gaussian projections $\mathcal{P}_{A_1,l} = \frac{1}{2}(1 + i\gamma_{A_1}\gamma_l)$ at time t and $\mathcal{P}_{A_1,l'}$ at time t'. Both can be expressed in the loop model framework by connecting the ancilla worldline $\gamma_{A,1}$ to bulk worldlines $\gamma_l(t)$ and $\gamma_{l'}(t')$. Between times t, t' this is equivalent to drawing a direct loop between $\gamma_l(t)$ and $\gamma_{l'}(t')$, i.e., replacing the ancilla loop by a space-time non-local swap $\mathcal{R}_{(l,t),(l',t')}$. Any two consecutive, single-Majorana measurements $\gamma_{l_n}, \gamma_{l_{n+1}}$ at times $t_n < t_{n+1}$ can thus be replaced by a swap $\mathcal{R}_{(l_n,t_n),(l_{n+1},t_{n+1})}$. By this procedure, the ambiguity in the bulk parity persists only along the loop connecting the first and the final parity breaking measurement via the ancilla. After the final parity violating measurement, the ancilla is removed by applying another Hadamard gate and then measuring Z_A. In the bulk, this implements a final swap $\tilde{\mathcal{R}}_{(l_N,t_N),(l_1,t_1)}$, which pushes the parity ambiguity into the qubit represented by the pair $\gamma_{l_1}\gamma_{l_N}$.

When measuring local Pauli operators, e.g., X or ZX, the effect of both the ancilla and JW strings need to be combined. Each measurement then results in a superposition of all possible loop configurations, including long-range swaps, which are compatible with the state in the circuit, e.g., as in Eq. (8.1). In a short loop phase, this again yields only a few possibilities so that the main effects of parity breaking measurements are orientability breaking and long-range swaps. By contrast, in a phase with extended loops, parity breaking measurements generate superpositions of many worldline configurations, leading to a rapid growth of entanglement.

8.3 Parity-breaking in Clifford circuits

Based on the analysis in the previous section, we expect that the non-orientable loop model physics will emerge when introducing finite probability to measure parity-odd, non-Gaussian operators to an otherwise orientable Gaussian stabilizer circuit. In this section we provide a concrete demonstration in a Clifford circuit. In particular, we consider Pauli-measurements of two qubit operators A_lB_{l+1} with $A, B \in \{X, Y, Z\}$ [1]. Each operator is measured with probability $p_{AB} = p_a p_b$, i.e., $p_{XY} = p_x p_y$, with $p_x + p_y + p_z = 1$. A global rotation $U_A \equiv \exp\left(i\frac{\pi}{4}\sum_l A_l\right)$ with $A \in \{X, Y, Z\}$ maps between parameters $p_x \overset{U_Z}{\leftrightarrow} p_y \overset{U_X}{\leftrightarrow} p_z \overset{U_Y}{\leftrightarrow} p_x$, yielding a highly symmetric circuit and phase diagram, which is shown in Fig. 8.3a.

By virtue of the symmetry above, we can focus on the parameter regime $p_x, p_y \gg p_z$, which corresponds to perturbing the orientable Gaussian circuit $\mathcal{O}_3 = \{XX, YY, XY, YX\}$ with parity breaking non-Gaussian operators $\{XZ, YZ, ZX, ZY\}$. Along the orientable boundary

[1] The phase diagram of this model was previously obtained in Ref. [156]. However, no logarithmic correction was observed for the considered system sizes.

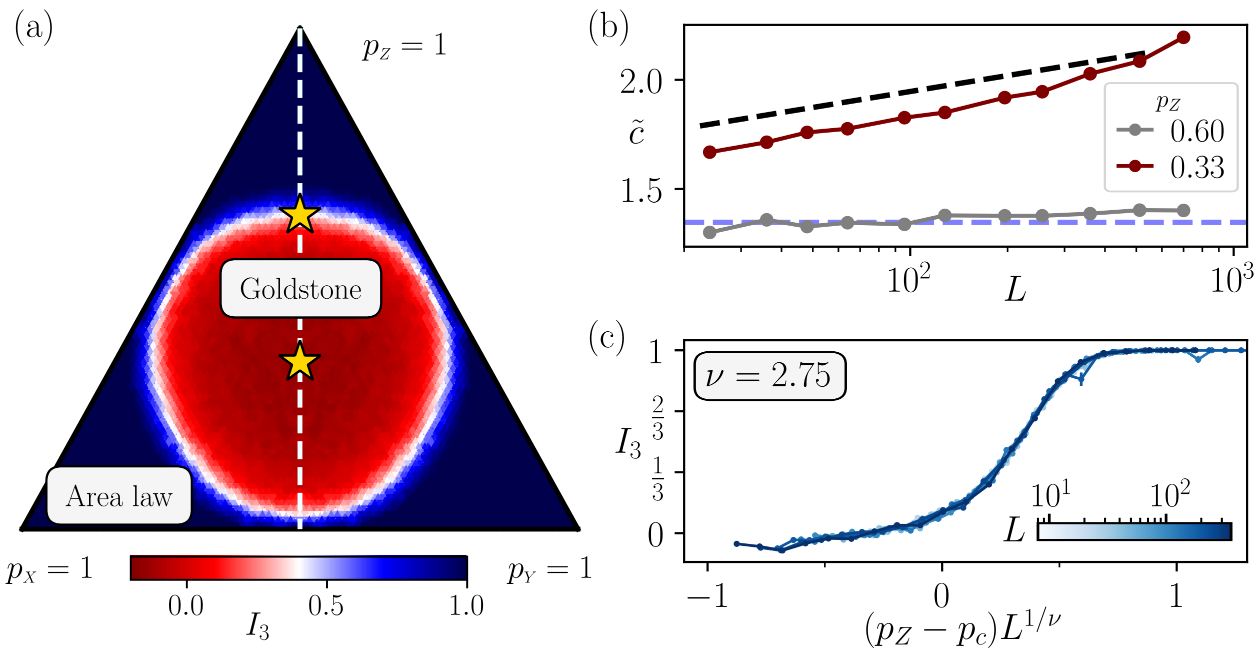

Figure 8.3: **Measurement phases in non-Gaussian, non-orientable circuits.** Interactions induce a CPLC Goldstone phase in the range-2 measurement-only circuit where Pauli operators $A_l B_{l+1}$ are measured with probability $p_A p_B$ with $A, B \in \{X, Y, Z\}$. (a) Phase diagram of the tripartite mutual information I_3 showing a Goldstone phase (red) and area-law phase (blue). The white dashed line marks $p_X = p_Y$, along which we mark the upper critical point and the center of the Goldstone phase. (b) The prefactor $\tilde{c}$ of the logarithmic growth of the entanglement entropy $S_L \sim \frac{\tilde{c}}{3}\log(L)$. In the Goldstone phase (maroon) we observe a logarithmic correction with magnitude comparable to the universal $3\log(2)/(2\pi^2)$ expected for the CPLC Goldstone phase (black dashed line). At the transition (gray) $\tilde{c}$ is independent of system size and consistent with $\tilde{c} \approx 1.33$ found along the critical line in CPLC. (c) The finite size scaling collapse of the tripartite mutual information I_3 confirms a critical exponent $\nu \approx 2.75$.

$p_z = 0$, we recover the bipartite two-leg ladder discussed in Ch. 7, which lies in an area-law phase for all $p_x + p_y = 1$. The short-loop area-law phase is robust against a small probability of orientability (parity) violating measurements. For sufficiently large probability of symmetry-breaking operations, one observes a transition into a Goldstone phase consistent with CPLC. The characteristic $(\log(L))^2$-growth of the entanglement entropy in this phase is shown in Fig. 8.3b. The critical line separating the Goldstone from the area law phase features the correlation length exponent $\nu = 2.75$ expected of the CPLC universality class, confirmed in Fig. 8.3c.

We note that taking the above example and replacing ZX, XZ, ZY, YZ-measurements by either X- or Y-measurements alone *neither* induces a non-orientable circuit *nor* a Goldstone phase. The effective swaps emerging from X or Y measurements preserve orientability when added to the set $\mathcal{O}_3$, since products of subsequent measurements, e.g., $X_l X_{l'}$, are obtained from a sequence of measurements from $\mathcal{O}_3$. The same applies to 4-qubit operators acting on four consecutive qubits, e.g., $XZXZ, ZXXZ$. The simplest non-trivial, orientability breaking terms arising from the random two-qubit measurements are the non-Gaussian operators $Z_l X_{l+1} Y_{l+2} \sim Z_l Y_{l+1} \times Z_{l+1} Y_{l+2}$.

8.4 Coupled loop models

Adding symmetry-preserving, non-Gaussian measurements is an irrelevant perturbation to an extended phase of Gaussian measurements, though it may become relevant in the vicinity of a Gaussian critical point. Furthermore, when non-Gaussian measurements become the dominant generator of evolution, they may drive the circuit towards a strong coupling fixed point. In this section we discuss three general examples for this scenario: (i) by adding non-Gaussian measurements in the vicinity of the percolation critical point of the 1-state Potts model, we split the critical point into two BKT transitions, which enclose an emergent critical phase, (ii) when inducing additional frustration by measuring incommensurate non-Gaussian operators, the critical phase transforms into a volume law entangled phase and (iii) when non-Gaussian measurements dominate, they give rise to a strong coupling tricritical point with an emergent Ising universality. We show how (i)-(iii) can be understood from an elementary version of the problem admitting an exact algebraic description.

Consider a stabilizer circuit wherein we measure the Gaussian operators $\{XY, YX\}$ with probability $\frac{s}{2} \equiv p_{XY} = p_{YX}$ and the non-Gaussian operators $Z_l Z_{l+1}$ and $X_l X_{l+2}$ with probabilities $p_{ZZ} = (1-s)r$ and $p_{XIX} = (1-s)(1-r)$, respectively. Here the choice of Gaussian operators admits a pair of independent TL algebras with generators $e_l \equiv \mathcal{P}_{2l-1,2l+1} = \frac{1}{2}(\mathbb{1} + X_l Y_{l+1})$ and $f_l \equiv \mathcal{P}_{2l,2l+2} = \frac{1}{2}(\mathbb{1} + Y_l X_{l+1})$, respectively. The transfer matrix for the Gaussian circuit then is equivalent to that of two uncoupled, critical 1-state Potts models. Our choice of four-fermion operators effectively couple these Majorana chains (TL algebras), as depicted in Fig. 8.4a. Treating the non-Gaussian operators as a perturbation, the transfer matrix T for the interacting circuit can be expressed in terms of the original TL generators

$$T = \sum_i \left[\lambda(e_i + f_i) + e_i\left((1+\delta r)f_i + (1-\delta r)f_{i+1}\right)\right], \tag{8.2}$$

$$\lambda \equiv \tfrac{s}{2(1-s)} - |\delta r|, \;\; \delta r \equiv 2r - 1.$$

We will now go through the scenarios (i)-(iii) in the phase diagram (see Fig. 7.5c) with the help of the transfer matrix T.

Emergent critical phase and splitting of the percolation critical point into two BKT transitions

Consider the limit $s \to 1$ and $\delta r = \pm 1$, which corresponds to two 1-state Potts models, which are tuned towards their critical point. Each is described by a TL algebra $\{e_i\}, \{f_i\}$. Then

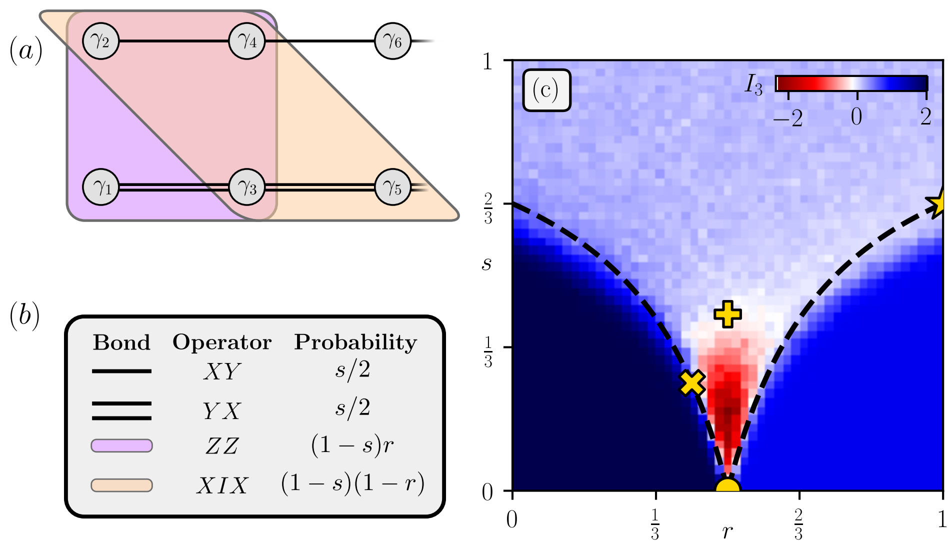

Figure 8.4: **Orientable non-Gaussian circuit:** (a) Majorana lattice representation of the circuit for a two-leg ladder with four-fermion measurements. Bonds represent Gaussian X_lY_{l+1} and Y_lX_{l+1} measurements, while shaded plaquettes denote Z_lZ_{l+1} (purple) and X_lX_{l+2} (orange) measurements. (b) Probabilities for the allowed two and four-fermion measurements. Quantity $s \in [0,1]$ sets the relative probability for two-fermion versus four-fermion measurements, while r determines which type of four-fermion terms are measured. (c) Phase diagram plotting the tripartite mutual information I_3 in the r-s plane showing three distinct phases: an area-law phase at strong 4-fermion measurement rate, a critical phase extending from the non-interacting limit, and a volume-law phase arising from frustration between 4-fermion terms. The dashed black line marks the analytic expression for the critical point $s_c = 2\,|2r-1|\,/(1+2\,|2r-1|)$. The apparent deviation of the data from expected critical line results from finite size effects which are particularly strong for larger $\left|r-\frac{1}{2}\right|$, where the BKT transition gives logarithmically slow convergence to the thermodynamic limit.

adding measurements of either $\{Z_lZ_{l+1}\}$ or $\{X_lX_{l+2}\}$ introduces the couplings e_if_i or e_if_{i+1}, which both generate yet another TL algebra for a single, critical 1-state Potts model. This coupling is known to be an irrelevant perturbation [111] and thus for $\lambda > 0$ the critical Gaussian state remains robust. Increasing the rate of non-Gaussian measurements, the circuit reaches a strong-coupling fixed point at $\lambda = 0$, i.e., at a critical $s = s_c = \frac{2}{3}$. Here, the two critical 1-state Potts models combine into a single emergent one. For $\lambda < 0$, i.e., $s < s_c$, non-Gaussian measurements dominate and induce an area law phase, whose topological properties depends on the sign of δr. With $\delta r = 1$ the area law phase is trivial, whereas for $\delta r = -1$ one pair of edge states $\sim i\gamma_1\gamma_{2L}$ is stabilized. This results in a quantized difference of tripartite mutual information I_3 between the two area law phases, as evident from the phase diagram in Fig. 7.5c. In both cases, the phase transition in the coupled Potts models

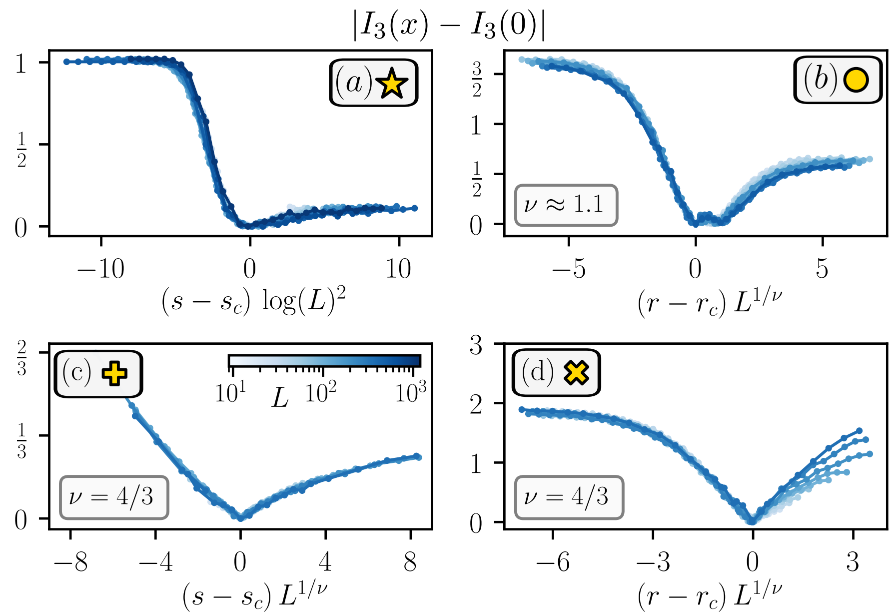

Figure 8.5: **Entanglement transitions in an orientable non-Gaussian circuit:** Critical rescaling of the tripartite mutual information I_3 along various cuts in the r-s plane as marked in Fig. 8.4c. In all plots, the critical value $I_3(x = 0)$ is subtracted off and data are shown for system sizes up to at least $L = 360$. (a) When $r = 1$, the critical and area-law phases are separated by a BKT transition at $s_c = \frac{2}{3}$. (b) With only interactions ($s = 0$), the two area-law phases are separated by a conventional second-order transition at $r_c = \frac{1}{2}$ with critical exponent $\nu \approx 1.1$, close to the expected $\nu = 1$ for Ising criticality. (c) Fixing $r = \frac{1}{2}$, we observe a percolation transition between a critical phase and a volume-law phase with logarithmic corrections. (d) A cut at $s = \frac{1}{4}$ reveals a percolation transition with $\nu = \frac{4}{3}$ separating the area- and volume-law phases.

follows a BKT scenario, which is visualized by the finite size scaling collapse of the mutual information in Fig. 8.5a.

When moving away from the limit $\delta r = \pm 1$, both $e_i f_i$ and $e_i f_{i+1}$ appear simultaneously, reflecting the competition between the two types of non-Gaussian measurements. For any δr, the dominant non-Gaussian term induces a robust area law phase for $\lambda < 0$, which becomes unstable for $\lambda \geq 0$. This yields a precise analytical estimate for the phase boundary at $s = s_c(\delta r) = \frac{2|\delta r|}{1+2|\delta r|}$, which is confirmed in Fig. 8.4c. For large anisotropy δr between the two couplings $e_i f_i, e_i f_{i+1}$ or for large $\lambda > 0$ the Gaussian critical phase remains robust. This is accompanied by a BKT transition into the area law phase at critical s_c. Numerical simulations of the circuit witness an extended critical phase for $\frac{1}{3} \lesssim s$ and correspondingly a BKT transition for $\frac{1}{4} \lesssim |\delta r|$.

The emergence of a robust critical phase, separated by a BKT critical line from an area law regime, appears to be generic when symmetry-preserving non-Gaussian measurements are added to the sets $\mathcal{O}_{1,2,3}$ defined previously in Ch. 7. The prerequisite is that the unperturbed circuit is in the vicinity of the 1-state Potts model critical point. This might be understood as follows. When an orientable set $\mathcal{O}_{1,2,3}$ is pushed to a percolation critical point, it can be decomposed into two 1-state Potts models, one of which is critical. Non-Gaussian measurements then couple both Potts models into a robust critical phase. The scenario in Fig. 8.4 represents one side of the broadened transition between two area law phases. A similar picture has been observed for orientable Gaussian measurements, which at the critical point are perturbed by unitary gates [27].

Tricritical strong coupling fixed point: Emergent Ising universality

The two critical lines with $\lambda = 0$ meet at the critical point $(s, \delta r) = (0, 0)$, see Fig. 8.4c. The merging of two critical lines is typical for a fine-tuned tricritical point, which then realizes a different universality class. Indeed, it has been shown that the tricritical point of the ferromagnetic Q-state Potts model with $\sqrt{Q} = 2\cos(\pi/k)$ is related to the critical point of the ferromagnetic Q'-state Potts model, with $\sqrt{Q'} = 2\cos(\pi/(k+1))$, via the so-called ϵ-η duality [90, 95, 96, 164, 264]. We argued above that each critical line at $\lambda = 0, \delta r \neq 0$ corresponds to a single, critical 1-state Potts model, i.e., $k = 3$. The duality then predicts the tricritical point at $(s, \delta r) = (0, 0)$ to be described by a critical 2-state Potts model ($k = 4$), i.e., the Ising universality class. This can be made rigorous by recalling that in the Potts model, four-spin interactions (e.g. the $e_i f_i$ coupling terms) are mapped to vacancies under a duality transformation [353, 263, 82, 195]. This maps the two coupled, dense Potts models to a single, dilute 1-state Potts model in which s tunes the temperature and δr tunes the vacancy density away from the critical point. Tuning $(s, \delta r) \to (0, 0)$ takes the model to its tricritical point and the $\epsilon - \eta$ duality yields the critical Ising model. Finite-size scaling analysis of the tripartite mutual information I_3 near this tricritical point confirms the correlation length critical exponent $\nu \approx 1$ of the Ising universality class (see Fig. 8.5b).

To further verify the Ising universality of the transition, we employ ancilla probes to extract the bulk critical exponent η and the surface critical exponent $\eta_\parallel$. For Ising universality realized via the 2-state Potts model we expect $\eta = \frac{1}{4}$ and $\eta_\parallel = 1$ [65]. These exponents can be determined by examining the mutual information between ancillas which are entangled with the system [138]. In particular, we take periodic boundary conditions (PBC) and evolve the bulk system under circuit dynamics until time $t_0 = 0, 2L$ for $a = \eta, \eta_\parallel$, respectively. We then maximally entangle qubit 1 with ancilla A and qubit $\lfloor L/2 \rfloor + 1$ with ancilla B. From the subsequent time evolution of the mutual information $I_2(t, L)$ between the ancilla, we extract exponents by scaling collapse of the form $I_2(t, L) \sim L^a F[(t - t_0)/L]$. The rescaled mutual information is shown in Fig. 8.6, from which we obtain $\eta \approx 0.23$ and $\eta_\parallel \approx 1.11$. These are comparable to the expected values for the Ising / 2-state Potts model, with $\eta_\parallel$ being unambiguously distinct from the percolation value $\eta_\parallel^{(\mathrm{perc})} = 2/3$.

We note three peculiar points: (i) Replacing $\{X_l X_{l+2}, Z_l Z_{l+1}\}$ by $\{X_l Z_{l+1} X_{l+2}, Z_l Z_{l+1}\}$ yields an identical measurement-frustration graph yet provides a more intuitive picture of the

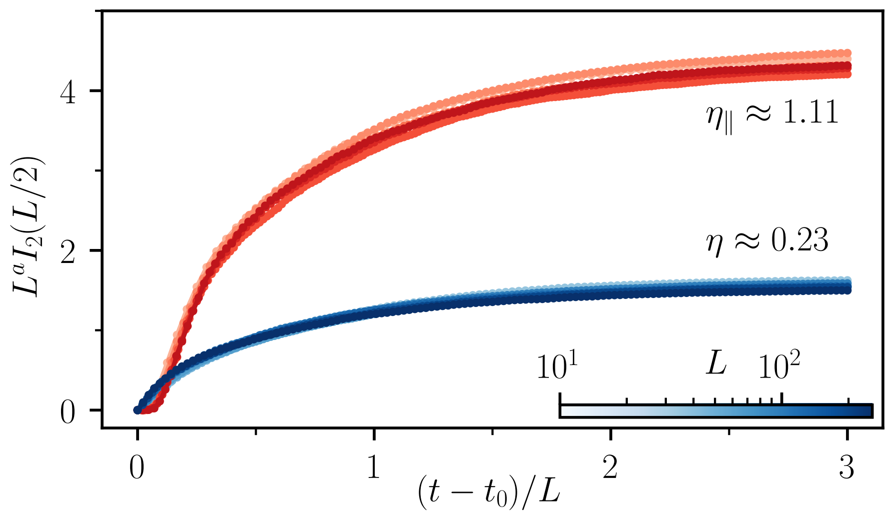

Figure 8.6: **Ancila probes for Ising criticality.** Evolution of the mutual information I_2 between ancilla coupled to the system at separation $L/2$ at time t_0. For the bulk exponent $a = \eta$ we take $t_0 = 2L$ and find $\eta \approx 0.25$, consistent with the expected $\eta = \frac{1}{4}$ for Ising universality. For the surface exponent $a = \eta_\parallel$ we take $t_0 = 0$, finding $\eta_\parallel \approx 1.1$, comparable to the Ising value $\eta_\parallel = 1$.

tricritical 1-state Potts model. The Gaussian set $\{X_l Z_{l+1} X_{l+2}\}$ realizes two identical Majorana chains, which are both coupled by $\{Z_l Z_{l+1}\}$ measurements and simultaneously pushed to the critical point. (ii) The same frustration graph is provided by the set $\{X_l X_{l+2} X_{l+3} X_{l+4}, Z_l\}$, which is the measurement-only version of an Ising chain with multi-spin interactions. The corresponding Hamiltonian has an 8-fold degenerate ground state and is related to the 8-state Potts model [9, 275, 237, 283, 284, 36, 312, 333, 268], which undergoes a first-order phase transition. This highlights the observed trend: orientable measurement-only circuits realize Q-state Potts models, for which Q is reduced compared to their Hamiltonian counterparts. (iii) Despite the critical exponents determining the Ising universality class, we observe an intriguing behavior of the entanglement entropy at the critical point. It grows logarithmically $S_{L/2} = \frac{\tilde{c}}{3} \log(L)$ with prefactor $\tilde{c} = 2$. This is significantly larger than the expected value $\tilde{c}_{Q=2} = (1 + \sqrt{2}) \log(2)/\pi \approx 0.53$ from the loop distribution of the 2-state Potts model [162]. This discrepancy may result from a difference in boundary CFTs between the critical Ising model and the tricritical 1-state Potts model.

Emerging volume law from competing non-Gaussian measurements

For small anisotropy $|\delta r| \ll 1$ and positive $\lambda > 0$, all the terms in the transfer matrix in Eq. (8.2) become relevant and none can be treated as a small perturbation. In this regime, the critical phase of the two 1-state Potts models for $\lambda > 0$ becomes unstable and the circuit enters a volume law entangled state. The volume law is signaled by a negative value of the tripartite information I_3 which scales with system size [138, 362], shown in Fig. 8.4c. The volume law phase is symmetric around $\delta r = 0$. It is separated from the critical phase of the Gaussian circuit by a critical line at $\tilde{s}_c(r) \approx \frac{1}{3}$ and from the area-law phases by the already established critical line $\lambda = 0$. At $(s, \delta r) = (0, 0)$ it terminates at the tricritical point. As a consequence, two additional tricritical points emerge at $(s, \delta r) \approx (\frac{1}{3}, \pm\frac{1}{4})$ where all three types of entanglement phases (area law, volume law, critical) meet. These latter tricritical points are, however, difficult to locate precisely. Along each boundary of the volume law phase, except for the tricritical points, we find the critical scaling behavior of the 1-state Potts model, i.e., percolation, see Fig. 8.5c,d.

While a percolation transition separating a volume-law phase from an area-law phase has been observed previously in measurement-only [156] and monitored unitary circuits [213, 257] a percolation transition separating the volume-law and critical phases is unconventional. We observe that the logarithmic growth of the entanglement entropy at this transition remains largely unaltered, while a volume-law contribution emerges on top. A possible explanation of this scenario and of the scaling behavior at the transition might be that the critical sector is decoupled from an otherwise area-law to volume-law transition.

The emergence of the volume law entangled phase can be explained from two complementary views in the Potts model framework. When starting from the BMW algebra for strongly coupled Potts models, the operator $e_i + f_i$ acts as a perturbation that generates line-crossings [111], i.e., emergent swap operations $\mathcal{R}_{\text{eff}}$. For $|\lambda/\delta r| \sim 1$ and $\lambda > 0$, this yields an effective circuit implementing frequent swap operations, which rapidly generate long, orientable loops and thus extensive entanglement. For $\lambda < 0$ the same types of swaps arise but the negative sign results in the cancellation of many trajectories in the partition function, suppressing the mobility of the worldlines.

In turn, when starting from the tricritical point at $(s, \delta r) = (0, 0)$, both $\delta r \neq 0$ and $s > 0$ correspond to relevant perturbations, as explained above [263]. The imbalance parameter $\delta r \neq 0$ tunes the chemical potential for vacancies in the dual dilute model and drives the system toward an ordered area-law fixed point. Tuning $s > 0$ reintroduces the generators e_i, f_i of the original 1-state Potts models. In the dual framework, taking finite s corresponds to tuning the temperature and pushing the 2-state Potts model into its high temperature phase. This removes the energetic penalty for forming long loops in the bulk and yields a disordered, volume law entangled state at the temporal boundary of the circuit.

8.5 Summary

In this chapter we built upon the loop model mapping developed in the previous chapters to explore the effect on interactions in (1+1)-dimensional Majorana stabilizer circuits. We revealed a more diverse range of phenomena which may be realized in monitored quantum circuits and which admit a clear explanation via mapping to loop models. In short loop phases, we argued that interaction terms are RG irrelevant, with multi-Majorana interaction vertices effectively unraveling, restoring loop model physics on long wavelengths. As a consequence, we demonstrated that parity non-conserving interactions effectively break orientability of the loop model, causing CPLC universality and a Goldstone phase to emerge in a rather generic random Clifford circuit. Considering an interacting Majorana circuit which maps to coupled loop models, we highlighted novel entanglement dynamics and criticality (e.g., BKT and Ising) which may arise when interactions dominate the evolution. As a whole, this chapter has exemplified the power of the Majorana loop model framework for random quantum circuits to provide deeper insight into the entanglement phases of a much broader class of circuits and new pathways toward engineering non-trivial entangled states of matter.

While the focus of this chapter was interacting circuits in $(1+1)$-dimensions, there remain a number of open questions in higher dimensions. Exploration of entanglement in parity-symmetric interacting circuits has been initiated already in Ref. [366], where one finds volume-law entanglement and a correlation length exponent consistent with the loop model in class BDI. Far from the Gaussian limit, large-scale numerical simulation of generic (2+1)-dimensional Clifford circuits give compelling evidence that the measurement-induced transition is in the same universality class as 3D percolation [315]. However, the exponent $\nu = 0.876 \pm 0.004$ [46, 199, 343, 355] for 3D percolation is markedly smaller than what we found in Ch. 7 for non-orientable Majorana circuits via loop simulations. At a basic level, the distinction here may be understood by noting that whereas loops are 1D objects embedded in spacetime, percolation in 3D concerns clusters and their 2D boundaries. Better understanding the flow from loop model universality in (2+1)-dimensional Gaussian Majorana circuits to percolation universality in generic Clifford circuits presents a natural avenue for extending the approach detailed in this chapter.

Chapter 9

Hybrid classical-quantum circuits for colored loop models

Analog quantum circuits, incorporating unitary gates, mid-circuit measurements, and quantum feedback, extend beyond traditional Hamiltonian or dissipative quantum systems. By utilizing measurement as a resource for irreversible quantum dynamics, quantum circuits offer a unique platform for shaping and manipulating entanglement. They enable applications such as quantum error correction [324, 296, 100, 200, 223, 37, 267, 228, 317], expedited state preparation, and the exploration of novel phenomena like measurement-induced entanglement transitions [213, 318, 80, 29, 56, 217, 216, 156, 302, 303, 248, 266, 112, 79]. In particular, the efficient preparation of entanglement patterns associated to circuit analogues of topologically nontrivial or gapless ground states has recently attracted attention due to the challenge of preparing such states by exclusively using unitary operations [277, 49, 331, 337, 225, 114, 158, 330, 329, 226, 157].

In the previous chapters, we explored phases and dynamics of entanglement which arise in random monitored quantum circuits. For practical applications involving measurements, such as state preparation and error correction, it is typically necessary to steer the dynamics toward a target manifold of states, e.g., by feedback operations conditioned on measurement outcomes. Broadly, such feedback and adaptive dynamics have been shown to give rise to a more diverse set of realizable entanglement phases and critical points [94, 55, 314, 289, 269, 288, 240, 148, 272]. This paradigm may be viewed more generally as a combined dynamics arising from the interaction of a quantum system and a classical agent, wherein the classical agent may act upon the quantum system utilizing state information such as measurement outcomes. Careful construction of this interaction may be used to impose new constraints on the quantum dynamics which are otherwise challenging to engineer and has practical applications in classically assisted simulation.

In this chapter we propose a novel route to implement enriched entanglement dynamics – the non-reciprocal coupling of a quantum circuit to a classical dynamical agent. Non-reciprocity indicates that the evolution of the quantum circuit is influenced by the classical agent, but not vice versa. The dynamical agent evolves according to a set of predetermined update rules and typically implements a non-Markovian environment, which governs the build-up of entanglement. We consider a system composed of a Majorana quantum circuit conditioned on a classical spin chain undergoing pair flip dynamics. Utilizing the loop model framework for Majorana circuits [188, 251], we show that this circuit features both a dynamical fragmentation of the Hilbert space and an algebraic growth of the entanglement entropy $S(L) \sim L^{\alpha}$ familiar from $SU(N)$-symmetric quantum models such as, e.g., the Fredkin chain [50, 298, 246, 245]. We validate this picture by extensive numerical simulations of the non-reciprocal circuit.

9.1 Colored loop models

$$e_{lm}^{(\alpha,\mu)} e_{mn}^{(\mu,\mu)} e_{lm}^{(\mu,\beta)} = e_{lm}^{(\alpha,\beta)} \mathbb{1}_n^{(\mu)} \qquad e_{lm}^{(\alpha,\mu)} e_{lm}^{(\mu,\beta)} = n_\mu e_{lm}^{(\alpha,\beta)}$$

Figure 9.1: **Colored Temperley-Lieb algebra.** The standard TL algebra is enriched here by endowing each loop with a color which must be the same everywhere along the loop. Monoid operators $e_{lm}^{(\alpha,\beta)}$ are now labeled by the color of the closing (β) and opening (α) arcs. Loops retain the ambient isotopy property (left) and are now given a color-dependent fugacity n_μ (right).

Entanglement dynamics in the Majorana circuits studied thus far have been constrained by the requirement that the corresponding loop model have fugacity $n = 1$, which is fixed by the properties of projective measurement. In order to go beyond the $n = 1$ paradigm and achieve enriched quantum dynamics in Majorana circuits, we introduce a non-reciprocal circuit architecture implementing a *colored* TL algebra [134, 136, 135]. This algebra is generated by operators $e_l^{(\alpha,\beta)}$ which are represented diagrammatically by the closure of a loop with color β and the opening of a loop with color α. As depicted in Fig. 9.2, these operators satisfy the multi-color monoid algebra relations,

$$e_{lm}^{(\alpha,\mu)} e_{mn}^{(\mu,\mu)} e_{lm}^{(\mu,\beta)} = e_{lm}^{(\alpha,\beta)} \mathbb{1}_n^{(\mu)}, \qquad e_{lm}^{(\alpha,\mu)} e_{lm}^{(\nu,\beta)} = n_\mu \delta_{\mu,\nu} e_{lm}^{(\alpha,\beta)}, \tag{9.1}$$

where $\mathbb{1}_n^{(\mu)}$ is a projector onto color μ at site n and n_μ are color-dependent loop fugacities.

Recall that the monitored Majorana circuits studied in the previous chapters have loop fugacity $n = 1$. Let us then consider N distinct colors each with fugacity $n_\mu = 1$. The ensemble of colored loop configurations produced by this algebra reproduces that of the uncolored loop model with fugacity N via the color decomposition of the TL generators [256, 179, 101],

$$E_{lm} = \sum_{\alpha,\beta=1}^{N} e_{lm}^{(\alpha\beta)}, \quad E_{lm}^2 = N E_{lm}, \quad E_{lm}E_{mn}E_{lm} = E_{lm}. \tag{9.2}$$

Such a colored TL algebra arises, e.g., in the pair-flip model [62, 144], where the color symmetry imposes kinetic constraints resulting in Hilbert space fragmentation and unconventional entanglement scaling in the ground-state.

9.2 Non-reciprocal circuit

In order to implement the algebra in Eq. (9.1), we augment the quantum circuit of L Majorana fermions with a "control" chain of L classical N-state Potts spins $\tau_l \in \{1, \ldots, N\}$. The classical spins influence the evolution of the Majorana chain via a non-reciprocal interaction: At each time step t, a "brick" $\{\gamma_l, \gamma_{l+1}, \tau_l, \tau_{l+1}\}$ consisting of two adjacent Majorana fermions and two corresponding Potts spins is chosen randomly from all $L-1$ possible pairings (OBC). *If and only-if* the two Potts spins have the same "color" ($\tau_l = \tau_{l+1} = \alpha$), two updates are performed: (i) the parity operator $i\gamma_l\gamma_{l+1}$ is measured, (ii) both Potts spins are flipped to a randomly and uniformly chosen color $\tau_l, \tau_{l+1} \to \beta \in \{1, ..., N\}$. This implements the generator of the colored TL algebra,

$$e_l^{(\alpha,\beta)} = |\alpha\alpha\rangle \langle\beta\beta|_{l,l+1} \otimes \mathcal{P}_{l,l+1}. \tag{9.3}$$

The Potts spins thus decorate the Majorana worldlines, yielding a colored loop model for the effective dynamics.

Ensemble Hamiltonian

Let $\epsilon_{\alpha\beta}^{(l)} \in [0,1]$ be the probability applying $e_l^{(\alpha,\beta)}$ site l in a unit time step. Averaging over all circuit trajectories then reproduces a loop ensemble generated by an effective transfer matrix T_l acting on each pair of neighboring sites as $T_l = \mathbb{1} + \epsilon_{\alpha\beta}^{(l)} e_l^{(\alpha,\beta)}$. This is exactly the transfer matrix arising from imaginary-time evolution with a Hamiltonian

$$H = \sum_l \sum_{\alpha,\beta} \epsilon_{\alpha\beta}^{(l)} e_l^{(\alpha,\beta)}. \tag{9.4}$$

Drawing the probabilities uniformly in space $\epsilon_{\alpha\beta}^{(l)} \equiv \epsilon_{\alpha\beta}$, Eq. (9.4) is the so-called pair-flip (PF) Hamiltonian. Choosing further identical transition rates $\epsilon_{\alpha\beta} \equiv \epsilon$ yields the TL Hamiltonian $H = \epsilon \sum_l E_l$. The transfer matrix picture elucidates that each trajectory of the random circuit represents an element of the stochastic series expansion for the partition function $\sim \exp(-\beta H)$ in the limit $\beta \to \infty$. The ensemble Hamiltonian thus is the Markov generator

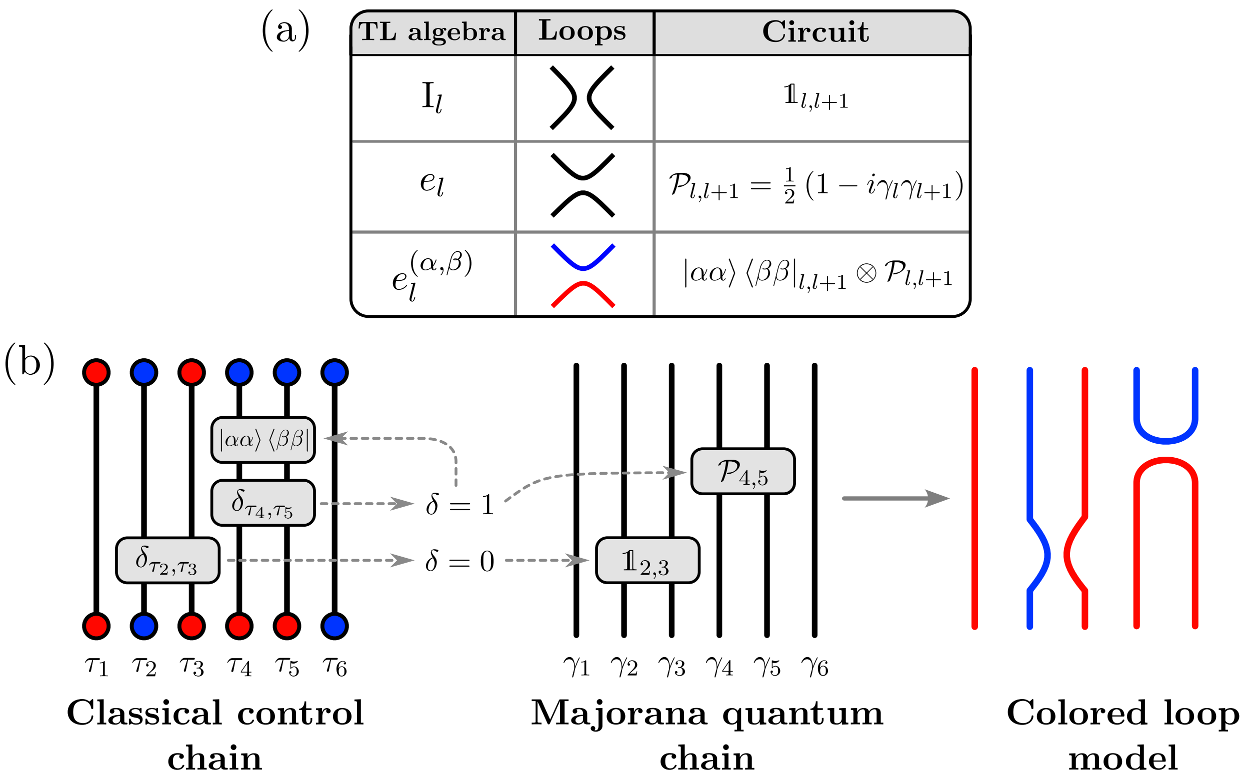

Figure 9.2: **Non-reciprocal circuit for colored loop models.** (a) A dictionary relating the TL algebra elements to their loop representation and corresponding circuit operation. (b) Effective non-reciprocal circuit for the colored loop model. If and only-if a brick $\{\tau_l, \tau_{l+1}, \gamma_l, \gamma_{l+1}\}$ has two identical Potts spins $\tau_l = \tau_{l+1}$ an update is performed: the parity $i\gamma_l\gamma_{l+1}$ is measured and the Potts spins are randomly flipped $\tau_l, \tau_{l+1} \to \beta$.

for a classical stochastic process which produces individual circuit trajectories (i.e. colored loop configurations) [274, 127, 367]. The statistical ensemble of wave functions produced by the circuit is identical to the ensemble that forms the quantum ground state of the Hamiltonian (9.4) by coherent superposition.

Symmetries and Fragmentation

The TL generators $e_l^{(\alpha,\beta)}$ induce pair-flip dynamics that conserve $N-1$ independent $U(1)$ charges $Q_\alpha = \sum_l (-1)^l |\alpha\rangle\langle\alpha|_l$ [146, 244]. Their presence implies a continuity equation yielding diffusive charge transport. The TL Hamiltonian maps exactly to the spin-1/2 Heisenberg chain for $N = 2$ and the spin-1 biquadratic chain $H_{N=3} = -\sum_l \left(\vec{S}_l \cdot \vec{S}_{l+1}\right)^2$ for $N = 3$ [193, 273, 30, 73], and the $U(1)^{N-1}$ symmetry is promoted to $SU(N)$. We note, however, that for the circuit, $SU(N)$ is a symmetry of the ensemble, not of individual trajectories. In addition to the global symmetries, there is an extensive number of additional conserved quantities, which for $N = 2$ can be attributed to integrability.

For $N \geq 3$, the TL and PF models are paradigmatic examples of strong Hilbert space fragmentation [244, 144], with the largest Krylov sector comprising a measure-zero subset of the Hilbert space in the thermodynamic limit [244, 62]. This separates $N \geq 3$ from $N = 2$: $N = 2$ has a commutant algebra of dimension $L + 1$ and thus fragmentation is absent. $N \geq 3$ gives an exponentially large commutant algebra of dimension $((N - 1)^{L+1} - 1)/(N - 2)$. We thus expect transport and the buildup of entanglement to be slower (subdiffusive) for $N \geq 3$ compared to diffusion for $N = 2$.

A note on the nature of fragmentation: While the PF model with $N \geq 3$ displays fragmentation in a local product basis – referred to as "classically" fragmented – the TL model displays fragmentation in an entangled basis – referred to as "quantum" fragmented. In our setup, the Potts spins undergo a stochastic classical pair-flip dynamics, with the colors always in a product state. Even though the ensemble retains a statistical $SU(N)$ symmetry, the trajectory-level dynamics ought to reflect the classical fragmentation of the PF model. This fragmentation is imprinted upon the entangled quantum dynamics of the Majorana chain via the non-reciprocal interaction.

9.3 Kinetically Constrained Height Model

Besides the link to fragmented quantum Hamiltonians, the dynamics of Majorana worldlines is directly connected to the dynamics of height models describing surface growth. This grants access to dynamical scaling exponents governing the growth of entanglement in the circuit.

Consider a stabilizer state and its loop configuration in the uncolored Majorana chain. We define a height field $h_l = S_{[1,l]}$ as the entanglement entropy of the first l Majorana fermions. The height field satisfies the boundary conditions $h_0 = h_L = 0$ and the restricted solid-on-solid (RSOS) constraint $h_{l+1} - h_l = \pm 1$. Edges connecting adjacent heights then define a Dyck path [127, 367] (i.e., one with $h_l \geq 0$), for which left (right) ends of loops correspond to an increase (decrease) in the height, see Fig. 9.3.

A projective measurement $\mathcal{P}_{l,l+1}$ then implements one of the following two processes: (i) single-site adsorption (Fig. 9.3a) or (ii) a desorption avalanche (Fig. 9.3b). Adsorption converts a local minimum $\{\dots, h, h - 1, h, \dots\}$ to a local maximum $\{\dots, h, h + 1, h, \dots\}$, increasing entanglement locally across a cut. Desorption occurs when measurement acts on a region of constant slope in the height field (e.g. $\{\dots, h - 1, h, h + 1, \dots\}$), corresponding to two nested loops, e.g., the two red loops in Fig. 9.3b. Desorption is disentangling and may cause a non-local "avalanche" wherein the whole region enclosed by the inner loop has its height reduced by two since the two previously nested loops no longer cross the intervening region.

The colored loop model in the non-reciprocal circuit then yields colored Dyck paths, where the edge connecting h_l and h_{l+1} has the color given by τ_l. This coloring imposes a kinetic constraint such that adsorption and desorption can occur only when adjacent edges

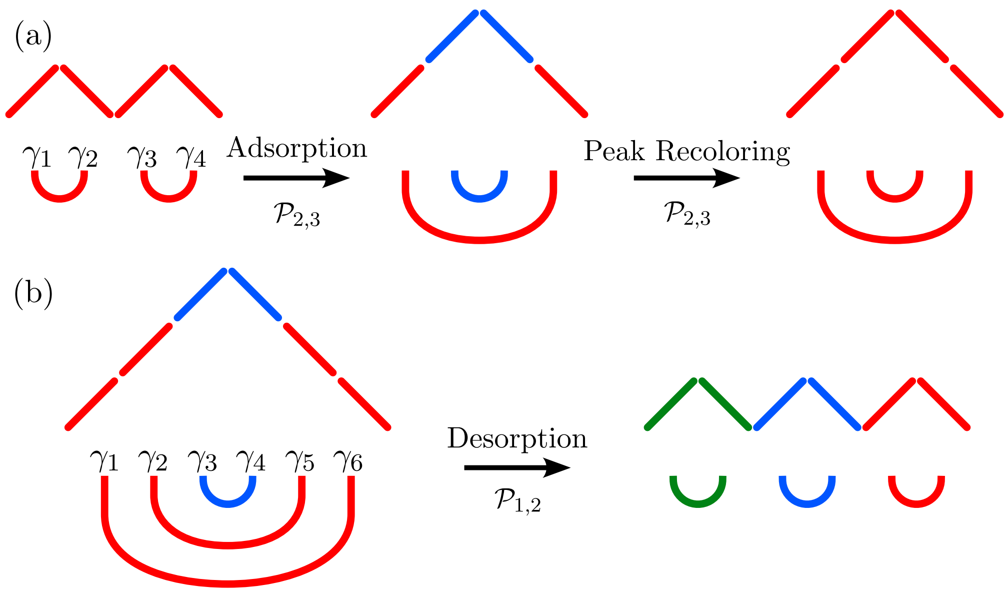

Figure 9.3: **Height model and Dyck path representation of the colored circuit.** Given a loop configuration, the corresponding Dyck path is defined by increasing (decreasing) the path height at the left (right) end of a loop. Measurement implements one of the following operations on the height field. (a) At a local minimum, measurement implements single-site adsorption, wherein the local height increases. At a local maximum, measurement can recolor the peak of the path. (b) Otherwise, measurements trigger a desorption avalanche, wherein the height is decreased in the whole region between the endpoints of the loop acted upon.

in the Dyck path have the same color. Moreover, we now have a third process wherein local maxima can be recolored without changing the heights (see Fig. 9.3a).

Surface growth models describing a height field h_l give rise to Family-Vicsek (FV) scaling $f(L,t) = L^{\alpha}F(tL^{-z})$ for quantities $f(L,t)$ related to surface roughness [338, 102, 120, 119, 121]. The scaling function $F(x)$ grows algebraically as x^{β} for small argument and approaches a constant for $x \gg 1$. The growth exponent β is related to the roughness exponent α and the dynamical exponent z via $\beta = \alpha/z$. The relation to surface growth provides lower bounds on the height field h_l, i.e., the entanglement growth, and estimates for the universal scaling exponents.

Entanglement bounds from surface growth

The color dynamics on the control chain is reversible, yielding detailed balance and a uniform distribution over states in the accessible Krylov sector. The largest Krylov sector in the classical chain yields Dyck paths with the average height growing as $\sqrt{L}$ for all N [62]. However, for a purely classical chain, i.e., without the Majorana worldlines in the quantum chain, the mapping between Dyck paths and color configurations is not unique. For example, the color configuration $|1111\rangle$ might arise in two different loop configurations shown in Fig. 9.3a. In Ref. [62] each color configuration is mapped to the Dyck path with the smallest possible height, providing a lower bound of $\sqrt{L}$ for the height field and the entanglement entropy.

Critical exponents from surface growth

For $N = 2$, the TL Hamiltonian (9.4) corresponds to the spin-1/2 Heisenberg chain, which is a Markov generator for the symmetric simple exclusion process (SSEP) [171, 140, 181, 262]. The dynamics of the SSEP lie in the Edwards-Wilkinson (EW) universality class, with exponents $z = 2$, $\alpha = \frac{1}{2}$ and $\beta = \frac{1}{4}$ [98, 171, 139, 140, 181] [1]. For $N \geq 3$, Hilbert space fragmentation will modify the critical exponents compared to $N = 2$. The dynamics of the Hamiltonian (9.4) with $N = 3$ has been explored in the context of classical deposition-evaporation models for colored dimers and trimers, where numerical results show subdiffusion with exponent $z \approx 2.5$ and growth exponent $\beta \approx 0.19$ [196, 235, 234, 31]. More recent studies on dynamics in the Fredkin chain, which admits a closely related description in terms of kinetically constrained surface growth, yield a dynamical exponent $z \approx 2.7$ in the zero magnetization sector [316, 73, 4].

9.4 Universality in the hybrid circuit entanglement

Steady-state

After a time $t \sim L^z$, the average entanglement entropy saturates to a sub-extensive value which scales algebraically in system size as $S_\ell(t \to \infty) \sim \left(\frac{\ell(L-\ell)}{L}\right)^{\alpha_N}$. In Fig. 9.4, we show the scaling of $S_{L/2}$ with respect to L as well as the data collapse of the full entanglement profile S_ℓ. For $N = 2$, we find $\alpha_2 = 0.506 \pm 0.003$, consistent with the expected EW universality. With more colors, $N \geq 3$, we observe a slightly larger exponent $\alpha_3 = 0.570 \pm 0.002$. Both values of α_N are consistent with that predicted by the dynamical scaling relation $\alpha = z\beta$. Nonetheless, it is surprising to find $\alpha_3 > \frac{1}{2}$, as one might expect $\alpha = \frac{1}{2}$ from previous numerical studies and the height distribution arising in the Dyck path ensemble.

The algebraic scaling of entanglement found here is *robust* so long as the color symmetry is preserved. For example, dimerization of the measurement probability on odd and even sublattices is a relevant perturbation in the $N = 1$ limit, driving the system into one of two topologically distinct area-law phases. In the colored loop ensemble with $N \geq 2$, however,

[1] By contrast, the asymmetric simple exclusion process (ASEP) exhibits KPZ dynamics. Tuning away from the symmetric point requires conditioning the measurement rates on the local height profile, akin to the unitary dynamics in Ref. [241]. However, the local Potts configuration does *not* confer information about the height field, thereby protecting the EW universality expected for our circuit with $N = 2$.

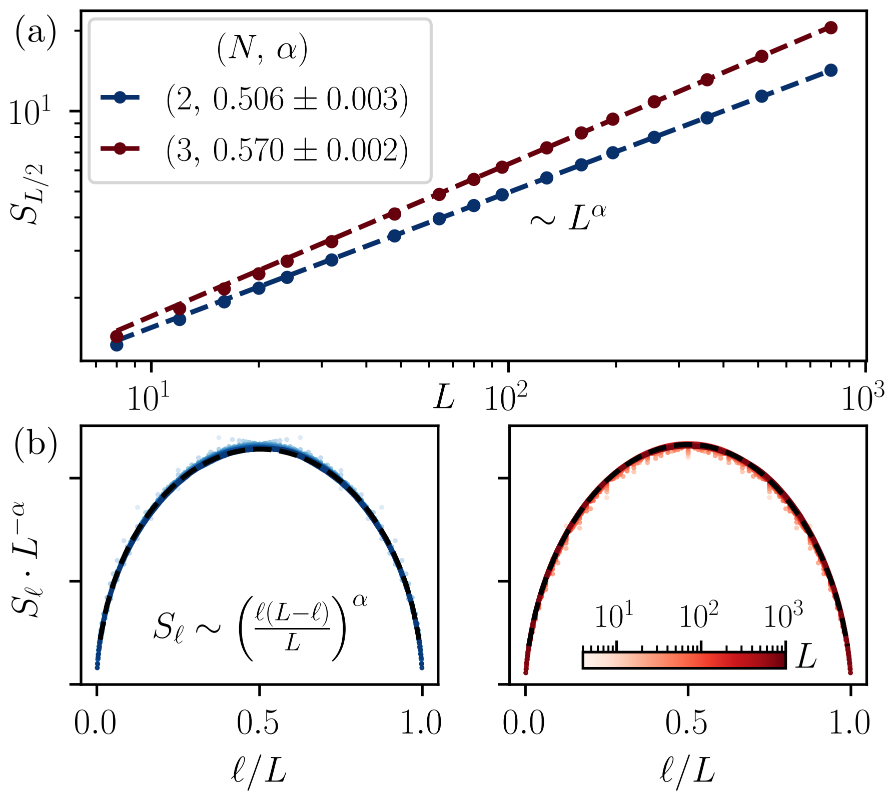

Figure 9.4: (a) Algebraic scaling of the steady-state half-chain entanglement entropy $S_{L/2} \sim L^\alpha$ for $N = 2, 3$ colors. The roughness exponent α_N is determined by fitting a power-law to the data for system sizes $L > L_0 = 100$, for which the resulting exponent is well converged. With $N = 2$ (blue), we find $\alpha = 0.506 \pm 0.003$, while for $N = 3$ (red) we instead find $\alpha = 0.570 \pm 0.002$. (b) Data collapse of the entanglement profile S_ℓ confirms scaling of the form $S_\ell \sim \left(\frac{\ell(L-\ell)}{L}\right)^\alpha$ (black dashed lines).

such dimerization fails to alleviate the kinetic constraints, instead it only renormalizes the effective diffusion constant (or timescale for $N \geq 3$).

Dynamics

We provide detailed simulation results of both $N = 2$ and $N = 3$ colors. Here $N = 3$ is a representative for generic $N \geq 3$, while $N = 2$ is special since it has distinct symmetries and no Hilbert space fragmentation. In general for $N \geq 2$ we observe an algebraic growth of the entanglement entropy with time, $S_{L/2}(t) \sim t^{\beta_N}$, as shown in Fig. 9.5a. For the growth

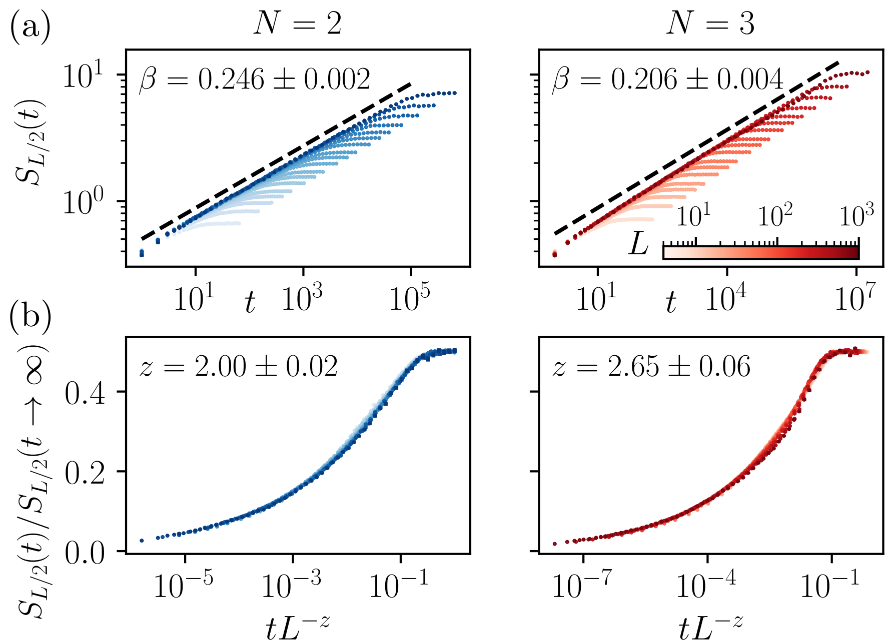

Figure 9.5: Growth of the half-chain entanglement entropy beginning from a trivial initial state for $N = 2$ (left) and $N = 3$ (right). (a) We observe an algebraic scaling $S_{L/2}(t) \sim t^{\beta_N}$, where the growth exponent is $\beta_2 = 0.246 \pm 0.002$ and $\beta_3 = 0.206 \pm 0.004$. (b) Rescaling of time yields a data collapse of the normalized entanglement entropy $S_{L/2}(t)/S_{L/2}(t \to \infty)$. For $N = 2$ we find dynamical exponent $z = 2.00 \pm 0.02$, while for $N = 3$ we find $z = 2.65 \pm 0.06$.

exponent β_N, we find $\beta_2 = 0.246 \pm 0.002$ for $N = 2$ [2] , consistent with the expected value of $\beta_2 = 1/4$ arising from the EW universality class. By contrast, for $N \geq 3$ we observe slower growth of the entanglement with $\beta_3 = 0.206 \pm 0.004$, comparable to the growth exponent found in the colored dimer deposition-evaporation model.

We assume FV scaling for the entanglement growth, yielding $S_{L/2}(t) \sim L^\alpha f(tL^{-z})$. The scaling function $f(x)$ approaches a constant as the argument x goes to infinity. Then we may extract the dynamical critical exponent z independent of the roughness exponent α by considering scaling collapse of the ratio $S_{L/2}(t)/S_{L/2}(t \to \infty) = f(tL^{-z})$, shown in Fig. 9.5b. [3] For $N = 2$, we observe diffusive dynamics with $z = 2.00 \pm 0.02$ as expected. With more colors,

[2] The reported values of β_N are obtained by fitting a power-law to the dynamics $S_{L/2}(t)$ over the growth regime $1 \ll t \ll L^z$. The lower-bound is taken to exclude transient initial state dependence, while the upper bound is taken to exclude late time saturation of the entanglement entropy. For $N = 2$ we take a window $20 < t < 0.1L^z$, and for $N = 3$ we take $100 < t < 0.03L^z$. The uncertainty is estimated from the fit uncertainty and further validated by (i) extrapolating to the thermodynamic limit and (ii) varying the upper and lower bounds for the fitted data range.

[3] Here the exponent z is determined by fitting a cubic B-spline and minimizing the squared residuals cost function. The reported uncertainty in z is estimated by the interval over which the cost function increases four-fold relative to the minimum.

we instead find subdiffusive behavior, with $N = 3$ giving $z = 2.65 \pm 0.06$. This value is consistent with the dynamical exponent in the Fredkin chain [316, 73, 4] and dimer models [196, 235, 234, 31].

9.5 Outlook

We have introduced a non-reciprocal Majorana circuit realizing the colored Temperley-Lieb algebra, for which symmetries and kinetic constraints of the classical dynamics are imprinted upon the quantum chain. This leads to robust power-law entanglement scaling and distinct dynamical exponents. Similar ideas can emerge in purely unitary random [144] and Floquet [203] circuits, where kinetic constraints modify ergodicity and thermalization time scales. More generally, we may consider coupling a stochastic classical cellular automaton on the control chain to the measurement-dynamics on the quantum chain, yielding a broader family of entanglement dynamics and related surface-growth models. A further step, enabled by spacetime locality of the interaction would be to promote the classical "control" chain to a quantum system, yielding a strictly quantum circuit. For example, with $N = 2$ we may promote the Potts spins to a chain of qubits where σ_l^z encodes the "color". Then projective measurement of $\sigma_l^z \sigma_{l+1}^z$ determines whether or not two adjacent spins have the same color.

The power-law entanglement scaling we observed here was protected by the fact that the local color configuration on the control chain did not provide direct access to the local height field, preventing us from steering toward area-law or volume-law entanglement. By contrast, a circuit using the Potts spins to encode left and right endpoints of Majorana loops would permit more precise tuning of transition rates in the surface growth model. Notably, however, this would introduce non-local updates into the evolution of the classical agent. The interplay of symmetry, locality, and operational constraints on the classical agent and its interactions with the quantum system is a key consideration. The non-reciprocal architecture we introduce here opens a new avenue for realizing a rich breadth of entanglement dynamics in quantum circuits.

An implementation of the reciprocal circuit can be envisioned for current quantum computing platforms with high fidelity mid-circuit measurements in the computational basis, including trapped ions [122, 296, 242], neutral atom arrays [89, 267, 37, 132, 221, 317], and superconducting qubits [356]. Here $2L$ Majorana fermions arise from a Jordan-Wigner transformation of an L-qubit array, i.e., by translating the nearest-neighbor fermionic parities to qubit operators $i\gamma_{2l}\gamma_{2l+1} \to \sigma_l^x \sigma_{l+1}^x$ and $i\gamma_{2l-1}\gamma_{2l} \to \sigma_l^z$, projective measurements of which are available [324, 296, 200, 223].

Bibliography

[1] Scott Aaronson and Daniel Gottesman. “Improved simulation of stabilizer circuits”. In: *Phys. Rev. A* 70 (5 Nov. 2004), p. 052328. DOI: 10.1103/PhysRevA.70.052328. URL: https://link.aps.org/doi/10.1103/PhysRevA.70.052328.

[2] David Aasen et al. “Electrical Probes of the Non-Abelian Spin Liquid in Kitaev Materials”. In: *Phys. Rev. X* 10 (3 July 2020), p. 031014. DOI: 10.1103/PhysRevX.10.031014. URL: https://link.aps.org/doi/10.1103/PhysRevX.10.031014.

[3] David Aasen et al. “Milestones Toward Majorana-Based Quantum Computing”. In: *Phys. Rev. X* 6 (3 Aug. 2016), p. 031016. DOI: 10.1103/PhysRevX.6.031016. URL: https://link.aps.org/doi/10.1103/PhysRevX.6.031016.

[4] Khagendra Adhikari and K. S. D. Beach. “Slow dynamics of the Fredkin spin chain”. In: *Physical Review B* 104.11 (Sept. 2021). ISSN: 2469-9969. DOI: 10.1103/physrevb.104.115149. URL: http://dx.doi.org/10.1103/PhysRevB.104.115149.

[5] Ian Affleck. “Nonlinear σ model at $\theta=\pi$: Euclidean lattice formulation and solid-on-solid models”. In: *Phys. Rev. Lett.* 66 (19 May 1991), pp. 2429–2432. DOI: 10.1103/PhysRevLett.66.2429. URL: https://link.aps.org/doi/10.1103/PhysRevLett.66.2429.

[6] Utkarsh Agrawal et al. “Entanglement and Charge-Sharpening Transitions in U(1) Symmetric Monitored Quantum Circuits”. In: *Phys. Rev. X* 12 (4 Oct. 2022), p. 041002. DOI: 10.1103/PhysRevX.12.041002. URL: https://link.aps.org/doi/10.1103/PhysRevX.12.041002.

[7] André Ahlbrecht, Lachezar S. Georgiev, and Reinhard F. Werner. “Implementation of Clifford gates in the Ising-anyon topological quantum computer”. In: *Phys. Rev. A* 79.3 (Mar. 2009), p. 032311. ISSN: 2469-9934. DOI: 10.1103/PhysRevA.79.032311.

[8] O. Alberton, M. Buchhold, and S. Diehl. “Entanglement Transition in a Monitored Free-Fermion Chain: From Extended Criticality to Area Law”. In: *Phys. Rev. Lett.* 126 (17 Apr. 2021), p. 170602. DOI: 10.1103/PhysRevLett.126.170602. URL: https://link.aps.org/doi/10.1103/PhysRevLett.126.170602.

[9] Francisco C. Alcaraz. "Order of phase transition for systems with multispin interactions: Monte Carlo simulations". In: *Phys. Rev. B* 34 (7 Oct. 1986), pp. 4885–4888. DOI: 10.1103/PhysRevB.34.4885. URL: https://link.aps.org/doi/10.1103/PhysRevB.34.4885.

[10] Jason Alicea. "Majorana fermions in a tunable semiconductor device". In: *Phys. Rev. B* 81.12 (Mar. 2010), p. 125318. ISSN: 2469-9969. DOI: 10.1103/PhysRevB.81.125318.

[11] Jason Alicea. "New directions in the pursuit of Majorana fermions in solid state systems". In: *Rep. Prog. Phys.* 75.7 (June 2012), p. 076501. ISSN: 0034-4885. DOI: 10.1088/0034-4885/75/7/076501.

[12] Jason Alicea et al. "Non-Abelian statistics and topological quantum information processing in 1D wire networks". In: *Nat. Phys.* 7 (May 2011), pp. 412–417. ISSN: 1745-2481. DOI: 10.1038/nphys1915.

[13] D J Amit. "Renormalization of the Potts model". In: *Journal of Physics A: Mathematical and General* 9.9 (Sept. 1976), p. 1441. DOI: 10.1088/0305-4470/9/9/006. URL: https://dx.doi.org/10.1088/0305-4470/9/9/006.

[14] P. W. Anderson. "Resonating valence bonds: A new kind of insulator?" In: *Materials Research Bulletin* 8.2 (1973), pp. 153–160. ISSN: 0025-5408. DOI: https://doi.org/10.1016/0025-5408(73)90167-0. URL: https://www.sciencedirect.com/science/article/pii/0025540873901670.

[15] Eddy Ardonne, Paul Fendley, and Eduardo Fradkin. "Topological order and conformal quantum critical points". In: *Annals of Physics* 310.2 (2004), pp. 493–551. ISSN: 0003-4916. DOI: 10.1016/j.aop.2004.01.004.

[16] S. Bachus et al. "Angle-dependent thermodynamics of α–$RuCl_3$". In: *Phys. Rev. B* 103.5 (Feb. 2021), p. 054440. ISSN: 2469-9969. DOI: 10.1103/PhysRevB.103.054440.

[17] S. Bachus et al. "Thermodynamic Perspective on Field-Induced Behavior of α–$RuCl_3$". In: *Phys. Rev. Lett.* 125.9 (Aug. 2020), p. 097203. ISSN: 1079-7114. DOI: 10.1103/PhysRevLett.125.097203.

[18] S.-H. Baek et al. "Evidence for a Field-Induced Quantum Spin Liquid in α-$RuCl_3$". In: *Phys. Rev. Lett.* 119 (3 July 2017), p. 037201. DOI: 10.1103/PhysRevLett.119.037201. URL: https://link.aps.org/doi/10.1103/PhysRevLett.119.037201.

[19] Leon Balents. "Spin liquids in frustrated magnets". In: *Nature* 464.7286 (Mar. 2010), pp. 199–208. ISSN: 1476-4687. DOI: 10.1038/nature08917. URL: https://doi.org/10.1038/nature08917.

[20] Christian Balz et al. "Finite field regime for a quantum spin liquid in α–$RuCl_3$". In: *Phys. Rev. B* 100 (6 Aug. 2019), p. 060405. DOI: 10.1103/PhysRevB.100.060405. URL: https://link.aps.org/doi/10.1103/PhysRevB.100.060405.

[21] Christian Balz et al. "Finite field regime for a quantum spin liquid in α-$RuCl_3$". In: *Phys. Rev. B* 100 (6 Aug. 2019), p. 060405. DOI: 10.1103/PhysRevB.100.060405. URL: https://link.aps.org/doi/10.1103/PhysRevB.100.060405.

[22] A. Banerjee et al. "Proximate Kitaev quantum spin liquid behaviour in a honeycomb magnet". In: *Nature materials* 7 (Apr. 2016), pp. 733–740. DOI: 10.1038/nmat4604. URL: http://dx.doi.org/10.1038/nmat4604.

[23] Arnab Banerjee et al. "Excitations in the field-induced quantum spin liquid state of α–$RuCl_3$". In: *npj Quantum Materials* 3.1 (Feb. 2018), p. 8. DOI: 10.1038/s41535-018-0079-2. URL: https://doi.org/10.1038/s41535-018-0079-2.

[24] Arnab Banerjee et al. "Neutron scattering in the proximate quantum spin liquid α–$RuCl_3$". In: *Science* 356.6342 (2017), pp. 1055–1059. ISSN: 0036-8075. DOI: 10.1126/science.aah6015.

[25] Mitali Banerjee et al. "Observation of half-integer thermal Hall conductance". In: *Nature* 559 (2018), p. 205. DOI: 10.1038/s41586-018-0184-1.

[26] Saikat Banerjee and Shi-Zeng Lin. "Emergent orbital magnetization in Kitaev quantum magnets". In: *SciPost Phys.* 14 (2023), p. 127. DOI: 10.21468/SciPostPhys.14.5.127. URL: https://scipost.org/10.21468/SciPostPhys.14.5.127.

[27] Yimu Bao, Soonwon Choi, and Ehud Altman. "Symmetry enriched phases of quantum circuits". In: *Annals of Physics* (2021), p. 168618. ISSN: 0003-4916. DOI: https://doi.org/10.1016/j.aop.2021.168618. URL: https://www.sciencedirect.com/science/article/pii/S0003491621002244.

[28] Yimu Bao, Soonwon Choi, and Ehud Altman. "Symmetry enriched phases of quantum circuits". In: *Annals of Physics* 435 (Dec. 2021), p. 168618. ISSN: 0003-4916. DOI: 10.1016/j.aop.2021.168618. URL: http://dx.doi.org/10.1016/j.aop.2021.168618.

[29] Yimu Bao, Soonwon Choi, and Ehud Altman. "Theory of the phase transition in random unitary circuits with measurements". In: *Phys. Rev. B* 101 (10 Mar. 2020), p. 104301. DOI: 10.1103/PhysRevB.101.104301. URL: https://link.aps.org/doi/10.1103/PhysRevB.101.104301.

[30] Michael N. Barber and Murray T. Batchelor. "Spectrum of the biquadratic spin-1 antiferromagnetic chain". In: *Phys. Rev. B* 40 (7 Sept. 1989), pp. 4621–4626. DOI: 10.1103/PhysRevB.40.4621. URL: https://link.aps.org/doi/10.1103/PhysRevB.40.4621.

[31] Mustansir Barma and Deepak Dhar. "Slow Relaxation in a Model with Many Conservation Laws: Deposition and Evaporation of Trimers on a Line". In: *Physical Review Letters* 73.15 (Oct. 1994), pp. 2135–2138. ISSN: 0031-9007. DOI: 10.1103/physrevlett.73.2135. URL: http://dx.doi.org/10.1103/PhysRevLett.73.2135.

[32] Alessandro Barp et al. “A numerical study of the 3D random interchange and random loop models”. In: *Journal of Physics A: Mathematical and Theoretical* 48.34 (Aug. 2015), p. 345002. DOI: 10.1088/1751-8113/48/34/345002. URL: https://doi.org/10.1088%2F1751-8113%2F48%2F34%2F345002.

[33] Tim Bauer et al. “Scanning tunneling spectroscopy of Majorana zero modes in a Kitaev spin liquid”. In: *Phys. Rev. B* 107 (5 Feb. 2023), p. 054432. DOI: 10.1103/PhysRevB.107.054432. URL: https://link.aps.org/doi/10.1103/PhysRevB.107.054432.

[34] E J Beamond, A L Owczarek, and J Cardy. “Quantum and classical localization and the Manhattan lattice”. In: *Journal of Physics A: Mathematical and General* 36.41 (Oct. 2003), p. 10251. DOI: 10.1088/0305-4470/36/41/001. URL: https://dx.doi.org/10.1088/0305-4470/36/41/001.

[35] C. W. J. Beenakker. “Search for Majorana Fermions in Superconductors”. In: *Annu. Rev. Condens. Matter Phys.* Volume 4, 2013 (Apr. 2013), pp. 113–136. DOI: 10.1146/annurev-conmatphys-030212-184337.

[36] H.W.J. Blöte et al. “Critical behaviour of two Ising models with multispin interactions”. In: *Physica A: Statistical Mechanics and its Applications* 139.2 (1986), pp. 395–411. ISSN: 0378-4371. DOI: https://doi.org/10.1016/0378-4371(86)90128-7. URL: https://www.sciencedirect.com/science/article/pii/0378437186901287.

[37] Dolev Bluvstein et al. “Logical quantum processor based on reconfigurable atom arrays”. In: *Nature* 626.7997 (Dec. 2023), pp. 58–65. ISSN: 1476-4687. DOI: 10.1038/s41586-023-06927-3. URL: http://dx.doi.org/10.1038/s41586-023-06927-3.

[38] H. Bombin. “Topological Order with a Twist: Ising Anyons from an Abelian Model”. In: *Phys. Rev. Lett.* 105 (3 July 2010), p. 030403. DOI: 10.1103/PhysRevLett.105.030403. URL: https://link.aps.org/doi/10.1103/PhysRevLett.105.030403.

[39] Parsa Bonderson, Michael Freedman, and Chetan Nayak. “Measurement-only topological quantum computation via anyonic interferometry”. In: *Annals of Physics* 324.4 (Apr. 2009), pp. 787–826. ISSN: 0003-4916. DOI: 10.1016/j.aop.2008.09.009. URL: http://dx.doi.org/10.1016/j.aop.2008.09.009.

[40] Parsa Bonderson, Alexei Kitaev, and Kirill Shtengel. “Detecting Non-Abelian Statistics in the $\nu = 5/2$ Fractional Quantum Hall State”. In: *Phys. Rev. Lett.* 96 (1 Jan. 2006), p. 016803. DOI: 10.1103/PhysRevLett.96.016803. URL: https://link.aps.org/doi/10.1103/PhysRevLett.96.016803.

[41] Parsa Bonderson, Alexei Kitaev, and Kirill Shtengel. “Detecting Non-Abelian Statistics in the $\nu = 5/2$ Fractional Quantum Hall State”. In: *Phys. Rev. Lett.* 96.1 (Jan. 2006), p. 016803. ISSN: 1079-7114. DOI: 10.1103/PhysRevLett.96.016803.

[42] Parsa Bonderson, Kirill Shtengel, and J. K. Slingerland. "Probing Non-Abelian Statistics with Quasiparticle Interferometry". In: *Phys. Rev. Lett.* 97 (1 July 2006), p. 016401. DOI: 10.1103/PhysRevLett.97.016401. URL: https://link.aps.org/doi/10.1103/PhysRevLett.97.016401.

[43] Parsa Bonderson, Kirill Shtengel, and J. K. Slingerland. "Probing Non-Abelian Statistics with Quasiparticle Interferometry". In: *Phys. Rev. Lett.* 97.1 (July 2006), p. 016401. ISSN: 1079-7114. DOI: 10.1103/PhysRevLett.97.016401.

[44] Parsa Bonderson et al. "Implementing Arbitrary Phase Gates with Ising Anyons". In: *Phys. Rev. Lett.* 104 (18 May 2010), p. 180505. DOI: 10.1103/PhysRevLett.104.180505. URL: https://link.aps.org/doi/10.1103/PhysRevLett.104.180505.

[45] Parsa Bonderson et al. *Twisted Interferometry*. 2013. arXiv: 1306.2379 [quant-ph].

[46] M. Borinsky et al. "Five-loop renormalization of ϕ^3 theory with applications to the Lee-Yang edge singularity and percolation theory". In: *Phys. Rev. D* 103 (11 June 2021), p. 116024. DOI: 10.1103/PhysRevD.103.116024. URL: https://link.aps.org/doi/10.1103/PhysRevD.103.116024.

[47] Sergey Bravyi. "Universal quantum computation with the $\nu = 5/2$ fractional quantum Hall state". In: *Phys. Rev. A* 73 (4 Apr. 2006), p. 042313. DOI: 10.1103/PhysRevA.73.042313. URL: https://link.aps.org/doi/10.1103/PhysRevA.73.042313.

[48] Sergey Bravyi and Alexei Kitaev. "Universal quantum computation with ideal Clifford gates and noisy ancillas". In: *Phys. Rev. A* 71 (2 Feb. 2005), p. 022316. DOI: 10.1103/PhysRevA.71.022316. URL: https://link.aps.org/doi/10.1103/PhysRevA.71.022316.

[49] Sergey Bravyi et al. *Adaptive constant-depth circuits for manipulating non-abelian anyons*. 2022. arXiv: 2205.01933 [quant-ph].

[50] Sergey Bravyi et al. "Criticality without Frustration for Quantum Spin-1 Chains". In: *Physical Review Letters* 109.20 (Nov. 2012). ISSN: 1079-7114. DOI: 10.1103/physrevlett.109.207202. URL: http://dx.doi.org/10.1103/PhysRevLett.109.207202.

[51] Sergey B. Bravyi and Alexei Yu. Kitaev. "Fermionic Quantum Computation". In: *Annals of Physics* 298.1 (May 2002), pp. 210–226. ISSN: 0003-4916. DOI: 10.1006/aphy.2002.6254. URL: http://dx.doi.org/10.1006/aphy.2002.6254.

[52] C. Broholm et al. "Quantum spin liquids". In: *Science* 367.6475 (2020), eaay0668. DOI: 10.1126/science.aay0668. URL: https://www.science.org/doi/abs/10.1126/science.aay0668.

[53] J. A. N. Bruin et al. "Robustness of the thermal Hall effect close to half-quantization in α–$RuCl_3$". In: *Nature Physics* 18.4 (Feb. 2022), pp. 401–405. ISSN: 1745-2481. DOI: 10.1038/s41567-021-01501-y. URL: http://dx.doi.org/10.1038/s41567-021-01501-y.

[54] J. A. N. Bruin et al. *Robustness of the thermal Hall effect close to half-quantization in a field-induced spin liquid state*. 2021. arXiv: 2104.12184 [cond-mat.str-el].

[55] M. Buchhold, T. Müller, and S. Diehl. *Revealing measurement-induced phase transitions by pre-selection*. 2022. arXiv: 2208.10506 [cond-mat.dis-nn]. URL: https://arxiv.org/abs/2208.10506.

[56] M. Buchhold et al. "Effective Theory for the Measurement-Induced Phase Transition of Dirac Fermions". In: *Phys. Rev. X* 11 (4 Oct. 2021), p. 041004. DOI: 10.1103/PhysRevX.11.041004. URL: https://link.aps.org/doi/10.1103/PhysRevX.11.041004.

[57] L. N. Bulaevskii et al. "Electronic orbital currents and polarization in Mott insulators". In: *Phys. Rev. B* 78 (2 July 2008), p. 024402. DOI: 10.1103/PhysRevB.78.024402. URL: https://link.aps.org/doi/10.1103/PhysRevB.78.024402.

[58] D.V. Bulgakova and O. Ogievetsky. "Fusion procedure for the walled Brauer algebra". In: *Journal of Geometry and Physics* 149 (Mar. 2020), p. 103580. DOI: 10.1016/j.geomphys.2019.103580. URL: https://doi.org/10.1016%5C%2Fj.geomphys.2019.103580.

[59] I.S. Burmistrov et al. "Entanglement entropy and particle number cumulants of disordered fermions". In: *Annals of Physics* 383 (Aug. 2017), pp. 140–156. ISSN: 0003-4916. DOI: 10.1016/j.aop.2017.05.011. URL: http://dx.doi.org/10.1016/j.aop.2017.05.011.

[60] C. de C. Chamon et al. "Two point-contact interferometer for quantum Hall systems". In: *Phys. Rev. B* 55.4 (Jan. 1997), pp. 2331–2343. ISSN: 2469-9969. DOI: 10.1103/PhysRevB.55.2331.

[61] Nils Caci et al. "Poisson-Dirichlet distributions and weakly first-order spin-nematic phase transitions". In: *Phys. Rev. B* 107 (2 Jan. 2023), p. L020409. DOI: 10.1103/PhysRevB.107.L020409. URL: https://link.aps.org/doi/10.1103/PhysRevB.107.L020409.

[62] Libor Caha and Daniel Nagaj. *The pair-flip model: a very entangled translationally invariant spin chain*. 2018. arXiv: 1805.07168 [quant-ph].

[63] Constantin Candu and Hubert Saleur. "A lattice approach to the conformal supercoset sigma model. Part I: Algebraic structures in the spin chain. The Brauer algebra". In: *Nuclear Physics B* 808.3 (Feb. 2009), pp. 441–486. ISSN: 0550-3213. DOI: 10.1016/j.nuclphysb.2008.09.034. URL: http://dx.doi.org/10.1016/j.nuclphysb.2008.09.034.

[64] John Cardy. "Linking Numbers for Self-Avoiding Loops and Percolation: Application to the Spin Quantum Hall Transition". In: *Phys. Rev. Lett.* 84 (16 Apr. 2000), pp. 3507–3510. DOI: 10.1103/PhysRevLett.84.3507. URL: https://link.aps.org/doi/10.1103/PhysRevLett.84.3507.

[65] John L. Cardy. “Conformal invariance and surface critical behavior”. In: *Nuclear Physics B* 240.4 (1984), pp. 514–532. ISSN: 0550-3213. DOI: https://doi.org/10.1016/0550-3213(84)90241-4. URL: https://www.sciencedirect.com/science/article/pii/0550321384902414.

[66] Matteo Carrega, Ivan J. Vera-Marun, and Alessandro Principi. “Tunneling spectroscopy as a probe of fractionalization in two-dimensional magnetic heterostructures”. In: *Phys. Rev. B* 102 (8 Aug. 2020), p. 085412. DOI: 10.1103/PhysRevB.102.085412. URL: https://link.aps.org/doi/10.1103/PhysRevB.102.085412.

[67] K. Chahine and M. Buchhold. *Entanglement phases, localization and multifractality of monitored free fermions in two dimensions*. 2023. arXiv: 2309.12391.

[68] Ahana Chakraborty et al. *Charge and Entanglement Criticality in a U(1)-Symmetric Hybrid Circuit of Qubits*. 2023. arXiv: 2307.13038 [cond-mat.dis-nn]. URL: https://arxiv.org/abs/2307.13038.

[69] J. T. Chalker, M. Ortuño, and A. M. Somoza. “Spin quantum Hall effect and plateau transitions in multilayer network models”. In: *Phys. Rev. B* 83 (11 Mar. 2011), p. 115317. DOI: 10.1103/PhysRevB.83.115317. URL: https://link.aps.org/doi/10.1103/PhysRevB.83.115317.

[70] Jiří Chaloupka, George Jackeli, and Giniyat Khaliullin. “Kitaev-Heisenberg Model on a Honeycomb Lattice: Possible Exotic Phases in Iridium Oxides A_2IrO_3”. In: *Phys. Rev. Lett.* 105 (2 July 2010), p. 027204. DOI: 10.1103/PhysRevLett.105.027204. URL: https://link.aps.org/doi/10.1103/PhysRevLett.105.027204.

[71] Jiří Chaloupka, George Jackeli, and Giniyat Khaliullin. “Zigzag Magnetic Order in the Iridium Oxide Na_2IrO_3”. In: *Phys. Rev. Lett.* 110 (9 Feb. 2013), p. 097204. DOI: 10.1103/PhysRevLett.110.097204. URL: https://link.aps.org/doi/10.1103/PhysRevLett.110.097204.

[72] Hua Chen et al. “Quasiparticle tunneling in the Moore-Read fractional quantum Hall state”. In: *Phys. Rev. B* 80 (23 Dec. 2009), p. 235305. DOI: 10.1103/PhysRevB.80.235305. URL: https://link.aps.org/doi/10.1103/PhysRevB.80.235305.

[73] Xiao Chen, Eduardo Fradkin, and William Witczak-Krempa. “Gapless quantum spin chains: multiple dynamics and conformal wavefunctions”. In: *Journal of Physics A: Mathematical and Theoretical* 50.46 (Oct. 2017), p. 464002. ISSN: 1751-8121. DOI: 10.1088/1751-8121/aa8dbc. URL: http://dx.doi.org/10.1088/1751-8121/aa8dbc.

[74] Xiao Chen et al. “Emergent conformal symmetry in nonunitary random dynamics of free fermions”. In: *Physical Review Research* 2.3 (July 2020). ISSN: 2643-1564. DOI: 10.1103/physrevresearch.2.033017. URL: http://dx.doi.org/10.1103/PhysRevResearch.2.033017.

[75] Xiao Chen et al. "Scaling of entanglement in 2 + 1-dimensional scale-invariant field theories". In: *Journal of Statistical Mechanics: Theory and Experiment* 2015.2 (Feb. 2015), P02010. DOI: 10.1088/1742-5468/2015/02/P02010. URL: https://dx.doi.org/10.1088/1742-5468/2015/02/P02010.

[76] Xie Chen, Zheng-Cheng Gu, and Xiao-Gang Wen. "Local unitary transformation, long-range quantum entanglement, wave function renormalization, and topological order". In: *Phys. Rev. B* 82 (15 Oct. 2010), p. 155138. DOI: 10.1103/PhysRevB.82.155138. URL: https://link.aps.org/doi/10.1103/PhysRevB.82.155138.

[77] Meng Cheng et al. "Splitting of Majorana-Fermion Modes due to Intervortex Tunneling in a $p_x + ip_y$ Superconductor". In: *Phys. Rev. Lett.* 103 (10 Aug. 2009), p. 107001. DOI: 10.1103/PhysRevLett.103.107001. URL: https://link.aps.org/doi/10.1103/PhysRevLett.103.107001.

[78] Li Ern Chern, Emily Z. Zhang, and Yong Baek Kim. "Sign Structure of Thermal Hall Conductivity and Topological Magnons for In-Plane Field Polarized Kitaev Magnets". In: *Phys. Rev. Lett.* 126.14 (Apr. 2021), p. 147201. ISSN: 1079-7114. DOI: 10.1103/PhysRevLett.126.147201.

[79] Eli Chertkov et al. "Characterizing a non-equilibrium phase transition on a quantum computer". In: *Nature Physics* 19.12 (Sept. 2023), pp. 1799–1804. ISSN: 1745-2481. DOI: 10.1038/s41567-023-02199-w. URL: http://dx.doi.org/10.1038/s41567-023-02199-w.

[80] Soonwon Choi et al. "Quantum Error Correction in Scrambling Dynamics and Measurement Induced Phase Transition". In: *Phys. Rev. Lett.* 125 (3 July 2020), p. 030505. DOI: 10.1103/PhysRevLett.125.030505. URL: https://link.aps.org/doi/10.1103/PhysRevLett.125.030505.

[81] David J. Clarke and Kirill Shtengel. "Improved phase-gate reliability in systems with neutral Ising anyons". In: *Phys. Rev. B* 82 (18 Nov. 2010), p. 180519. DOI: 10.1103/PhysRevB.82.180519. URL: https://link.aps.org/doi/10.1103/PhysRevB.82.180519.

[82] A Coniglio and F Peruggi. "Clusters and droplets in the q-state Potts model". In: *Journal of Physics A: Mathematical and General* 15.6 (June 1982), p. 1873. DOI: 10.1088/0305-4470/15/6/028. URL: https://dx.doi.org/10.1088/0305-4470/15/6/028.

[83] Y.-T. Cui et al. "Single-Shot Time-Domain Studies of Spin-Torque-Driven Switching in Magnetic Tunnel Junctions". In: *Phys. Rev. Lett.* 104 (9 Mar. 2010), p. 097201. DOI: 10.1103/PhysRevLett.104.097201. URL: https://link.aps.org/doi/10.1103/PhysRevLett.104.097201.

[84] Peter Czajka et al. "Oscillations of the thermal conductivity in the spin-liquid state of α-RuCl3". In: *Nat. Phys.* 17 (Aug. 2021), pp. 915–919. ISSN: 1745-2481. DOI: 10.1038/s41567-021-01243-x.

[85] Peter Czajka et al. "Planar thermal Hall effect of topological bosons in the Kitaev magnet α–$RuCl_3$". In: *Nature Materials* 22.1 (Nov. 2022), pp. 36–41. ISSN: 1476-4660. DOI: 10.1038/s41563-022-01397-w. URL: http://dx.doi.org/10.1038/s41563-022-01397-w.

[86] S. D. Das, K. Dhochak, and V. Tripathi. "Kondo route to spin inhomogeneities in the honeycomb Kitaev model". In: *Phys. Rev. B* 94 (2 July 2016), p. 024411. DOI: 10.1103/PhysRevB.94.024411. URL: https://link.aps.org/doi/10.1103/PhysRevB.94.024411.

[87] Sankar Das Sarma, Michael Freedman, and Chetan Nayak. "Topologically Protected Qubits from a Possible Non-Abelian Fractional Quantum Hall State". In: *Phys. Rev. Lett.* 94 (16 Apr. 2005), p. 166802. DOI: 10.1103/PhysRevLett.94.166802. URL: https://link.aps.org/doi/10.1103/PhysRevLett.94.166802.

[88] Sankar Das Sarma, Michael Freedman, and Chetan Nayak. "Topologically Protected Qubits from a Possible Non-Abelian Fractional Quantum Hall State". In: *Phys. Rev. Lett.* 94.16 (Apr. 2005), p. 166802. ISSN: 1079-7114. DOI: 10.1103/PhysRevLett.94.166802.

[89] Emma Deist et al. "Mid-Circuit Cavity Measurement in a Neutral Atom Array". In: *Phys. Rev. Lett.* 129 (20 Nov. 2022), p. 203602. DOI: 10.1103/PhysRevLett.129.203602. URL: https://link.aps.org/doi/10.1103/PhysRevLett.129.203602.

[90] Gesualdo Delfino and Elena Tartaglia. "Classifying Potts critical lines". In: *Phys. Rev. E* 96 (4 Oct. 2017), p. 042137. DOI: 10.1103/PhysRevE.96.042137. URL: https://link.aps.org/doi/10.1103/PhysRevE.96.042137.

[91] T. Devolder et al. "Single-Shot Time-Resolved Measurements of Nanosecond-Scale Spin-Transfer Induced Switching: Stochastic Versus Deterministic Aspects". In: *Phys. Rev. Lett.* 100 (5 Feb. 2008), p. 057206. DOI: 10.1103/PhysRevLett.100.057206. URL: https://link.aps.org/doi/10.1103/PhysRevLett.100.057206.

[92] Kusum Dhochak, R. Shankar, and V. Tripathi. "Magnetic Impurities in the Honeycomb Kitaev Model". In: *Phys. Rev. Lett.* 105 (11 Sept. 2010), p. 117201. DOI: 10.1103/PhysRevLett.105.117201. URL: https://link.aps.org/doi/10.1103/PhysRevLett.105.117201.

[93] Seung-Hwan Do et al. "Majorana fermions in the Kitaev quantum spin system α –$RuCl_3$". In: *Nature Physics* 13.11 (Nov. 2017), pp. 1079–1084. ISSN: 1745-2481. DOI: 10.1038/nphys4264. URL: https://doi.org/10.1038/nphys4264.

[94] T. Dörstel et al. *Frustration-Free Control and Absorbing-State Transport in Entangled State Preparation*. 2025. arXiv: 2510.24845 [quant-ph]. URL: https://arxiv.org/abs/2510.24845.

[95] Bertrand Duplantier. “Two-dimensional fractal geometry, critical phenomena and conformal invariance”. In: *Physics Reports* 184.2 (1989), pp. 229–257. ISSN: 0370-1573. DOI: https://doi.org/10.1016/0370-1573(89)90042-2. URL: https://www.sciencedirect.com/science/article/pii/0370157389900422.

[96] Bertrand Duplantier and Hubert Saleur. “Exact tricritical exponents for polymers at the FTHETA point in two dimensions”. In: *Phys. Rev. Lett.* 59 (5 Aug. 1987), pp. 539–542. DOI: 10.1103/PhysRevLett.59.539. URL: https://link.aps.org/doi/10.1103/PhysRevLett.59.539.

[97] Ondrej Dyck et al. “Atom-by-atom fabrication with electron beams”. In: *Nature Reviews Materials* 4.7 (July 2019), pp. 497–507. ISSN: 2058-8437. DOI: 10.1038/s41578-019-0118-z. URL: https://doi.org/10.1038/s41578-019-0118-z.

[98] Sam F. Edwards and D. R. Wilkinson. “The surface statistics of a granular aggregate”. In: *Proceedings of the Royal Society of London. A. Mathematical and Physical Sciences* 381 (1982), pp. 17–31. URL: https://api.semanticscholar.org/CorpusID:119927969.

[99] Samuel J. Elman, Adrian Chapman, and Steven T. Flammia. “Free Fermions Behind the Disguise”. In: *Communications in Mathematical Physics* 388.2 (Oct. 2021), pp. 969–1003. DOI: 10.1007/s00220-021-04220-w. URL: https://doi.org/10.1007%5C%2Fs00220-021-04220-w.

[100] Alexander Erhard et al. “Entangling logical qubits with lattice surgery”. In: *Nature* 589.7841 (Jan. 2021), pp. 220–224. ISSN: 1476-4687. DOI: 10.1038/s41586-020-03079-6. URL: http://dx.doi.org/10.1038/s41586-020-03079-6.

[101] H. G. Evertz. “The loop algorithm”. In: *Advances in Physics* 52.1 (Jan. 2003), pp. 1–66. ISSN: 1460-6976. DOI: 10.1080/0001873021000049195. URL: http://dx.doi.org/10.1080/0001873021000049195.

[102] F Family and T Vicsek. “Scaling of the active zone in the Eden process on percolation networks and the ballistic deposition model”. In: *Journal of Physics A: Mathematical and General* 18.2 (Feb. 1985), p. L75. DOI: 10.1088/0305-4470/18/2/005. URL: https://dx.doi.org/10.1088/0305-4470/18/2/005.

[103] Michele Fava et al. “Nonlinear Sigma Models for Monitored Dynamics of Free Fermions”. In: *Phys. Rev. X* 13 (4 Dec. 2023), p. 041045. DOI: 10.1103/PhysRevX.13.041045. URL: https://link.aps.org/doi/10.1103/PhysRevX.13.041045.

[104] Michele Fava et al. *Nonlinear sigma models for monitored dynamics of free fermions*. 2023. DOI: 10.48550/ARXIV.2302.12820. arXiv: 2302.12820 [cond-mat]. URL: https://arxiv.org/abs/2302.12820.

[105] P. Fazekas and P. W. Anderson. "On the ground state properties of the anisotropic triangular antiferromagnet". In: *The Philosophical Magazine: A Journal of Theoretical Experimental and Applied Physics* 30.2 (1974), pp. 423–440. DOI: 10.1080/14786439808206568. eprint: https://doi.org/10.1080/14786439808206568. URL: https://doi.org/10.1080/14786439808206568.

[106] Johannes Feldmeier et al. "Local probes for charge-neutral edge states in two dimensional quantum magnets". In: *Phys. Rev. B* 102 (13 Oct. 2020), p. 134423. DOI: 10.1103/PhysRevB.102.134423. URL: https://link.aps.org/doi/10.1103/PhysRevB.102.134423.

[107] Paul Fendley, Matthew P. A. Fisher, and Chetan Nayak. "Dynamical Disentanglement across a Point Contact in a Non-Abelian Quantum Hall State". In: *Phys. Rev. Lett.* 97 (3 July 2006), p. 036801. DOI: 10.1103/PhysRevLett.97.036801. URL: https://link.aps.org/doi/10.1103/PhysRevLett.97.036801.

[108] Paul Fendley, Matthew P. A. Fisher, and Chetan Nayak. "Edge states and tunneling of non-Abelian quasiparticles in the 5/2 quantum Hall state and $p+ip$ superconductors". In: *Phys. Rev. B* 75 (4 Jan. 2007), p. 045317. DOI: 10.1103/PhysRevB.75.045317. URL: https://link.aps.org/doi/10.1103/PhysRevB.75.045317.

[109] Paul Fendley, Matthew P.A. Fisher, and Chetan Nayak. "Boundary conformal field theory and tunneling of edge quasiparticles in non-Abelian topological states". In: *Annals of Physics* 324.7 (July 2009), pp. 1547–1572. ISSN: 0003-4916. DOI: 10.1016/j.aop.2009.03.005. URL: http://dx.doi.org/10.1016/j.aop.2009.03.005.

[110] Paul Fendley, Matthew P.A. Fisher, and Chetan Nayak. "Boundary conformal field theory and tunneling of edge quasiparticles in non-Abelian topological states". In: *Annals of Physics* 324.7 (July 2009), pp. 1547–1572. ISSN: 0003-4916. DOI: 10.1016/j.aop.2009.03.005. URL: http://dx.doi.org/10.1016/j.aop.2009.03.005.

[111] Paul Fendley and Jesper L Jacobsen. "Critical points in coupled Potts models and critical phases in coupled loop models". In: *Journal of Physics A: Mathematical and Theoretical* 41.21 (May 2008), p. 215001. DOI: 10.1088/1751-8113/41/21/215001. URL: https://doi.org/10.1088%5C%2F1751-8113%5C%2F41%5C%2F21%5C%2F215001.

[112] Matthew P.A. Fisher et al. "Random Quantum Circuits". In: *Annual Review of Condensed Matter Physics* 14.Volume 14, 2023 (2023), pp. 335–379. ISSN: 1947-5462. DOI: https://doi.org/10.1146/annurev-conmatphys-031720-030658. URL: https://www.annualreviews.org/content/journals/10.1146/annurev-conmatphys-031720-030658.

[113] Matthew P.A. Fisher et al. "Random Quantum Circuits". In: *Annual Review of Condensed Matter Physics* 14.1 (2023), pp. 335–379. DOI: 10.1146/annurev-conmatphys-031720-030658. URL: https://doi.org/10.1146/annurev-conmatphys-031720-030658.

[114] Michael Foss-Feig et al. *Experimental demonstration of the advantage of adaptive quantum circuits*. 2023. arXiv: 2302.03029 [quant-ph].

[115] Michael Freedman, Chetan Nayak, and Kevin Walker. "Towards universal topological quantum computation in the $\nu = \frac{5}{2}$ fractional quantum Hall state". In: *Phys. Rev. B* 73.24 (June 2006), p. 245307. ISSN: 2469-9969. DOI: 10.1103/PhysRevB.73.245307.

[116] Lucas R. D. Freitas et al. "Electric polarization near vortices in the extended Kitaev model". In: *npj Quantum Materials* 9.1 (Mar. 2024), p. 33. ISSN: 2397-4648. DOI: 10.1038/s41535-024-00643-5. URL: https://doi.org/10.1038/s41535-024-00643-5.

[117] Liang Fu. "Electron Teleportation via Majorana Bound States in a Mesoscopic Superconductor". In: *Phys. Rev. Lett.* 104.5 (Feb. 2010), p. 056402. ISSN: 1079-7114. DOI: 10.1103/PhysRevLett.104.056402.

[118] Liang Fu and C. L. Kane. "Superconducting Proximity Effect and Majorana Fermions at the Surface of a Topological Insulator". In: *Phys. Rev. Lett.* 100.9 (Mar. 2008), p. 096407. ISSN: 1079-7114. DOI: 10.1103/PhysRevLett.100.096407.

[119] Kazuya Fujimoto, Ryusuke Hamazaki, and Yuki Kawaguchi. "Dynamical Scaling of Surface Roughness and Entanglement Entropy in Disordered Fermion Models". In: *Phys. Rev. Lett.* 127 (9 Aug. 2021), p. 090601. DOI: 10.1103/PhysRevLett.127.090601. URL: https://link.aps.org/doi/10.1103/PhysRevLett.127.090601.

[120] Kazuya Fujimoto, Ryusuke Hamazaki, and Yuki Kawaguchi. "Family-Vicsek Scaling of Roughness Growth in a Strongly Interacting Bose Gas". In: *Phys. Rev. Lett.* 124 (21 May 2020), p. 210604. DOI: 10.1103/PhysRevLett.124.210604. URL: https://link.aps.org/doi/10.1103/PhysRevLett.124.210604.

[121] Kazuya Fujimoto, Ryusuke Hamazaki, and Yuki Kawaguchi. "Impact of Dissipation on Universal Fluctuation Dynamics in Open Quantum Systems". In: *Phys. Rev. Lett.* 129 (11 Sept. 2022), p. 110403. DOI: 10.1103/PhysRevLett.129.110403. URL: https://link.aps.org/doi/10.1103/PhysRevLett.129.110403.

[122] J. P. Gaebler et al. "Suppression of midcircuit measurement crosstalk errors with micromotion". In: *Phys. Rev. A* 104 (6 Dec. 2021), p. 062440. DOI: 10.1103/PhysRevA.104.062440. URL: https://link.aps.org/doi/10.1103/PhysRevA.104.062440.

[123] Lachezar S Georgiev. "Computational equivalence of the two inequivalent spinor representations of the braid group in the Ising topological quantum computer". In: *J. Stat. Mech.: Theor. Exp.* 2009.12 (Dec. 2009), P12013. ISSN: 1742-5468. DOI: 10.1088/1742-5468/2009/12/p12013. URL: http://dx.doi.org/10.1088/1742-5468/2009/12/P12013.

[124] Lachezar S. Georgiev. *Topological Quantum Computation with Non-Abelian Anyons in Fractional Quantum Hall States*. 2016. arXiv: 1602.05035 [cond-mat.str-el]. URL: https://arxiv.org/abs/1602.05035.

[125] Lachezar S. Georgiev. “Topologically protected gates for quantum computation with non-Abelian anyons in the Pfaffian quantum Hall state”. In: *Phys. Rev. B* 74 (23 Dec. 2006), p. 235112. DOI: 10.1103/PhysRevB.74.235112. URL: https://link.aps.org/doi/10.1103/PhysRevB.74.235112.

[126] Lachezar S. Georgiev. “Towards a universal set of topologically protected gates for quantum computation with Pfaffian qubits”. In: *Nuclear Physics B* 789.3 (Feb. 2008), pp. 552–590. ISSN: 0550-3213. DOI: 10.1016/j.nuclphysb.2007.07.016. URL: http://dx.doi.org/10.1016/j.nuclphysb.2007.07.016.

[127] Jan de Gier. *Loops, matchings and alternating-sign matrices*. 2003. arXiv: math/0211285 [math.CO].

[128] Dimitri Gioev and Israel Klich. “Entanglement Entropy of Fermions in Any Dimension and the Widom Conjecture”. In: *Phys. Rev. Lett.* 96 (10 Mar. 2006), p. 100503. DOI: 10.1103/PhysRevLett.96.100503. URL: https://link.aps.org/doi/10.1103/PhysRevLett.96.100503.

[129] G. Goldstein and C. Chamon. “Decay rates for topological memories encoded with Majorana fermions”. In: *Phys. Rev. B* 84 (20 Nov. 2011), p. 205109. DOI: 10.1103/PhysRevB.84.205109. URL: https://link.aps.org/doi/10.1103/PhysRevB.84.205109.

[130] S. Goldstein. “On diffusion by discontinuous movements and on the telegraph equation”. In: *J. Mech. Appl. Math.* 4 (1951), pp. 129–156. DOI: 10.1093/qjmam/4.2.129. URL: https://doi.org/10.1093/qjmam/4.2.129.

[131] Daniel Gottesman. *The Heisenberg Representation of Quantum Computers*. 1998. arXiv: quant-ph/9807006 [quant-ph]. URL: https://arxiv.org/abs/quant-ph/9807006.

[132] T. M. Graham et al. “Midcircuit Measurements on a Single-Species Neutral Alkali Atom Quantum Processor”. In: *Phys. Rev. X* 13 (4 Dec. 2023), p. 041051. DOI: 10.1103/PhysRevX.13.041051. URL: https://link.aps.org/doi/10.1103/PhysRevX.13.041051.

[133] Eva Grimaldi et al. “Single-shot dynamics of spin–orbit torque and spin transfer torque switching in three-terminal magnetic tunnel junctions”. In: *Nat. Nanotechnol.* 15 (Feb. 2020), pp. 111–117. ISSN: 1748-3395. DOI: 10.1038/s41565-019-0607-7.

[134] U Grimm and P A Pearce. “Multi-colour braid-monoid algebras”. In: *Journal of Physics A: Mathematical and General* 26.24 (Dec. 1993), pp. 7435–7459. ISSN: 1361-6447. DOI: 10.1088/0305-4470/26/24/018. URL: http://dx.doi.org/10.1088/0305-4470/26/24/018.

[135] U Grimm and S O Warnaar. “Yang-Baxter algebras based on the two-colour BWM algebra”. In: *Journal of Physics A: Mathematical and General* 28.24 (Dec. 1995), pp. 7197–7207. ISSN: 1361-6447. DOI: 10.1088/0305-4470/28/24/017. URL: http://dx.doi.org/10.1088/0305-4470/28/24/017.

[136] Uwe Grimm and Paul P Martin. "The bubble algebra: structure of a two-colour Temperley–Lieb Algebra". In: *Journal of Physics A: Mathematical and General* 36.42 (Oct. 2003), pp. 10551–10571. ISSN: 1361-6447. DOI: 10.1088/0305-4470/36/42/010. URL: http://dx.doi.org/10.1088/0305-4470/36/42/010.

[137] Stefan Grosskinsky, Alexander A. Lovisolo, and Daniel Ueltschi. "Lattice Permutations and Poisson-Dirichlet Distribution of Cycle Lengths". In: *Journal of Statistical Physics* 146.6 (Mar. 2012), pp. 1105–1121. DOI: 10.1007/s10955-012-0450-9. URL: https://doi.org/10.1007%2Fs10955-012-0450-9.

[138] Michael J. Gullans and David A. Huse. "Scalable Probes of Measurement-Induced Criticality". In: *Phys. Rev. Lett.* 125 (7 Aug. 2020), p. 070606. DOI: 10.1103/PhysRevLett.125.070606. URL: https://link.aps.org/doi/10.1103/PhysRevLett.125.070606.

[139] Leh-Hun Gwa and Herbert Spohn. "Bethe solution for the dynamical-scaling exponent of the noisy Burgers equation". In: *Phys. Rev. A* 46 (2 July 1992), pp. 844–854. DOI: 10.1103/PhysRevA.46.844. URL: https://link.aps.org/doi/10.1103/PhysRevA.46.844.

[140] Leh-Hun Gwa and Herbert Spohn. "Six-vertex model, roughened surfaces, and an asymmetric spin Hamiltonian". In: *Phys. Rev. Lett.* 68 (6 Feb. 1992), pp. 725–728. DOI: 10.1103/PhysRevLett.68.725. URL: https://link.aps.org/doi/10.1103/PhysRevLett.68.725.

[141] Gábor B. Halász. "Gate-Controlled Anyon Generation and Detection in Kitaev Spin Liquids". In: *Phys. Rev. Lett.* 132.20 (May 2024), p. 206501. ISSN: 1079-7114. DOI: 10.1103/PhysRevLett.132.206501.

[142] Gábor B. Halász, J. T. Chalker, and R. Moessner. "Doping a topological quantum spin liquid: Slow holes in the Kitaev honeycomb model". In: *Phys. Rev. B* 90 (3 July 2014), p. 035145. DOI: 10.1103/PhysRevB.90.035145. URL: https://link.aps.org/doi/10.1103/PhysRevB.90.035145.

[143] Bertrand I. Halperin et al. "Theory of the Fabry-Pérot quantum Hall interferometer". In: *Phys. Rev. B* 83 (15 Apr. 2011), p. 155440. DOI: 10.1103/PhysRevB.83.155440. URL: https://link.aps.org/doi/10.1103/PhysRevB.83.155440.

[144] Yiqiu Han, Xiao Chen, and Ethan Lake. *Exponentially slow thermalization and the robustness of Hilbert space fragmentation.* 2024. arXiv: 2401.11294 [quant-ph].

[145] Chihiro Harada, Atsushi Ono, and Joji Nasu. "Field-driven spatiotemporal manipulation of Majorana zero modes in a Kitaev spin liquid". In: *Phys. Rev. B* 108 (24 Dec. 2023), p. L241118. DOI: 10.1103/PhysRevB.108.L241118. URL: https://link.aps.org/doi/10.1103/PhysRevB.108.L241118.

[146] Oliver Hart. *Exact Mazur bounds in the pair-flip model and beyond.* 2023. arXiv: 2308.00738 [cond-mat.stat-mech].

[147] F Hassler, A R Akhmerov, and C W J Beenakker. "The top-transmon: a hybrid superconducting qubit for parity-protected quantum computation". In: *New Journal of Physics* 13.9 (Sept. 2011), p. 095004. ISSN: 1367-2630. DOI: 10.1088/1367-2630/13/9/095004. URL: http://dx.doi.org/10.1088/1367-2630/13/9/095004.

[148] Jacob Hauser et al. "Continuous symmetry breaking in adaptive quantum dynamics". In: *Phys. Rev. B* 109 (21 June 2024), p. 214305. DOI: 10.1103/PhysRevB.109.214305. URL: https://link.aps.org/doi/10.1103/PhysRevB.109.214305.

[149] Michael Hell et al. "Time scales for Majorana manipulation using Coulomb blockade in gate-controlled superconducting nanowires". In: *Phys. Rev. B* 94 (3 July 2016), p. 035424. DOI: 10.1103/PhysRevB.94.035424. URL: https://link.aps.org/doi/10.1103/PhysRevB.94.035424.

[150] Richard Hentrich et al. "Unusual Phonon Heat Transport in α–$RuCl_3$: Strong Spin-Phonon Scattering and Field-Induced Spin Gap". In: *Phys. Rev. Lett.* 120 (11 Mar. 2018), p. 117204. DOI: 10.1103/PhysRevLett.120.117204. URL: https://link.aps.org/doi/10.1103/PhysRevLett.120.117204.

[151] M. Hermanns, I. Kimchi, and J. Knolle. "Physics of the Kitaev Model: Fractionalization, Dynamic Correlations, and Material Connections". In: *Annu. Rev. Condens. Matter Phys.* Volume 9, 2018 (Mar. 2018), pp. 17–33. DOI: 10.1146/annurev-conmatphys-033117-053934.

[152] Ying Hu et al. "Majorana fermions in noisy Kitaev wires". In: *Phys. Rev. B* 92 (16 Oct. 2015), p. 165118. DOI: 10.1103/PhysRevB.92.165118. URL: https://link.aps.org/doi/10.1103/PhysRevB.92.165118.

[153] Barry d. Hughes. "The Self-Avoiding Walk". In: *Random Walks And Random Environments*. Oxford University Press, Mar. 1995. ISBN: 9780198537885. DOI: 10.1093/oso/9780198537885.003.0007. URL: https://doi.org/10.1093/oso/9780198537885.003.0007.

[154] Kumpei Imamura et al. "Majorana-fermion origin of the planar thermal Hall effect in the Kitaev magnet α–$RuCl_3$". In: *Science Advances* 10.11 (2024), eadk3539. DOI: 10.1126/sciadv.adk3539. URL: https://www.science.org/doi/abs/10.1126/sciadv.adk3539.

[155] Stephen Inglis and Roger G Melko. "Entanglement at a two-dimensional quantum critical point: a $T = 0$ projector quantum Monte Carlo study". In: *New Journal of Physics* 15.7 (July 2013), p. 073048. ISSN: 1367-2630. DOI: 10.1088/1367-2630/15/7/073048. URL: http://dx.doi.org/10.1088/1367-2630/15/7/073048.

[156] Matteo Ippoliti et al. "Entanglement Phase Transitions in Measurement-Only Dynamics". In: *Phys. Rev. X* 11 (1 Feb. 2021), p. 011030. DOI: 10.1103/PhysRevX.11.011030. URL: https://link.aps.org/doi/10.1103/PhysRevX.11.011030.

[157] Mohsin Iqbal et al. "Non-Abelian topological order and anyons on a trapped-ion processor". In: *Nature* 626.7999 (Feb. 2024), pp. 505–511. ISSN: 1476-4687. DOI: 10.1038/s41586-023-06934-4. URL: http://dx.doi.org/10.1038/s41586-023-06934-4.

[158] Mohsin Iqbal et al. *Topological Order from Measurements and Feed-Forward on a Trapped Ion Quantum Computer*. 2023. arXiv: 2302.01917 [quant-ph].

[159] G. Jackeli and G. Khaliullin. "Mott Insulators in the Strong Spin-Orbit Coupling Limit: From Heisenberg to a Quantum Compass and Kitaev Models". In: *Phys. Rev. Lett.* 102 (1 Jan. 2009), p. 017205. DOI: 10.1103/PhysRevLett.102.017205. URL: https://link.aps.org/doi/10.1103/PhysRevLett.102.017205.

[160] G. Jackeli and G. Khaliullin. "Mott Insulators in the Strong Spin-Orbit Coupling Limit: From Heisenberg to a Quantum Compass and Kitaev Models". In: *Phys. Rev. Lett.* 102.1 (Jan. 2009), p. 017205. ISSN: 1079-7114. DOI: 10.1103/PhysRevLett.102.017205.

[161] J. L. Jacobsen, N. Read, and H. Saleur. "Dense Loops, Supersymmetry, and Goldstone Phases in Two Dimensions". In: *Phys. Rev. Lett.* 90 (9 Mar. 2003), p. 090601. DOI: 10.1103/PhysRevLett.90.090601. URL: https://link.aps.org/doi/10.1103/PhysRevLett.90.090601.

[162] J. L. Jacobsen and H. Saleur. "Exact Valence Bond Entanglement Entropy and Probability Distribution in the XXX Spin Chain and the Potts Model". In: *Phys. Rev. Lett.* 100 (8 Feb. 2008), p. 087205. DOI: 10.1103/PhysRevLett.100.087205. URL: https://link.aps.org/doi/10.1103/PhysRevLett.100.087205.

[163] Seong-Hoon Jang, Yasuyuki Kato, and Yukitoshi Motome. "Vortex creation and control in the Kitaev spin liquid by local bond modulations". In: *Phys. Rev. B* 104 (8 Aug. 2021), p. 085142. DOI: 10.1103/PhysRevB.104.085142. URL: https://link.aps.org/doi/10.1103/PhysRevB.104.085142.

[164] Wolfhard Janke and Adriaan M.J. Schakel. "Geometrical vs. Fortuin–Kasteleyn clusters in the two-dimensional q-state Potts model". In: *Nuclear Physics B* 700.1 (2004), pp. 385–406. ISSN: 0550-3213. DOI: https://doi.org/10.1016/j.nuclphysb.2004.08.030. URL: https://www.sciencedirect.com/science/article/pii/S055032130400611X.

[165] Nejc Janša et al. "Observation of two types of fractional excitation in the Kitaev honeycomb magnet". In: *Nature Physics* 14.8 (2018), pp. 786–790. DOI: 10.1038/s41567-018-0129-5. URL: https://doi.org/10.1038/s41567-018-0129-5.

[166] Lukas Janssen and Matthias Vojta. "Heisenberg–Kitaev physics in magnetic fields". In: *J. Phys.: Condens. Matter* 31.42 (July 2019), p. 423002. ISSN: 0953-8984. DOI: 10.1088/1361-648X/ab283e.

[167] Chao-Ming Jian et al. *Measurement-induced entanglement transitions in quantum circuits of non-interacting fermions: Born-rule versus forced measurements.* 2023. arXiv: 2302.09094.

[168] R. D. Johnson et al. “Monoclinic crystal structure of $\alpha - \mathrm{RuCl}_3$ and the zigzag antiferromagnetic ground state”. In: *Phys. Rev. B* 92 (23 Dec. 2015), p. 235119. DOI: 10.1103/PhysRevB.92.235119. URL: https://link.aps.org/doi/10.1103/PhysRevB.92.235119.

[169] M. Kac. “A stochastic model related to the telegrapher’s equation”. In: *Rocky Mountain Journal of Mathematics* 4 (1974), pp. 497–509.

[170] Ann B. Kallin et al. “Anomalies in the entanglement properties of the square-lattice Heisenberg model”. In: *Phys. Rev. B* 84 (16 Oct. 2011), p. 165134. DOI: 10.1103/PhysRevB.84.165134. URL: https://link.aps.org/doi/10.1103/PhysRevB.84.165134.

[171] D Kandel, E Domany, and B Nienhuis. “A six-vertex model as a diffusion problem: derivation of correlation functions”. In: *Journal of Physics A: Mathematical and General* 23.15 (Aug. 1990), p. L755. DOI: 10.1088/0305-4470/23/15/011. URL: https://dx.doi.org/10.1088/0305-4470/23/15/011.

[172] C. L. Kane and Matthew P. A. Fisher. “Quantized thermal transport in the fractional quantum Hall effect”. In: *Phys. Rev. B* 55 (23 June 1997), pp. 15832–15837. DOI: 10.1103/PhysRevB.55.15832. URL: https://link.aps.org/doi/10.1103/PhysRevB.55.15832.

[173] Wen-Han Kao, Gábor B. Halász, and Natalia B. Perkins. “Dynamics of vacancy-induced modes in the non-Abelian Kitaev spin liquid”. In: *Phys. Rev. B* 109 (12 Mar. 2024), p. 125150. DOI: 10.1103/PhysRevB.109.125150. URL: https://link.aps.org/doi/10.1103/PhysRevB.109.125150.

[174] Wen-Han Kao, Natalia B. Perkins, and Gábor B. Halász. “Vacancy Spectroscopy of Non-Abelian Kitaev Spin Liquids”. In: *Phys. Rev. Lett.* 132 (13 Mar. 2024), p. 136503. DOI: 10.1103/PhysRevLett.132.136503. URL: https://link.aps.org/doi/10.1103/PhysRevLett.132.136503.

[175] Wen-Han Kao et al. “Vacancy-Induced Low-Energy Density of States in the Kitaev Spin Liquid”. In: *Phys. Rev. X* 11 (1 Feb. 2021), p. 011034. DOI: 10.1103/PhysRevX.11.011034. URL: https://link.aps.org/doi/10.1103/PhysRevX.11.011034.

[176] Torsten Karzig et al. “Scalable designs for quasiparticle-poisoning-protected topological quantum computation with Majorana zero modes”. In: *Phys. Rev. B* 95.23 (June 2017), p. 235305. ISSN: 2469-9969. DOI: 10.1103/PhysRevB.95.235305.

[177] Y Kasahara et al. “Majorana quantization and half-integer thermal quantum Hall effect in a Kitaev spin liquid”. In: *Nature* 559.7713 (2018), pp. 227–231. ISSN: 1476-4687. DOI: 10.1038/s41586-018-0274-0. URL: https://doi.org/10.1038/s41586-018-0274-0.

[178] Y Kasahara et al. "Majorana quantization and half-integer thermal quantum Hall effect in a Kitaev spin liquid". In: *Nature* 559.7713 (2018), pp. 227–231. ISSN: 1476-4687. DOI: 10.1038/s41586-018-0274-0. URL: https://doi.org/10.1038/s41586-018-0274-0.

[179] Ribhu K. Kaul, Roger G. Melko, and Anders W. Sandvik. "Bridging Lattice-Scale Physics and Continuum Field Theory with Quantum Monte Carlo Simulations". In: *Annual Review of Condensed Matter Physics* 4.1 (Apr. 2013), pp. 179–215. ISSN: 1947-5462. DOI: 10.1146/annurev-conmatphys-030212-184215. URL: http://dx.doi.org/10.1146/annurev-conmatphys-030212-184215.

[180] D I Khomskii. "Spin chirality and nontrivial charge dynamics in frustrated Mott insulators: spontaneous currents and charge redistribution*". In: *Journal of Physics: Condensed Matter* 22.16 (Mar. 2010), p. 164209. DOI: 10.1088/0953-8984/22/16/164209. URL: https://dx.doi.org/10.1088/0953-8984/22/16/164209.

[181] Doochul Kim. "Bethe ansatz solution for crossover scaling functions of the asymmetric XXZ chain and the Kardar-Parisi-Zhang-type growth model". In: *Phys. Rev. E* 52 (4 Oct. 1995), pp. 3512–3524. DOI: 10.1103/PhysRevE.52.3512. URL: https://link.aps.org/doi/10.1103/PhysRevE.52.3512.

[182] Eun-Ah Kim. "Aharanov-Bohm Interference and Fractional Statistics in a Quantum Hall Interferometer". In: *Phys. Rev. Lett.* 97.21 (Nov. 2006), p. 216404. ISSN: 1079-7114. DOI: 10.1103/PhysRevLett.97.216404.

[183] A. Yu Kitaev. "Unpaired Majorana fermions in quantum wires". In: *Phys.-Usp.* 44.10S (Oct. 2001), p. 131. ISSN: 1063-7869. DOI: 10.1070/1063-7869/44/10S/S29.

[184] A. Yu. Kitaev. "Fault-tolerant quantum computation by anyons". In: *Ann. Phys.* 303.1 (Jan. 2003), pp. 2–30. ISSN: 0003-4916. DOI: 10.1016/S0003-4916(02)00018-0.

[185] Alexei Kitaev. "Anyons in an exactly solved model and beyond". In: *Ann. Phys.* 321.1 (Jan. 2006), pp. 2–111. ISSN: 0003-4916. DOI: 10.1016/j.aop.2005.10.005.

[186] Alexei Kitaev. "Anyons in an exactly solved model and beyond". In: *Annals of Physics* 321.1 (2006), pp. 2–111. DOI: 10.1016/j.aop.2005.10.005.

[187] Alexei Kitaev and John Preskill. "Topological Entanglement Entropy". In: *Phys. Rev. Lett.* 96 (11 Mar. 2006), p. 110404. DOI: 10.1103/PhysRevLett.96.110404. URL: https://link.aps.org/doi/10.1103/PhysRevLett.96.110404.

[188] Kai Klocke and Michael Buchhold. "Majorana Loop Models for Measurement-Only Quantum Circuits". In: *Phys. Rev. X* 13 (4 Nov. 2023), p. 041028. DOI: 10.1103/PhysRevX.13.041028. URL: https://link.aps.org/doi/10.1103/PhysRevX.13.041028.

[189] Kai Klocke et al. "Entanglement dynamics in monitored Kitaev circuits: Loop models, symmetry classification, and quantum Lifshitz scaling". In: *Physical Review B* 111.22 (June 2025). ISSN: 2469-9969. DOI: 10.1103/physrevb.111.224301. URL: http://dx.doi.org/10.1103/PhysRevB.111.224301.

[190] Kai Klocke et al. "Thermal Probes of Phonon-Coupled Kitaev Spin Liquids: From Accurate Extraction of Quantized Edge Transport to Anyon Interferometry". In: *Phys. Rev. X* 12 (1 Feb. 2022), p. 011034. DOI: 10.1103/PhysRevX.12.011034. URL: https://link.aps.org/doi/10.1103/PhysRevX.12.011034.

[191] Kai Klocke et al. "Time-Domain Anyon Interferometry in Kitaev Honeycomb Spin Liquids and Beyond". In: *Phys. Rev. Lett.* 126 (17 Apr. 2021), p. 177204. DOI: 10.1103/PhysRevLett.126.177204. URL: https://link.aps.org/doi/10.1103/PhysRevLett.126.177204.

[192] Kai Klocke et al. "Time-Domain Anyon Interferometry in Kitaev Honeycomb Spin Liquids and Beyond". In: *Phys. Rev. Lett.* 126 (17 Apr. 2021), p. 177204. DOI: 10.1103/PhysRevLett.126.177204. URL: https://link.aps.org/doi/10.1103/PhysRevLett.126.177204.

[193] A. Klümper. "New Results for q-State Vertex Models and the Pure Biquadratic Spin-1 Hamiltonian". In: *Europhysics Letters* 9.8 (Aug. 1989), p. 815. DOI: 10.1209/0295-5075/9/8/013. URL: https://dx.doi.org/10.1209/0295-5075/9/8/013.

[194] J. Knolle and R. Moessner. "A Field Guide to Spin Liquids". In: *Annual Review of Condensed Matter Physics* 10.Volume 10, 2019 (2019), pp. 451–472. ISSN: 1947-5462. DOI: https://doi.org/10.1146/annurev-conmatphys-031218-013401. URL: https://www.annualreviews.org/content/journals/10.1146/annurev-conmatphys-031218-013401.

[195] Y M M Knops, H W J Blote, and B Nienhuis. "Multicriticality in a self-dual Potts model". In: *Journal of Physics A: Mathematical and General* 26.3 (Feb. 1993), p. 495. DOI: 10.1088/0305-4470/26/3/014. URL: https://dx.doi.org/10.1088/0305-4470/26/3/014.

[196] Hari M. Koduvely and Deepak Dhar. "A Model of Subdiffusive Interface Dynamics with a Local Conservation of Minimum Height". In: *Journal of Statistical Physics* 90 (1998), pp. 57–77. URL: https://api.semanticscholar.org/CorpusID:118573505.

[197] Mahito Kohmoto and Yonathan Shapir. "Antiferromagnetic correlations of the resonating valence-bond state". In: *Phys. Rev. B* 37 (16 June 1988), pp. 9439–9442. DOI: 10.1103/PhysRevB.37.9439. URL: https://link.aps.org/doi/10.1103/PhysRevB.37.9439.

[198] Elio J. König, Mallika T. Randeria, and Berthold Jäck. "Tunneling Spectroscopy of Quantum Spin Liquids". In: *Phys. Rev. Lett.* 125 (26 Dec. 2020), p. 267206. DOI: 10.1103/PhysRevLett.125.267206. URL: https://link.aps.org/doi/10.1103/PhysRevLett.125.267206.

[199] Zbigniew Koza and Jakub Poła. “From discrete to continuous percolation in dimensions 3 to 7”. In: *Journal of Statistical Mechanics: Theory and Experiment* 2016.10 (Oct. 2016), p. 103206. ISSN: 1742-5468. DOI: 10.1088/1742-5468/2016/10/103206. URL: http://dx.doi.org/10.1088/1742-5468/2016/10/103206.

[200] Sebastian Krinner et al. “Realizing repeated quantum error correction in a distance-three surface code”. In: *Nature* 605.7911 (May 2022), pp. 669–674. ISSN: 1476-4687. DOI: 10.1038/s41586-022-04566-8. URL: http://dx.doi.org/10.1038/s41586-022-04566-8.

[201] Yumi Kubota et al. “Successive magnetic phase transitions in $\alpha - \mathrm{RuCl}_3$: XY-like frustrated magnet on the honeycomb lattice”. In: *Phys. Rev. B* 91 (9 Mar. 2015), p. 094422. DOI: 10.1103/PhysRevB.91.094422. URL: https://link.aps.org/doi/10.1103/PhysRevB.91.094422.

[202] Nicolai Lang and Hans Peter Büchler. “Entanglement transition in the projective transverse field Ising model”. In: *Phys. Rev. B* 102 (9 Sept. 2020), p. 094204. DOI: 10.1103/PhysRevB.102.094204. URL: https://link.aps.org/doi/10.1103/PhysRevB.102.094204.

[203] Christopher M. Langlett and Shenglong Xu. “Hilbert space fragmentation and exact scars of generalized Fredkin spin chains”. In: *Phys. Rev. B* 103 (22 June 2021), p. L220304. DOI: 10.1103/PhysRevB.103.L220304. URL: https://link.aps.org/doi/10.1103/PhysRevB.103.L220304.

[204] Ali Lavasani, Yahya Alavirad, and Maissam Barkeshli. “Measurement-induced topological entanglement transitions in symmetric random quantum circuits”. In: *Nature Physics* 17.3 (Jan. 2021), pp. 342–347. DOI: 10.1038/s41567-020-01112-z. URL: https://doi.org/10.1038%5C%2Fs41567-020-01112-z.

[205] Ali Lavasani, Yahya Alavirad, and Maissam Barkeshli. “Topological Order and Criticality in $(2+1)$D Monitored Random Quantum Circuits”. In: *Phys. Rev. Lett.* 127 (23 Dec. 2021), p. 235701. DOI: 10.1103/PhysRevLett.127.235701. URL: https://link.aps.org/doi/10.1103/PhysRevLett.127.235701.

[206] Ali Lavasani, Zhu-Xi Luo, and Sagar Vijay. “Monitored quantum dynamics and the Kitaev spin liquid”. In: *Phys. Rev. B* 108 (11 Sept. 2023), p. 115135. DOI: 10.1103/PhysRevB.108.115135. URL: https://link.aps.org/doi/10.1103/PhysRevB.108.115135.

[207] Ian A. Leahy et al. “Anomalous Thermal Conductivity and Magnetic Torque Response in the Honeycomb Magnet α-RuCl_3”. In: *Phys. Rev. Lett.* 118 (18 May 2017), p. 187203. DOI: 10.1103/PhysRevLett.118.187203. URL: https://link.aps.org/doi/10.1103/PhysRevLett.118.187203.

[208] Jong Yeon Lee, Chao-Ming Jian, and Cenke Xu. "Quantum Criticality Under Decoherence or Weak Measurement". In: *PRX Quantum* 4 (3 Aug. 2023), p. 030317. DOI: 10.1103/PRXQuantum.4.030317. URL: https://link.aps.org/doi/10.1103/PRXQuantum.4.030317.

[209] É. Lefran çois et al. "Evidence of a Phonon Hall Effect in the Kitaev Spin Liquid Candidate α–$RuCl_3$". In: *Phys. Rev. X* 12 (2 Apr. 2022), p. 021025. DOI: 10.1103/PhysRevX.12.021025. URL: https://link.aps.org/doi/10.1103/PhysRevX.12.021025.

[210] Leonardo A. Lessa et al. *Strong-to-Weak Spontaneous Symmetry Breaking in Mixed Quantum States*. 2024. arXiv: 2405.03639 [quant-ph]. URL: https://arxiv.org/abs/2405.03639.

[211] Michael Levin and Xiao-Gang Wen. "Detecting Topological Order in a Ground State Wave Function". In: *Phys. Rev. Lett.* 96 (11 Mar. 2006), p. 110405. DOI: 10.1103/PhysRevLett.96.110405. URL: https://link.aps.org/doi/10.1103/PhysRevLett.96.110405.

[212] Weifei Li et al. "Scaling behavior of entanglement in two- and three-dimensional free-fermion systems". In: *Phys. Rev. B* 74 (7 Aug. 2006), p. 073103. DOI: 10.1103/PhysRevB.74.073103. URL: https://link.aps.org/doi/10.1103/PhysRevB.74.073103.

[213] Yaodong Li, Xiao Chen, and Matthew P. A. Fisher. "Measurement-driven entanglement transition in hybrid quantum circuits". In: *Phys. Rev. B* 100 (13 Oct. 2019), p. 134306. DOI: 10.1103/PhysRevB.100.134306. URL: https://link.aps.org/doi/10.1103/PhysRevB.100.134306.

[214] Yaodong Li, Xiao Chen, and Matthew P. A. Fisher. "Quantum Zeno effect and the many-body entanglement transition". In: *Phys. Rev. B* 98 (20 Nov. 2018), p. 205136. DOI: 10.1103/PhysRevB.98.205136. URL: https://link.aps.org/doi/10.1103/PhysRevB.98.205136.

[215] Yaodong Li and Matthew P. A. Fisher. *Robust decoding in monitored dynamics of open quantum systems with Z_2 symmetry*. 2021. DOI: 10.48550/ARXIV.2108.04274. arXiv: 2108.04274 [quant-ph]. URL: https://arxiv.org/abs/2108.04274.

[216] Yaodong Li et al. "Conformal invariance and quantum nonlocality in critical hybrid circuits". In: *Phys. Rev. B* 104 (10 Sept. 2021), p. 104305. DOI: 10.1103/PhysRevB.104.104305. URL: https://link.aps.org/doi/10.1103/PhysRevB.104.104305.

[217] Yaodong Li et al. *Statistical Mechanics Model for Clifford Random Tensor Networks and Monitored Quantum Circuits*. 2021. arXiv: 2110.02988 [cond-mat.stat-mech].

[218] Zhi Li and Zhu-Xi Luo. *Exact, Average, and Broken Symmetries in a Simple Adaptive Monitored Circuit*. 2023. arXiv: 2312.17309.

[219] Biao Lian and Juven Wang. "Theory of the disordered $\nu = \frac{5}{2}$ quantum thermal Hall state: Emergent symmetry and phase diagram". In: *Phys. Rev. B* 97 (16 Apr. 2018), p. 165124. DOI: 10.1103/PhysRevB.97.165124. URL: https://link.aps.org/doi/10.1103/PhysRevB.97.165124.

[220] Elliott H. Lieb. "Flux Phase of the Half-Filled Band". In: *Physical Review Letters* 73.16 (Oct. 1994), pp. 2158–2161. ISSN: 0031-9007. DOI: 10.1103/physrevlett.73.2158. URL: http://dx.doi.org/10.1103/PhysRevLett.73.2158.

[221] Joanna W. Lis et al. "Midcircuit Operations Using the omg Architecture in Neutral Atom Arrays". In: *Phys. Rev. X* 13 (4 Nov. 2023), p. 041035. DOI: 10.1103/PhysRevX.13.041035. URL: https://link.aps.org/doi/10.1103/PhysRevX.13.041035.

[222] Yue Liu et al. "Dynamical Anyon Generation in Kitaev Honeycomb Non-Abelian Spin Liquids". In: *Phys. Rev. Lett.* 129 (3 July 2022), p. 037201. DOI: 10.1103/PhysRevLett.129.037201. URL: https://link.aps.org/doi/10.1103/PhysRevLett.129.037201.

[223] William P. Livingston et al. "Experimental demonstration of continuous quantum error correction". In: *Nature Communications* 13.1 (Apr. 2022). ISSN: 2041-1723. DOI: 10.1038/s41467-022-29906-0. URL: http://dx.doi.org/10.1038/s41467-022-29906-0.

[224] Hugo Lóio et al. *Purification Timescales in Monitored Fermions*. 2023. arXiv: 2303.12216 [cond-mat.stat-mech].

[225] Tsung-Cheng Lu et al. "Measurement as a Shortcut to Long-Range Entangled Quantum Matter". In: *PRX Quantum* 3 (4 Dec. 2022), p. 040337. DOI: 10.1103/PRXQuantum.3.040337. URL: https://link.aps.org/doi/10.1103/PRXQuantum.3.040337.

[226] Tsung-Cheng Lu et al. "Mixed-State Long-Range Order and Criticality from Measurement and Feedback". In: *PRX Quantum* 4 (3 Aug. 2023), p. 030318. DOI: 10.1103/PRXQuantum.4.030318. URL: https://link.aps.org/doi/10.1103/PRXQuantum.4.030318.

[227] Roman M. Lutchyn, Jay D. Sau, and S. Das Sarma. "Majorana Fermions and a Topological Phase Transition in Semiconductor-Superconductor Heterostructures". In: *Phys. Rev. Lett.* 105.7 (Aug. 2010), p. 077001. ISSN: 1079-7114. DOI: 10.1103/PhysRevLett.105.077001.

[228] Shuo Ma et al. "High-fidelity gates and mid-circuit erasure conversion in an atomic qubit". In: *Nature* 622.7982 (Oct. 2023), pp. 279–284. ISSN: 1476-4687. DOI: 10.1038/s41586-023-06438-1. URL: http://dx.doi.org/10.1038/s41586-023-06438-1.

[229] Ettore Majorana. "Teoria simmetrica dell'elettrone e del positrone". In: *Il Nuovo Cimento* 14.4 (Apr. 1937), pp. 171–184. DOI: 10.1007/BF02961314.

[230] M. Majumder et al. "Anisotropic $Ru^{3+}4d^5$ magnetism in the $\alpha - RuCl_3$ honeycomb system: Susceptibility, specific heat, and zero-field NMR". In: *Phys. Rev. B* 91 (18 May 2015), p. 180401. DOI: 10.1103/PhysRevB.91.180401. URL: https://link.aps.org/doi/10.1103/PhysRevB.91.180401.

[231] Paul Martin. *Potts Models and Related Problems in Statistical Mechanics*. WORLD SCIENTIFIC, 1991. DOI: 10.1142/0983. URL: https://www.worldscientific.com/doi/abs/10.1142/0983.

[232] M. J. Martins, B. Nienhuis, and R. Rietman. "Intersecting Loop Model as a Solvable Super Spin Chain". In: *Phys. Rev. Lett.* 81 (3 July 1998), pp. 504–507. DOI: 10.1103/PhysRevLett.81.504. URL: https://link.aps.org/doi/10.1103/PhysRevLett.81.504.

[233] A.J. McKane, D.J. Wallace, and R.K.P. Zia. "Models for strong interactions in 6-ϵ dimensions". In: *Physics Letters B* 65.2 (1976), pp. 171–173. ISSN: 0370-2693. DOI: https://doi.org/10.1016/0370-2693(76)90024-1. URL: https://www.sciencedirect.com/science/article/pii/0370269376900241.

[234] Gautam I. Menon, Mustansir Barma, and Deepak Dhar. "Conservation laws and integrability of a one-dimensional model of diffusing dimers". In: *Journal of Statistical Physics* 86.5–6 (Mar. 1997), pp. 1237–1263. ISSN: 1572-9613. DOI: 10.1007/bf02183622. URL: http://dx.doi.org/10.1007/BF02183622.

[235] M K Hari Menon and D Dhar. "The irreducible string and an infinity of additional constants of motion in a deposition-evaporation model on a line". In: *Journal of Physics A: Mathematical and General* 28.23 (Dec. 1995), p. 6517. DOI: 10.1088/0305-4470/28/23/008. URL: https://dx.doi.org/10.1088/0305-4470/28/23/008.

[236] Hu Miao and Gábor B. Halász. "Structural tweaking of 2D quantum magnetism". In: *Nature Materials* 22.1 (Jan. 2023), pp. 8–9. ISSN: 1476-4660. DOI: 10.1038/s41563-022-01445-5. URL: https://doi.org/10.1038/s41563-022-01445-5.

[237] A. Milsted et al. "Statistical translation invariance protects a topological insulator from interactions". In: *Phys. Rev. B* 92 (8 Aug. 2015), p. 085139. DOI: 10.1103/PhysRevB.92.085139. URL: https://link.aps.org/doi/10.1103/PhysRevB.92.085139.

[238] Tomonari Mizoguchi, Tohru Koma, and Yasuhito Yoshida. "Oriented propagation of magnetization due to chiral edge modes in Kitaev-type models". In: *Phys. Rev. B* 101 (1 Jan. 2020), p. 014442. DOI: 10.1103/PhysRevB.101.014442. URL: https://link.aps.org/doi/10.1103/PhysRevB.101.014442.

[239] Gregory Moore and Nicholas Read. "Nonabelions in the fractional quantum Hall effect". In: *Nucl. Phys. B* 360.2 (Aug. 1991), pp. 362–396. ISSN: 0550-3213. DOI: 10.1016/0550-3213(91)90407-O.

[240] Samuel Morales et al. “Engineering unsteerable quantum states with active feedback”. In: *Phys. Rev. Res.* 6 (1 Mar. 2024), p. 013244. DOI: 10.1103/PhysRevResearch.6.013244. URL: https://link.aps.org/doi/10.1103/PhysRevResearch.6.013244.

[241] Raúl Morral-Yepes et al. “Entanglement Transitions in Unitary Circuit Games”. In: *PRX Quantum* 5 (1 Jan. 2024), p. 010309. DOI: 10.1103/PRXQuantum.5.010309. URL: https://link.aps.org/doi/10.1103/PRXQuantum.5.010309.

[242] S. A. Moses et al. “A Race-Track Trapped-Ion Quantum Processor”. In: *Phys. Rev. X* 13 (4 Dec. 2023), p. 041052. DOI: 10.1103/PhysRevX.13.041052. URL: https://link.aps.org/doi/10.1103/PhysRevX.13.041052.

[243] Yukitoshi Motome and Joji Nasu. “Hunting Majorana Fermions in Kitaev Magnets”. In: *J. Phys. Soc. Jpn.* 89.1 (Dec. 2019), p. 012002. ISSN: 0031-9015. DOI: 10.7566/JPSJ.89.012002.

[244] Sanjay Moudgalya et al. “Spectral statistics in constrained many-body quantum chaotic systems”. In: *Physical Review Research* 3.2 (June 2021). ISSN: 2643-1564. DOI: 10.1103/physrevresearch.3.023176. URL: http://dx.doi.org/10.1103/PhysRevResearch.3.023176.

[245] Ramis Movassagh. “Entanglement and correlation functions of the quantum Motzkin spin-chain”. In: *Journal of Mathematical Physics* 58.3 (Mar. 2017). ISSN: 1089-7658. DOI: 10.1063/1.4977829. URL: http://dx.doi.org/10.1063/1.4977829.

[246] Ramis Movassagh and Peter W. Shor. “Supercritical entanglement in local systems: Counterexample to the area law for quantum matter”. In: *Proceedings of the National Academy of Sciences* 113.47 (Nov. 2016), pp. 13278–13282. ISSN: 1091-6490. DOI: 10.1073/pnas.1605716113. URL: http://dx.doi.org/10.1073/pnas.1605716113.

[247] David F. Mross et al. “Theory of Disorder-Induced Half-Integer Thermal Hall Conductance”. In: *Phys. Rev. Lett.* 121 (2 July 2018), p. 026801. DOI: 10.1103/PhysRevLett.121.026801. URL: https://link.aps.org/doi/10.1103/PhysRevLett.121.026801.

[248] T. Müller, S. Diehl, and M. Buchhold. “Measurement-Induced Dark State Phase Transitions in Long-Ranged Fermion Systems”. In: *Phys. Rev. Lett.* 128 (1 Jan. 2022), p. 010605. DOI: 10.1103/PhysRevLett.128.010605. URL: https://link.aps.org/doi/10.1103/PhysRevLett.128.010605.

[249] Sara Murciano et al. *Measurement-altered Ising quantum criticality*. 2023. arXiv: 2302.04325 [cond-mat.stat-mech].

[250] Adam Nahum and J. T. Chalker. “Universal statistics of vortex lines”. In: *Phys. Rev. E* 85 (3 Mar. 2012), p. 031141. DOI: 10.1103/PhysRevE.85.031141. URL: https://link.aps.org/doi/10.1103/PhysRevE.85.031141.

[251] Adam Nahum and Brian Skinner. "Entanglement and dynamics of diffusion annihilation processes with Majorana defects". In: *Phys. Rev. Res.* 2 (2 June 2020), p. 023288. DOI: 10.1103/PhysRevResearch.2.023288. URL: https://link.aps.org/doi/10.1103/PhysRevResearch.2.023288.

[252] Adam Nahum et al. "3D Loop Models and the CP^{n-1} Sigma Model". In: *Phys. Rev. Lett.* 107 (11 Sept. 2011), p. 110601. DOI: 10.1103/PhysRevLett.107.110601. URL: https://link.aps.org/doi/10.1103/PhysRevLett.107.110601.

[253] Adam Nahum et al. "Deconfined Quantum Criticality, Scaling Violations, and Classical Loop Models". In: *Phys. Rev. X* 5 (4 Dec. 2015), p. 041048. DOI: 10.1103/PhysRevX.5.041048. URL: https://link.aps.org/doi/10.1103/PhysRevX.5.041048.

[254] Adam Nahum et al. "Length Distributions in Loop Soups". In: *Phys. Rev. Lett.* 111 (10 Sept. 2013), p. 100601. DOI: 10.1103/PhysRevLett.111.100601. URL: https://link.aps.org/doi/10.1103/PhysRevLett.111.100601.

[255] Adam Nahum et al. "Loop models with crossings". In: *Phys. Rev. B* 87 (18 May 2013), p. 184204. DOI: 10.1103/PhysRevB.87.184204. URL: https://link.aps.org/doi/10.1103/PhysRevB.87.184204.

[256] Adam Nahum et al. "Phase transitions in three-dimensional loop models and the CP^{n-1} sigma model". In: *Phys. Rev. B* 88 (13 Oct. 2013), p. 134411. DOI: 10.1103/PhysRevB.88.134411. URL: https://link.aps.org/doi/10.1103/PhysRevB.88.134411.

[257] Adam Nahum et al. "Quantum Entanglement Growth under Random Unitary Dynamics". In: *Phys. Rev. X* 7 (3 July 2017), p. 031016. DOI: 10.1103/PhysRevX.7.031016. URL: https://link.aps.org/doi/10.1103/PhysRevX.7.031016.

[258] J. Nakamura et al. "Aharonov-Bohm interference of fractional quantum Hall edge modes". In: *Nature Physics* 15.6 (June 2019), pp. 563–569. ISSN: 1745-2481. DOI: 10.1038/s41567-019-0441-8. URL: https://doi.org/10.1038/s41567-019-0441-8.

[259] James Nakamura et al. *Direct observation of anyonic braiding statistics at the ν=1/3 fractional quantum Hall state*. 2020. arXiv: 2006.14115 [cond-mat.mes-hall].

[260] Chetan Nayak and Frank Wilczek. "2n-quasihole states realize 2^{n-1}-dimensional spinor braiding statistics in paired quantum Hall states". In: *Nuclear Physics B* 479.3 (Nov. 1996), pp. 529–553. ISSN: 0550-3213. DOI: 10.1016/0550-3213(96)00430-0. URL: http://dx.doi.org/10.1016/0550-3213(96)00430-0.

[261] Chetan Nayak et al. "Non-Abelian anyons and topological quantum computation". In: *Rev. Mod. Phys.* 80.3 (Sept. 2008), pp. 1083–1159. ISSN: 1539-0756. DOI: 10.1103/RevModPhys.80.1083.

[262] John Neergaard and Marcel den Nijs. "Crossover Scaling Functions in One Dimensional Dynamic Growth Models". In: *Phys. Rev. Lett.* 74 (5 Jan. 1995), pp. 730–733. DOI: 10.1103/PhysRevLett.74.730. URL: https://link.aps.org/doi/10.1103/PhysRevLett.74.730.

[263] B Nienhuis. "Analytical calculation of two leading exponents of the dilute Potts model". In: *Journal of Physics A: Mathematical and General* 15.1 (Jan. 1982), p. 199. DOI: 10.1088/0305-4470/15/1/028. URL: https://dx.doi.org/10.1088/0305-4470/15/1/028.

[264] B. Nienhuis et al. "First- and Second-Order Phase Transitions in Potts Models: Renormalization-Group Solution". In: *Phys. Rev. Lett.* 43 (11 Sept. 1979), pp. 737–740. DOI: 10.1103/PhysRevLett.43.737. URL: https://link.aps.org/doi/10.1103/PhysRevLett.43.737.

[265] Johan Nilsson and A. R. Akhmerov. "Theory of non-Abelian Fabry-Perot interferometry in topological insulators". In: *Phys. Rev. B* 81 (20 May 2010), p. 205110. DOI: 10.1103/PhysRevB.81.205110. URL: https://link.aps.org/doi/10.1103/PhysRevB.81.205110.

[266] Crystal Noel et al. "Measurement-induced quantum phases realized in a trapped-ion quantum computer". In: *Nature Physics* 18.7 (June 2022), pp. 760–764. ISSN: 1745-2481. DOI: 10.1038/s41567-022-01619-7. URL: http://dx.doi.org/10.1038/s41567-022-01619-7.

[267] M. A. Norcia et al. "Midcircuit Qubit Measurement and Rearrangement in a ^{171}Yb Atomic Array". In: *Phys. Rev. X* 13 (4 Nov. 2023), p. 041034. DOI: 10.1103/PhysRevX.13.041034. URL: https://link.aps.org/doi/10.1103/PhysRevX.13.041034.

[268] Edward O'Brien and Paul Fendley. "Lattice Supersymmetry and Order-Disorder Coexistence in the Tricritical Ising Model". In: *Phys. Rev. Lett.* 120 (20 May 2018), p. 206403. DOI: 10.1103/PhysRevLett.120.206403. URL: https://link.aps.org/doi/10.1103/PhysRevLett.120.206403.

[269] Nicholas O'Dea et al. "Entanglement and absorbing-state transitions in interactive quantum dynamics". In: *Phys. Rev. B* 109 (2 Jan. 2024), p. L020304. DOI: 10.1103/PhysRevB.109.L020304. URL: https://link.aps.org/doi/10.1103/PhysRevB.109.L020304.

[270] Yuval Oreg, Gil Refael, and Felix von Oppen. "Helical Liquids and Majorana Bound States in Quantum Wires". In: *Phys. Rev. Lett.* 105.17 (Oct. 2010), p. 177002. ISSN: 1079-7114. DOI: 10.1103/PhysRevLett.105.177002.

[271] M. Ortuño, A. M. Somoza, and J. T. Chalker. "Random Walks and Anderson Localization in a Three-Dimensional Class C Network Model". In: *Phys. Rev. Lett.* 102 (7 Feb. 2009), p. 070603. DOI: 10.1103/PhysRevLett.102.070603. URL: https://link.aps.org/doi/10.1103/PhysRevLett.102.070603.

[272] Haining Pan et al. “Local and nonlocal stochastic control of quantum chaos: Measurement and control-induced criticality”. In: *Phys. Rev. B* 110 (5 Aug. 2024), p. 054308. DOI: 10.1103/PhysRevB.110.054308. URL: https://link.aps.org/doi/10.1103/PhysRevB.110.054308.

[273] J B Parkinson. “The S=1 quantum spin chain with pure biquadratic exchange”. In: *Journal of Physics C: Solid State Physics* 21.20 (July 1988), p. 3793. DOI: 10.1088/0022-3719/21/20/014. URL: https://dx.doi.org/10.1088/0022-3719/21/20/014.

[274] Paul A Pearce et al. “Temperley-Lieb stochastic processes”. In: *Journal of Physics A: Mathematical and General* 35.45 (Oct. 2002), pp. L661–L668. ISSN: 0305-4470. DOI: 10.1088/0305-4470/35/45/105. URL: http://dx.doi.org/10.1088/0305-4470/35/45/105.

[275] K. A. Penson, R. Jullien, and P. Pfeuty. “Phase transitions in systems with multispin interactions”. In: *Phys. Rev. B* 26 (11 Dec. 1982), pp. 6334–6337. DOI: 10.1103/PhysRevB.26.6334. URL: https://link.aps.org/doi/10.1103/PhysRevB.26.6334.

[276] Rodrigo G. Pereira and Reinhold Egger. “Electrical Access to Ising Anyons in Kitaev Spin Liquids”. In: *Phys. Rev. Lett.* 125 (22 Nov. 2020), p. 227202. DOI: 10.1103/PhysRevLett.125.227202. URL: https://link.aps.org/doi/10.1103/PhysRevLett.125.227202.

[277] Lorenzo Piroli, Georgios Styliaris, and J. Ignacio Cirac. “Quantum Circuits Assisted by Local Operations and Classical Communication: Transformations and Phases of Matter”. In: *Phys. Rev. Lett.* 127 (22 Nov. 2021), p. 220503. DOI: 10.1103/PhysRevLett.127.220503. URL: https://link.aps.org/doi/10.1103/PhysRevLett.127.220503.

[278] S. Plugge et al. “Roadmap to Majorana surface codes”. In: *Phys. Rev. B* 94.17 (Nov. 2016), p. 174514. ISSN: 2469-9969. DOI: 10.1103/PhysRevB.94.174514.

[279] Stephan Plugge et al. “Majorana box qubits”. In: *New J. Phys.* 19.1 (Jan. 2017), p. 012001. ISSN: 1367-2630. DOI: 10.1088/1367-2630/aa54e1.

[280] K. W. Plumb et al. “α–$RuCl_3$: A spin-orbit assisted Mott insulator on a honeycomb lattice”. In: *Phys. Rev. B* 90 (4 July 2014), p. 041112. DOI: 10.1103/PhysRevB.90.041112. URL: https://link.aps.org/doi/10.1103/PhysRevB.90.041112.

[281] Igor Poboiko et al. “Theory of Free Fermions under Random Projective Measurements”. In: *Phys. Rev. X* 13 (4 Dec. 2023), p. 041046. DOI: 10.1103/PhysRevX.13.041046. URL: https://link.aps.org/doi/10.1103/PhysRevX.13.041046.

[282] Andrew C. Potter and Romain Vasseur. “Entanglement Dynamics in Hybrid Quantum Circuits”. In: *Entanglement in Spin Chains: From Theory to Quantum Technology Applications*. Ed. by Abolfazl Bayat, Sougato Bose, and Henrik Johannesson. Cham: Springer International Publishing, 2022, pp. 211–249. ISBN: 978-3-031-03998-0. DOI: 10.1007/978-3-031-03998-0_9. URL: https://doi.org/10.1007/978-3-031-03998-0_9.

[283] Armin Rahmani et al. "Emergent Supersymmetry from Strongly Interacting Majorana Zero Modes". In: *Phys. Rev. Lett.* 115 (16 Oct. 2015), p. 166401. DOI: 10.1103/PhysRevLett.115.166401. URL: https://link.aps.org/doi/10.1103/PhysRevLett.115.166401.

[284] Armin Rahmani et al. "Phase diagram of the interacting Majorana chain model". In: *Phys. Rev. B* 92 (23 Dec. 2015), p. 235123. DOI: 10.1103/PhysRevB.92.235123. URL: https://link.aps.org/doi/10.1103/PhysRevB.92.235123.

[285] Diego Rainis and Daniel Loss. "Majorana qubit decoherence by quasiparticle poisoning". In: *Phys. Rev. B* 85 (17 May 2012), p. 174533. DOI: 10.1103/PhysRevB.85.174533. URL: https://link.aps.org/doi/10.1103/PhysRevB.85.174533.

[286] D.C. Ralph and M.D. Stiles. "Spin transfer torques". In: *J. Magn. Magn. Mater.* 320.7 (Apr. 2008), pp. 1190–1216. ISSN: 0304-8853. DOI: 10.1016/j.jmmm.2007.12.019. URL: http://dx.doi.org/10.1016/j.jmmm.2007.12.019.

[287] Jeffrey G. Rau, Eric Kin-Ho Lee, and Hae-Young Kee. "Spin-Orbit Physics Giving Rise to Novel Phases in Correlated Systems: Iridates and Related Materials". In: *Annual Review of Condensed Matter Physics* 7.1 (2016), pp. 195–221. DOI: 10.1146/annurev-conmatphys-031115-011319. URL: https://doi.org/10.1146/annurev-conmatphys-031115-011319.

[288] Vikram Ravindranath, Zhi-Cheng Yang, and Xiao Chen. "Free fermions under adaptive quantum dynamics". In: *Quantum* 9 (Apr. 2025), p. 1685. ISSN: 2521-327X. DOI: 10.22331/q-2025-04-03-1685. URL: http://dx.doi.org/10.22331/q-2025-04-03-1685.

[289] Vikram Ravindranath et al. "Entanglement steering in adaptive circuits with feedback". In: *Phys. Rev. B* 108 (4 July 2023), p. L041103. DOI: 10.1103/PhysRevB.108.L041103. URL: https://link.aps.org/doi/10.1103/PhysRevB.108.L041103.

[290] N. Read and Dmitry Green. "Paired states of fermions in two dimensions with breaking of parity and time-reversal symmetries and the fractional quantum Hall effect". In: *Phys. Rev. B* 61.15 (Apr. 2000), pp. 10267–10297. ISSN: 2469-9969. DOI: 10.1103/PhysRevB.61.10267.

[291] Daniel S. Rokhsar and Steven A. Kivelson. "Superconductivity and the Quantum Hard-Core Dimer Gas". In: *Phys. Rev. Lett.* 61 (20 Nov. 1988), pp. 2376–2379. DOI: 10.1103/PhysRevLett.61.2376. URL: https://link.aps.org/doi/10.1103/PhysRevLett.61.2376.

[292] B. Rosenow and B. I. Halperin. "Influence of Interactions on Flux and Back-Gate Period of Quantum Hall Interferometers". In: *Phys. Rev. Lett.* 98.10 (Mar. 2007), p. 106801. ISSN: 1079-7114. DOI: 10.1103/PhysRevLett.98.106801.

[293] B. Rosenow and Steven H. Simon. "Telegraph noise and the Fabry-Perot quantum Hall interferometer". In: *Phys. Rev. B* 85.20 (May 2012), p. 201302. ISSN: 2469-9969. DOI: 10.1103/PhysRevB.85.201302.

[294] Felix Roser, Hans Peter Büchler, and Nicolai Lang. "Decoding the projective transverse field Ising model". In: *Phys. Rev. B* 107 (21 June 2023), p. 214201. DOI: 10.1103/PhysRevB.107.214201. URL: https://link.aps.org/doi/10.1103/PhysRevB.107.214201.

[295] Eric C. Rowell and Zhenghan Wang. "Degeneracy and non-Abelian statistics". In: *Phys. Rev. A* 93 (3 Mar. 2016), p. 030102. DOI: 10.1103/PhysRevA.93.030102. URL: https://link.aps.org/doi/10.1103/PhysRevA.93.030102.

[296] C. Ryan-Anderson et al. "Realization of Real-Time Fault-Tolerant Quantum Error Correction". In: *Phys. Rev. X* 11 (4 Dec. 2021), p. 041058. DOI: 10.1103/PhysRevX.11.041058. URL: https://link.aps.org/doi/10.1103/PhysRevX.11.041058.

[297] Pablo Sala et al. *Spontaneous Strong Symmetry Breaking in Open Systems: Purification Perspective*. 2024. arXiv: 2405.02402 [quant-ph]. URL: https://arxiv.org/abs/2405.02402.

[298] Olof Salberger and Vladimir Korepin. *Fredkin Spin Chain*. 2016. arXiv: 1605.03842 [quant-ph].

[299] Luke J. Sandilands et al. "Scattering Continuum and Possible Fractionalized Excitations in α–$RuCl_3$". In: *Phys. Rev. Lett.* 114 (14 Apr. 2015), p. 147201. DOI: 10.1103/PhysRevLett.114.147201. URL: https://link.aps.org/doi/10.1103/PhysRevLett.114.147201.

[300] Luke J. Sandilands et al. "Spin-orbit excitations and electronic structure of the putative Kitaev magnet $\alpha - RuCl_3$". In: *Phys. Rev. B* 93 (7 Feb. 2016), p. 075144. DOI: 10.1103/PhysRevB.93.075144. URL: https://link.aps.org/doi/10.1103/PhysRevB.93.075144.

[301] Anders W. Sandvik. "Ground State Projection of Quantum Spin Systems in the Valence-Bond Basis". In: *Phys. Rev. Lett.* 95 (20 Nov. 2005), p. 207203. DOI: 10.1103/PhysRevLett.95.207203. URL: https://link.aps.org/doi/10.1103/PhysRevLett.95.207203.

[302] Shengqi Sang and Timothy H. Hsieh. "Measurement-protected quantum phases". In: *Phys. Rev. Res.* 3 (2 June 2021), p. 023200. DOI: 10.1103/PhysRevResearch.3.023200. URL: https://link.aps.org/doi/10.1103/PhysRevResearch.3.023200.

[303] Shengqi Sang et al. "Entanglement Negativity at Measurement-Induced Criticality". In: *PRX Quantum* 2 (3 July 2021), p. 030313. DOI: 10.1103/PRXQuantum.2.030313. URL: https://link.aps.org/doi/10.1103/PRXQuantum.2.030313.

[304] Shengqi Sang et al. "Entanglement Negativity at Measurement-Induced Criticality". In: *PRX Quantum* 2 (3 July 2021), p. 030313. DOI: 10.1103/PRXQuantum.2.030313. URL: https://link.aps.org/doi/10.1103/PRXQuantum.2.030313.

[305] Sankar Das Sarma, Michael Freedman, and Chetan Nayak. "Majorana zero modes and topological quantum computation". In: *npj Quantum Information* 1.1 (Oct. 2015). ISSN: 2056-6387. DOI: 10.1038/npjqi.2015.1. URL: http://dx.doi.org/10.1038/npjqi.2015.1.

[306] Jay D. Sau et al. "Generic New Platform for Topological Quantum Computation Using Semiconductor Heterostructures". In: *Phys. Rev. Lett.* 104.4 (Jan. 2010), p. 040502. ISSN: 1079-7114. DOI: 10.1103/PhysRevLett.104.040502.

[307] Lucile Savary and Leon Balents. "Quantum spin liquids: a review". In: *Rep. Prog. Phys.* 80.1 (Nov. 2016), p. 016502. ISSN: 0034-4885. DOI: 10.1088/0034-4885/80/1/016502.

[308] Manuel J. Schmidt, Diego Rainis, and Daniel Loss. "Decoherence of Majorana qubits by noisy gates". In: *Phys. Rev. B* 86 (8 Aug. 2012), p. 085414. DOI: 10.1103/PhysRevB.86.085414. URL: https://link.aps.org/doi/10.1103/PhysRevB.86.085414.

[309] K. Schwab et al. "Measurement of the quantum of thermal conductance". In: *Nature* 404.6781 (Apr. 2000), pp. 974–977. ISSN: 1476-4687. DOI: 10.1038/35010065. URL: https://doi.org/10.1038/35010065.

[310] J. A. Sears et al. "Magnetic order in $\alpha-$RuCl$_3$: A honeycomb-lattice quantum magnet with strong spin-orbit coupling". In: *Phys. Rev. B* 91 (14 Apr. 2015), p. 144420. DOI: 10.1103/PhysRevB.91.144420. URL: https://link.aps.org/doi/10.1103/PhysRevB.91.144420.

[311] J. A. Sears et al. "Phase diagram of α-RuCl$_3$ in an in-plane magnetic field". In: *Phys. Rev. B* 95 (18 May 2017), p. 180411. DOI: 10.1103/PhysRevB.95.180411. URL: https://link.aps.org/doi/10.1103/PhysRevB.95.180411.

[312] Walter Selke. "The ANNNI model — Theoretical analysis and experimental application". In: *Physics Reports* 170.4 (1988), pp. 213–264. ISSN: 0370-1573. DOI: https://doi.org/10.1016/0370-1573(88)90140-8. URL: https://www.sciencedirect.com/science/article/pii/0370157388901408.

[313] Pablo Serna. *3D Unoriented loop models and the* RP^{n-1} *sigma model*. 2021. arXiv: 2107.13366.

[314] P. Sierant and X. Turkeshi. "Entanglement and Absorbing State Transitions in (d+1)-Dimensional Stabilizer Circuits". In: *Acta Physica Polonica A* 144.6 (Dec. 2023), pp. 474–485. ISSN: 0587-4246. DOI: 10.12693/aphyspola.144.474. URL: http://dx.doi.org/10.12693/APhysPolA.144.474.

[315] Piotr Sierant et al. "Measurement-induced phase transitions in $(d+1)$-dimensional stabilizer circuits". In: *Phys. Rev. B* 106 (21 Dec. 2022), p. 214316. DOI: 10.1103/PhysRevB.106.214316. URL: https://link.aps.org/doi/10.1103/PhysRevB.106.214316.

[316] Hansveer Singh et al. “Subdiffusion and Many-Body Quantum Chaos with Kinetic Constraints”. In: *Physical Review Letters* 127.23 (Dec. 2021). ISSN: 1079-7114. DOI: 10.1103/physrevlett.127.230602. URL: http://dx.doi.org/10.1103/PhysRevLett.127.230602.

[317] K. Singh et al. “Mid-circuit correction of correlated phase errors using an array of spectator qubits”. In: *Science* 380.6651 (June 2023), pp. 1265–1269. ISSN: 1095-9203. DOI: 10.1126/science.ade5337. URL: http://dx.doi.org/10.1126/science.ade5337.

[318] Brian Skinner, Jonathan Ruhman, and Adam Nahum. “Measurement-Induced Phase Transitions in the Dynamics of Entanglement”. In: *Phys. Rev. X* 9 (3 July 2019), p. 031009. DOI: 10.1103/PhysRevX.9.031009. URL: https://link.aps.org/doi/10.1103/PhysRevX.9.031009.

[319] Adithya Sriram et al. “Topology, criticality, and dynamically generated qubits in a stochastic measurement-only Kitaev model”. In: *Phys. Rev. B* 108 (9 Sept. 2023), p. 094304. DOI: 10.1103/PhysRevB.108.094304. URL: https://link.aps.org/doi/10.1103/PhysRevB.108.094304.

[320] Jean-Marie Stéphan, Grégoire Misguich, and Vincent Pasquier. “Rényi entanglement entropies in quantum dimer models: from criticality to topological order”. In: *Journal of Statistical Mechanics: Theory and Experiment* 2012.02 (Feb. 2012), P02003. ISSN: 1742-5468. DOI: 10.1088/1742-5468/2012/02/p02003. URL: http://dx.doi.org/10.1088/1742-5468/2012/02/P02003.

[321] Jean-Marie Stéphan et al. “Entanglement in gapless resonating-valence-bond states”. In: *New Journal of Physics* 15.1 (Jan. 2013), p. 015004. ISSN: 1367-2630. DOI: 10.1088/1367-2630/15/1/015004. URL: http://dx.doi.org/10.1088/1367-2630/15/1/015004.

[322] Ady Stern and Bertrand I. Halperin. “Proposed Experiments to Probe the Non-Abelian $\nu = 5/2$ Quantum Hall State”. In: *Phys. Rev. Lett.* 96 (1 Jan. 2006), p. 016802. DOI: 10.1103/PhysRevLett.96.016802. URL: https://link.aps.org/doi/10.1103/PhysRevLett.96.016802.

[323] Ady Stern and Bertrand I. Halperin. “Proposed Experiments to Probe the Non-Abelian $\nu = 5/2$ Quantum Hall State”. In: *Phys. Rev. Lett.* 96.1 (Jan. 2006), p. 016802. ISSN: 1079-7114. DOI: 10.1103/PhysRevLett.96.016802.

[324] Roman Stricker et al. “Experimental deterministic correction of qubit loss”. In: *Nature* 585.7824 (Sept. 2020), pp. 207–210. ISSN: 1476-4687. DOI: 10.1038/s41586-020-2667-0. URL: http://dx.doi.org/10.1038/s41586-020-2667-0.

[325] Bill Sutherland. “Systems with resonating-valence-bond ground states: Correlations and excitations”. In: *Phys. Rev. B* 37 (7 Mar. 1988), pp. 3786–3789. DOI: 10.1103/PhysRevB.37.3786. URL: https://link.aps.org/doi/10.1103/PhysRevB.37.3786.

[326] Brian Swingle. “Entanglement Entropy and the Fermi Surface”. In: *Phys. Rev. Lett.* 105 (5 July 2010), p. 050502. DOI: 10.1103/PhysRevLett.105.050502. URL: https://link.aps.org/doi/10.1103/PhysRevLett.105.050502.

[327] Hidenori Takagi et al. “Concept and realization of Kitaev quantum spin liquids”. In: *Nat. Rev. Phys.* 1 (Apr. 2019), pp. 264–280. ISSN: 2522-5820. DOI: 10.1038/s42254-019-0038-2.

[328] Masahiro O. Takahashi et al. “Nonlocal Spin Correlation as a Signature of Ising Anyons Trapped in Vacancies of the Kitaev Spin Liquid”. In: *Phys. Rev. Lett.* 131 (23 Dec. 2023), p. 236701. DOI: 10.1103/PhysRevLett.131.236701. URL: https://link.aps.org/doi/10.1103/PhysRevLett.131.236701.

[329] N. Tantivasadakarn, R. Verresen, and A. Vishwanath. “Shortest Route to Non-Abelian Topological Order on a Quantum Processor”. In: *Phys. Rev. Lett.* 131 (6 Aug. 2023), p. 060405. DOI: 10.1103/PhysRevLett.131.060405. URL: https://link.aps.org/doi/10.1103/PhysRevLett.131.060405.

[330] Nathanan Tantivasadakarn, Ashvin Vishwanath, and Ruben Verresen. “Hierarchy of Topological Order From Finite-Depth Unitaries, Measurement, and Feedforward”. In: *PRX Quantum* 4 (2 June 2023), p. 020339. DOI: 10.1103/PRXQuantum.4.020339. URL: https://link.aps.org/doi/10.1103/PRXQuantum.4.020339.

[331] Nathanan Tantivasadakarn et al. *Long-range entanglement from measuring symmetry-protected topological phases*. 2022. arXiv: 2112.01519 [cond-mat.str-el].

[332] Simon Trebst. *Kitaev Materials*. 2017. arXiv: 1701.07056 [cond-mat.str-el]. URL: https://arxiv.org/abs/1701.07056.

[333] Loïc Turban. “One-dimensional Ising model with multispin interactions”. In: *Journal of Physics A: Mathematical and Theoretical* 49.35 (Aug. 2016), p. 355002. DOI: 10.1088/1751-8113/49/35/355002. URL: https://doi.org/10.1088%5C%2F1751-8113%5C%2F49%5C%2F35%5C%2F355002.

[334] Masafumi Udagawa and Roderich Moessner. *Spectroscopy of Majorana modes of non-Abelian vortices in Kitaev’s chiral spin liquid*. 2019. arXiv: 1912.01545 [cond-mat]. URL: https://arxiv.org/abs/1912.01545.

[335] Masafumi Udagawa, Shintaro Takayoshi, and Takashi Oka. “Scanning Tunneling Microscopy as a Single Majorana Detector of Kitaev’s Chiral Spin Liquid”. In: *Phys. Rev. Lett.* 126 (12 Mar. 2021), p. 127201. DOI: 10.1103/PhysRevLett.126.127201. URL: https://link.aps.org/doi/10.1103/PhysRevLett.126.127201.

[336] Ruben Verresen, Roderich Moessner, and Frank Pollmann. “One-dimensional symmetry protected topological phases and their transitions”. In: *Physical Review B* 96.16 (Oct. 2017). ISSN: 2469-9969. DOI: 10.1103/physrevb.96.165124. URL: http://dx.doi.org/10.1103/PhysRevB.96.165124.

[337] Ruben Verresen, Nathanan Tantivasadakarn, and Ashvin Vishwanath. *Efficiently preparing Schrödinger's cat, fractons and non-Abelian topological order in quantum devices*. 2022. arXiv: 2112.03061 [quant-ph].

[338] Tamás Vicsek and Fereydoon Family. "Dynamic Scaling for Aggregation of Clusters". In: *Phys. Rev. Lett.* 52 (19 May 1984), pp. 1669–1672. DOI: 10.1103/PhysRevLett.52.1669. URL: https://link.aps.org/doi/10.1103/PhysRevLett.52.1669.

[339] Sagar Vijay and Liang Fu. "Teleportation-based quantum information processing with Majorana zero modes". In: *Phys. Rev. B* 94.23 (Dec. 2016), p. 235446. ISSN: 2469-9969. DOI: 10.1103/PhysRevB.94.235446.

[340] Yuval Vinkler-Aviv and Achim Rosch. "Approximately Quantized Thermal Hall Effect of Chiral Liquids Coupled to Phonons". In: *Phys. Rev. X* 8 (3 Aug. 2018), p. 031032. DOI: 10.1103/PhysRevX.8.031032. URL: https://link.aps.org/doi/10.1103/PhysRevX.8.031032.

[341] Matthias Vojta, Andrew K. Mitchell, and Fabian Zschocke. "Kondo Impurities in the Kitaev Spin Liquid: Numerical Renormalization Group Solution and Gauge-Flux-Driven Screening". In: *Phys. Rev. Lett.* 117 (3 July 2016), p. 037202. DOI: 10.1103/PhysRevLett.117.037202. URL: https://link.aps.org/doi/10.1103/PhysRevLett.117.037202.

[342] Chong Wang, Ashvin Vishwanath, and Bertrand I. Halperin. "Topological order from disorder and the quantized Hall thermal metal: Possible applications to the $\nu = 5/2$ state". In: *Physical Review B* 98.4 (July 2018). ISSN: 2469-9969. DOI: 10.1103/physrevb.98.045112. URL: http://dx.doi.org/10.1103/PhysRevB.98.045112.

[343] Junfeng Wang et al. "Bond and site percolation in three dimensions". In: *Phys. Rev. E* 87 (5 May 2013), p. 052107. DOI: 10.1103/PhysRevE.87.052107. URL: https://link.aps.org/doi/10.1103/PhysRevE.87.052107.

[344] Zezhu Wei, V. F. Mitrovi ć, and D. E. Feldman. "Thermal Interferometry of Anyons in Spin Liquids". In: *Phys. Rev. Lett.* 127 (16 Oct. 2021), p. 167204. DOI: 10.1103/PhysRevLett.127.167204. URL: https://link.aps.org/doi/10.1103/PhysRevLett.127.167204.

[345] Zezhu Wei et al. "Thermal interferometry of anyons". In: *Phys. Rev. B* 107 (10 Mar. 2023), p. 104406. DOI: 10.1103/PhysRevB.107.104406. URL: https://link.aps.org/doi/10.1103/PhysRevB.107.104406.

[346] S. Widmann et al. "Thermodynamic evidence of fractionalized excitations in α-$RuCl_3$". In: *Phys. Rev. B* 99 (9 Mar. 2019), p. 094415. DOI: 10.1103/PhysRevB.99.094415. URL: https://link.aps.org/doi/10.1103/PhysRevB.99.094415.

[347] A. J. Willans, J. T. Chalker, and R. Moessner. "Disorder in a Quantum Spin Liquid: Flux Binding and Local Moment Formation". In: *Phys. Rev. Lett.* 104 (23 June 2010), p. 237203. DOI: 10.1103/PhysRevLett.104.237203. URL: https://link.aps.org/doi/10.1103/PhysRevLett.104.237203.

[348] A. J. Willans, J. T. Chalker, and R. Moessner. "Site dilution in the Kitaev honeycomb model". In: *Phys. Rev. B* 84 (11 Sept. 2011), p. 115146. DOI: 10.1103/PhysRevB.84.115146. URL: https://link.aps.org/doi/10.1103/PhysRevB.84.115146.

[349] R. L. Willett et al. "Interference measurements of non-Abelian $e/4$ and Abelian $e/2$ quasiparticle braiding". unpublished. 2019. arXiv: 1905.10248.

[350] Stephen M. Winter et al. "Models and materials for generalized Kitaev magnetism". In: *J. Phys.: Condens. Matter* 29.49 (Nov. 2017), p. 493002. ISSN: 0953-8984. DOI: 10.1088/1361-648X/aa8cf5.

[351] Michael M. Wolf. "Violation of the Entropic Area Law for Fermions". In: *Phys. Rev. Lett.* 96 (1 Jan. 2006), p. 010404. DOI: 10.1103/PhysRevLett.96.010404. URL: https://link.aps.org/doi/10.1103/PhysRevLett.96.010404.

[352] A. U. B. Wolter et al. "Field-induced quantum criticality in the Kitaev system α-$RuCl_3$". In: *Phys. Rev. B* 96 (4 July 2017), p. 041405. DOI: 10.1103/PhysRevB.96.041405. URL: https://link.aps.org/doi/10.1103/PhysRevB.96.041405.

[353] F Y Wu. "Dilute Potts model, duality and site-bond percolation". In: *Journal of Physics A: Mathematical and General* 14.2 (Feb. 1981), p. L39. DOI: 10.1088/0305-4470/14/2/004. URL: https://dx.doi.org/10.1088/0305-4470/14/2/004.

[354] F. Y. Wu. "The Potts model". In: *Rev. Mod. Phys.* 54 (1 Jan. 1982), pp. 235–268. DOI: 10.1103/RevModPhys.54.235. URL: https://link.aps.org/doi/10.1103/RevModPhys.54.235.

[355] Xiao Xu et al. "Simultaneous analysis of three-dimensional percolation models". In: *Frontiers of Physics* 9.1 (Nov. 2013), pp. 113–119. ISSN: 2095-0470. DOI: 10.1007/s11467-013-0403-z. URL: http://dx.doi.org/10.1007/s11467-013-0403-z.

[356] Yilun Xu et al. *QubiC 2.0: An Extensible Open-Source Qubit Control System Capable of Mid-Circuit Measurement and Feed-Forward*. 2023. arXiv: 2309.10333 [quant-ph].

[357] M. Yamashita et al. "Sample dependence of half-integer quantized thermal Hall effect in the Kitaev spin-liquid candidate $\alpha-RuCl_3$". In: *Phys. Rev. B* 102.22 (Dec. 2020), p. 220404. ISSN: 2469-9969. DOI: 10.1103/PhysRevB.102.220404.

[358] Bowen Yang et al. "Magnetic anisotropy reversal driven by structural symmetry-breaking in monolayer $\alpha-RuCl_3$". In: *Nature Materials* 22.1 (Jan. 2023), pp. 50–57. ISSN: 1476-4660. DOI: 10.1038/s41563-022-01401-3. URL: https://doi.org/10.1038/s41563-022-01401-3.

[359] Hong Yao and Steven A. Kivelson. "Exact Chiral Spin Liquid with Non-Abelian Anyons". In: *Phys. Rev. Lett.* 99 (24 Dec. 2007), p. 247203. DOI: 10.1103/PhysRevLett.99.247203. URL: https://link.aps.org/doi/10.1103/PhysRevLett.99.247203.

[360] Mengxing Ye et al. "Quantization of the Thermal Hall Conductivity at Small Hall Angles". In: *Phys. Rev. Lett.* 121 (14 Oct. 2018), p. 147201. DOI: 10.1103/PhysRevLett.121.147201. URL: https://link.aps.org/doi/10.1103/PhysRevLett.121.147201.

[361] T. Yokoi et al. "Half-integer quantized anomalous thermal Hall effect in the Kitaev material candidate α–$RuCl_3$". In: *Science* 373.6554 (July 2021), pp. 568–572. ISSN: 1095-9203. DOI: 10.1126/science.aay5551. URL: http://dx.doi.org/10.1126/science.aay5551.

[362] Aidan Zabalo et al. "Critical properties of the measurement-induced transition in random quantum circuits". In: *Phys. Rev. B* 101 (6 Feb. 2020), p. 060301. DOI: 10.1103/PhysRevB.101.060301. URL: https://link.aps.org/doi/10.1103/PhysRevB.101.060301.

[363] B. Zeng et al. *Quantum Information Meets Quantum Matter: From Quantum Entanglement to Topological Phases of Many-Body Systems*. Quantum Science and Technology. Springer New York, 2019. ISBN: 9781493990849. DOI: 10.1007/978-1-4939-9084-9. URL: https://doi.org/10.1007/978-1-4939-9084-9.

[364] Heda Zhang et al. *Evidence of chiral fermion edge modes through geometric engineering of thermal Hall in α-$RuCl_3$*. 2025. arXiv: 2505.05417 [cond-mat.str-el]. URL: https://arxiv.org/abs/2505.05417.

[365] Yi Zhou, Kazushi Kanoda, and Tai-Kai Ng. "Quantum spin liquid states". In: *Rev. Mod. Phys.* 89 (2 Apr. 2017), p. 025003. DOI: 10.1103/RevModPhys.89.025003. URL: https://link.aps.org/doi/10.1103/RevModPhys.89.025003.

[366] Guo-Yi Zhu, Nathanan Tantivasadakarn, and Simon Trebst. *Structured volume-law entanglement in an interacting, monitored Majorana spin liquid*. 2023. arXiv: 2303.17627.

[367] P. Zinn-Justin. *Six-Vertex, Loop and Tiling models: Integrability and Combinatorics*. 2009. arXiv: 0901.0665 [math-ph].

[368] Z. Zou and P. W. Anderson. "Neutral fermion, charge-e boson excitations in the resonating-valence-bond state and superconductivity in La_2CuO_4-based compounds". In: *Phys. Rev. B* 37 (1 Jan. 1988), pp. 627–630. DOI: 10.1103/PhysRevB.37.627. URL: https://link.aps.org/doi/10.1103/PhysRevB.37.627.

Appendix A

Appendices for Part I

A.1 Perturbative Temperature Calculation

Here we elaborate on the perturbative approach from the main text and provide derivations of the first-order edge and bulk temperatures in Eqs. (3.14) and (3.15). The unperturbed (zeroth-order) temperatures correspond to vanishing edge-bulk coupling λ. As we describe in the main text, since the hot and cold leads couple to the bulk phonons rather than the edge mode, the zeroth-order edge temperature vanishes: $T_{\mathrm{e}}^{(0)}(r,\vartheta) = 0$. Furthermore, the zeroth-order bulk temperature within the right lobe is imposed by the boundary conditions to be $T_{\mathrm{b}}^{(0)}(r,\vartheta) = A + B\ln(r/r_0)$, where $A = \delta T[1+\alpha\ln(R/r_0)]^{-1}$ and $B = \alpha A$ [see Eq. (3.7)]. We now seek the first-order perturbative corrections to these edge and bulk temperatures within the right lobe as a result of finite edge-bulk coupling λ.

Let us first focus on the first-order correction to the edge temperature, $T_{\mathrm{e}}^{(1)}(r,\vartheta)$. By considering Eqs. (3.8) and (3.9) with $n = 1$, this first-order correction must satisfy the ordinary differential equations

$$\begin{aligned}
\frac{\partial T_{\mathrm{e}}^{(1)}(R,\vartheta)}{\partial\vartheta} &= \frac{R}{\ell}\left[T_{\mathrm{b}}^{(0)}(R,\vartheta) - T_{\mathrm{e}}^{(1)}(R,\vartheta)\right],\\
\frac{\partial T_{\mathrm{e}}^{(1)}(r,\pm\vartheta_0)}{\partial r} &= \mp\frac{1}{\ell}\left[T_{\mathrm{b}}^{(0)}(r,\pm\vartheta_0) - T_{\mathrm{e}}^{(1)}(r,\pm\vartheta_0)\right],
\end{aligned} \tag{A.1}$$

along with the corresponding boundary condition

$$T_{\mathrm{e}}^{(1)}(r_0,-\vartheta_0) = (2\beta-1)\,T_{\mathrm{e}}^{(1)}(r_0,\vartheta_0). \tag{A.2}$$

As described in the main text, we assume that the edge-bulk thermalization length ℓ is much larger than the central region, $\ell \gg r_0$, but much smaller than the lobe width, $\ell \ll R\vartheta_0 \lesssim R$. In this regime, the edge temperature thermalizes well along the outer edge of the right lobe, and we can thus write $T_{\mathrm{e}}^{(1)}(R,\vartheta_0) = \delta T$. Solving Eq. (A.1) for the top edge of the right lobe ($\vartheta = \vartheta_0$), the edge temperature along this edge is then given by

$$T_{\mathrm{e}}^{(1)}(r,\vartheta_0) = A + B\ln(r/r_0) + Be^{r/\ell}\left[\mathrm{Ei}(-R/\ell) - \mathrm{Ei}(-r/\ell)\right], \tag{A.3}$$

where $\mathrm{Ei}(x)$ is the exponential integral function with asymptotic forms

$$\mathrm{Ei}(-x) = \begin{cases} \ln x + \gamma & (x \ll 1), \\ -\frac{1}{x} e^{-x} & (x \gg 1). \end{cases} \tag{A.4}$$

We note that, as a result of edge-bulk thermalization, this edge temperature is independent of β. Next, if we drop exponentially small terms from Eq. (A.3), and employ Eq. (A.2), the edge temperatures of the top and bottom edges at the interface with the central region ($r = r_0$) are found to be

$$\begin{aligned} T_{\mathrm{e}}^{(1)}(r_0, \vartheta_0) &= A + B e^{r_0/\ell} \left[\ln(\ell/r_0) - \gamma\right] \approx A + B \left[\ln(\ell/r_0) - \gamma\right], \\ T_{\mathrm{e}}^{(1)}(r_0, -\vartheta_0) &\approx (2\beta - 1) \left\{A + B \left[\ln(\ell/r_0) - \gamma\right]\right\}. \end{aligned} \tag{A.5}$$

Solving Eq. (A.1) for the bottom edge of the right lobe ($\vartheta = -\vartheta_0$), the edge temperature along this edge is then

$$\begin{aligned} T_{\mathrm{e}}^{(1)}(r, -\vartheta_0) \approx & A + B \ln(r/r_0) + B e^{-r/\ell} \left[\mathrm{Ei}(r_0/\ell) - \mathrm{Ei}(r/\ell)\right] \\ & - \left[A + (1 - 2\beta) \left\{A + B \left[\ln(\ell/r_0) - \gamma\right]\right\}\right] e^{-r/\ell}. \end{aligned} \tag{A.6}$$

This edge temperature has both a β-independent and a β-linear part. Differentiating with respect to β, and recalling the definitions of A and B, we immediately recover the result in Eq. (3.14) of the main text.

Having found the first-order correction to the edge temperature, we may now consider the corresponding correction to the bulk (phonon) temperature, $T_{\mathrm{b}}^{(1)}(r, \vartheta)$. This first-order correction must satisfy Laplace's equation [see Eq. (3.10)],

$$\frac{\partial^2 T_{\mathrm{b}}^{(1)}(r, \vartheta)}{(\partial \ln r)^2} + \frac{\partial^2 T_{\mathrm{b}}^{(1)}(r, \vartheta)}{\partial \vartheta^2} = 0, \tag{A.7}$$

subject to the corresponding boundary conditions [see Eqs. (3.11)-(3.13)],

$$\begin{aligned} T_{\mathrm{b}}^{(1)}(R, \vartheta) &= 0, \\ \frac{\partial T_{\mathrm{b}}^{(1)}(r = r_0, \vartheta)}{\partial \ln r} &= \alpha T_{\mathrm{b}}^{(1)}(r_0, \vartheta), \\ \frac{\partial T_{\mathrm{b}}^{(1)}(r, \vartheta = \vartheta_0)}{\partial \vartheta} &= -\frac{\lambda r}{\kappa_{\mathrm{b}}} \left[T_{\mathrm{b}}^{(0)}(r, \vartheta_0) - T_{\mathrm{e}}^{(1)}(r, \vartheta_0)\right] \\ &= \frac{\lambda r}{\kappa_{\mathrm{b}}} B e^{r/\ell} \left[\mathrm{Ei}(-R/\ell) - \mathrm{Ei}(-r/\ell)\right], \\ \frac{\partial T_{\mathrm{b}}^{(1)}(r, \vartheta = -\vartheta_0)}{\partial \vartheta} &= \frac{\lambda r}{\kappa_{\mathrm{b}}} \left[T_{\mathrm{b}}^{(0)}(r, -\vartheta_0) - T_{\mathrm{e}}^{(1)}(r, -\vartheta_0)\right] \\ &= -\frac{\lambda r}{\kappa_{\mathrm{b}}} \Big\{ B e^{-r/\ell} \left[\mathrm{Ei}(r_0/\ell) - \mathrm{Ei}(r/\ell)\right] \\ &\quad - \left[A + (1 - 2\beta) \left\{A + B \left[\ln(\ell/r_0) - \gamma\right]\right\}\right] e^{-r/\ell} \Big\}. \end{aligned} \tag{A.8}$$

Let us briefly recall the origin of these boundary conditions from the main text. The first boundary condition reflects that the bulk temperature along the outer edge is fixed due to contact with the thermal lead and, thus, all corrections to the bulk temperature must vanish there. The second boundary condition relates the bulk heat current through the narrow channel in the central region and the bulk heat current through the right lobe. The remaining two boundary conditions enforce that the perpendicular heat current along the boundary of the bulk is consistent with the edge-bulk heat exchange which, in turn, depends on the edge temperatures previously found.

Given that Laplace's equation is linear and all inhomogeneities come from $T_{\mathrm{b}}^{(0)}(r,\pm\vartheta_0)$ and $T_{\mathrm{e}}^{(1)}(r,\pm\vartheta_0)$ in the last two boundary conditions, we may decompose the bulk temperature into a β-independent and a β-linear component, $T_{\mathrm{b}}^{(1)}(r,\vartheta) = \bar{T}_{\mathrm{b}}^{(1)}(r,\vartheta) + \beta\hat{T}_{\mathrm{b}}^{(1)}(r,\vartheta)$, where $\bar{T}_{\mathrm{b}}^{(1)}(r,\vartheta)$ and $\hat{T}_{\mathrm{b}}^{(1)}(r,\vartheta)$ carry no β dependence. Since we are interested in the sensitivity of the bulk temperature to tunneling processes in the central region, we focus on the β derivative $\hat{T}_{\mathrm{b}}^{(1)}(r,\vartheta) = \partial T_{\mathrm{b}}^{(1)}(r,\vartheta)/\partial\beta$. By linearity, this temperature sensitivity must satisfy the same Laplace's equation,

$$\frac{\partial^2 \hat{T}_{\mathrm{b}}^{(1)}(r,\vartheta)}{(\partial \ln r)^2} + \frac{\partial^2 \hat{T}_{\mathrm{b}}^{(1)}(r,\vartheta)}{\partial\vartheta^2} = 0, \tag{A.9}$$

but the relevant boundary conditions are now given by

$$\begin{aligned}
\hat{T}_{\mathrm{b}}^{(1)}(R,\vartheta) &= 0,\\
\frac{\partial \hat{T}_{\mathrm{b}}^{(1)}(r=r_0,\vartheta)}{\partial \ln r} &= \alpha \hat{T}_{\mathrm{b}}^{(1)}(r_0,\vartheta),\\
\frac{\partial \hat{T}_{\mathrm{b}}^{(1)}(r,\vartheta=\vartheta_0)}{\partial\vartheta} &= 0,\\
\frac{\partial \hat{T}_{\mathrm{b}}^{(1)}(r,\vartheta=-\vartheta_0)}{\partial\vartheta} &= -\frac{2\lambda}{\kappa_{\mathrm{b}}}\left\{A + B\left[\ln(\ell/r_0) - \gamma\right]\right\} r e^{-r/\ell}.
\end{aligned} \tag{A.10}$$

Expanding in a basis of orthogonal eigenfunctions, we seek a separable solution of the general form

$$\hat{T}_{\mathrm{b}}^{(1)}(r,\vartheta) = \sum_{n=0}^{\infty} \sin\left[\mu_n \ln(R/r)\right]\left\{C_n \cosh[\mu_n\vartheta] + S_n \sinh[\mu_n\vartheta]\right\}, \tag{A.11}$$

where μ_n is the $(n+1)$-th smallest positive $[(n+\frac{1}{2})\pi < \mu_n \ln(R/r_0) < (n+1)\pi]$ solution of the transcendental equation

$$\mu_n = -\alpha \tan[\mu_n \ln(R/r_0)]. \tag{A.12}$$

The expression in Eq. (A.11) automatically satisfies the first two boundary conditions ($r = r_0$ and $r = R$), while it may satisfy the remaining boundary conditions ($\vartheta = \pm\vartheta_0$) for appropriately chosen coefficients C_n and S_n. To find these coefficients, we consider the angular derivatives,

$$\frac{\partial \hat{T}_{\mathrm{b}}^{(1)}(r,\vartheta=\pm\vartheta_0)}{\partial\vartheta} = \sum_{n=0}^{\infty} \mu_n \sin[\mu_n \ln(R/r)]\{S_n \cosh[\mu_n\vartheta_0] \pm C_n \sinh[\mu_n\vartheta_0]\}, \tag{A.13}$$

as well as the orthogonality relations between the radial eigenfunctions,

$$\begin{aligned}\int_{r_0}^{R} \frac{\mathrm{d}r}{r} \sin[\mu_n \ln(R/r)] \sin[\mu_{n'} \ln(R/r)] &= \frac{\delta_{n,n'}}{2} \left\{1 - \frac{\sin[2\mu_n \ln(R/r_0)]}{2\mu_n \ln(R/r_0)}\right\} \ln(R/r_0) \\ &\equiv \delta_{n,n'} N_n \ln(R/r_0),\end{aligned} \tag{A.14}$$

where N_n are appropriate normalization constants for these eigenfunctions. By comparing these expressions with the boundary conditions in Eq. (A.10), the coefficients C_n and S_n are then found to satisfy

$$\begin{aligned}C_n \sinh[\mu_n \vartheta_0] = -S_n \cosh[\mu_n \vartheta_0] &= \frac{\lambda\{A + B[\ln(\ell/r_0) - \gamma]\}}{\kappa_\mathrm{b} \mu_n N_n \ln(R/r_0)} \int_{r_0}^{R} \mathrm{d}r \sin[\mu_n \ln(R/r)] e^{-r/\ell} \\ &\equiv \frac{I_n}{\mu_n}.\end{aligned} \tag{A.15}$$

Next, we calculate the angular average of the temperature sensitivity in the first-order approximation:

$$\langle \hat{T}_\mathrm{b}^{(1)}(r) \rangle \equiv \frac{1}{2\vartheta_0} \int_{-\vartheta_0}^{\vartheta_0} \mathrm{d}\vartheta \, \hat{T}_\mathrm{b}^{(1)}(r, \vartheta). \tag{A.16}$$

This angular average is a lower bound to the maximal temperature sensitivity at the given radius, $\hat{T}_\mathrm{b}^{(1)}(r, -\vartheta_0)$, which corresponds to the bottom edge ($\vartheta = -\vartheta_0$), and becomes an accurate lower bound in the limit of $\vartheta_0 \ll 1$. Employing the compact notation from Eq. (A.15), the average temperature sensitivity may then be written as

$$\langle \hat{T}_\mathrm{b}^{(1)}(r) \rangle = \sum_{n=0}^{\infty} \frac{C_n \sinh[\mu_n \vartheta_0] \sin[\mu_n \ln(R/r)]}{\mu_n \vartheta_0} = \sum_{n=0}^{\infty} \frac{I_n \sin[\mu_n \ln(R/r)]}{\mu_n^2 \vartheta_0}. \tag{A.17}$$

Since the magnitude of $I_n \sin[\mu_n \ln(R/r)]$ is bounded from above, it follows from $\mu_n > (n + \frac{1}{2})\pi / \ln(R/r_0)$ that the summand decays as $1/n^2$. Thus, the sum in n is convergent, and we may approximate it by its leading ($n = 0$) term:

$$\begin{aligned}\langle \hat{T}_\mathrm{b}^{(1)}(r) \rangle &\approx \frac{I_0 \sin[\mu_0 \ln(R/r)]}{\mu_0^2 \vartheta_0} \\ &= \frac{\sin[\mu_0 \ln(R/r)]}{\mu_0^2 \vartheta_0} \frac{\lambda\{A + B[\ln(\ell/r_0) - \gamma]\}}{\kappa_\mathrm{b} N_0 \ln(R/r_0)} \int_{r_0}^{R} \mathrm{d}r \sin[\mu_0 \ln(R/r)] e^{-r/\ell}.\end{aligned} \tag{A.18}$$

Recalling the assumption $r_0 \ll \ell \ll R$, we may then approximate the integrand as

$$\int_{r_0}^{R} \mathrm{d}r \sin[\mu_0 \ln(R/r)] e^{-r/\ell} \approx \ell \sin[\mu_0 \ln(R/\ell)], \tag{A.19}$$

and obtain the following general expression for the average temperature sensitivity:

$$\langle \hat{T}_\mathrm{b}^{(1)}(r) \rangle \approx \frac{\kappa_\mathrm{e} \{A + B[\ln(\ell/r_0) - \gamma]\} \sin[\mu_0 \ln(R/\ell)] \sin[\mu_0 \ln(R/r)]}{\kappa_\mathrm{b} \vartheta_0 \mu_0^2 N_0 \ln(R/r_0)}. \tag{A.20}$$

Finally, we take the limits of large and small $\alpha = \kappa_c/(\kappa_b\vartheta_0)$. In the first limit ($\alpha \gg 1$), the smallest positive solution of Eq. (A.12) is $\mu_0 \ln(R/r_0) \approx \pi$, and the normalization constant N_0 is approximately 1/2. Since $A \approx \delta T[\alpha \ln(R/r_0)]^{-1}$ and $B \approx \delta T[\ln(R/r_0)]^{-1} \gg A$, the average temperature sensitivity becomes

$$\langle \hat{T}_b^{(1)}(r)\rangle \approx \frac{2}{\pi^2}\left[\ln(\ell/r_0) - \gamma\right]\frac{\kappa_e \delta T}{\kappa_b \vartheta_0}\sin\left[\frac{\pi \ln(R/\ell)}{\ln(R/r_0)}\right]\sin\left[\frac{\pi\ln(R/r)}{\ln(R/r_0)}\right]. \tag{A.21}$$

In the second limit ($\alpha \ll 1$), the smallest positive solution of Eq. (A.12) is $\mu_0 \ln(R/r_0) \approx \pi/2$, and the normalization constant N_0 is again approximately 1/2. Since $A \approx \delta T$ and $B \approx \alpha\delta T \ll A$, the average temperature sensitivity reads

$$\langle \hat{T}_b^{(1)}(r)\rangle \approx \frac{8\ln(R/r_0)}{\pi^2}\frac{\kappa_e \delta T}{\kappa_b \vartheta_0}\sin\left[\frac{\pi \ln(R/\ell)}{2\ln(R/r_0)}\right]\sin\left[\frac{\pi\ln(R/r)}{2\ln(R/r_0)}\right]. \tag{A.22}$$

These final expressions for large and small α are identical to those in Eq. (3.15) of the main text.

A.2 Derivation of Tunneling Conductance

Deriving the scaling function F_ϕ

Here we give an explicit derivation of the scaling function F_h which arises in the generic expression for tunneling conductance. First let us recall the expression for the tunneling current given in Eq. (3.33). Taking $T_{1/2} = T \pm \delta T$, the tunneling conductance is given by $\kappa = \lim_{\delta T \to T} \frac{\langle J_{\text{tun}}\rangle}{2\delta T}$. Denote $G'(k) = \partial_T G(k)$ such that $G_{1/2}(k) = G(k) \pm \delta T G'(k)$. The tunneling current is then given by

$$\langle J_{\text{tun}}\rangle = e^{-i2\pi h_\phi}\sum_{ij} t_{\phi,i}t_{\phi,j}\int_{-\infty}^{\infty}\frac{\mathrm{d}k}{2\pi}\left(G(k) + \delta T G'(k)\right)\left(G(-k) - \delta T G'(-k)\right) k\cos(k\Delta_{ij}) \tag{A.23}$$

Isolating the term linear in δT gives the tunneling conductance,

$$\begin{aligned}
\kappa_{\text{tun}} &= \frac{1}{2}e^{-i2\pi h_\phi}\sum_{ij} t_{\phi,i}t_{\phi,j}\int_{-\infty}^{\infty}\frac{\mathrm{d}k}{2\pi}\left(G'(k)G(-k) - G(k)G'(-k)\right)k\cos(k\Delta_{ij}) \\
&= -\sum_{ij} t_{\phi,i}t_{\phi,j}(2\pi T)^{4h_\phi}\frac{\pi}{\Gamma(2h_\phi)^2}\int_{-\infty}^{\infty}\mathrm{d}u\, u^2\left|\Gamma(h_\phi - iu)\right|^4\cos(2\pi T\Delta_{ij}u) \\
&= -\sum_{ij} t_{\phi,i}t_{\phi,j}(2\pi T)^{4h_\phi}F_\phi(2\pi T\Delta_{ij})
\end{aligned} \tag{A.24}$$

where we have defined the scaling function $F_\phi(x)$ in the last line to contain subleading temperature dependence set by $x = 2\pi T\Delta_{ij}$.

Let us then evaluate the integral entering the definition of $F_\phi(x)$,

$$\begin{aligned}
F_\phi(x) &\equiv \frac{\pi}{\Gamma^2(2h_\phi)} \int_{-\infty}^{\infty} \mathrm{d}u\, u^2 \left|\Gamma(h_\phi - iu)\right|^4 \cos(xu) \\
&= \frac{i\pi}{\Gamma^2(2h_\phi)} \int_{-i\infty}^{+i\infty} \mathrm{d}v\, v^2 \left|\Gamma(h_\phi - v)\right|^4 \cosh(xv) \qquad \text{(with } v = iu\text{)} \\
&= \frac{i\pi}{\Gamma^2(2h_\phi)} \int_{-i\infty}^{+i\infty} \mathrm{d}v\, v^2 e^{xv} \left|\Gamma(h_\phi - v)\right|^4 \\
&= \frac{i\pi}{\Gamma^2(2h_\phi)} \frac{\partial^2}{\partial x^2} \int_{-i\infty}^{+i\infty} \mathrm{d}v\, z^v \Gamma^2(h_\phi - v)^2 \Gamma^2(h_\phi + v) \qquad \text{(with } z = e^x\text{)} \\
&= \frac{-2\pi^2}{\Gamma^2(2h_\phi)} \frac{\partial^2}{\partial x^2} G^{2,2}_{2,2}\left(e^x \middle| \begin{array}{c} 1-h_\phi, 1-h_\phi \\ h_\phi, h_\phi \end{array}\right) \\
&= \frac{-2\pi^2}{\Gamma^2(2h_\phi)} G^{2,4}_{4,4}\left(e^x \middle| \begin{array}{c} 0, 0, 1-h_\phi, 1-h_\phi \\ h_\phi, h_\phi, 1, 1 \end{array}\right).
\end{aligned} \tag{A.25}$$

In the last two lines we have identified the integral with the Meijer-G function, yielding a compact and analytic expression for the tunneling conductance κ_{tun}. We may alternatively express the scaling function $F_\phi(x)$ in terms of more familiar hypergeometric functions,

$$\begin{aligned}
F_\phi(x) = \frac{-2\pi^2\Gamma^2(2h_\phi)h_\phi^2}{\Gamma(4h_\phi)} \frac{z^h}{(z-1)^2} \Big[&(1 + z(6+z))\,{}_2F_1(2h_\phi, 2h_\phi; 4h_\phi; 1-z) \\
&- 4z(1+z)\,{}_2F_1(2h_\phi, 1+2h_\phi; 4h_\phi; 1-z) \Big]
\end{aligned} \tag{A.26}$$

Ising Anyon Tunneling

In this appendix we show that the second order correction from Ising anyon tunneling in a single-pinch geometry diverges at zero temperature and show the appropriate power-scaling for a finite temperature effective tunneling coefficient. Throughout this appendix we will work in units where $v = 1$. The appropriate factors of v can be restored by dimensional analysis.

At second order the correction to the fermion Green's function takes the form

$$-\int_{-\infty}^{\infty} \mathrm{d}s_1 \int_{-\infty}^{s_1} \mathrm{d}s_2 \langle \gamma_1(\delta x, t) \Big[H_{\text{tun}}(s_1) H_{\text{tun}}(s_2) - \langle H_{\text{tun}}(s_1) H_{\text{tun}}(s_2) \rangle \Big] \gamma_1(-\delta x, 0) \rangle, \tag{A.27}$$

where we now adopt the convention that the heat current is measured at coordinate δx along the top edge and fermions are thermally excited by the heating due to a bath connected on the left edge (in the direction of $x = -\delta x$). Since we only care about the transmission across the constriction, we may freely take $\delta x \to 0^+$. Recall that the Ising anyon tunneling Hamiltonian for a single pinch takes the form

$$H_{\text{tun}} = t_\sigma e^{-i\pi/16} \sigma_{\text{top}}(0) \sigma_{\text{bot}}(0), \tag{A.28}$$

where $x = 0$ is the coordinate of the pinch. Evaluating the correction to the Green's function then requires that we evaluate a correlator which, after cluster decomposition between the top and bottom edges, takes the generic form

$$\langle\sigma(y_1)\sigma(y_2)\rangle_{\text{bot}}\left[\langle\gamma(z_1)\sigma(\eta_1)\sigma(\eta_2)\gamma(z_2)\rangle_{\text{top}} - \langle\sigma(\eta_1)\sigma(\eta_2)\rangle_{\text{top}}\langle\gamma(z_1)\gamma(z_2)\rangle_{\text{top}}\right]. \tag{A.29}$$

Closely related calculations have been carried out in detail in several other works [265, 2, 191]. In particular, Aasen *et al.* [2] consider the first order Ising anyon tunneling correction in a loop interferometer, while Nilsson and Akhmerov [265] calculate the backscattered component for the same two pinch geometry we consider in the main text, but working explicitly with the finite temperature correlations for the primary fields. At zero temperature, the correlator is given explicitly by

$$\frac{1}{2y_{12}^{1/8}\eta_{12}^{1/8}z_{12}}\left[-2+\sqrt{\frac{(z_1-\eta_1)(z_2-\eta_2)}{(z_1-\eta_2)(z_2-\eta_1)}}+\sqrt{\frac{(z_1-\eta_2)(z_2-\eta_1)}{(z_1-\eta_1)(z_2-\eta_2)}}\right]. \tag{A.30}$$

In this generic formulation we can treat both the single pinch and double pinch geometries. For concrete purposes though, let us focus our attention on the single pinch case, fixing $y_{1,2} = \eta_{1,2} = is_{1,2} \mp \epsilon$, $z_1 = i(t-\delta x)$, and $z_2 = i\delta x$. Let us also define $s_1 = s$ and $s_2 = s - \Delta_s$ where $\Delta_s \geq 0$. Here ϵ regulates divergences in the correlator. A similar regulator can be taken in the coordinates $z_{1,2}$, but it should be taken smaller than ϵ to preserve the placement of a branch cut in later steps.

Since we are interested in the frequency-space transmission amplitude, let us Fourier transform this expression with $\omega = vk$ and insert our definitions for the coordinates into Eq. (A.30). Taking the limit $\delta x \to 0^+$ and making a shift of variables $s \to s + (\Delta_s + t)/2$, the expression takes on a simple form,

$$-e^{-i\pi/8}t_\sigma^2\int_{-\infty}^{\infty}\mathrm{d}t\int_{-\infty}^{\infty}\mathrm{d}s\int_0^{\infty}\mathrm{d}\Delta_s\frac{e^{i\omega t}}{2it(i\Delta_s-2\epsilon)^{1/4}}\left[-2+\sqrt{\frac{s^2+a^2}{s^2+b^2}}+\sqrt{\frac{s^2+b^2}{s^2+a^2}}\right], \tag{A.31}$$

where $a \equiv \epsilon + i(t-\Delta_s)/2$ and $b \equiv \epsilon - i(t+\Delta_s)/2$.

For $\epsilon > 0$, we see that $\mathrm{Re}\,a, \mathrm{Re}\,b > 0$. Then we may invoke an integral identity to evaluate the integral with respect to s, giving

$$-e^{-i\pi/8}t_\sigma^2\int_{-\infty}^{\infty}\mathrm{d}t\int_0^{\infty}\mathrm{d}\Delta_s\frac{e^{i\omega t}}{2it(i\Delta_s-2\epsilon)^{1/4}}4(a+b)\left[K\left(\frac{a-b}{a+b}\right)-E\left(\frac{a-b}{a+b}\right)\right], \tag{A.32}$$

where K and E are the complete elliptic integrals of the first and second kind. Now substituting the definitions of a and b, one finds that the expression becomes

$$-e^{-i\pi/8}t_\sigma^2\int_{-\infty}^{\infty}\mathrm{d}t\int_0^{\infty}\mathrm{d}\Delta_s\frac{e^{i\omega t}}{2it(i\Delta_s-2\epsilon)^{1/4}}4(-i\Delta_s+2\epsilon)\left[K\left(-\frac{t}{\Delta_s+2i\epsilon}\right)-E\left(-\frac{t}{\Delta_s+2i\epsilon}\right)\right]. \tag{A.33}$$

Taking $\epsilon \to 0^+$, one can then straightforwardly integrate with respect to Δ_s and obtain

$$-e^{-i\pi/8}t_\sigma^2 \frac{2\pi^2\Gamma\left(\frac{1}{8}\right)}{\left(1+(-1)^{1/4}\right)\Gamma\left(-\frac{3}{8}\right)\Gamma\left(\frac{5}{8}\right)\Gamma\left(\frac{15}{8}\right)} \int_0^\infty \mathrm{d}t \left(e^{i\omega t} - e^{-i\omega t}\right) t^{3/4} \tag{A.34}$$

Now integrating with respect to t just gives

$$\frac{8\left(-1\right)^{1/8}\sqrt{-7+5\sqrt{2}}\pi^{7/2}t_\sigma^2}{\omega^{7/4}\Gamma\left(-\frac{3}{8}\right)^2\Gamma\left(\frac{5}{8}\right)\Gamma\left(\frac{15}{8}\right)} \tag{A.35}$$

The above corresponds to the transmission probability at the point contact.

Consider then calculating the correction to the thermal conductance associated with this term. Temporarily neglecting the constant prefactor, we calculate the heat current

$$I_\sigma(T) = v\int_0^\infty \frac{\mathrm{d}k}{2\pi}\varepsilon(k)n(k,T)(vk)^{-7/4} \propto T^{1/4} \tag{A.36}$$

Then differentiating with respect to temperature we get the correction to the conductance

$$\kappa_{\text{tun}} \propto T^{-3/4} \propto \kappa_e T^{-7/4} \tag{A.37}$$

Indeed then we have recovered the Ising anyon tunneling correction to thermal transport reported in the main text.

A.3 Interferometry-based phase gates

In Ch. 4.5 of the main text we laid out several approaches for implementing arbitrary (non-Clifford) single-qubit phase gates using anyon interferometry. Here we provide additional details on how the gate angle θ depends on microscopic tuning parameters, with consideration of the typical parameters expected for candidate material α-RuCl$_3$3. Furthermore, we discuss sources of decoherence and errors, as well as mitigation strategies therein. In Ch. A.3, we focus on the continuous-time scheme in the magnetic tunnel junction setup. Then in Ch. A.3, we consider the discrete-time approach more generically, with application to both the tunnel junction and electrically gated setups.

Continuous-time scheme with magnetic tunnel junctions

The continuous-time interferometry phase gate described in Ch. 4.5 was originally introduced in Ref. [44] and further refined for the case of neutral anyons in Ref. [81]. Here we consider the tunnel junction scheme depicted in Fig. 4.14. Recall that tunnel junctions are employed to temporarily deform the spin liquid edge, producing a pinch point. At this point contact we have a finite rate of Ising anyon tunneling, described by the Hamiltonian $H_{\text{tunnel}} = t_\sigma\sigma(x_1)\sigma(x_2) + \text{h.c.}$, where $x_{1,2}$ are the coordinates of the pinch point along the edge. After a time Δt, the edge is returned to normal, destroying the point contact and thus tuning the tunneling coefficient t_σ to zero. The two interfering paths enclose qubit anyons σ_3 and σ_4 (see Fig. 4.14), for which the fusion channel is diagonal in the computational (Z) basis of the qubit. The interferometry process thus yields a final logical state described by the density matrix $\rho_1 \approx R_Z(\theta)\rho_0 R_Z^\dagger(\theta)$.

The phase-gate angle θ depends on several microscopic parameters. Let us assume that the spin liquid edge has finite temperature T_{edge} and velocity v_{edge}. Defining the dimensionless quantity $\tilde{T} \equiv T_{\text{edge}}\pi\left|x_2 - x_1\right|/v_{\text{edge}}$, the interferometry implements a phase-gate with angle

$$\theta = 4\Delta t \left(\frac{\lambda \tilde{T}}{|x_2 - x_1| \sinh(\tilde{T})}\right)^{1/8} \text{Re}(t_\sigma), \tag{A.38}$$

where λ is a short-range cutoff [81].

Coherent tunneling at the point contact generates entanglement between the edge and the bulk anyons. Tracing out the edge therefore results in decoherence of the logically encoded qubit, with off-diagonal density matrix elements being suppressed by a factor of $e^{-\zeta^2/2}$. Assuming a separation of scales $\Delta t \gg \left|x_2 - x_1\right|/v_{\text{edge}}$ and $\tilde{T} \ll 1$, Ref. [81] obtained

$$\zeta^2 = \frac{|x_2 - x_1|}{48\Delta t v_{\text{edge}}}\theta^2\tilde{T}^3. \tag{A.39}$$

Observe that both the angle θ and the decoherence ζ^2 grow linearly with the tunneling time Δt. Our aim is then to realize robust control over θ while minimizing the decoherence rate. At sufficiently low temperatures $\tilde{T} \to 0$, the phase θ approaches a $\tilde{T}$-independent value

$$\theta = 4\Delta t \text{Re}(t_\sigma)\left(\frac{\lambda}{|x_2 - x_1|}\right)^{1/8} + \mathcal{O}\left(\tilde{T}^2\right).$$

If the tunneling strength t_σ and lengthscale $|x_2 - x_1|$ are fixed, this allows for straightforward tuning of θ by means of the tunneling time. Moreover, in this limit the decoherence rate scales as T_{edge}^3. Thus by cooling the system sufficiently so that $\tilde{T} \ll 1$, decoherence may be almost entirely suppressed.

Let us now comment on the feasibility of such a phase gate scheme in the context of the Kitaev material α-$\text{RuCl}_3$3. We assume an edge velocity $v_{\text{edge}} \sim 10^3\,\text{m}\,\text{s}^{-1}$, lattice constant $a \sim 0.6\,\text{nm}$, and bulk correlation length $\xi_{\text{bulk}} \sim 5\,\text{nm}$. The device geometry is constrained by the requirements that the anyons be well separated (relative to ξ_{bulk}) with respect to one another, the spin liquid edge, and the tunnel junctions used to deform the edge. Moreover, we require that the path length $|x_2 - x_1|$ not be much larger than the thermal coherence length along the edge $\xi_T \sim v_{\text{edge}}/T_{\text{edge}}$. To this end, consider fixing $|x_2 - x_1| \sim 100\,\text{nm}$. Coherence then requires $T_{\text{edge}} \lesssim 76\,\text{mK}$. Similarly, achieving $\tilde{T} \ll 1$ requires temperatures $T_{\text{edge}} \lesssim 24\,\text{mK}$. Note that even for higher temperatures $\tilde{T} \sim 1$, the decoherence given in Eq. (A.39) is negligible for gate timescales Δt on the order of a nanosecond. The tunneling strength t_σ decays exponentially with the ratio d/ξ_{bulk}, where the distance across the point contact d is fixed by device geometry. By calibrating the tunneling time Δt with respect to experimentally determined t_σ, the magnetic tunnel junction architecture should enable robust non-topological phase gates with minimal decoherence. While the requisite temperature T_{edge} is rather small, a noisy demonstration of the non-topological phase gate can be readily achieved even for $T_{\text{edge}} \sim 1\,\text{K}$. Moreover, this temperature constraint is absent in the gate-controlled setup and in the discrete-time phase gate scheme described in the next section.

Discrete-time scheme

We now elaborate upon the discrete-time phase gate scheme wherein interferometry takes place one anyon at a time. The interferometry process, as depicted in Figs. 4.15 and 4.16, acts upon the logical qubit as

$$\rho \to \tilde{\rho} = \frac{\hat{O}\rho\hat{O}^\dagger}{\text{Tr}\left[\hat{O}\rho\hat{O}^\dagger\right]},$$
$$\hat{O} = \cos\left(\frac{\theta}{2}\right) I + \sin\left(\frac{\theta}{2}\right) e^{i\phi} Z.$$

Here, θ and ϕ parameterize the relative amplitude and dynamical phase difference between the two interfering paths, respectively. In Ch. 4.5, we describe how the phase ϕ may be tuned in the tunnel-junction and gate-controlled setups. The logical operator Z appearing in $\hat{O}$ reflects the braid phase accumulated by probe anyon σ_p encircling qubit anyons σ_1 and σ_2. In particular, Z is diagonal in the basis where σ_1 and σ_2 have definite fusion channel I or ψ, for which the braid phase is $+1$ or -1, respectively. For a generic initial state ρ, the resulting matrix elements are

$$\begin{aligned}\tilde{\rho}_{00/11} &= \rho_{00/11}\frac{1 \pm \sin\theta\cos\phi}{1 + \sin\theta\cos\phi(\rho_{00} - \rho_{11})},\\ \tilde{\rho}_{01} &= \rho_{01}\frac{\cos\theta + i\sin\theta\sin\phi}{1 + \sin\theta\cos\phi(\rho_{00} - \rho_{11})}.\end{aligned} \tag{A.40}$$

As seen above, the operator $\hat{O}$ is non-unitary for general values of θ except for when the dynamical phases of the two paths differ by exactly $\phi = \pm\pi/2$. Precisely at $\phi = \pm\pi/2$, this reduces to a simple phase gate $R_Z(\theta)$, yielding the final state

$$\tilde{\rho} = R_Z(\theta)\rho R_Z^\dagger(\theta) = \begin{pmatrix} \rho_{00} & \rho_{01}e^{i\theta} \\ \rho_{10}e^{-i\theta} & \rho_{11} \end{pmatrix}.$$

Then to achieve a desired gate angle (e.g., $\theta = \pi/4$ for the magic gate), the probability of the probe anyon taking one path over the other must be tuned.

Moving away from the unitary limit introduces a finite degree of decoherence. Consider a small phase error $\phi = \frac{\pi}{2} + \epsilon$ with $|\epsilon| \ll 1$ such that $\hat{O} = R_Z(\theta) - \epsilon\sin(\theta/2)Z + \mathcal{O}(\epsilon^2)$. This yields a corresponding correction to the final state $\tilde{\rho} = R_Z(\theta)\,\rho R_Z^\dagger(\theta) + \Delta\tilde{\rho}$, where

$$\Delta\tilde{\rho} = 2\sin\theta\left[-\rho_{00}\rho_{11}Z + (\rho_{00} - \rho_{11})(X\cos\theta - Y\sin\theta)\right].$$

Notably, this correction includes both diagonal and off-diagonal terms, in contrast to the purely off-diagonal decoherence of the continuous-time scheme in Ch. A.3.

When the initial state lies in the equatorial plane of the Bloch sphere (i.e., $\rho_{00} = \rho_{11}$), the leading order effect of phase error $\epsilon \neq 0$ is an induced polarization of the qubit. Namely, $\Delta\tilde{\rho} = -\frac{1}{2}\sin(\theta)Z$ is entirely diagonal. If we further require that ρ is a pure state ($|\rho_{01}| = 1/2$), then the action of $\hat{O}$ is described by an effective unitary,

$$U_{\text{eff}} = R_X\left(\frac{\pi}{2} - \phi\right) R_Z(\theta)\,,$$

such that $\tilde{\rho} = U_{\text{eff}}\rho U_{\text{eff}}^{\dagger}$. Here the R_X gate captures the polarization induced by the interferometry. Such polarization errors can be mitigated by a two-step procedure akin to a spin-echo wherein one first performs the interferometry with parameters (θ, ϕ) and then again with parameters $(\theta, \pi - \phi)$. In the tunnel-junction setup, this phase reversal could be realized by inducing the dynamical phase ϕ on the other hole (by modifying the hole size) after pinching and applying a Z-gate by a braiding operation. Similarly, we can perform this tuning of ϕ in the gate-controlled setup via the Aharonov-Bohm effect by altering the magnetic flux piercing the interferometry loop. The total operator applied by this process is now unitary and for $\phi = \pi/2 + \epsilon$ is simply $R_Z(2\theta) + \mathcal{O}(\epsilon^2)$. While this discrete-time phase gate scheme still requires careful tuning of parameters to achieve the desired phase gate, it yields distinct error channels which we have shown may be controlled and partially mitigated. Moreover, by eliminating the spin liquid edge from the process, it alleviates the temperature constraints for the tunnel-junction setup discussed in Ch. A.3.

Appendix B

Appendices for Part II

B.1 Effective Transfer Matrix for Interacting Majorana Circuits

In this section we derive an effective transfer matrix description for the family of orientable, interacting Majorana circuits considered in Ch. 8.4.

Measurement-only XXZ-chain

Let us consider the decoupled limit of the two-leg ladder (XY and YX) perturbed by four-fermion (ZZ) measurements. Moreover, let us impose a brickwall structure such that the circuit consists of alternating layers of two-qubit bricks. The two types of layers are given identical probabilities for measuring the different operators: $p_{XY} = p_{YX} = sp/2$, $p_{ZZ} = s(1-p)$ and $p_{\mathbb{1}} = 1 - s$. The transfer matrix for this circuit can be written as

$$\hat{T} = \hat{T}_1\hat{T}_2 = \left(\prod_{j=1}^{\lfloor L/2 \rfloor} T_{2j-1}\right)\left(\prod_{j=1}^{\lfloor L/2 \rfloor} T_{2j}\right),$$
$$T_l = (1-s)\mathbb{1} + \frac{sp}{2}\left(\mathcal{P}_{XY} + \mathcal{P}_{YX}\right) + s(1-p)\mathcal{P}_{ZZ}$$

where T_l is the transfer matrix corresponding to a brick acting on qubits l and $l+1$. The projectors $\mathcal{P}_{X_l Y_{l+1}}$ and $\mathcal{P}_{Y_l X_{l+1}}$ individually form the generators of a TL algebra which we denote e_l and f_l, respectively. For forced projections onto the +1 outcome, we may write $\mathcal{P}_{Z_l Z_{l+1}} = \mathbb{1}_{l,l+1} + 2\mathcal{P}_{X_l Y_{l+1}}\mathcal{P}_{Y_l X_{l+1}} - \mathcal{P}_{X_l Y_{l+1}} - \mathcal{P}_{Y_l X_{l+1}}$. Averaging over the possible two-qubit states, a forced projection onto the +1 eigenstate of $Z_l Z_{l+1}$ followed by normalization of the wavefunction may be approximated as $\mathcal{P}_{Z_l Z_{l+1}} \to 1 - e_l - f_l + 2e_l f_l$. The transfer matrix then takes the form

$$T_l = (1 + s(1-2p))\mathbb{1} + \frac{s(3p-2)}{2}(e_l + f_l) + 2s(1-p)e_l f_l$$

Observe that the set $\{E_l \equiv e_l f_l\}$ generates a TL algebra. When $p = \frac{2}{3}$, the transfer matrix involves only this new set of generators,

$$T_l|_{p=\frac{2}{3}} = \left(1 - \frac{s}{3}\right)\mathbb{1} + \frac{2s}{3}E_l$$

Since the odd and even layers of the circuit have the same measurement probabilities, this corresponds to a critical 1-state Potts model with TL algebra generators E_l. Then one can identify $p_c = \frac{2}{3}$ as a strong-coupling fixed point, in agreement with the numerical results presented in Ch. 8.4.

Competing Four-Fermion Measurements

Let us now consider adding XIX measurements which compete with the other four-fermion ZZ measurements. This generally spoils the previous solution for a strong coupling fixed point. Nonetheless, suppose we now take $r_{ZZ} \neq 1$. The circuit must now involve 3-qubit bricks, each of which has a transfer matrix like

$$T_l \sim (1-s)\mathbb{1} + \frac{sp}{2}\left(\mathcal{P}_{XY} + \mathcal{P}_{YX}\right) + s(1-p)\left(r\mathcal{P}_{ZZ} + (1-r)\mathcal{P}_{XIX}\right)$$

As before, we may effectively write $\mathcal{P}_{X_l X_{l+2}} \sim \mathbb{1} - e_l - f_{l+1} + 2e_l f_{l+1}$. Then writing the transfer matrix in terms of the TL generators we have

$$T_l \sim \frac{1-sp}{s}\mathbb{1} + \frac{3p-2}{2}e_l + \frac{p-2(1-p)r}{2}f_l - (1-p)(1-r)f_{l+1} + 2(1-p)e_l\left((1-r)f_{l+1} + rf_l\right)$$

As before, the coefficient on e_l vanishes for $p = 2/3$. Now however there remains finite magnitude of f_i and f_{i+1}. Letting $p = \frac{2}{3} + \delta$, the two terms become $\frac{1-r}{3} + \delta(r + \frac{1}{2})$ and $\frac{1-r}{3} - \delta(1-r)$. We see that these deviate from $(1-r)/3$ in opposite directions. They take on equal and opposite magnitude at $p_c(r) = 2(1-2r)/(1-4r)$, which falls in the interval $[0,1]$ for $r \in [1/2, 1]$. Since the phase diagram must be symmetric under $r \to 1-r$, up to the presence of edge modes, in the interval $r \in [0, 1/2]$ we have a phase boundary at $p_c(r) = 2(1-2r)/(3-4r)$. This is in agreement with the phase diagram obtained from numerical simulation, shown by the black dashed line in Fig. 8.4c.

This argument can be made more precise by considering a full row transfer matrix,

$$T \sim \sum_l \left[\frac{s}{2}(\mathcal{P}_{X_l Y_{l+1}} + \mathcal{P}_{Y_l X_{l+1}}) + (1-s)r\mathcal{P}_{Z_l Z_{l+1}} + (1-r)\mathcal{P}_{X_l X_{l+2}}\right]$$

It is now useful to take the XY and YX measurements to be forced projections onto +1 and −1 on opposite sublattices such that $e_{2l-1} = \mathcal{P}_{X_{2l-1}Y_{2l}}$ while $e_{2l} = \mathbb{1} - \mathcal{P}_{X_{2l}Y_{2l+1}}$. Then forcing ZZ and XIX measurements onto the +1 outcome gives

$$\begin{aligned} T &= \sum_l \left[\lambda(e_l + f_l) + 2(re_l f_l - (1-r)e_l f_{l+1})\right] \\ &= \sum_l \left[\lambda(e_l + f_l) + e_l\left(\delta r(f_l + f_{l+1}) + (f_l - f_{l+1})\right)\right] \end{aligned}$$

where we have defined $\lambda = \frac{s}{2(1-s)} - |\delta r|$ and $\delta r = 2r - 1$. We see that for $s_c(r) = 2|\delta r|/(1+2|\delta r|)$, the linear term vanishes (i.e. $\lambda = 0$), leaving only the couplings $e_l f_l$ and $e_l f_{l+1}$. While we cannot construct a TL algebra from this mixture, we retain a well defined continuum limit. Identifying ϵ and $\bar{\epsilon}$ as the energy-density fields in the CFT for e_l and f_l, respectively, the coupling generally takes the form $\epsilon\,(2\delta r\bar{\epsilon} - \partial_x\bar{\epsilon})$. A shift in the coordinates for $\bar{\epsilon}$ then reduces the coupling to simply $2\delta r\epsilon\bar{\epsilon}$ so that the effective long-wavelength description of the circuit is simply that of the earlier interacting circuit but with a modified interaction strength.